Tailored Cerium-based Metal Organic Frameworks for Preferential Adsorption of Fluoride Ions

A Thesis
Submitted in Partial
Fulfilment of the Requirements for the Degree of

DOCTOR OF PHILOSOPHY

by

Sikha

(186107017)

Department of Chemical Engineering
Indian Institute of Technology Guwahati
Guwahati – 781039, Assam, India

May 2024

Dedicated

To

My Parent, Husband, Daughter and my mentors

Department of Chemical Engineering
Indian Institute of Technology Guwahati
Guwahati – 781039, Assam, India

STATEMENT

I hereby declare that the content embodied in this thesis entitled "**Tailored Cerium-based Metal Organic Frameworks for Preferential Adsorption of Fluoride Ions**" is the result of investigations carried out by me at the Department of Chemical Engineering, Indian Institute of Technology Guwahati, Guwahati, India, under the guidance of Prof. Bishnupada Mandal. In keeping with the general practice of reporting scientific observations, due acknowledgements have been made wherever the work described is based on the findings of other investigators.

May, 2024 Sikha

Department of Chemical Engineering
Indian Institute of Technology Guwahati
Guwahati – 781039, Assam, India

CERTIFICATE

It is certified that the work contained in this thesis entitled **"Tailored Cerium-based Metal-Organic Frameworks for Preferential Adsorption of Fluoride Ions"** submitted by **Sikha** (Roll No. 186107017) for the award of the degree of Doctor of Philosophy has been carried out in Department of Chemical Engineering, Indian Institute of Technology Guwahati under my supervision and this work has not been submitted elsewhere for the award of any other degree or diploma.

This thesis in my opinion, has reached the standard of fulfilling the requirements for the award of the degree of Doctor of Philosophy in accordance with the regulations of the institute.

May, 2024

Prof. Bishnupada Mandal
Professor
Department of Chemical Engineering
Indian Institute of Technology Guwahati
Guwahati, India-781039

ACKNOWLEDGEMENTS

The completion of this thesis would have not been possible without the support and encouragement of various people and institutions. I take this opportunity to thank all those people and institutions who have been an integral part of the successful completion of this thesis.

I express my sincere thanks to my research supervisor **Prof. Bishnupada Mandal** for his valuable guidance towards the completion of my research work. His continuous support towards research and given me enough freedom to think, plan, and execute my ideas towards my work, which has provided a good basis for the present thesis. I would like to thank him for spending his precious time for discussion by which I have gained immense skills of knowledge in terms of research. I am also indebted to Prof. Bishnupada Mandal for instilling in me a craving for perfection. I believe it will always remain with me in my future life. It has been a notable working experience with him.

Besides my supervisor, I would like to thank my doctoral committee member, **Prof. Animes Kr. Golder, Prof. Chandan Das,** Department of Chemical Engineering, and **Prof. Lal Mohan Kundu,** Department of Chemistry, for their valuable suggestion and efforts which made my thesis successful.

I acknowledge with thanks to the **IIT Guwahati** specifically, the **Analytical Lab Facility** (Department of Chemical Engineering), **Central Instrument Facility** (CIF), **Center for Environment**, and **Department of Chemistry** for various instruments used for characterization during the research work carried out.

My special thanks to **Advanced Materials Group**, Materials Sciences and Technology Division, CSIR-North East Institute of Sciences and Technology, Jorhat-785006, Assam for the help in XPS analysis.

I am also grateful to all the **staff and faculty members** of the Department of Chemical Engineering for helping and providing the necessary facilities.

I am very much grateful and lucky to get help from my seniors **Dr. Jinesh Machale, a** postdoctoral fellow at Memorial University of Newfound, Canada**, Dr. Pradip Das** and **Dr.**

Thangsei Nengneilhing Baite of the Chemical Engineering Department for their timely help during my research.

I was fortunate enough to get excellent and close friends like **Sudeshna Gupta, Dr. Ananya Bardhan**, **Aviti Katare, Dr. Sukanya Kundu, Ahana Datta, Shashi Bhushan Singh, Subham Kumar, and Geetanjali Di** for their friendly support and helping nature during my stay in IITG.

I would like to thank all my **seniors**, **juniors**, **friends, lab mates,** and other **well-wishers** whoever made my stay at IITG memorable.

I express my gratitude to my beloved **parents, sisters, and brother** for showering their love, care, sacrifices, and encouragement which have made it possible for me to come so far. Furthermore, and most importantly, I would like to thank my husband **Shiv Pratap Singh**, who has been with me all these years with his love, support, encouragement, and appreciation. He stands with me personally as well as professionally. Thank you for being my muse, editor, proof-reader, and sounding board. But most of all, thank you for being my best friend. Finally, I would like to thank my cute little angel **Samishka Singh** (*Kuhu*) for her immense sacrifices. I owe you everything.

Sikha

May, 2024

TABLE CONTENTS

CHAPTER 4

LIST OF FIGURES

List of Tables

ABSTRACT

Activated carbon possesses a wide-ranging ability to absorb various pollutants, and its adsorption effectiveness can be heightened through chemical and physical modifications. Recently, there has been notable interest in adsorbents impregnated with metals, particularly rare earth metal cerium, due to their biocompatibility, non-toxicity, and redox properties. Cerium, abundant in the earth's crust, exhibits a robust bond strength with fluoride, making it effective for water treatment. Despite the efficiency of individual rare earth metals in fluoride removal, their small particle size often makes them impractical. Consequently, we employed cerium and iron to modify activated carbon, synthesizing an adsorbent using co-precipitation and ultrasonication. This research investigates the efficacy of a sonochemical method in synthesizing an adsorbent (AC/Ce/Fe-1) and studying its adsorption capacity for fluoride ions. Characterization techniques, including SEM, EDX, BET analysis, FTIR, and XRD, confirm fluoride capture and reveal enhanced kinetics via ultrasound activation. The adsorption process exhibits rapid fluoride removal, reaching equilibrium in 20 minutes with a maximum capacity of 52.3 mg/g. The adsorbent maintains high efficiency over multiple cycles and demonstrates a spontaneous exothermic reaction. This study highlights the advantages of sonochemical methods, providing an efficient and cost-effective technique for fluoride removal. Additionally, the study introduces nanoporous Ce-based MOFs to further enhance the adsorption process by modifying material morphology, structure, and functional groups. Different Ce-based metal–organic–frameworks such as Ce-Fu, Ce-BDC, and Ce- H_3BTC were synthesised and investigated for fluoride removal. Ce–Fu MOFs exhibit a maximum adsorption capacity of 64.2 mg/g, and ultrasound-assisted adsorption enhances kinetics. Co-existing ions and electrostatic forces contribute to fluoride removal efficiency. Ce–Fu MOFs maintain high adsorption capabilities over multiple cycles. The research continued to develop hybrid MOFs

(bimetal MOFs) to further enhance the fluoride adsorption capacity. We explore the synthesis of bimetallic MOFs (Ce@Fe1:1, Ce@Al1:1, Ce@La1:1) with inorganic nodes connected by a fumaric acid linker for fluoride removal. The adsorbents show rapid kinetics, achieving maximum capacities of 101.3, 94.33, and 90.9 mg/g, respectively. Zeta potential analysis and XPS spectra confirm electrostatic attraction and ligand exchange reactions. The stability of bimetal MOFs under different pH levels suggests suitability for aqueous environments. Ce@Fe1:1 exhibits relatively weaker hydrophilic characteristics and maintains adsorption efficiency through multiple cycles. This work explores promising adsorbents for fluoride removal from wastewater. Scaling up from batch results to fixed bed adsorption columns (FBAC) is challenging, necessitating a comprehensive assessment of column operations for practical applicability. In overcoming these challenges, our study aims to utilize Ce@Fe1:1/PS beads in a fixed-bed adsorption column for F^- ion removal. Parameters such as bed height, flow rate, and initial fluoride concentration significantly influence column performance. The Thomas model best fits breakthrough curves, demonstrating peak performance at specific conditions. In practical application, Ce@Fe1:1/PS achieves successful fluoride removal from simulated Brahmaputra River water. Regeneration with a NaOH solution maintains column efficiency over three cycles. Ce@Fe1:1/PS proves effective for continuous fluoride removal, showcasing potential for industrial applications.

CHAPTER 1

Introduction, background to the problem, and objectives

CHAPTER 1

An overview of water contamination, its main types, and how they affect both aquatic and terrestrial life are discussed in this chapter. In depth review of fluoride ions paying particular attention to the global scenario, origins, toxicity, and removal methods has been discussed. Additionally, based on a thorough assessment of the literature, the different methods for removing these ions are emphasized. There has been extensive discussion of various adsorbents used so for in the literature. In particular, the advantages of metal-organic frameworks, which have been proposed as workable materials for future adsorption technology. Based on the gaps and challenges, the research objectives were defined and the chapter also briefly highlights the organizational structure of the thesis.

1.1. Introduction

The most vulnerable natural resource water on earth has recently been under increasing threat from several impurities [1]. As a result, poor access to clean drinking water has emerged as the most important and difficult environmental issue [2]. Many emerging nations experience water and atmospheric pollution as a result of rapid economic development. The definition of pollution is the release of unfavorable substances into the atmosphere, which can harm ecosystems and human existence [3]. Water pollution is defined as the presence of chemicals or other foreign substances in water that have negative impacts on living organisms [4].

1.2. Types of water contaminants

Elaborate discussions of both the categories of organic and inorganic pollutants found in water are discussed below:

1.2.1. Organic contaminants

Organic pollutants that end up in water have extremely toxic and cancer-causing impacts on living things [5]. The various kinds of organic water contaminants include organic dyes, fertilizers, pesticides, hydrocarbons, phenols, biphenyls, plasticizers, greases, oils, detergents, and medicines [6]. The disposal of colored wastewater from the dye industry is the most problematic of these since it includes hazardous substances, dissolved solids, acids, and bases, among other things [7]. High textile dye concentrations in water restrict the capacity of the reoxygenation capability and prevent it from reaching sunshine. As a result, it impairs the biological activity and photosynthesis of aquatic plants. Dye includes cationic, anionic, and non-ionic dyes. In an aqueous environment, the non-ionic dyes are disseminated in a unionized condition. Anionic dyes include reactive orange, methyl orange, and brilliant red, whereas cationic dyes include methylene blue, rhodamine B, and crystal violet [8]. The anionic dyes are reactive, naturally acidic, vividly pigmented, and water-soluble, and they are challenging to remove using traditional water treatment techniques. Injurious consequences such as skin allergies, eye injuries, diarrhea, gastrointestinal irritation with nausea, and harm to the liver, central nervous, reproductive, and respiratory systems are brought on by the presence of methylene blue, methyl orange, and phenolic compounds in drinking/usable water [9]. It is vital to remove these toxins from water in order to have a clean water system that will protect human health and aquatic habitats. Because of urbanisation and population increase, wastewater purification is given a lot of importance [10].

1.2.2. Inorganic contaminants

Toxic metals, minerals, and salts present in the form of dissolved anions and cations are examples of inorganic pollutants. Cadmium, lead, hexavalent chromium, copper, mercury, nickel, arsenate/arsenite, fluorine, iron, and other inorganic pollutants are the most frequently discovered ones [6]. Drinking water contamination by mineral ions is dangerous for people, vegetation, and animals [7]. A quick review of several inorganic pollutants has been emphasized in this section.

Due to its detrimental impact on human health, arsenic contamination in groundwater stands as a prominent environmental challenge [11]. As per the recommendation of WHO the arsenic level in drinking water should not exceed 10 μgL^{-1} [12]. Humans frequently suffer from neurological disorders, cardiovascular ailments, and skin problems while drinking water that has arsenic levels of 10–50 μgL^{-1} [13]. The reports have found that over 200 million people suffer from nonfatal infectious death and every year 10–20 million population die because of waterborne diseases [14]. The main causes of arsenic pollution in ground water include a variety of reasons, including the reductive dissolution of minerals containing arsenic, mining operations, industrial discharge, and the use of fertilisers and pesticides [15]. Arsenic exists in two distinct forms: organic and inorganic. While organic arsenic components are frequently found in diet and have few harmful effects on human health, inorganic arsenic components are mostly discovered from natural exposure. Reduced and oxidised forms of As(III) and As(V) coexist. While As(V) is the dominating form in oxygenated water and occurs as anionic forms of H_2AsO^{4-}, $HAsO_4^{2-}$, and AsO_4^{3-} throughout a wide pH range, As(III) is available in a large range of pH (below pH 9.2) as a non-ionic form. Long-term low-concentration ingestion results in both cancer and non-cancerous health issues [16].

Lead ions are existed in the environment in two forms viz., 0 and +2 oxidation states [17]. Between the two forms, the Pb(II) ion is commonly present as a soluble species in water [18]. Lead is widely used in different industries because of its corrosion resistant, high density, ductility, and malleability properties. It is used in water pipes, cosmetics, paints, pigment in glaze ceramics, building materials, and glass industries [19]. Lead toxicity in the environment and water is enhanced due to rapid industrialization and/or industrial growth to fulfill the people's demand. Leaching of Pb(II) ions from industrial effluents causes water contamination affecting human health like headaches, brain and kidney damage, memory loss, dullness, nervous breakdown, and hypertension [20]. According to the World Health Organization (WHO) and US−EPA guidelines, the maximum allowable limits of Pb(II) ions are 0.01 ppm and 0.015 ppm in drinking water, respectively.

The presence of iron in groundwater is a worldwide problem [21,22]. The corrosion of iron pipes and the release of iron-containing effluents from industries are the two major foundations of iron contamination in groundwater. It is present in water in two states, either in the reduced soluble form of Fe^{2+} (ferrous salt) or oxidized insoluble form of Fe^{3+} (ferric salt)[22]. The existence of less amount of iron in drinking water is advantageous to human health. However, its presence above a certain limit is not desirable because it creates bad taste, discoloration, aesthetic problems, staining, and high turbidity. WHO recommended, the allowable limit of iron is 0.3 mgL^{-1} in drinking water [23]. It is worth mentioning that long-term exposure to drinking water containing a high level of Fe^{2+}/Fe^{3+} may cause severe health diseases like anemia, kidney disease, metabolic disorders, and cancer-causing effects.

The transition metal chromium was revealed in 1797 by the French chemist Lous Vauquelin. The principal chromium component Ferric chromite is mostly discovered in the Philippines, India, Kazakhstan, Russia, and South Africa [24]. There are three primary oxidation states (II),

(III), and (VI) for chromium, in which Cr(II) being the least stable [25]. It displays biological importance in aqueous solution in the trivalent (III), and hexavalent (VI) forms. However, the two states have very different levels of toxicity, with Cr(VI) being much more hazardous than Cr(III) [26]. Cr(III) is insoluble and is a micronutrient of biological relevance [27]. Cr(VI) occurs in several forms depending on the pH including H_2CrO_4, $HCrO_4^-$, CrO_4^{2-}, and $Cr_2O_7^{2-}$ and is extremely soluble (1680 g/L) throughout a broad pH range [24].

1.3. Fluoride in water worldwide

Fluoride levels in the potable water of many countries currently vary from 0.2 to 48 mg/L. According to BIS, the ideal fluorine level is 1 ppm. The allowable limit of fluoride set by the WHO is 0.8 to 1.5 mg L^{-1} vital for the mineralization of bone and assurance against dental cavities [28]. The fluoride pollution in groundwater is a major concern in countries such as Argentina, Pakistan, Ethiopia, Kenya, India, and China [29–31]. The groundwater consumers in the states of India i.e, Delhi, Gujrat, Madhya Pradesh, Rajasthan, Chhattisgarh, Punjab, Andhra Pradesh, and Karnataka are at considerable threat and children are at higher threat than adults [31–33]. There have been reports of high fluoride levels in 230 municipalities across 20 Indian states. The worst-affected regions are Andhra Pradesh, Gujarat, and Rajasthan. States that are moderately impacted include Maharashtra, Madhya Pradesh, Haryana, and Punjab, while states that are slightly affected include Assam, Bihar, Uttar Pradesh, West Bengal, and Tamil Nadu.

1.4. Source of fluoride

The most electronegative fluoride ions are primarily generated through natural sources [34]. In the lithosphere, fluorine is found in a variety of minerals, including fluorspar (CaF_2), cryolite

(Na_3AlF_6), and apatite ($Ca_5(PO_4)_3F$), as well as in families of minerals, including mica, hornblende, and pegmatites, which include topaz and tourmaline [2,35,36]. The dissociation of fluoride from fluoride-rich rocks is demonstrated by the reaction given below:

$$CaF_2 + 2NaHCO_3 \rightarrow 2F^- + CaCO_3 + 2Na^+ + H_2O + CO_2 \quad (1.1)$$

$$Ca_5\,(PO_4)_3F + 3H^+ \rightarrow 5Ca^{2+} + 3HPO_4^{3-} + F^- \quad (1.2)$$

Fluoride leaches out of the rocks as groundwater percolates through them as a result concentration increases far above the safe level. Additionally, fluoride can leak into groundwater from anthropogenic sources such as coal burning, septic tank seepage, and agricultural applications of pesticides and fertilizers [29]. The fluorine mineral fluorapatite is thought to be the most prevalent one on earth [37]. It has also been noted that sediments contain additional fluorides, such as CaF_2 and AlF_3, as well as aluminosilicates, such as $Al_2(SiF_6)_3$. The degradation of water quality is also a result of industrialization and urbanization processes such as mining and the dumping of unprocessed household and commercial refuse covering various toxic substances [3]. The industrial sources include iron and steel metallurgy industries, zinc smelting, tantalum niobium smelting, copper smelting, aluminium electrolysis, lead smelting, photovoltaic industry, etc.[38–40]. The industrial discharge carries high levels of fluoride typically ranging from 250 to 1500 mg/L, and in rare instances can even exceed 10,000 mg/L [40].

1.5. Trails of human exposure

Fluoride is primarily absorbed by people through the gastrointestinal track from topical (dental goods) and systemic (drinking water, food, drinks, and nutritional fluoride supplements) sources of fluoride administration [41]. The primary source of fluoride exposure is through water [42]. This mainly depends on how much water people use each day for drinking,

cleaning, bathing, and numerous other household and commercial tasks. The amount of fluoride in the water being used will determine the dose. As was previously stated, the majority of water used in developing nations is groundwater, exposing people to the largest geogenic source of fluorides. Administrations routinely assess the fluoride levels in potable water because most nations have a maximum concentration cap[43]. Fluoride levels in natural waterways vary from trace amounts to toxic levels. Based on the guideline value established in 1984 and confirmed in 1993, the World Health Organization (WHO) set the drinking water F^- concentration guideline value at 1.5 mg L^{-1} in 2010. It's noteworthy to observe that the WHO Expert Committee on Oral Health Status and Fluoride Use recommended in 1994 that 1.0 mg L^{-1} of F^- be regarded as the maximum amount of fluoride that should be present in drinking water, even in frigid regions. Fluoride is purposefully introduced to water sources in some nations as per the limit set by the WHO. The previously advised optimum fluoride content in water in the United States (US) was recently lowered from 0.7-1.2 mg L^{-1} to 0.7 mg L^{-1}. It should be noted that municipal water fluoridation is one of the most contentious medical topics ever. Although 69% of the population receives fluoridated drinking water, the US Centers for Disease Control and Prevention (CDC) ranked water fluoridation as one of the top ten public health achievements of the 20th century in the US. However, many developed European and Asian countries rejected, halted, or outright banned water fluoridation.

Numerous commonly consumed foods including wine, veggies, seafood, meat, and fruits, contain small amounts of fluoride. The amount of fluoride in food is typically very low, but bioaccumulation is an issue. It is essential to remove the fluoride from the food to measure the amount of fluoride in it. The two most popular techniques are dry ashing (alkali fusing) and facilitated diffusion, but both call for extended procedures. According to Rocha et al., [41] the fluoride amounts in shrimp/crab/prawn was 11.1 mg/kg on a dry basis. According to the research, shrimp/lobster/prawn and sardine/anchovy had the highest amounts (3.05 and 2.40

mg/kg, respectively), which may be due to the prevalence of skeleton remnants (bones or exoskeleton) in the samples examined. Additionally, salted fish had a high percentage of the analyte (5.01 mg/kg), which may have been due to the salt's high fluorine content during processing or water loss during the salting process. Ready-to-serve beverages and snacks have a high quantity of fluoride because of the ingredients like black or red rock salts added to them. Exposure of fluoride to the food produced using fluoridated water and also food contaminated with post-harvest fumigants and pesticides.

Fluoride is present in the air in both diffuse and particle forms. Its spread and deposition rely on the intensity of the emission, the weather, the terrain, the size of the particles, and the chemical reaction. The atmospheric forms include hydrogen fluoride (HF), tetrafluoromethane (CF_4), hexafluoroethane (C_2F_6), and silicon tetrafluoride (SiF_4) [44]. Gaseous HF and SiF_4 are between 1 and 3 orders of magnitude more toxic than other common pollutants (O_3, SO_2, peroxyacyl nitrates, and Cl_2). Modern fluoride-emitting businesses typically have little to no environmental effect; however, there may be times when emissions are greater than usual because of regular maintenance or scrubbing equipment failure. The highest recorded levels of fluoride in outdoor air were 1.89 g m^{-3} in metropolitan areas and 0.16 g m^{-3} in nonurban areas. Dust and fumes containing fluoride are produced by industries that produce steel, metal, enamel, pottery, glass, bricks, phosphate fertilizer, water fluoridation facilities, cooling, rust removal, oil processing, polymers, medicines, chemicals, and cars.

The user may choose to receive fluoride through systemic routes other than through water, drinks, or food. Examples of such routes include salt and milk fluoridation and fluoride-containing supplements. When municipal water fluoridation is not feasible or there is a low quantity of F^- in the natural water supply, salt fluoridation is sometimes recommended. The majority of the 40–280 million users of fluoridated salt are found in European, South American,

and Central American nations. A reasonably inexpensive and efficient technique for delivering fluoride to avoid tooth caries was proposed, involving milk. For the proper application of dietary fluoride supplements, the trade-off between the advantages of preventing caries and the danger of oral fluorosis must be assessed. Compounds with fluoride atoms can be found in some cosmetics and medications. Ironically, fluoridated toothpaste can help to avoid dental caries, but regular use will lead to calcium fluoride buildup in the mouth. This is promoted by ingesting mouthwash containing fluoride.

1.6. Fluoride toxicity

Overconsumption of fluoride through potable water, food, and air over an extended period causes fluorosis, a debilitating illness that deposits in the tissues of the body [42,45]. However, the main way that excess fluoride affects the teeth and bones is through consuming water. Major health conditions like oral fluorosis, skeleton fluorosis, and non-skeletal fluorosis are caused by it [30]. Acute high-level exposure is uncommon and typically results from flames, blasts, or unintentional contaminating of potable water. The typical cause is the extremely high amounts of fluoride in some regions of groundwater [37,46]. The excess level of fluoride in the body causes bone damage, arthritis, muscular damage, osteoporosis, joint-related problems, and fatigue [45]. The arteries, heart, liver, kidney, neuron system, endocrine glands, and various other sensitive elements of a living creature might suffer negative effects under severe circumstances [29]. People overexposure to fluoride show dental effects much earlier before six years of age, before their permanent teeth develop under their gums. Teeth that have already developed can’t get fluorosis. Dental fluorosis is a cosmetic dental condition evident by staining and pitting of the teeth, which may have white, yellow, brown, or black spots. It isn’t harmful to your health and in more severe cases all the enamel may be damaged. Persons who have fluorosis are more resistant to cavities. This discovery spurred health officials to add

fluoride to public water sources at a safe level that contains enough fluoride to help prevent tooth decay but not enough to induce fluorosis. Skeletal fluorosis is a serious condition, resulting from prolonged ingestion of excessive fluoride during periods of bone growth and/or remodeling [47]. The bones are generally weaker than normal with brittleness and joint pain increase are some of the common early symptoms of skeleton fluorosis. In severe cases, accumulated fluoride alters bone metabolism, muscle wasting, and deformities, particularly of the weight-bearing bones, and also leads to neurological problems like crippling [48]. Vertebral canal and intervertebral foramen compression places strain on blood vessels and nerves, causing immobility and discomfort. Skeletal fluorosis affects the main joints of the body and bones, including the knee joints, hip, back bone, and, neck causing excruciating pain and paralysis of the affected joints. Those who have severe bone fluorosis experience significant impairment. Only attempts can be made to lessen the disability that has already happened in extreme instances of skeletal fluorosis. However, the condition is readily avoidable if it is identified early and measures are made to avoid consuming too much fluoride by providing safe drinking water, promoting nutrition, and avoiding foods rich in fluoride. Since there is no cure for dental and skeletal fluorosis, the only option is to avoid it by limiting your consumption of fluoride.

1.7. Mechanism after fluoride intake

The initial stages of fluoride toxicity are the decrease in food consumption fallowed by body weight reduction. Pitting of the teeth with black, brown, yellow, or white spots refers to dental fluorosis. Dental and skeletal fluorosis may develop after continued exposure to F^- ions concentrations between 3 and more mg/L [49]. The many tissues and organs in the body get fluoride after it has entered *via* the blood vessels in the mouth or the gastrointestinal tract. Fluoride is excreted in the urine in about 50% of cases, while the remaining 50% is eliminated

from the bloodstream and accumulates in the bones [50]. The electronegative element fluoride is drawn to positively charged ions like calcium (Ca^{++}). The largest concentration of calcium found in bone and teeth attracts the most fluoride. Fluoride taken in sufficient amounts replaces the OH ions present in calcium hydroxy-phosphate, which is then deposited as calcium fluorapatite crystals. Calcium fluorapatite has acid resistance properties, which prevent tooth decay, stimulate bone formation, and increase bone mass. If excessive fluoride is present in bone reacts with the calcium fluorapatite to form calcium fluoride (CaF_2) [51]. Through this process, the formation of calcium fluoride increases the bone density but bone becomes hard, brittle, and unsuitable as skeletal, hence normal bone formation may be deformed. When the normal processes of bone growth and resorption do not occur, it causes several bone disorders such as osteomalacia (bone softening as a result of insufficient bone mineralization), osteoporosis (bones become brittle), and osteoarthritis (the most typical kind of arthritis that affects different bodily joints) [52].

1.8. Techniques for fluoride removal

For the decontamination of water, different techniques like conventional, established recovery, and emerging removal processes are broadly used. Chemical precipitation [53], coagulation/flocculation, biodegradation, electrodialysis [54], and filtration [55] are the different methods of the conventional process [56–58]. In this process, colloidal substances, organic matter, soluble metals, and organic pollutants (metals, organics, etc.) as their solid forms are removed from effluents via physical, chemical, and/or biological processes [59]. Solvent extraction, evaporation, oxidation, electrochemical treatment, membrane filtration, ion exchange, etc. are the different established recovery processes whereas advanced oxidation, adsorption, and bio-adsorption are the classifications of emerging removal processes.

1.8.1. Precipitation and coagulation/flocculation

For industrial waste water treatment, precipitation followed by flocculation and sedimentation is a well-established and conventional process [60]. It is used specifically for the decontamination of fluorides, heavy metal ions, and phosphates. It is one of the simplest processes for the purification of water. In the precipitation technique, water contaminants are removed as insoluble solid residues by the addition of chemical reagents. However, this process is ineffective for the removal of trace amounts of metal ions and also a large amount of sludge is produced in this technique which creates management and disposal-related problems [38].

1.8.2. Electrochemical oxidation

The electrochemical oxidation process is a potential technique for the treatment of highly concentrated organics, toxic, and hazardous because of its advantages of easy implementation, high effectiveness, less time-consumption, environmental compatibility, and stability. In this process, organic pollutants are oxidized into H_2O, CO_2, and other intermediates by indirect electrochemical oxidation facilitated by electrogenerated oxidants while direct electrochemical oxidation on the anode surface. The effectiveness of oxidation is dependent on the anode, electrode activity, diffusion rate of pollutants, and current density [40,61]. Different anode materials like Pt, boron-doped diamond, PbO_2, graphite, SnO_2, and RuO_2 etc. have been used. Among these, PbO_2 electrodes are most widely used as an anode in the electrochemical oxidation process because of their low cost, good resistance to corrosion, and long lifetime. The electrochemical oxidation of organic pollutants (R) through metal oxide (MO_x) electrode is shown as:

$$MO_x + H_2O \rightarrow MO_x(*OH) + H^+ + e^- \quad (1.3)$$

$$R + MO_x(*OH) \rightarrow CO_2 + H^+ + MO_x + +e^- + \text{ inorganic ions} \quad (1.4)$$

$$MO_x(*OH) \rightarrow MO_{x+1} + H^+ + e^- \quad (1.5)$$

$$R + \mathrm{MO_{x+1}} \rightarrow \mathrm{RO} + \mathrm{MO_x} \quad (1.6)$$

The organic pollutants (R) in wastewater react with physisorbed active oxygen (*OH) with the formation of CO_2, H_2O, and MO_{x+1}. The chemisorbed active oxygen (MO_{x+1}) undergoes the selective oxidation. It has been reported that oxides of Ru, Pb, and Sn are used for the oxidation of dye. Several researchers worked on the removal of different organic components like phenols, and pesticides using Pt, IrO_2, and boron-doped diamond (BDD) electrodes. Water purification using electrochemical oxidation is beneficial due to its efficient degradation ability of highly concentrated pollutants, easy control, environmental compatibility, and degradation at low temperatures and pressure. However, it has some limitations:

- High energy consumption renders high operating costs.
- Fouling of electrodes requires frequent replacement.
- Due to the conductive nature of the effluent in this process, the addition of electrolytes is essential.

1.8.3. Membrane filtration

Membrane filtration is considered a considerably effective process for the elimination of contaminants from water. Membranes are semipermeable materials having a high number of pores that allow certain components to flow through while rejecting others. Removal of water contaminants using membrane technologies is of two types: one is pressure-driven and the other is the electrically driven membrane process. For the pressure-driven membrane filtration process, the driving force for the motion of the molecules through the membrane is due to the pressure difference between the two sides of the membrane. There are various types of pressure-driven membrane filtration processes namely microfiltration (MF), ultra-filtration (UF), nanofiltration (NF), and reverse osmosis (RO) to be utilized for the removal of water contaminants [62].

1.8.4. Ultrafiltration

Another form of membrane filtering technology is ultra-filtration (UF), which uses a pressure or concentration gradient to drive separation across a semi-permeable membrane. It is a membrane filter with a size exclusion based on low pressure. The membrane pores range in size from 10 to 1000 Å. Molecules with a molecular weight of more than 1000 Daltons are kept, whereas molecules with a lower molecular weight flow through the membrane as a filtrate [39]. Similar to the MF membrane, UF may not be the possible method for the elimination of arsenic or other water contaminants. Separation of harmful water pollutants like arsenic *via* UF with electric repulsion technique is reported as a better technique than the removal through normal size elimination based UF method [40].

1.8.5. Microfiltration

Micro-filtration (MF) is a class of low-pressure driven membrane filtration process for removing suspended and colloidal particles of the size 0.02-10 μm from the fluid mixture. Microfiltration is size size-dependent process like the sieving process. It cannot eliminate harmful water contaminants because the size of the pores is larger. The involvement of the chemical flocculates the targeted compounds, which ultimately increases the size of the particle and gets separated efficiently through the MF membrane. Flocculation followed by MF technique shows improved removal as compared to flocculation followed by sedimentation and removal only by MF membrane.

1.8.6. Reverse osmosis

Reverse osmosis (RO) is one of the most promising and extensively used water treatment processes. It is used for the purification of household water to eliminate toxic contaminants like fluoride, arsenic, organic pollutants, dyes, and microbes. In RO, water is forced via the dense membrane filter containing very small-sized pores (< 0.001 μm), which prevent the

passing of impurities. It is effective for the removal of low-molecular-mass compounds and ions. All Membranes are fabricated using synthetic and natural polymers like polyamide, polysulfone, cellulose triacetate, and cellulose acetate. However, the RO membrane is a thin film composite membrane, where the polyamide layer is obtained by interfacial polymerization of acyl halide and diamine showing the charge-holding capability. RO is a size and charge-selective membrane. Among all other membrane processes, RO is beneficial in terms of the removal of all types of water contaminants like fluoride, chloride, arsenate, sulfate, sodium, potassium, lead, organics, and micro-organisms. It is considered as eco-friendly process as it does not produce any harmful chemicals or by-products. However, the waste water treatment by this process has some limitations:

- The water obtained after purification using the RO system is devoid of useful minerals.
- Membranes are commonly obstructed, and fouling occurs at high pollutant concentrations. Therefore, the requirement of periodical replacement of membrane is an important factor.
- Chemical assault or temperature fluctuation may quickly destroy membranes.
- Because of high energy requirements, it is not economically possible. Operational costs and maintenance are also very high.

1.8.7. Electrodialysis membrane treatment

Electrodialysis (ED) process is used for waste water treatment where ions are moved from one side of the selectively permeable membrane to the other side of the membrane under the influence of electrical potential [63]. This is the charge-dependent separation process where electrical potential acts as a driving force. Positive and negative ions are moved toward the respective electrodes based on their polarity by the application of direct current between the two electrodes. Anionic membrane with fixed positive groups rejects the positive ions whereas negative ions are rejected by the cationic membrane having fixed negative groups [64,65]. As

the membrane is ion-selective, it removes opposite-charged ions. The efficiency of the ED process depends on several parameters like flow rate, pH, current density, ED cell structure, and ionic concentration of feed water. This process is considered pollution-free and is useful to remove dissolved ionic particles, and heavy metals [66]. The electrodialysis process is also useful for the treatment of feed water containing a higher silt density index (SDI), total organic carbon (TOC), and silica concentrations. The disadvantages of this process are:

- It is not applicable for the removal of non-charged, higher molecular weight, and less mobile ionic species.
- It is not a robust technology and feed water pre-treatment is necessary to prevent fouling of the membrane.

1.8.8. Ion exchange

Ion exchange is defined as the coulombic force of attraction between the ions and charged functional groups that causes the exchange of ions from solution with the similarly charged ion bonded to the immobile resin. The ion exchange is a reversible chemical process. Consequently, ion exchangers can be reused many times. Ion exchange resin consists of a cross-linked polymer matrix with a diameter of 0.6-1.0 mm [67]. It is fabricated in two physical forms, gel and porous. The gel resin structure consists of cross-linked polymer without porosity, whereas porous resin has pores (micropores, mesopores, and macropores) in which ions can attach. Cation and anion exchange resin are the two types of ion exchange resin based on the functional groups linked with polymer matrix [68]. Cation-exchanged resin is used for the removal of cations like magnesium, calcium, radium, and heavy metal ions. On the other hand anion exchange resin is used for the exchange of anions like NO_3^-, $H_2AsO_4^-$ /$HAsO_4^{2-}$, and CrO_4^{2-}/$Cr_2O_7^{2-}$ [69]. Cation and anion exchange resin are further divided into four sub-categories viz. strongly basic, strongly acidic, weakly basic, and weakly acidic. Another class

of ion-exchange resin is amphoteric which may exchange cations or anions depending on the solution pH. These ion-exchanger are termed as zwitterionic exchangers and bipolar electrolyte exchange resins (BEE). Sodium chloride is used to regenerate all types of resins. The elimination of water pollutants using the ion exchange method is very modest and cost-effective [70]. It is beneficial for the recovery of precious material from industrial discharge. An additional significant benefit of the ion-exchange technique is the easy regeneration and the resin can be used for several years. However, some drawbacks of this process are:

- Water treated by ion exchange resin contains sodium which is unhealthy for the person who is suffering from heart-related health issues.
- Ion exchange resin is not useful for the removal of organic contaminants or biological contaminants.
- It has limitations on the concentration of the treated effluent.
- Regular sanitization and regeneration are essential to get contamination-free drinking water otherwise bacterial growth occurs on the surface of resin which can pollute the drinking water.

1.8.9. Advanced oxidation process

Advanced oxidation process (AOP) is used for the treatment of waste-water which has a great potential in degrading chlorinated organic components in particular. The ozone (O_3), hydrogen peroxide (H_2O_2), hypochlorite (ClO_2), $KMnO_4$, etc. are considered as a strong oxidizing agent. However, due to the mild oxidizing property of H_2O_2, it is not efficient solely for the removal of highly concentrated contaminants containing chlorinated aromatic and inorganic contaminants (cyanides). In the presence of ozone and UV light, H_2O_2 is activated and formed hydroxyl radical (*OH) which acts as a strong oxidizing agent. The advanced oxidation process is used in different reacting systems like chemical oxidation process (O_3, O_3/H_2O_2, H_2O_2/Fe^{2+}),

photocatalysis (TiO_2/UV, photo-Fenton reagent), photo chemical degradation process (UV/O_3, UV/H_2O_2). Light-driven AOP involves the production of *OH which reacts with the organic pollutants degrading into inorganic matter, CO_2, and H_2O [71].

1.8.10. Adsorption

Adsorption is the most commonly used traditional process for water purification [72]. It is a separation process by which substances in the form of liquid, fluid, or gas are adsorbed onto the surfaces of solid materials due to the liquid-solid intermolecular force of attraction [56,73]. The solute retained on the solid surface during the adsorption process is called adsorbate, whereas the solid on which solute is adsorbed is termed adsorbent [73]. The separation of water contaminants by the adsorption process is dependent on the interaction between the adsorption sites of the adsorbent and water contaminants. The adsorption process is categorized as physisorption or chemisorption. Adsorption may also take place due to the electrostatic force of attraction. In this process, mass transfer occurs from the liquid phase to the solid surface and the substance is bound by chemical or physical interactions. The quantitative interactions between adsorbate and adsorbent can be determined by the different isotherm models. The three isotherm models Langmuir, Freundlich, and linear model are commonly used for the interpretation of the adsorption process. It is noteworthy that large surface area materials showed high adsorption efficiency and high reactivity. All microporous (<2 nm) and mesoporous (2-50 nm) materials can act as good adsorbents. Adsorbents are broadly classified as natural and synthetic. Charcoal, clays, zeolites, clay minerals, and ores are characterized as natural adsorbents [74]. Natural materials are cheap, abundantly available, and have significant potential for modification to obtain enhanced adsorption capacity. Synthetic adsorbents are synthesized using different chemicals or physical modifications of agricultural or industrial waste. Each adsorbent has different physicochemical characteristics like porosity, surface area, and microstructural features. Different adsorbent materials like metal-organic frameworks

(MOFs), mineral oxides (e.g., iron oxide/hydroxide-based materials, TiO_2 nano particles, CuO, and layered double hydroxides), biological materials (bone char, peels of fruits and vegetables, tamarind seeds, etc.), activated carbons [75–78], activated alumina, and polymer resins are widely used in the adsorption process. Charcoal was utilized for water purification by ancient Hindus in India. In Egypt, carbonized wood was used as an adsorbent material for decontamination of water. The adsorption capacity of adsorbents is influenced by different parameters like pH, temperature, ionic strength, coexisting ions, adsorbate, and adsorbent concentrations. Adsorption capacity is also dependent on the chemical and physical properties of the adsorbent. Surface textural properties of the adsorbent play a significant role in the removal efficiency of the adsorbent. With the enhancement of surface area and pore volume of the adsorbent, the active adsorption sites can be increased resulting in high adsorption capacity. Modulating the structure in three dimensions along with the pore orientations is easily achievable during the synthesis of Metal-Organic Frameworks.

1.8.10.1. Metal-Organic Farmwork (MOF)

In recent years, a new class of fluoride remediation material called MOFs has proved to be a very promising adsorbent and attracted countless attention due to its 3D structure, tuneable crystallinity, remarkable surface area, and chemical, and thermal stability [79,80]. MOFs are compounds consisting of metal nodes that serve as connecting points to organic molecules to form a porous 3D framework and show the highest adsorption capacity for fluoride ion removal than available adsorbents [81]. The broad range of applications of this wonder material is for characteristics like high surface area, tuneable porosity, adjustable surface properties, crystallinity, and catalytic properties which further allow the addition of functional groups by post-synthesis modification [82]. Metal clusters, such as Ce, Al, Zn, Cu, Mg, Ca, Co, Fe, Cd, Zr, and Ti are commonly used, whereas terephthalic acid (BDC), fumaric acid, trimesic acid

(BTC), oxalic acid, amino acids, 2-amino terephthalic acid (ABDC), and cyclodextrins are used as organic linker, which is very important in the synthesis of MOFs [81]. Commonly applied techniques for the synthesis of MOFs are hydrothermal, microwave, solvothermal, layer-by-layer growth, high-throughput syntheses, mechanochemical, electrochemical, and ultrasonic [83–85]. Organic linkers and metal salt dissolved into suitable solvents are mixed under specific conditions to get the oriented porous structure of MOFs [86]. Oriented pore size can be obtained after washing the synthesis material with a suitable solvent to remove the residue linker sitting in the pore to give accessible micropore volumes [81,87]. The pore volume, pore apertures, and BET (Brunauer Emmet Teller) surface area of the MOFs are typically ranging from 1.5 to 2 cm^3/ g, 0.25 to 3.4 nm, and 1000-4000 m^2/g, respectively [81]. MOFs are applied in gas storage, heterogeneous catalysis, water sorption for heat transformation, drug delivery, separation process optical, electronic, carbon dioxide sequestration, pervaporation, and removal of dye and organic pollutants in water treatment [80,87]. Oriented porous MOFs with various functional groups and ion exchange characteristics are preferred for applications of wastewater purification [87]. However, all MOFs are not hydrolytic/thermal stable and involve expansive toxic organic reagents [88]. Water stability, absorption capacity, mechanism, and regeneration are the main criteria to look at in the MOFs for water treatment [80]. MOFs such as MIL-53, UiO-66, ZIF-8, MIL-68, ZIF-7, CAU-6, and ZIF-9 were studied for defluoridation and found equilibrium uptake capacity of the UiO-66 (zirconium-based MOF) was 44.92 mg g^{-1} greater as compared to the adsorbents used in this study [89]. To increase the equilibrium AC of UiO-66, the amine group was introduced by using 2-amino terephthalic acid as a ligand, and found amine group slightly increased the capacity from 44.92 mg/g to 55.7 mg/g [90,91]. Iron-based MOF (MIL-53) is well known for its magnetic properties, which are easily separable from water. MOFs namely MIL-88A, MIL-100, and MIL-53 were synthesized for defluoridation and MIL-88A has the highest adsorption capacity 40.42 mg/g [92]. The iron-

based MOFs using two different linkers ABDC and BDC, which give Fe@ABDC and Fe@BDC MOFs for F^- ions remediation were reported with the adsorption capacity of 4.90 and 4.92 mg/g, respectively [93]. The lanthanum-based MOFs using different linkers such as BDC, BTC, biphenyl-4,4-dicarboxylic acid, 1,2,4,5-benzene tetracarboxylic acid, and 2,5-dihydroxyterephthalic acid were synthesised to study the defluoridation capacity [94,95]. The water-stable Al-based MOF (MIL-96) with specific a surface area of adsorbent 220 m^2/g was synthesised by hydrothermal method and investigated for fluoride removal efficiency by varying different parameters. The maximum adsorption capacity found from isotherm fittings was 42.19 mg/g at 298 K [96]. Recently, aluminium fumarate MOFs having a surface area of 1156 m^2/g characterised as super adsorbent for fluoride because of their excellent AC 600 mg/g at neutral pH [97]. Jeyaseelan et al. [98] presented work focused on rare earth metal ions-based MOFs, which are abbreviated as La@BTC and Ce@BTC using La^{3+} and Ce^{3+} metal ions with BTC as a linker. The synthesized Ce@BTC and La@BTC MOFs disclose F^- ions adsorption capacities of 4.930 and 4.985 mg g^{-1}, respectively. They also fabricated lanthanum-based MOFs by hydrothermal method using two different linkers BDC and ABDC and found the adsorption capacities 4920 and 4950 mg kg^{-1}, respectively [94]. Huang et al. [99] used 2,5-thiophenedicarboxylate (2,5-TDCA) ligand with different metals ions i.e., Ce^{4+}, Zr^{4+}, and Al^{3+} to develop MOFs for F^- ion removal namely, Ce–TDC, Zr-TDC, and Al–TDC, respectively. The maximum fluoride uptake with Ce–TDC, Al–TDC, and Zr–TDC were estimated as 94.9, 107.5, and 97.0 mg g^{-1} at 298 K [99]. Iron salt with different linkers such as trimesic acid, dihydroxy terephthalic acid, biphenyl-4,4-dicarboxylic acid, 1,2,4,5- benzene tetracarboxylic acid, and terephthalic acid have been utilized for the fabrication of water-stable MOFs [100]. Weifeng et al. [101] synthesized iron-based MOFs (MIL-100) at room temperature to study the performance of fluoride removal from an aqueous medium having a maximum F^- ion adsorption capacity of 23.53 mg/g at 298 K.

1.9. Motivation

A broad variety of pollutants can be absorbed by AC, and its adsorption capability and effectiveness can be increased by making some chemical and physical changes [75–78]. In this view, adsorbents impregnated with one or more metals due to their strong attraction for fluorine have recently attracted significant attention. It has been observed that the biocompatible, non-toxic, rare earth metal cerium with redox properties is abundant in the earth's crust and has stronger bond strength with fluoride [102–104]. Notably, rare earth metals possess large ionic radius and numerous extranuclear electron orbitals that effectively remove fluoride present in water [95]. This individual is not cost-effective, because this incredibly small particle frequently passes through standard filters [105]. As a result of their magnetic qualities and unequaled dopant with vast resources, low costs, and non-polluting attributes, iron-based adsorbents enable easy separation from solution. Consequently, the metals cerium and iron were employed to alter activated carbon. The adsorbent was synthesized using the co-precipitation ultra-sonication-aided technique. The use of ultrasonic-assisted fluoride adsorption utilizing a synthesized AC/Ce/Fe-1 composite decreases adsorbent dosage and contact time while increasing process efficiency [106]. Further, enhancement in the adsorption process can be done by synthesizing MOFs, which in turn modifies the morphology, structure, and functional groups of the material. In this view, the nanoporous Ce-based MOFs were introduced in the study. Despite the advantages, research on Ce-based adsorbents for defluoridation remains limited, particularly concerning the synthesis of MOFs using different organic ligands. Hence, our study concentrates on cerium-based MOFs to explore their defluoridation capabilities and understand the impact of various organic ligands on their structure and performance. Furthermore, the synthesis of hybrid MOFs can enhance electron transfer, thereby facilitating catalytic reactions [107]. Even though MOF and hybrid materials

derived from MOFs have been extensively described for their adaptable structures, bimetal MOFs have rarely been studied as an adsorbent in wastewater treatment.[108] To bridge this research gap, we explore the synthesis of bimetallic MOFs in which the nodes consist of inorganic compounds connected by a fumaric acid linker. Additionally, it is challenging to obtain precise scale-up data for fixed bed adsorption columns (FBAC) solely from batch results, making it necessary to assess the column operations to meet the practical applicability [109]. To overcome these challenges, we aim to utilize novel bimetallic MOFs to eliminate fluoride from drinking water.

1.10. Objectives of the present study

The objective of research is to synthesised novel adsorbents in order to remove fluoride from water in effective and economical way by methodological modification during synthesis of material and adsorption study. To meet this objective, the specific research plan is listed below:

1. Efficient synthesis of activated carbon impregnated with Ce/Fe nanoparticles for ultrasound-assisted fluoride remediation.
2. Cerium-based MOFs with ligand tuning of the microstructures for fluoride adsorption.
3. Cerium-based nanoporous bimetallic MOFs for remediation of fluoride ion from water.
4. Investigating the efficacy of bimetallic MOFs as fluoride adsorbent in fixed-bed adsorption columns.

1.11. Outline of dissertation work

According to the discussion in the preceding section, the creation of new adsorbents has enormous value to add valuable input in the water treatment research. The current work is broken into six chapters. The outline of the dissertation work is as follows:

Chapter 1: This chapter describes a general overview on water pollutant specifically targets fluoride contaminants and their sources, global scenario, exposer trails, toxicity, and the removal methods. Based on the literature reports, emphasis was given on adsorption, the various types of adsorbents and their properties used for removal of fluoride ions from water are highlighted in this chapter.

Chapter 2: This chapter describes the efficient synthesis and characterization of activated carbon impregnated with Ce/Fe nanoparticles for ultrasound-assisted fluoride remediation. It also includes the linear and nonlinear fitting of kinetic and isotherm adsorption models.

Chapter 3: This chapter describes the synthesis and characterization of cerium-based MOFs for the removal of fluoride at ambient conditions. Chapter also describes the adsorption kinetic and isotherm model fittings with data obtained from experiments, thermodynamic studies and possible adsorption mechanisms in detail.

Chapter 4: This chapter describes the synthesis and characterization of cerium-based MOFs incorporated with different metals for tuning of the microstructures of adsorbents for remediation of fluoride ion from water. This chapter describes in detail the various kinetic and isotherm model fits, thermodynamic investigations, and adsorption processes of contaminants with adsorbent.

Chapter 5: This chapter describes the synthesis and characterization of bimetallic MOFs matrix with polysulfone to make beads, which has been used in fixed-bed adsorption columns. Additionally, experimental findings were validated using multiple accessible mathematical models.

Chapter 6: This chapter describes the conclusion and future scope of the present dissertation work. This chapter also makes some suggestions for further study in the relevant topic.

A portion of the work in this thesis has been published or accepted for publication in various international journals, internal and national conference proceedings, and some other publications will be communicated in due course. At the conclusion, the details of articles published/accepted, to be transmitted, and conference presentations have been attached.

CHAPTER 2

Ultrasound-Assisted Facile Synthesis of Ce/Fe Nanoparticles Impregnated AC for Fluoride Remediation

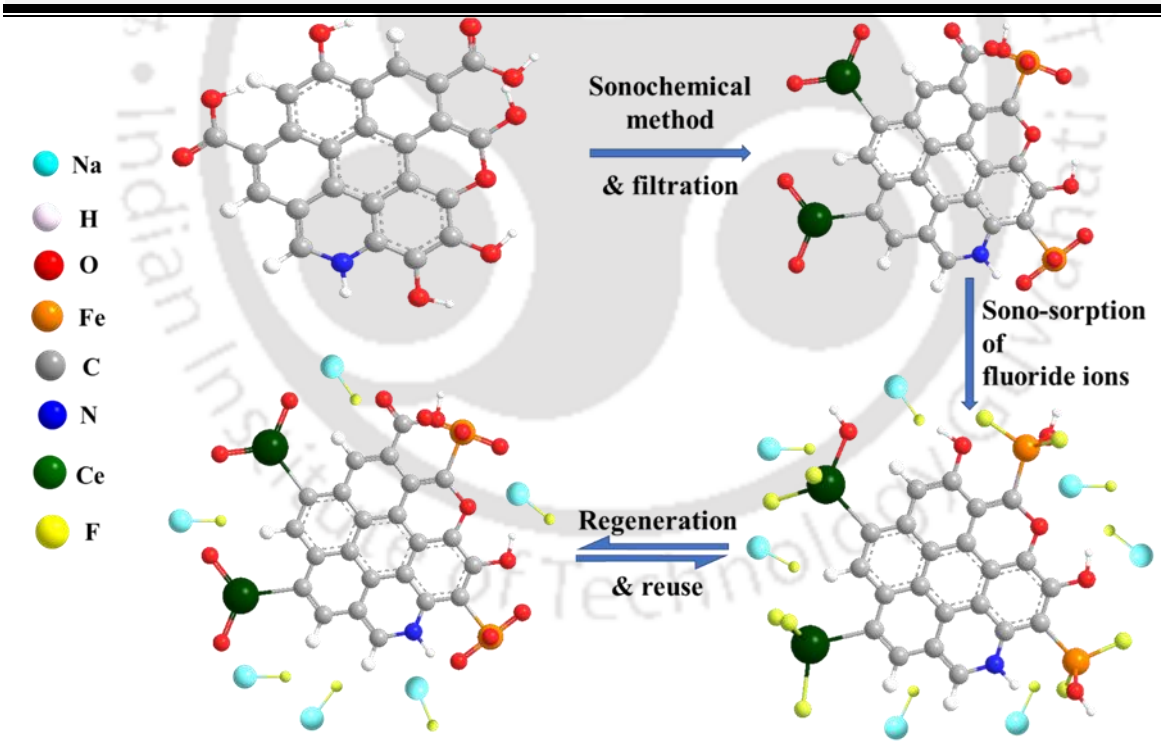

CHAPTER 2

This chapter covers the valuable insights into the modification of activated carbon for fluoride removal, with a focus on the synthesis process, material characterization, fluoride adsorption performance, and the potential mechanisms involved. The study also addresses the practical aspects of regeneration and reusability, providing a comprehensive understanding of the developed AC/Ce/Fe-1 composite material. The research outcome has been scientifically acknowledged by *'**Separations and Purification Technology**'*.

2.1. Introduction

A broad variety of pollutants can be absorbed by AC and its adsorption capacity and effectiveness can be increased by making some chemical and physical changes [75–78]. In this view, adsorbents impregnated with one or more metals due to their strong attraction for fluorine have recently attracted significant attention. It has been observed that the biocompatible, non-toxic, rare earth metal cerium with redox properties is abundant in the earth's crust and has stronger bond strength with fluoride [102–104]. Notably, rare earth metals possess large ionic radius and numerous extranuclear electron orbitals that effectively removes fluoride present in water [95]. This individual is not cost-effective, and this incredibly small particle frequently passes through standard filters [105]. As a result of their magnetic qualities and unequalled dopant with vast resources, low costs, and non-polluting attributes, iron-based adsorbents enable easy separation from solution. Consequently, the metals cerium and iron were employed to alter activated carbon at different molar ratios. The co-precipitation technique with ultrasonication assistance was used to create the materials for the purpose of eliminating fluoride from water. Material with highest fluoride adsorption capacity were utilized for

detailed study. A comparison studies were conducted to understand the effect of ultrasonic-assisted fluoride adsorption over conventional shaking method. Using an improved AC/Ce/Fe-1, the detailed examinations of equilibrium adsorption isotherms, kinetics, thermodynamics, solution pH, and initial fluoride concentration were investigated. Characterization of AC/Ce/Fe-1 involved techniques such as scanning electron microscopy (SEM), energy-dispersive spectroscopy (EDS), transmission electron microscopy (TEM), thermogravimetry, N_2 adsorption–desorption analysis, and X-ray diffraction (XRD). Moreover, the potential mechanism of AC/Ce/Fe-1 with commendable fluoride repair performance was elucidated through X-ray photoelectron spectroscopy (XPS) and Fourier transform infrared spectroscopy (FTIR) analyses of the adsorbed materials. Ultimately, the regeneration and reusability of AC/Ce/Fe-1 were also studied to understand the effectiveness.

2.2. Experimental

2.2.1. Materials

The analytical grade sodium fluoride (NaF; 97%), AC, cerium nitrate hexahydrate ($Ce(NO_3)_3.6H_2O$; 99%), hydrochloric acid (HCl, 37%), and sodium hydroxide were purchased from Merck Ltd., India. NaF was taken to prepare a standard solution of 1000 ppm of fluoride ion solution. The HCl/NaOH were used to maintain the pH. The ferric nitrate nonahydrate ($Fe(NO_3)_3.9H_2O$; 98%) was procured from Sigma Aldrich, USA. Millipore Milli-Q® water (M/s Millipore, USA) was taken for synthesis and in the adsorption studies. Analytical grade total ionic strength adjustment buffer (TISAB III) was supplied by M/s Thermo Scientific.

2.2.2. Material characterization

The composites for fluoride ion adsorption were prepared by impregnating the Ce $(NO_3)_3.6H_2O$ and Fe $(NO_3)_3.9H_2O$ on the AC using a sonication bath (Elma, Germany) at a constant frequency of 37 kHz throughout the experiment. The functional groups of the composites were detected using Fourier-transform infrared (FTIR) spectroscopy (SHIMADZU, IR Affinity 1, Japan) in diffused reflectance spectra (DRS) mode. The FTIR spectra were obtained by scanning over a range of 4000 to 500 cm^{-1} with an average of 30 scans. X-Ray Diffraction (XRD) was done with Rigaku SmartLab using Cu-Kα radiation (9 kW power, 40mA, λ-1.5406 Å) to determine the crystalline nature and composite. The XRD spectrum was obtained by scanning of material from 10° to 80° (2 theta) with a step size of 0.02º. The surface morphology, nature of pore, and compositional analysis were investigated via field emission scanning electron microscope (FESEM) (Sigma 300, Zeiss, Germany). For this, the samples were drop cast and coated with gold before loading, and images were recorded at the voltage of 3 kV using an Inlens detector. The further confirmation of topography, size, and crystallinity of the drop cast sample on the copper grid was done through field emission transmission electron microscope (FETEM; 2100F, JEOL) after drying in the oven at 80ºC overnight. X-ray photoelectron spectroscopy (XPS; Thermo-Scientific ESCALAB Xi spectrometer) measurements were performed using a monochromatic Al Kα X-ray source (1486.6 eV) and a spherical energy analyzer. The BET surface area analyzer (Tristar II; Micromeritics) was used to perform the N_2 adsorption-desorption studies to investigate the type of pores, total pores volume, specific surface area, and average pore size, under nitrogen bath (77.3 K) after and before the metal impregnation. The degassing was carried out at 180 °C for 3 h. The concentration of fluoride ions after adsorption was measured through the fluoride ions selective electrode (Orion™ Versa Star Pro™) after the adsorption study using TISAB III as a reagent.

The measurement of Zeta potential was completed using Delsa^{TM} Nano C Particle analyzer (Beckman Coulter) to evaluate the polarity of the adsorbent surface charge with a voltage of 110 – 240 V and frequency of 50 – 60 Hz.

2.2.3. Cerium and iron modified AC preparation

2.2.3.1. Ultrasound-assisted synthesis of AC/Ce

A sonochemical method was used to prepare metal-loaded AC [106,110]. Enough water was taken to disperse raw AC and ultrasonicated for 30 min. This ensures the separation of any impurity that adheres to the AC. It was then dried thoroughly for 5 h in a hot air oven at 110 ºC. Further, 0.5 g of AC obtained after ultrasonication was dispersed into 5 ml of 0.1 mol/L of Ce $(NO_3)_3.6H_2O$ and kept under ultrasonic irradiation for 60 min at 37 kHz frequency to allow appropriate impregnation of metals followed by resting for 6 h at room temperature. Then the suspension was filtered and dried overnight at 80ºC in a vacuum oven.

2.2.3.2. Ultrasound-assisted synthesis of AC/Fe

0.5 g of ultrasonicated AC has been added into 5 ml of 0.1 mol/L Fe $(NO_3)_3.9H_2O$ solution. The dispersed solution was kept in the sonication bath for 1 h and then kept at 25˚C for 6 h to allow proper deposition of Fe metal. This mixture was filtered using Whatman® no.1 filter paper and retentate was dried at 80 ºC overnight using a vacuum oven for complete removal of the residual solvent.

2.2.3.3. Ultrasound-assisted synthesis of AC/Ce/Fe at different Ce/Fe ratio

5 g of ultrasonicated AC was dispersed into 50 ml of the solution by adding 0.1 mol/L of Ce $(NO_3)_3.6H_2O$ and Fe $(NO_3)_3.9H_2O$ solution in molar ratios of 2:1, 1:1, and 3:1. The resulting

composites were named AC/Ce/Fe–1, AC/Ce/Fe–2, and AC/Ce/Fe–3, respectively. The solution mixture was then sonicated for 60 min to allow proper modification of AC, and then it was kept at room temperature for 6 h. Subsequently, the suspension was separated and dried at 80 ^{o}C for 12 h in a vacuum oven.

2.2.3.4. A conventional method to prepare AC/Ce/Fe–1.

AC/Ce/Fe-1 was prepared by adding 5 g of ultrasonicated AC into 50 ml of the solution having 0.1 mol/L of Ce $(NO_3)_3.6H_2O$ and Fe $(NO_3)_3.9H_2O$ solution in a 2:1 molar ratio [111]. The solution mixture was then stirred for 1 h followed by 6 h of resting at room temperature. Eventually, the suspension was separated and dried at 80 ^{o}C for 12 h in a vacuum oven. The comparative study of the ultrasound-assisted and conventional methods was done to understand the significance of both the methods for material synthesis.

2.2.3.5. Fluoride Adsorption Test

The 1000 mg/L standard (STD) fluoride solution was made by adding 0.221 g of sodium fluoride to 100 ml of Millipore® water and further diluted to make 10 mg/L, 20 mg/L, 30 mg/L, and 40 mg/L of fluoride ions solution. The batch study was conducted by adding 10 mg of adsorbent in 20 ml of a solution having an initial fluoride concentration of 10 mg/L in a 30 ml polyethylene (PE) bottle. For the comparative study, the samples were kept in a shaker incubator at 200 rpm and sonicator by maintaining the instrument's temperature at 25 °C for 60 min. Further studies were conducted with the help of a sonicator to optimize the adsorption process. The optimization was done by varying time (0–30 min), initial concentration of fluoride ion (5– 40 mg/L), pH (3–11), and temperature (15–35 °C). The pH was maintained over the range of 3–11 using 0.1 M HCl and a 0.1 M NaOH solution. Samples were collected at different contact times until equilibrium was reached for every variable and immediately

filtered by filter paper to remove the adsorbent. The filtrate was measured using an ion meter (Thermo ORION) in the form of conductance using a TISAB III reagent to evaluate the residual concentration of the fluoride at different times. The fluoride adsorption and the percentage removal of fluoride were calculated using Eqs. (2.1) and (2.2), respectively.

$$Q_e = \frac{(C_0 - C_e) \times V}{m} \tag{2.1}$$

$$R = \left(\frac{C_0 - C_e}{C_0}\right) \times 100\ \% \tag{2.2}$$

The adsorption capacity of the adsorbent at equilibrium is represented as Q_e (mg/g). C_0 (mg/L), and C_e (mg/L) are the initial concentrations and equilibrium concentration of fluoride in the supernatant, respectively. The volume of solution used for the adsorption study is V (L) and the weight of the adsorbent taken is represented as m (g). R is the percentage removal of fluoride.

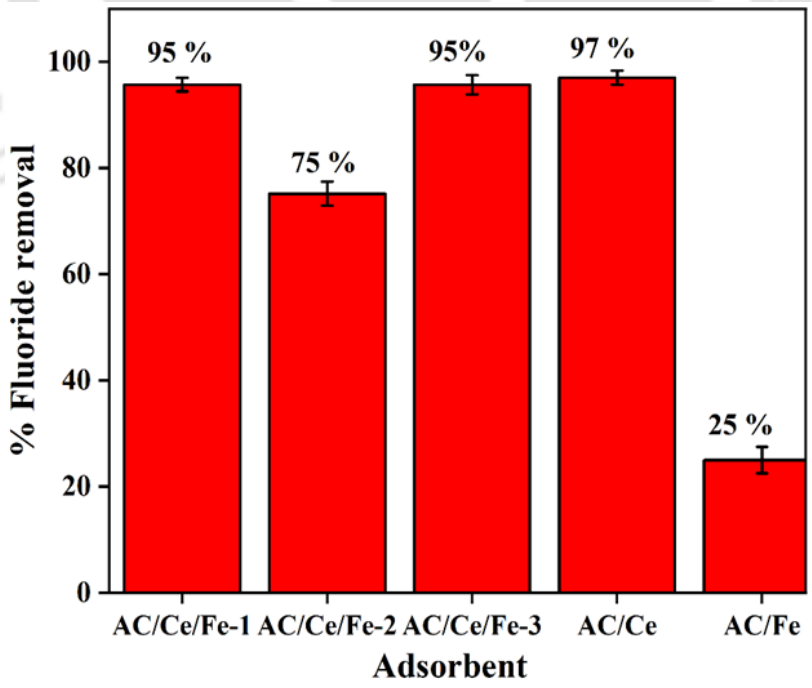

Figure 2.1. Removal of F^- ions using different composites.

2.3. Result and discussions

2.3.1. Ce/Fe molar ratio optimization

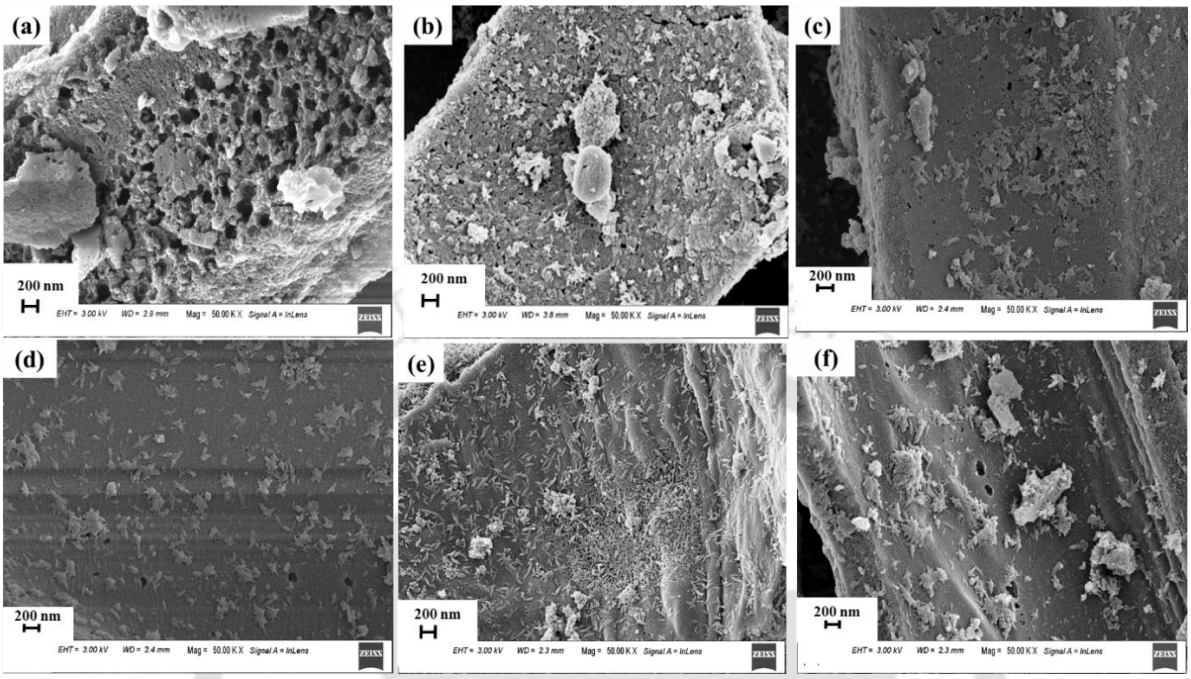

Figure 2.2. FESEM Structural image of (a) AC, (b) AC/Ce composite, (c) AC/Fe composite, (d) AC/Ce/Fe–2, (e), A/Ce/Fe–1, and (f) AC/Ce/Fe–3.

The as-synthesized adsorbent AC/Ce, AC/Fe, and the composites having different Ce/Fe molar ratios of 2:1, 1:1, and 3:1 (AC/Ce/Fe–1, AC/Ce/Fe–2, and AC/Ce/Fe–3) were compared for fluoride removal. The composites exhibiting maximum removal efficiency were used for further characterization and adsorption studies. The maximum uptake of fluoride was shown by AC/Ce having a percentage removal of 97 %, as seen from **Figure 2.1**. Although this gives excellent removal, the large-scale application may not be economical owing to the higher amount of Ce, which contributes significantly to the cost. On the other hand, the composite AC/Ce/Fe-1 exhibited fluoride removal of 95.7 %, which is almost the same efficiency as AC/Ce. This may be attributed to the high affinity of Ce toward the fluoride ion owing to high ionic potential and small size [112]. Considering the lesser amount of Ce used in this

composite, it is more economical to use AC/Ce/Fe–1 composite over AC/Ce for further adsorption studies.

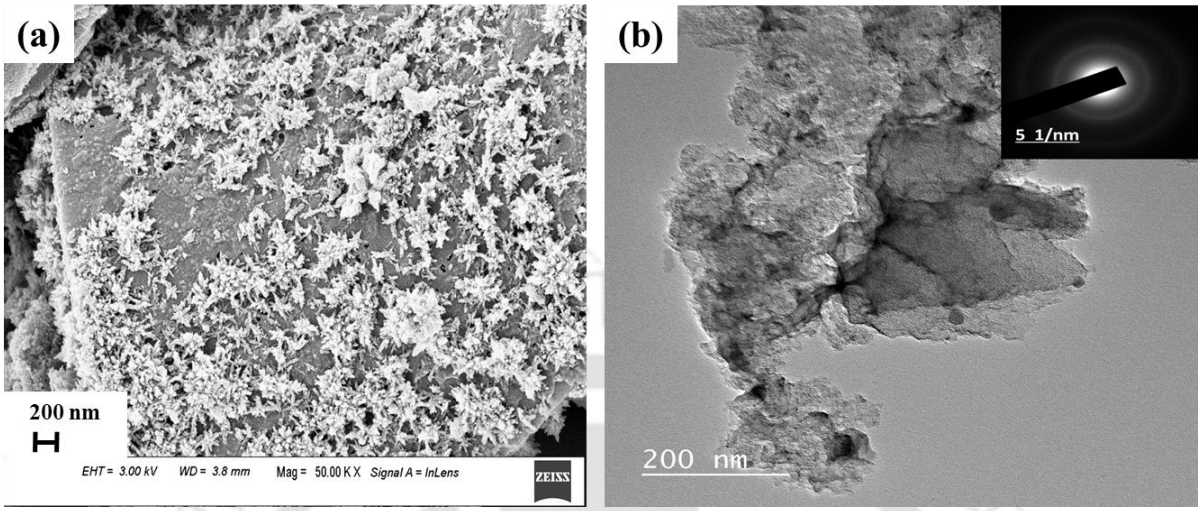

Figure 2.3. (a) FESEM image of A/Ce/Fe–1 after fluoride loading, and (b) FETEM image AC/Ce/Fe–1.

2.3.2. Material characterization

The FESEM examination was done to demonstrate a change in the morphology and nature of the material upon loading the binary metals Ce and Fe. The uniform multiple pores are visible on the surface of AC (**Figure 2.2**a). Furthermore, pores in the composites (AC/Ce, AC/Fe, AC/Ce/Fe–2, and AC/Ce/Fe–3) are homogeneously modified and appeared to be highly compacted with small metal particles constitute on the surface (**Figure 2.2**). A uniform loading of nanoparticles (Ce and Fe) promotes fluoride ion adsorption [106,113,114]. Additionally, when we increase the Ce/Fe molar ratio from 2:1 to 3:1, agglomeration of nanoparticles on the surface is visible. The diminution in surface area and pore volume was significant, which was validated by the nitrogen (N_2) adsorption-desorption study. Result from the EFSEM image (**Figure 2.3**a) shows, after loading the fluoride ions, the accumulations of fluoride on the surface was very much prominent. The FETEM bright-field images of composites (**Figure**

2.3b) showed a similar pattern of uniform dispersion of nanoparticles in the range of 3–5 nm on the AC.

The elemental analysis of as-prepared composites was done using EDX (**Figure 2.4)**. The metal loading was confirmed for different composites and the carbon weight percentage in the AC decreased from 90.5 to 77.9 upon Fe and Ce loading on the surface of the AC. Different spectra region supports the uniform and homogeneous impregnation of metals on the surface. The additional peak of fluoride in **Figure 2.5**d are seen after the adsorption. The results obtained from EDX correlate with the BET, XRD, and FTIR analysis.

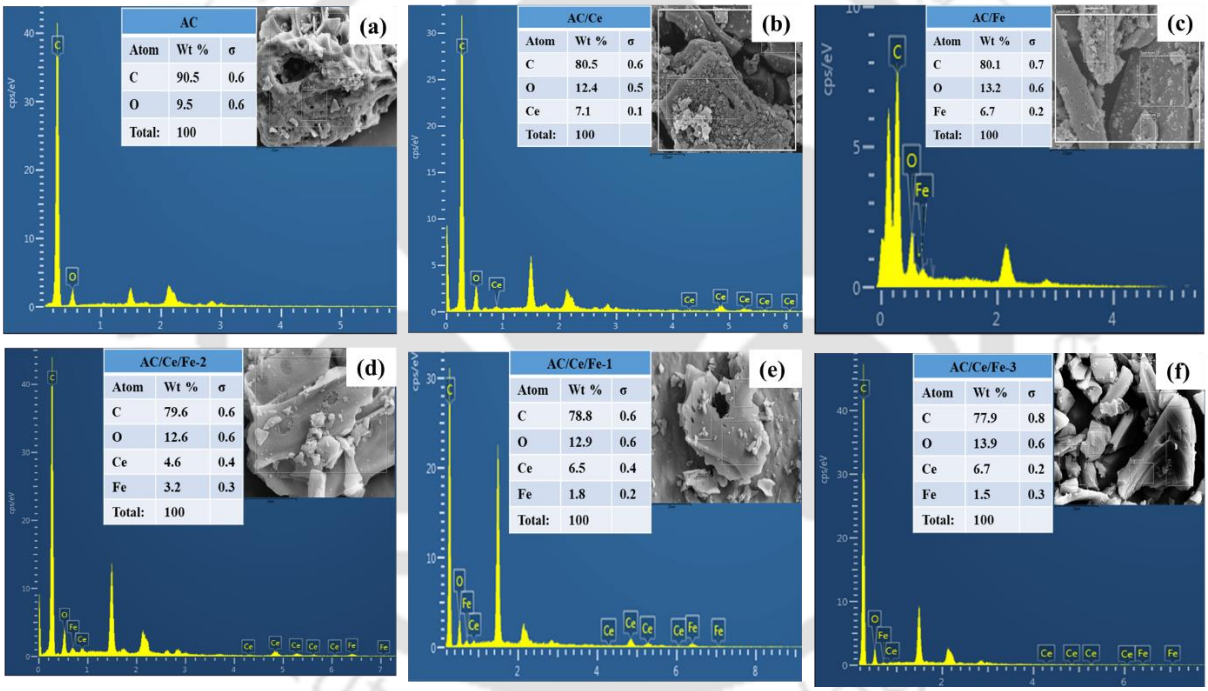

Figure 2.4. EDS of (a) AC, (b) AC/Ce composite, (c) AC/Fe composite, (d) AC/Ce/Fe–2 (Ce/Fe = 1:1), (e), A/Ce/Fe–1 (Ce/Fe = 2:1), and (f) AC/Ce/Fe–3 (Ce/Fe = 3:1).

The XRD spectrum of commercial AC is in good agreement with earlier reported data and as-synthesized composites at different Ce/Fe molar ratios show different spectra when it is visible to the X-ray beam (**Figure 2.**6a) [111]. The diffraction patterns exhibit the characteristic of CeO_2 (JCPDS card No.: 00-004-0593) at 2-theta value signifies the occurrence of Ce in AC/Ce

and AC/Ce/Fe–1 at 28.5 (111), 33 (200), 47.5 (220), 56.3 (311), 59.1 (222), 69.4 (400), 76.74 (311) and 79.08 (420) [102]. The typical peak of Fe_2O_3 (card No.: 00-001-1053) in the sample AC/Fe and AC/Ce/Fe–1 appears at 24.16 (012), 33.3 (104), 35.7(110), 40.9 (113), 49.5°(024), 54.2 (116), 57.5 (122), 62.3 (214), and 64.2°(300) [111,115,116]. The occurrence of cubic CeO_2 and Fe_2O_3 may be confirmed in the synthesized AC/Ce/Fe–1 adsorbent by the EDX data. The XRD diffractogram further confirms that the relative intensity of AC is less than the metals-loaded adsorbent, signifying the semi-crystalline nature of the as-synthesized adsorbent. Moreover, the XRD pattern of as-prepared AC/Ce/Fe–1 before and after the adsorption of F^- ions are slightly different which could be because of the presence of F^- ion.

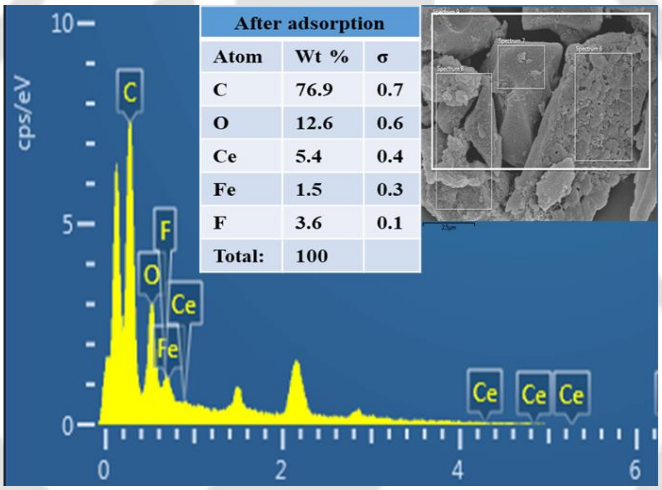

Figure 2.5. EDX scan of AC/Ce/Fe-1 after fluoride adsorption.

The FTIR spectrum of raw AC shows peaks at 3336, 1550, 1215, and 1080 cm^{-1} (**Figure 2. 6b)** [117]. The peak at 3336 cm^{-1} may be attributed to the hydroxyl functional group due to stretching vibration. Besides, the peak at 1550, 1215, and 1080 cm^{-1} resemble C=C symmetrical stretching, C=O of carboxylic groups, and C–O stretching vibration, respectively. On the other hand, the bands at 3384 cm^{-1} and 1565 cm^{-1} in different composites resemble the stretching and bending vibration of H_2O and surface-bonded OH groups [102]. The peak at 1130 cm^{-1} can be assigned to –C–O due to the bending vibration of OH groups of the metal

oxides. The peak at 779 cm^{-1} may be attributed to the Fe–O/Ce–O bonds [76]. In the spectrum of AC/Ce/Fe-1 after fluoride loading, the bands at 3284, 1565, and 1385 cm^{-1} shifted to 3339 cm^{-1}, 1547 cm^{-1}, and 1367 cm^{-1}, respectively [117]. The shift in the peaks may be due to the attachment of F^- ions. The intensity of the peak at 1367 cm^{-1} reduced, which signifies the adsorption of the F^- ions onto the active sites.

The elemental composition and the chemical oxidation state of AC/Ce/Fe–1 with and without loading of fluoride were examined through XPS investigations. The spectra of the samples were obtained by scanning over the range of 0 to 1200 eV to find C, O, Ce, Fe, and F, displayed in **Figure 2.6**c. The presence of the cerium can also be confirmed at binding energies of 884.5 and 903.9 eV. Iron was attached to the surface with the binding energies at 752 and 711 eV in two different states. This indicates that the binding energy of the cerium is comparatively higher than its iron. XPS measurement of a fluoride-loaded sample reveals a new peak at a binding energy of 684 eV assigned to F1s which confirms the presence of fluoride as shown in **Figure 2.6**d.

A comparative N_2 adsorption-desorption study was performed to evaluate isotherms of synthesized nanocomposite adsorbent (**Figure 2.7**a). This study favourably evaluates the pore size, pore-volume, and BET surface area of the adsorbent mentioned in **Table 2.1** [118]. The sample exhibits type IV isotherm with unrestricted monolayer-multilayer adsorption, which has slit shape pores [119]. The shape of the hysteresis loop from 0–0.3 indicates a rapid increase in adsorption of N_2 at low relative pressure corresponding to the microspores. Additionally, low uptake of the N_2 can be noted at higher relative pressure indicating the mesopore nature of the sample. The average pore diameter of AC/Ce/Fe–1 has been estimated at around 2.59 nm which proves that fluoride ions with a diameter of 0.266 nm can freely enter the pores of the optimized adsorbent.

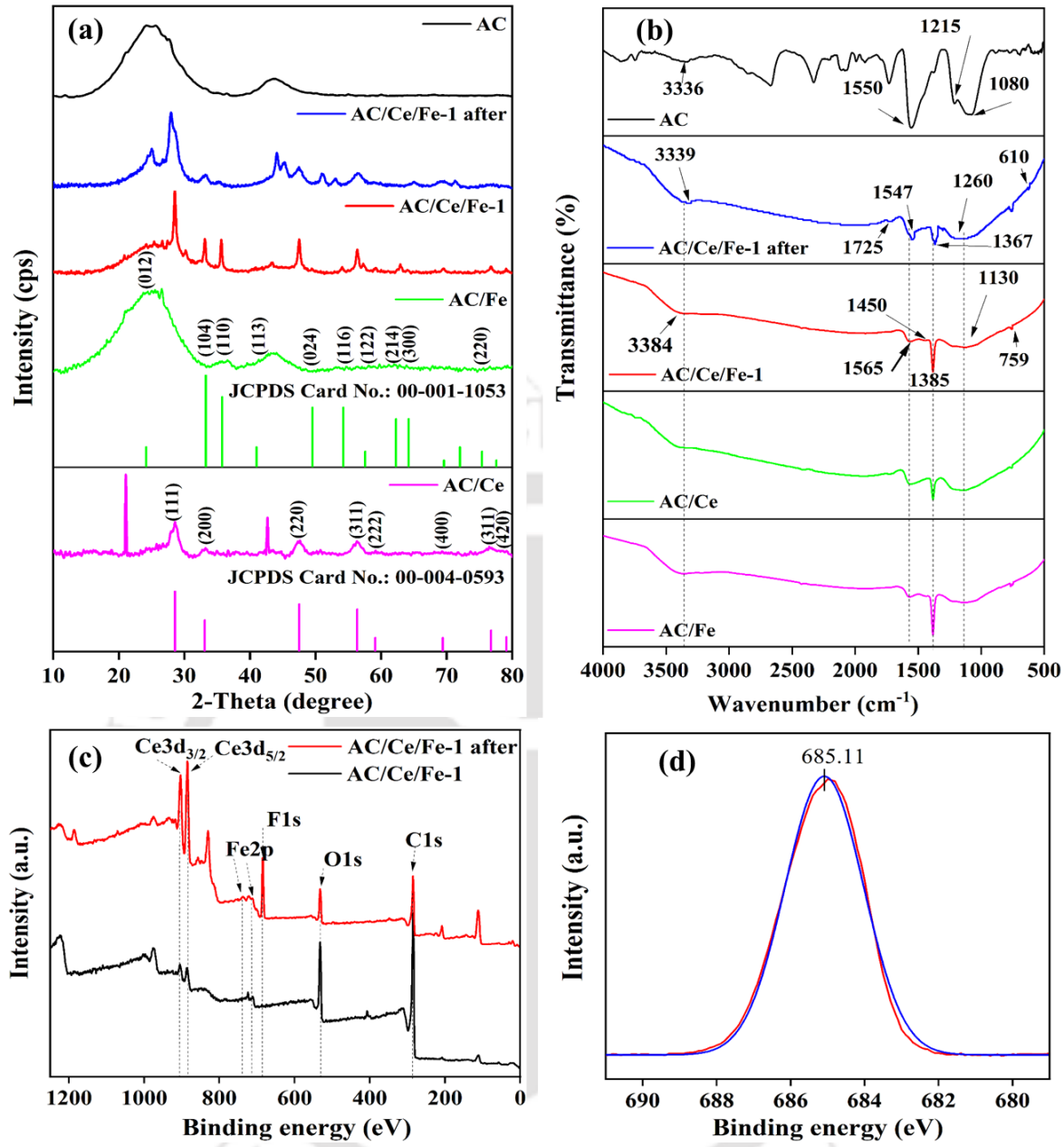

Figure 2.6. (a) XRD patterns of AC and its composites. FTIR spectrum of AC and its composites is displayed in (b), the elemental survey of AC/Ce/Fe–1 after and before the adsorption of fluoride in XPS (c), and (d) XPS spectra of F1s.

Table 2.1. Data obtained from BET adsorption-desorption analysis of Fe/Ce/AC–1.

Adsorbents	**AC**	**AC/Ce/Fe–1**
Average pore diameter (nm)	2.6	1.4

BET surface area (m^2/g)	1243	908.3
Total pore volume (cm^3/g)	0.6	0.48

The magnitude of zeta potential is based on the degree of electrostatic repulsion between the scattering medium and the dispersed particles in the medium [120]. The zeta potential ranging from 0 to 5 and 10 to 30 refers to the rapid coagulation or flocculation and incipient instability, respectively [121]. The AC–based adsorbent can act both as a base and as an acid because of the presence of different functional groups. The zeta potential was measured to estimate the pH range to target the anionic pollutant from the containing water. The isoelectric point (IEP) and zeta potential of AC/Ce/Fe–1 were evaluated by dispersing the same amount of adsorbent in the different pH ranges (2, 4, 6, 8, 2 10, and 12) of water (**Figure 2.7b)** [122]. The IEP of the as-synthesized adsorbent is about 10, at which the value of zeta potential is zero. At pH lower than the IEP, the net charge of the adsorbent surface becomes positive and gives relatively higher removal of fluoride adsorption on the active sites. Hence, the Coulomb attraction of F^- ions was observed at a relatively lower pH than the IEP. The zeta potential was found to be +23.98 mV, which is favourable for the remediation of negatively charged F^- ions at pH below the IEP by electrostatic interactions. Whereas, the zeta potential of AC is only +0.9 Mv in aqueous medium, this validates the rationale for AC's unsuitability as an adsorbent for fluoride ions.

2.3.3. Adsorption of fluoride ion

2.3.3.1. Effect of pH

The adsorption process depends on the pH of the solution since the net surface charge of the material is controlled by it [105]. **Figure 2.7**c shows the trend of F^- ions adsorption by the AC/Ce/Fe-1 in the pH ranges of 3 to 11 using 10 mg of adsorbent. The volume and the initial

concentration of fluoride solution taken for this study were 20 mL of 10 mg/L, respectively. During the sorption study, the removal of F^- ion increased from 80 to 90 % over the range of 3 to 8. This may be because the adsorbent surface remains positively charged and gives relatively higher removal of F^- ion adsorption on the active sites as shown in Eqs. (2.3) and (2.4):

$$(A)OH + H_3O^+ + F^- \rightleftharpoons (A)OH_2^- + F^- + OH \quad (2.3)$$

$$(A)OH + H_3O^+ + F^- \rightleftharpoons (A) - F^- + 2H_2O \quad (2.4)$$

Where (A) signifies the surface of the adsorbent. Furthermore, as the pH increase above 9, the percentage removal of F^- ions decrease to 40 %. This may be due to an increase in hydroxyl ions which compete with the target ions for the active spots at pH above the pH_{pzc} [123]. The increase in the OH^- ions neutralize the positive charge of the active sites, and the ion exchange takes place only in case of excess of OH^- ions as shown in Eq. (2.5). This consequently decreases the effectiveness of adsorption at pH above 9.

$$(A)OH + F^- \rightleftharpoons (A)F + OH^- \quad (2.5)$$

2.3.3.2. Optimization of AC/Ce/Fe-1 dose

The effect of AC/Ce/Fe-1 amount used for the remediation of F^- ions at pH 6.5 was studied within the range of 2.5 to 50 mg in 20 ml of F^- ion solution having an initial concentration of 20 mg/L. It can be observed from **Figure 2.7**d that the removal of fluoride increased from 50 % to 90 % as the AC/Ce/Fe–1 weight increased from 2.5 mg to 10 mg for an equilibrium time of 30 min at the same conditions. This is due to a surge of inaccessible active spots on the surface of the AC/Ce/Fe–1 for F^- ions adsorption [77]. Further addition of the adsorbent from 10 to 50 mg in the fixed solution did not show a significant increase in the removal of F^- ions.

This is possibly due to overlapping of the active sites at high adsorbent dosage, resulting in no further accessibility of binding sites on the exterior of the AC/Ce/Fe–1 for fluorine uptake. Thus, 10 mg of as-synthesized adsorbent was considered as the optimum dosage for the current adsorption study.

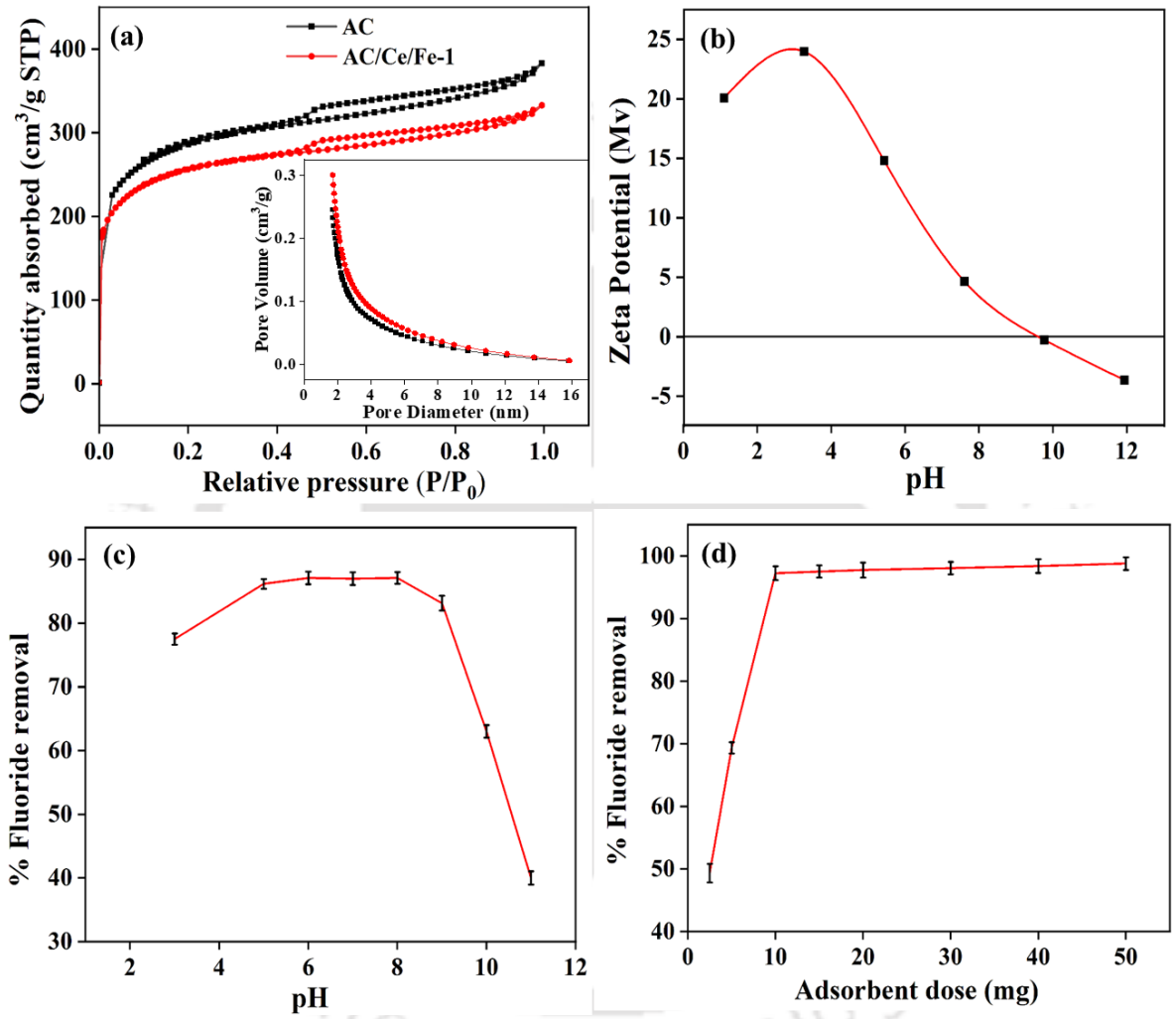

Figure 2.7. (a) N_2 adsorption-desorption isotherm of the adsorbents (inset: BJH pore size distribution), (b) Zeta potential of AC/Ce/Fe–1at different pH, (c) Effect of pH on the adsorbent for fluoride removal, and (d) optimization of AC/Ce/Fe–1 dose on the F^- ion remediation in fluoride solution.

2.3.3.3. Adsorption isotherm study

Adsorption isotherm is the basic requirement to understand the surface adsorption mechanism between fluoride ion and as-synthesized adsorbent at a constant temperature [124,125]. The isotherm was studied at different temperatures, 288, 298, and 308 K, to investigate the best-fitted model as shown in **Figure 2.8**. The equilibrium information gained from the experimental data was tuned with isotherm models, i.e., Langmuir, Freundlich, and Temkin, for both linear and non-linear equations **(Table 2.2)** to estimate the surface properties and interaction mechanism of newly developed adsorbent [125].

Table 2.2. Equations of Linear and non-linear adsorption isotherms.

Models	**Linear**	**Non-linear**
Langmuir	$\frac{C_e}{Q_e} = \frac{1}{Q_0} C_e + \frac{1}{Q_0 K_L}$	$Q_e = \frac{Q_0 K_L C_e}{K_L C_e + 1}$
Freundlich	$\ln Q_e = \log K_F + \frac{1}{n} \ln C_e$	$Q_e = K_F C_e^{\frac{1}{n}}$
Temkin	$Q_e = B \ln K_T + B \ln C_e$	$Q_e = \mathrm{B} \ln K_T C_e$

Where, C_e and Q_e are the concentration and quantity of F^- ion uptake per gram of adsorbent at equilibrium, Q_0 (mg/g) is the maximum monolayer adsorption capacity. K_L (L/mg), K_F (mg/g). $(L/mg)^{1/n}$ and K_T (mg/g) are the Langmuir, Freundlich, and Temkin constants associated with the net enthalpy change in the reaction, respectively. 1/n is the heterogeneity factor and indicates the adsorption strength, which is considered favourable for n >1, where n is the adsorption intensity. B (J/mol), R (J/mol. K), and T(K) are the heat of adsorption, the universal gas constant, and the temperature of the solution, respectively. The calculated isotherm parameters with the help of linearized and non-linearized models are presented in **Table 2.3**. The investigation shows a reduction of adsorption capacity with the increase in temperature.

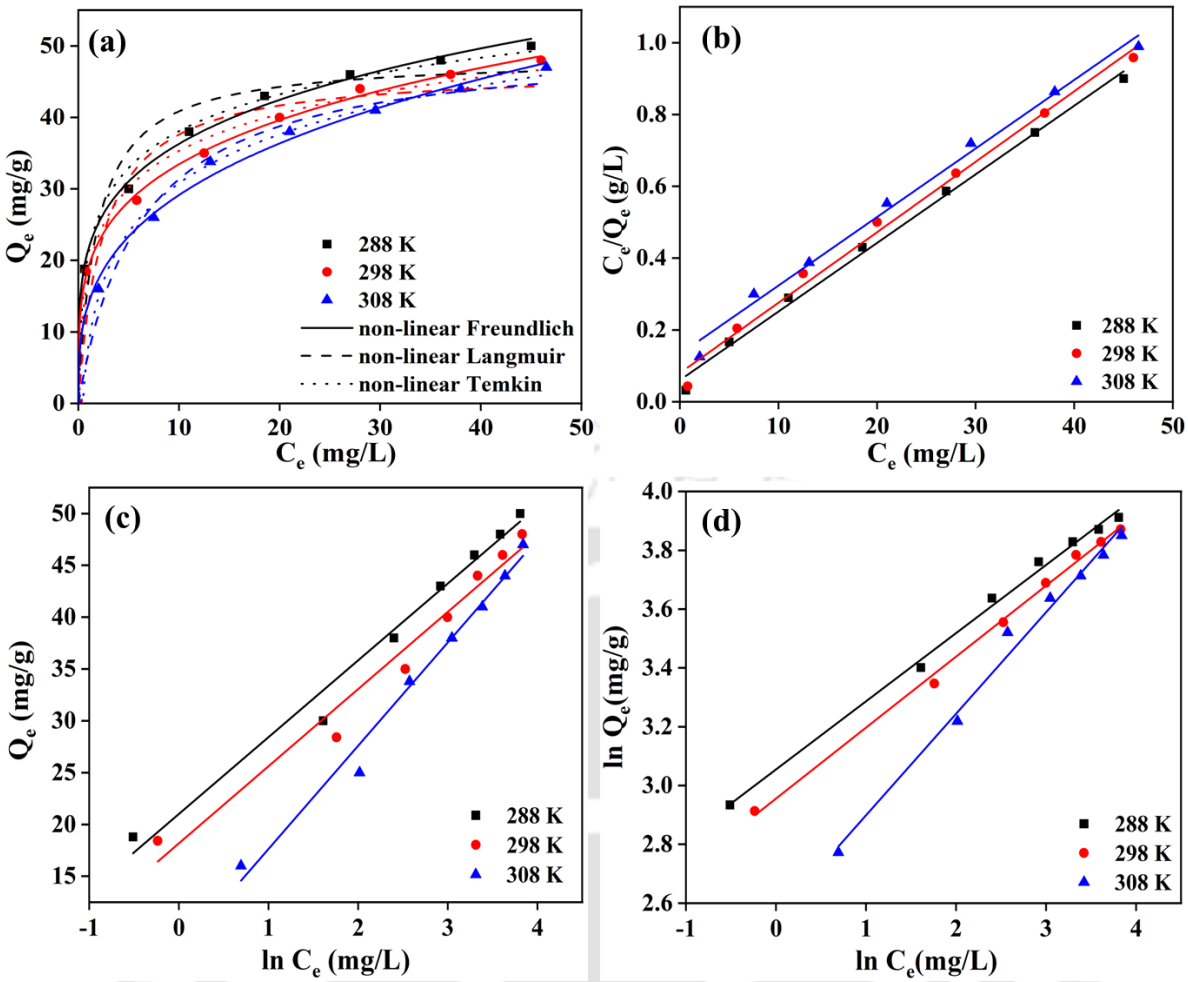

Figure 2.8. (a) Non-linear fittings of Langmuir, Freundlich, and Temkin isotherm models for remediation of F^- ion by AC/Ce/Fe-1 (b) Fitting of linearized Langmuir model (c) Fitting of linearized Freundlich model (d) Fitting to linearized Temkin isotherm.

Therefore, the exothermic reaction in which the binding ability of the adsorbent decreases due to an increase in kinetic energy of the adsorbent molecules at a higher temperature[126]. The R^2 values ranging from (0.994-0.998) are higher for the non-linear Freundlich model, making it the best-fitted isotherm model for this experiment. An empirical Freundlich isotherm model assumes multilayer adsorption onto heterogeneous surfaces of an adsorbent with different affinities. The Freundlich equation has a significant flaw in that it does not explain a limit in adsorption capacity, theoretically: as the concentration of solutes rises, the quantity adsorbed may become limitless [127]. However, the R^2 value for the linear fittings of Langmuir and Temkin is slightly smaller, i.e. (0.991-0.995) and (0.986-0.994), respectively. The q_0 value was found to be in the range of 50 to 52.3 mg/g. The fluoride uptake by AC/Ce/Fe–1 was

compared with other existing adsorbents in the literature. AC/Ce/Fe–1 shows relatively higher adsorption capacity and lower equilibrium time within the wide pH range listed in **Table 2.4**.

Table 2.3. Langmuir, Freundlich and Temkin isotherms parameters for the sorption of ion onto AC/Ce/Fe-1.

Isotherm models		**Temperature (K)**		
		288	**298**	**308**
Langmuir				
Linear	$Q_0\left(\frac{mg}{g}\right)$	52.30	50.91	49.35
	$K_L\left(\frac{L}{mg}\right)$	0.319	0.247	0.144
	R^2	0.995	0.991	0.992
Non-linear	$Q_0\left(\frac{mg}{g}\right)$	50.73	48.31	46.71
	$K_L\left(\frac{L}{mg}\right)$	0.546	0.412	0.161
	R^2	0.949	0.943	0.986
Freundlich				
Linear	$K_F\left(\frac{mg}{g}\right)$	21.208	19.21	12.847
	n	4.313	4.322	2.921
	R^2	0.994	0.996	0.986
Non-linear	$K_F\left(\frac{mg}{g}\right)$	21.560	19.033	13.948
	n	4.421	4.087	3.127
	R^2	0.998	0.994	0.997
Temkin				
Linear				

	B	7.413	7.446	9.963
	K_T	16.993	11.469	2.157
	R^2	0.979	0.964	0.981
Non-linear	B	7.413	7.446	9.863
	K_T	16.993	11.469	2.268
	R^2	0.993	0.989	0.996

Table 2.4. Comparative assessment of AC/Ce/Fe–1 used for F^- ions adsorption with other AC-based adsorbents reported in the literature.

Adsorbent	**Surface Area (m^2/g)**	**Q_0 (mg/g)**	**pH**	**Equilibrium time**	**Ref.**
Mg/Mn/Zr AC	834	26.27	2-10	180	[106]
Al/Ce AC	Not available	3.05	5-10	180	[76]
AIAABC	3.7	21.1	5-9	180	[77]
Zr modified AC	1178.95	28.50	3-11	360	[128]
Sawdust raw	Not available	1.73	4-6	60	[129]
La modified AC	852	9.96	4-6	300	[130]
$CaCl_2$ AC	Not available	2.02	4.9-9.5	70	[131]
AC/Ce/Fe-1	908.3	52.3	3-9	20	Present work

2.3.3.4. Adsorption kinetics

The adsorption kinetic models were used in this study to predict the rate of adsorption, the performance of the adsorbent, and the overall mechanism of mass transfer to design an optimized adsorption system [68]. Several models such as the external mass transfer model, internal mass transfer model, complex diffusion model, and adsorption models were applied which describe the diffusion of solute on the surface and in the pores of the adsorbent [132,133]. The Pseudo first order (PFO), Pseudo second-order (PSO), and intra-particle diffusion (IPD) adsorption model have been frequently applied to explain the rate of adsorption [28,134]. The expressions of these three models were obtained by integrating the following general Eq. (2.6):

$$\frac{dQ_t}{dt} = k_n(Q_e - Q_t)^n \quad (2.6)$$

Where, Q_t (mg/g) is the mass of fluoride uptake per gram of AC/Ce/Fe-1 at any time t (min) and rate constant of the pseudo n^{th} order kinetic model is expressed as k_n. The expression for the PFO kinetic model is obtained by integrating Eq. (2.8) for (t=0, Q_t=0 and t=t, Q_t=Q_t) and keeping n = 1.

$$\ln(Q_e - Q_t) = \ln Q_t - k_1 t \quad (2.7)$$

Where k_1 (1/min) is the rate constant of the PFO kinetic model. Additionally, the PSO kinetic model may be obtained after integrating Eq. (2.8) at n = 2.

$$Q_t = \frac{Q_e^2 k_2 t}{k_2 Q_e t + 1} \quad (2.8)$$

Eq. (2.8) can be arranged to get a linear form:

$$\frac{t}{Q_t} = \frac{1}{k_2 Q_e^2} + \frac{t}{Q_e} \quad (2.9)$$

The data obtained from the experiment were fitted to the IPD model to find the rate-determining step to understand the diffusion process during the adsorption and represented by Eq. (2.10).

$$Q_t = K_i t^{0.5} + C \quad (2.10)$$

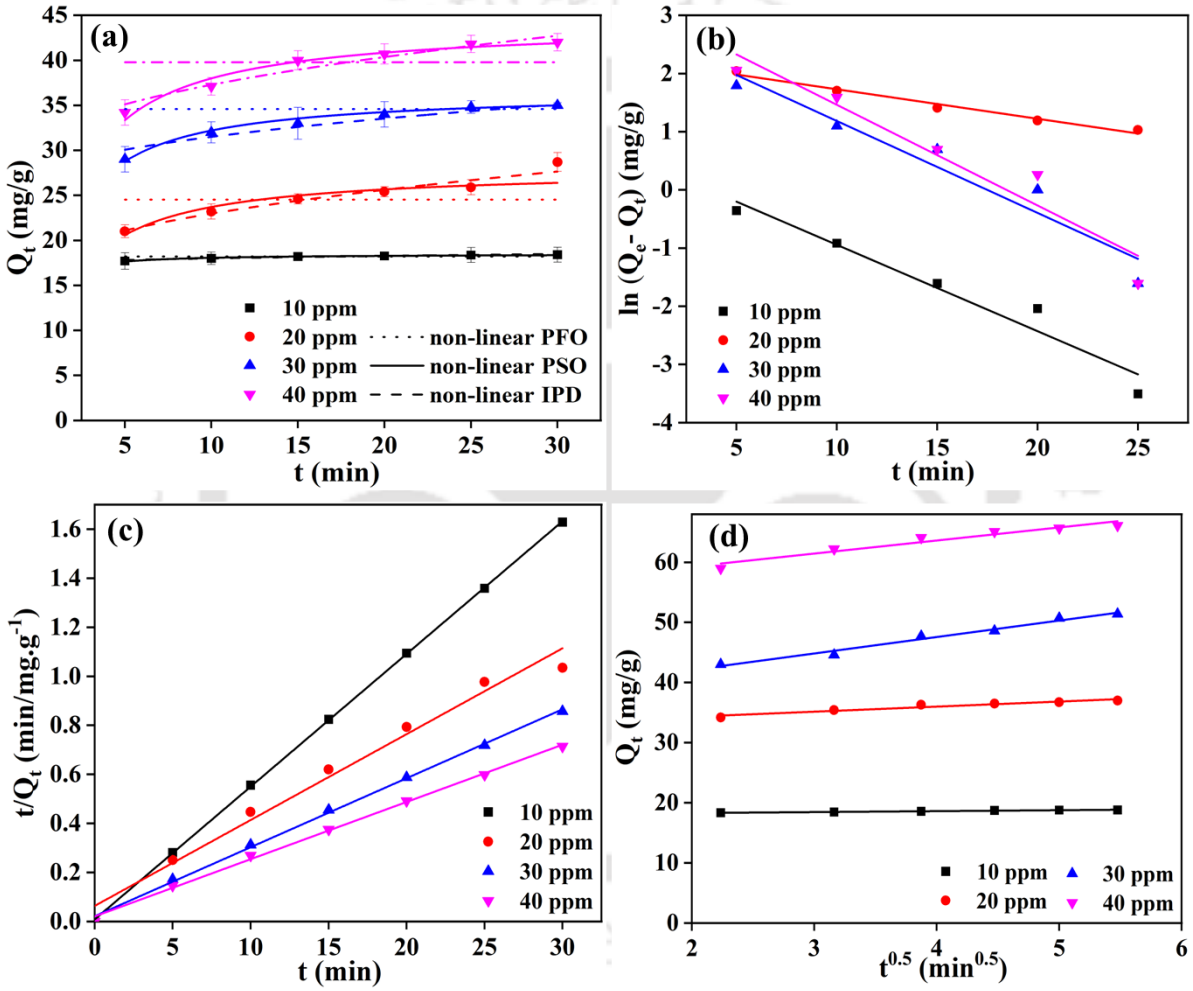

Figure 2.9. Effect of time for F^- ions removal by Ac/Ce/Fe-1 (a) PFO, PSO, and IPD non-linear fitting; (b) linearized PFO kinetic model fitting (c) linearized PSO and (d) linearized IPD model.

The rate constants of PSO and IPD kinetic model are k_2 (g/mg.min) and k_i (g/mg.min), respectively. The kinetics of the adsorption was studied by varying the initial concentration of the fluoride (10 mg/L, 20 mg/L, 30 mg/L and 40 mg/L) at 298 K temperature. The amount of the AC/Ce/Fe-1 throughout the kinetic study was 10 mg per 20 ml of fluoride solution at 6.5 pH for a contact time of 30 min. **Figure 2.9** shows the linear and non-linear fittings of the PFO, PSO, and IPD kinetic model. The values of the parameters obtained from kinetic fittings are presented in **Table 2.5**. The R^2 value of the PSO ranges from 0.95 to 0.99 and is very close to 1 and is greater than that of other models used. Furthermore, linearization of kinetic models is shown for each model, and it can be noted that the value of R^2 for PSO is 0.99, which is greater than the values for PIO and IPD model where it ranges from 0.93 to 0.98 and 0.93 to 0.98, respectively. Hence, the PSO model is chosen as the best suited kinetic model. The PSO kinetic model assumes that the chemical sorption is the rate-limiting step and may involve valency forces through ion exchange between anions and adsorbents. Furthermore, it anticipates the response across the whole adsorption range. In this case, the rate of adsorption is determined by the adsorption capacity rather than the adsorbate concentration [135]. One significant benefit of the PSO model over the PFO model is that the equilibrium adsorption capacity can be determined from the model; hence, there is no need to assess adsorption equilibrium capacity from the experiment [136]. The adsorption rate of the as-prepared adsorbent is much higher than the other reported literature (**Table 2.4**) as it attains equilibrium within 20 min. Furthermore, the solid diffuses from the solution to the surface of the Ac/Ce/Fe-1 and then within the pores. This process can be defined by the boundary layer and pore diffusion phenomena. The value of found from the intercept of the Q_t vs. plot evaluates the extent of the boundary layer effect. Hence, the boundary layer diffusion becomes dominant toward the overall process.

Table 2.5. Linear and non-linear fittings of PFO, PSO, and IPD kinetic model of ions adsorption on AC/Ce/Fe-1.

Kinetic models	**Initial concentration (mg/L)**			
	10	**20**	**30**	**40**
PFO				

Linear	$Q_e\left(\frac{mg}{g}\right)$	1.7181	9.358	15.880	24.387
	$k_1\left(\frac{1}{\text{min}}\right)$	0.148	0.050	0.158	0.173
	R^2	0.949	0.980	0.930	0.924
Non-linear	$Q_e\left(\frac{mg}{g}\right)$	18.195	24.521	34.593	39.777
	$k_1\left(\frac{1}{\text{min}}\right)$	35.980	100	100	100
	R^2	-1.61E-12	1.92E-14	-1.86E-13	3.08E-14
PSO					
Linear	$Q_e\left(\frac{mg}{g}\right)$	18.580	27.847	36.643	44.38
	$k_2\left(\frac{g}{\text{mg.min}}\right)$	0.1905	0.016	0.018	0.013
	R^2	0.999	0.999	0.999	0.999
Non-linear	$Q_e\left(\frac{mg}{g}\right)$	18.498	27.326	36.579	44.165
	$k_2\left(\frac{g}{\text{mg.min}}\right)$	0.223	0.023	0.020	0.013
	R^2	0.962	0.967	0.991	0.959
IPD					
Linear	k_{int}	15659	0.841	2.737	2.172
	$C\left(\frac{1}{\text{min}}\right)$	17.979	32.623	36.614	54.928
	R^2	0.974	0.935	0.981	0.942
Non-linear	k_{int}	20662	1.704	1.550	2.353
	$C\left(\frac{1}{\text{min}}\right)$	17.348	17.625	26.593	29.836
	R^2	0.923	0.954	0.940	0.936

2.3.3.5. Thermodynamic parameter analysis

The thermodynamic assessment was conducted to investigate the practicality of the adsorption process. The thermodynamic parameters such as standard enthalpy ΔH° (kJ/mol) standard Gibb's free energy ΔG° (kJ/mol) and standard entropy ΔS° (J/mol. K) were estimated using thermodynamic relations given below:

$$\triangle G° = -RT \log K_c = -RT \ln\left(\frac{mQ_e}{C_e}\right) \tag{2.11}$$

$$\ln\left(\frac{m\,Q_e}{C_e}\right) = \frac{\triangle S°}{R} - \frac{\triangle H°}{RT} \tag{2.12}$$

ΔS° and ΔH° are constants calculated from the intercept and slope of the straight line of Van't Hoff's plot of $\ln(Q_e/C_e)$ vs 1/T, as shown in **Figure 2.10**a. ΔG° was determined at various temperatures using **Eq. (2.11)**. The thermodynamic parameters for fluoride adsorption are presented in **Table 2.6**. The negative values of ΔG° denote the process is spontaneous whereas, the negative values of ΔH° signify the exothermic nature. The small ΔS° value decreases the randomness of the adsorption on the solid-liquid interface [137,138].

Table 2.6. Thermodynamic parameters for fluoride adsorption reaction AC/Ce/Fe-1 at pH 6.5.

Temperature	$\triangle G° \left(\frac{kJ}{mol}\right)$	$\triangle H° \left(\frac{kJ}{mol}\right)$	$\triangle S° \left(\frac{kJ}{mol.K}\right)$	R^2
288 K	-15.4	-47.7	-0.136	0.839
298 K	-15.04			
308 K	-13.08			

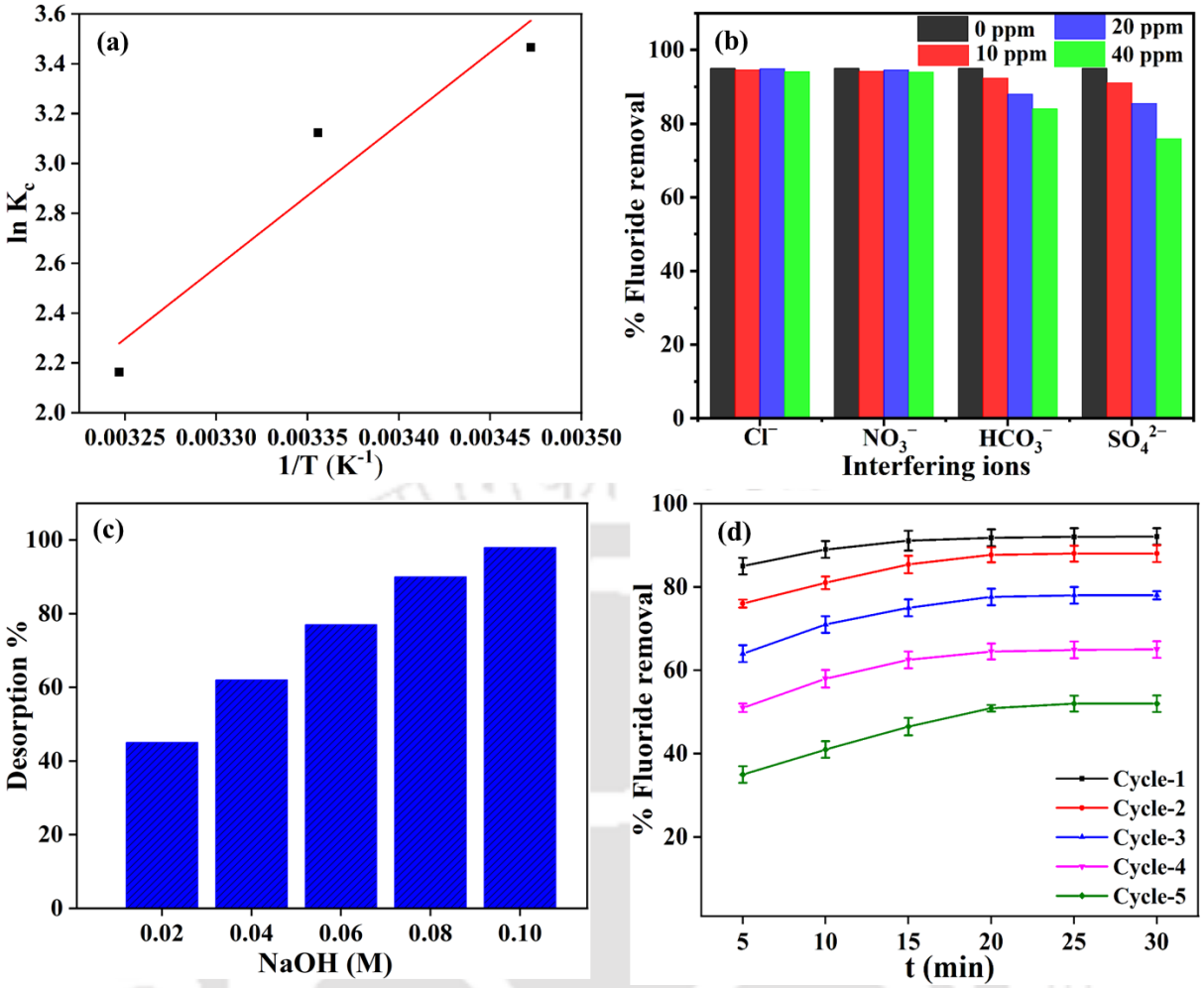

Figure 2.10. (a) Van't Hoff's plot, (b) the effect of interfering ions on the fluoride removal efficiency, (c) Comparison of fluoride desorption using different molar of NaOH, and (d) Regeneration study of AC/Ce/Fe-1 up to 5th cycle.

2.3.3.6. Effect of co-existing ions

The drinking water from groundwater often includes multiple anions in addition to F^- ions, such as SO_4^{2-}, Cl^-, NO_3^- and HCO_3^-, which may compete for adsorption sites with F^- ions [102,105]. Fluoride ion uptake in the presence of those ions is critical to demonstrate the selectivity and unlocking the full potential of AC/Ce/Fe-1. The studies were carried out by adding the required amount of Na_2SO_4, NaCl, $NaNO_3$, and $NaHCO_3$ to a 50 mL of 20 mg/L fluoride concentration. The results presented in **Figure 2.10**b indicate that various anions at

different concentrations have a different effect on fluoride adsorption. The effects of Cl^- and NO_3^- on fluoride adsorption are negligible. However, the co-existence of HCO_3^- and SO_4^{2-} slightly decreases the F^- ions uptake, and this is presumably attributed to the lower affinity of Ce–Fu for fluoride and competition between the fluoride ion and HCO_3^- and SO_4^{2-} occur during the process [139]. Furthermore, the order of interference matches favourably with the charge/radius values of competing anions. The higher the charge/radius, the more likely the anion will be attracted to the adsorbent surface, interfering with the adsorption of F^- ions [140].

2.3.3.7. Regeneration test

The regeneration of as-prepared AC/Ce/Fe-1 was evaluated to ensure the reusability of AC/Ce/Fe-1, displayed in **Figure 2.10**c and **Figure 2.10**d. This was achieved by collecting the F^- ions loaded AC/Ce/Fe-1 after adsorption and soaking in 50 ml of Millipore water for 30 min. AC/Ce/Fe–1 was then treated with 0.01, 0.02, 0.04 and 0.1M sodium hydroxide solutions. 0.1M NaOH was found to exhibit the highest desorption ability [102,130]. The adsorbent AC/Ce/Fe-1 was defluorinated and the solid was collected carefully after drying. 10 mg of exhausted adsorbent was used to replicate the adsorption-desorption study to remove 10 mg/L of ion from 20 ml of the solution to estimate the reusability of the adsorbent. The adsorbent was able to remove 50 % of fluoride on the fifth cycle. The percentage desorption was calculated using Eq. (2.13).

$$D = \frac{C_{des}}{C_{ads}} x100 \qquad (2.13)$$

The percentage desorption is represented as D, C_{ads} is the adsorbed concentration at equilibrium and C_{des} is the desorbed concentration.

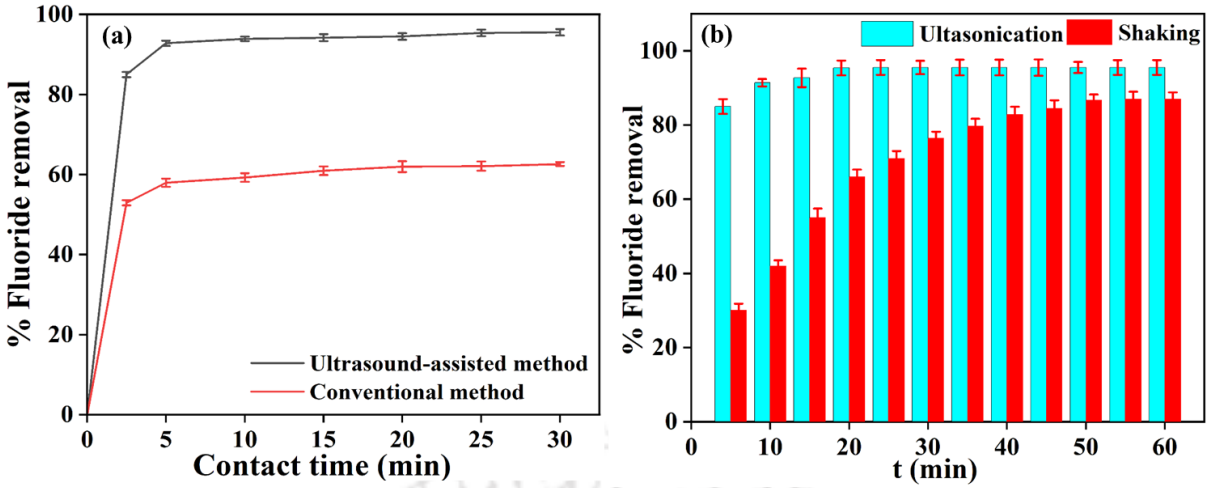

Figure 2.11. The comparative study of ultrasound-assisted over conventional methods for the (a) AC/Ce/Fe-1 synthesis, and (b) adsorption process.

2.3.4. Effect of ultrasound

An eco-friendly approach for both adsorbent synthesis and adsorption study was achieved by using an ultra-sonicator. Acoustic cavitation is the prime principle of the low-frequency ultrasonic treatment that includes the generation and breakdown of the tiny vapor bubbles formed in the aqueous medium at the solid-liquid interface [106]. This enhances the mass transfer rate from the liquid to the interface and also within the pore of the adsorbent by the transmission in form of a pressure wave [105].

2.3.4.1. Role of ultrasound in material synthesis

The comparative study of ultrasound-assisted over conventional method for the synthesis of AC/Ce/Fe-1 shows a significant difference in the fluoride removal efficiency **(Figure 2.11a)**. The experiment was repeated thrice to confirm the outcome of the experiments. The study shows only 62.6 % of fluoride was removed by AC/Ce/Fe-1 prepared via a conventional method, whereas removal efficiency obtained from the ultrasound-assisted method was 95.4 %.

In this work, the interaction mechanism becomes a little complicated because of the impregnation of two metals (Ce and Fe) on AC, as shown in **Figure 2.12a**. For ease of comprehension, the entire mechanism may be broken down into a few phases.

i. Acoustic streaming during sonication induces distinct energy, leading to a disturbance on the surface of the AC by cleaving the OH^- bonds [141]. The hot spot generated during the acoustic cavitation increases the chance of molecular interaction with metals which consequently enhances the active site on the surface and in the pores of the material [142].

ii. Dissociation of water molecules also occurs as a result of sonic cavitation, resulting in hydrogen (H*) and hydroxyl (OH*) radicals and behaves as the Lewis sites.

iii. The metal salts Ce $(NO_3)_3$ and Fe $(NO_3)_3$ break into metal ions and behave as Lewis's acid. Metal aqua ions are generated when they are introduced to an aqueous solution, and they are further hydrolysed. The hydrolysis of the metals are given below [102]:

$$Ce\,(NO_3)_3.6H_20 \rightarrow Ce^{3+} + 3NO_3^- + 6H_2O \quad (2.14)$$

$$Ce^{3+} + 3H_2O \rightarrow Ce\,(HO)_3 + 3H^+ \quad (2.15)$$

Similarly,

$$Fe\,(NO_3)_3.9H_20 \rightarrow Fe^{3+} + 3NO_3^- + 9H_2O \quad (2.16)$$

$$Fe^{3+} + 3H_2O \rightarrow Fe\,(HO)_3 + 3H^+ \quad (2.17)$$

iv. Polycondensation occurs after the formation of Ce $(OH)_3$ and Fe $(OH)_3$ by the olation and oxolation processes, resulting in hydroxyl and oxo-bridges between the tetramer units.

$$Ce - OH + H_2O - Ce \rightarrow Ce - OH - Ce + H_2O \quad (2.18)$$

$$Ce - OH + OH - Ce \rightarrow Ce - O - Ce + H_2O \quad (2.19)$$

Similarly,

$$Fe - OH + H_2O - Fe \rightarrow Fe - OH - Fe + H_2O \quad (2.20)$$

$$Fe-OH\ +OH-Fe \rightarrow Fe-O-Fe\ +H_2O \quad (2.21)$$

v. During cavitation bubble collapse, the film thickness adjacent to the AC decreases, and the surface reaction gets enhanced, leading to the uniform crystallization of metals on the surface of AC.

Therefore, an ultrasound-assisted method was utilized for the synthesis of adsorbent impregnated with binary metals in different Ce/Fe molar ratios for effective fluoride uptake.

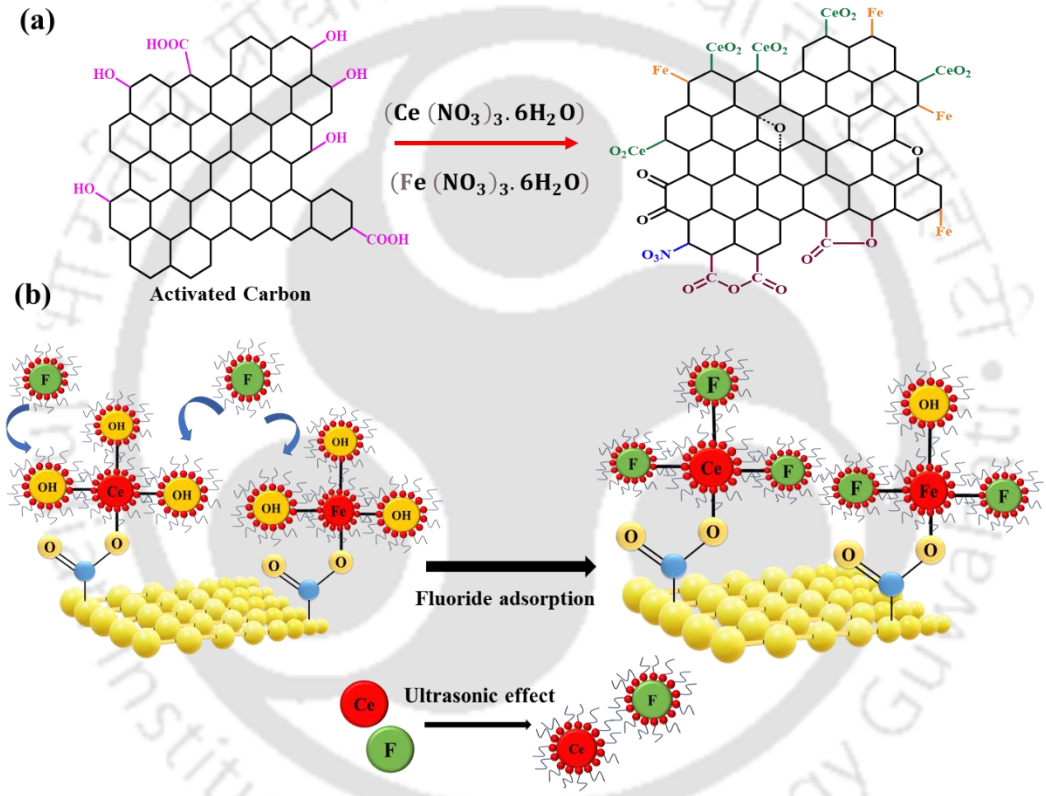

Figure 2.12. (a) Interaction mechanism of two metals (Ce and Fe) on AC and (b) Adsorption mechanism for fluoride removal.

2.3.4.2. Effect of ultrasound in the adsorption process

Batch-wise studies for the fluoride adsorption show a significant increase in the removal efficiency upon the application of ultrasonic waves compared to the conventional shaker (**Figure 2.11b**). The comparative study of the ultrasonication method over conventional

shaking methods shows a much higher removal efficiency of 95.4% in 20 min. Whereas, only 87% of removal efficiency in 60 min was noted via the conventional method. Furthermore, a drastic reduction in the equilibrium time from 60 min to 20 min after the application of sonication was noted over the traditional shaking method. The hydrolysis of metals in the aqueous medium formed Ce $(OH)_3$ and Fe $(OH)_3$ that attract the fluoride ions by protonation or deprotonating depending upon the pH of the solution. In this way, F^- ion get attached to Ce $(OH)_3$ and Fe $(OH)_3$ in the following ways [106]:

$$Ce\ (HO)_3 + xF^- \leftrightarrow Ce\ (HO)_{3-x}\ F_x + OH^- \quad (2.22)$$

Similarly,

$$Fe\ (HO)_3 + xF^- \leftrightarrow Fe\ (HO)_{3-x}\ F_x + OH^- \quad (2.23)$$

The fluoride ion attaching to the adsorbent surface through the electrostatic force is termed protonation [143]. This results in the replacement of OH^- by F^- ion through the ion exchange process, as displayed in **Figure 2.12**b [113]. The rate of adsorption by sonication is much faster than the traditional shaking study because of the turbulence produced in the aqueous medium during the bubble collapse [110,142]. This reduces film thickness near the adsorbent surface, which in turn decreases the time required to reach equilibrium drastically. The system reaches the equilibrium just after 20 min by the acoustic cavitation phenomenon, contrary to shaking that takes 1 hr to reach equilibrium. Thus, ultra-sonication enhances the adsorption rate as well as the adsorption capacity of the material.

2.4. Conclusions

The utilization of ultrasound was done to activate the interior of the material during the synthesis of the adsorbent and in the adsorption study. The collapse of microbubbles resulted in enhancement of molecular interaction and shorter diffusion path, thereby enhancing the

kinetics of the reaction. Therefore, adsorbent synthesized and adsorption study via sonochemical method over conventional method is advantageous and effective for further use. The positive adsorption of ions onto the AC/Ce/Fe-1 with Ce/Fe molar ratio (2:1) was confirmed by the EDX, and FTIR spectra. Utilization of sonochemical method enhances the kinetics of the reaction and reached equilibrium within 20 min where 80% of the fluoride removal was observed just in 5 min. The adsorption kinetics data was found to match well with the pseudo-second-order model. The maximum adsorption capacity of as-synthesized adsorbent was 52.3 mg/g within an equilibrium time of 20 min at 25 °C, and AC/Ce/Fe–1 continued its relatively high adsorption efficiency up to 4^{th} cycles. Additionally, a spontaneous exothermic reaction with less randomness at the adsorbent-solution interface was confirmed by thermodynamic data. Results of the current study suggest that the use of a sonochemical method for both material synthesis and adsorption studies increases the active site on the interior of the adsorbent. This results in rapid and high adsorption of fluoride on the as-synthesized material, which has potential for practical use. Hence, ultrasound-assisted adsorption using AC/Ce/Fe-1 is an efficient technique for enhanced removal of fluoride ions having relatively low cost and thus has scope for industrial application.

CHAPTER 3

Cerium-based Metal-Organic-Frameworks with Ligand Tuning of the Microstructures for Fluoride Adsorption: Linear and Nonlinear Kinetic and Isotherm Adsorption Models

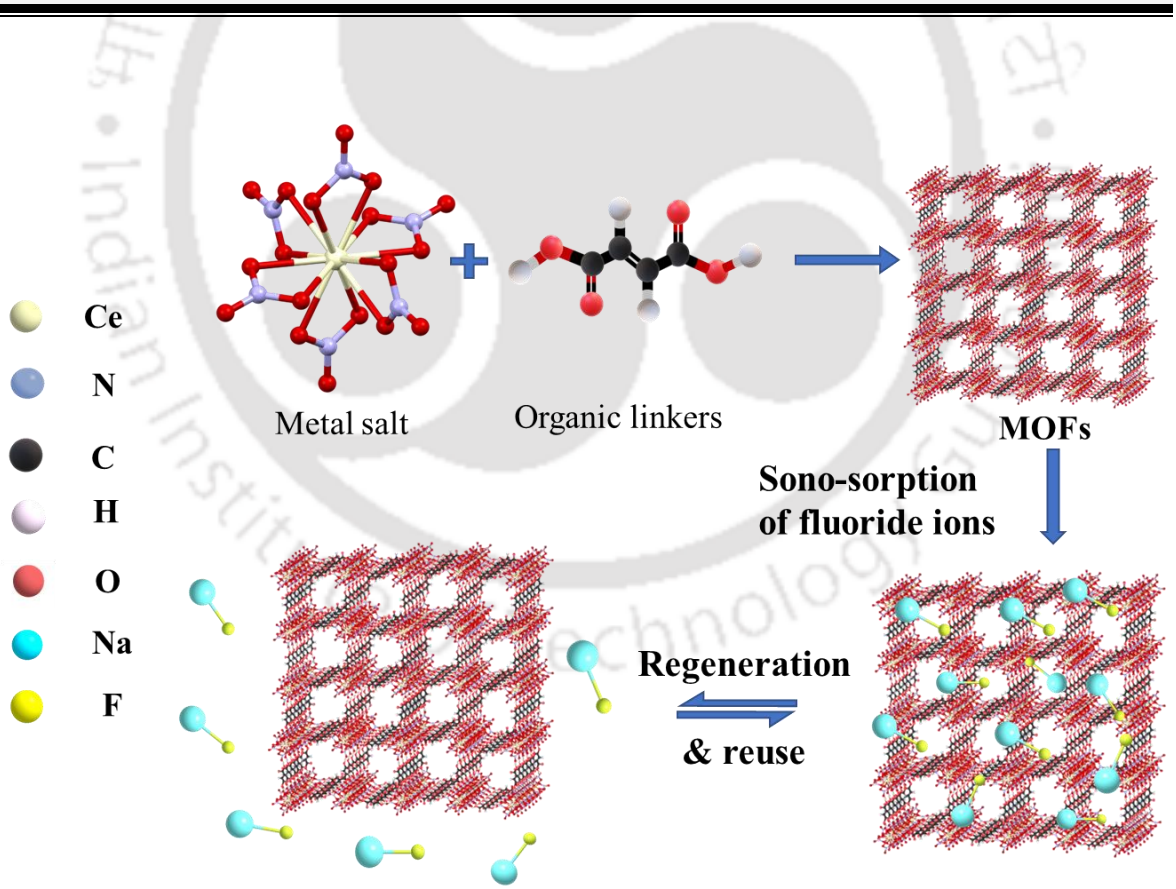

CHAPTER 3

This chapter covers the valuable insights into the synthesis of Ce-based MOFs for fluoride removal, with a focus on the synthesis process, material characterization, fluoride adsorption performance, and the potential mechanisms involved. The study also addresses the practical aspects of regeneration and reusability, providing a comprehensive understanding of the developed MOFs.

3.1. Introduction

AC impregnated with binary metals Ce/Fe in the molar ratio 2:1 explained in chapter 2 displayed a satisfactory result when it was compared with the other AC based adsorbent available in fluoride removal application. Still, there is an urge to develop a material having outstanding adsorption capacity, this enhancement can be done by the use of MOFs. Biocompatible, non-toxic, rare earth metal cerium with redox properties is abundant in the earth's crust and has stronger bond strength with fluoride [144]. Ce-based MOFs react with fluoride by the ion-exchange method. The water-stable Ce-based MOFs have excellent structure adjustability, which provides a large surface area [145]. In this view, the nanoporous Ce-based MOFs were introduced in the study. Despite the advantages, research on Ce-based adsorbents for defluoridation remains limited, particularly concerning the synthesis of MOFs using different organic ligands. Hence, our study concentrates on cerium-based MOFs to explore their defluoridation capabilities and understand the impact of various organic ligands on performance [107]. Therefore, this study aimed to develop Ce-based MOFs using three different linkers terephthalic acid (BDC), fumaric acid, and trimesic acid (H_3BTC), which affords Ce–BDC, Ce–Fu, and Ce–H_3BTC MOFs for powerful elimination of F^- ions from

water. The synthesis and application of novel Ce–Fu MOF has not been reported best of our findings. The effect of co-existing ions and the water stability test were conducted to check the sustainability of the Ce–Fu MOF in water treatment applications. The adsorption behaviour of the material was observed after the investigation of adsorption isotherms and kinetics models. A regeneration study of the MOFs was accomplished to estimate their effectiveness for long term application in wastewater treatment containing fluoride as a contaminant.

3.2. Experimental section

3.2.1. Chemicals

The compounds N, N-dimethylformamide (DMF, 99%), and ethanol used in this experiment were supplied by Merck Ltd., Mumbai, India. Terephthalic acid (BDC, 98.9%), trimesic acid (H_3BTC) and ammonium cerium (IV) nitrate (CAN) were supplied by Sigma-Aldrich. Fumaric acid was purchased from HiMedia, Mumbai, India. The suppler of other chemicals used in this study has been mentioned in chapter 2.

3.2.2. Material synthesis

The synthesis of Ce–BDC MOF was carried out according to reported procedures with little modification [146]. 1 g of BDC was dissolved into 40 ml of DMF by sonication and to this solution, 1g of CAN in 10 ml of H_2O was mixed. Finally, the solution mixture was kept at 100 ˚C in a hot air oven for 24 h in a 100 ml polypropylene bottle. The precipitation was observed within 30 min. The precipitate obtained was stirred in DMF for 1 h and centrifuged to separate the solid mass. This step was repeated 3 times followed by overnight stirring in ethanol to remove all the impurities trapped within the pores. The precipitate collected from the last step was oven-dried for 14 h at 100 ˚C to get powdered Ce–BDC MOFs.

Similarly, Ce–Fu and Ce–H_3BTC MOFs were synthesised using a specified amount of fumaric acid and trimesic acid dissolved into DMF by sonication in separate PP bottle, respectively. To this mixture, CAN dissolved in 10 ml of H_2O was added following the same procedure for Ce–BDC MOF synthesis as described in the preceding section.

3.2.3. Fluoride Adsorption Tests

Previously synthesised fluoride STD solution mentioned in section 2.4 was further diluted as per the initial concentration (C_0; mg L^{-1}) of fluoride required for the adsorption study. The batch-wise experiment was employed for fluoride adsorption at a pH of 6.8±0.3 by varying the initial concentration of fluoride from 10 to 50 mg/L (10, 20, 30, 40, and 50 mg/L) at room temperature. The effect of solution pH over the range from 3−11 was studied with 10 mg/20mL of prepared MOFs. The solution volume for this study was taken 20 mL in a 25 mL polypropylene bottle having 10 mg/L of initial concentration of fluoride. The temperature range for the isotherm study was selected from 15 to 35 °C (15, 25, and 35 °C). The kinetic study was investigated at different initial concentrations to understand the adsorption rate for 30 min. The effect of the adsorbent amount was examined using 20 mL of 10 mg/L fluoride solution by adding 10–50 mg (10, 20, 30, 40, and 50 mg) of adsorbent. The fluoride adsorption and the percentage removal of fluoride were calculated using Eqs. (2.1) and (2.2), respectively.

3.2.4. Characterization techniques

Apart from the characterization techniques mentioned in the section 2.2, we utilized a thermogravimetric analyzer (TGA, TG209 F^1 Libra, Netzsch, Germany) was used to check the thermal stability of Ce–based MOFs by changing the temperature under N_2 environment.

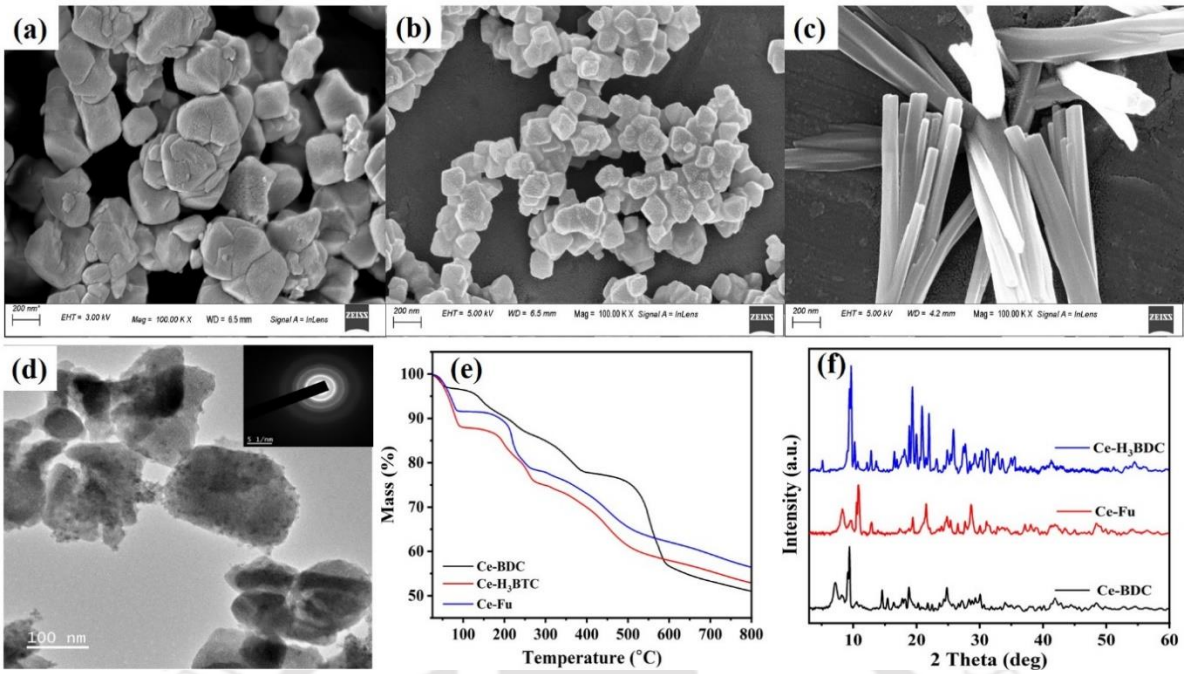

Figure 3.1. FESEM image of (a) Ce–BDC, (b) Ce–Fu, (c) Ce–H_3BTC MOFs; (d) FETEM image of Ce–Fu MOFs, (e) TGA analysis of Ce–based MOFs, and (f) FTIR spectra of Ce–based MOFs.

3.3. Results and discussion

3.3.1. Characterization

The FESEM analysis of drop cast specimen was done after sputter coating of gold on to poorly conducting specimen. The gold coating prevents charging of the specimen, reduces microscope beam damage, increases thermal conduction, and improves secondary electron emission for better image projection. FESEM images of the particle morphology of Ce–based MOFs are illustrated in **Figure 3.1**(a-c). Ce–BDC, and Ce–Fu are formed primarily as agglomerates of octahedral particles having average size of 200±10 and 150±10 nm, respectively. On the other hand, and Ce–H_3BTC MOFs shows a rod flower like structure (**Figure 3.1**c). The FETEM

images of Ce–Fu MOFs illustrated in **Figure 3.1**d confirms the shape, size of the morphology, and their amorphous nature.

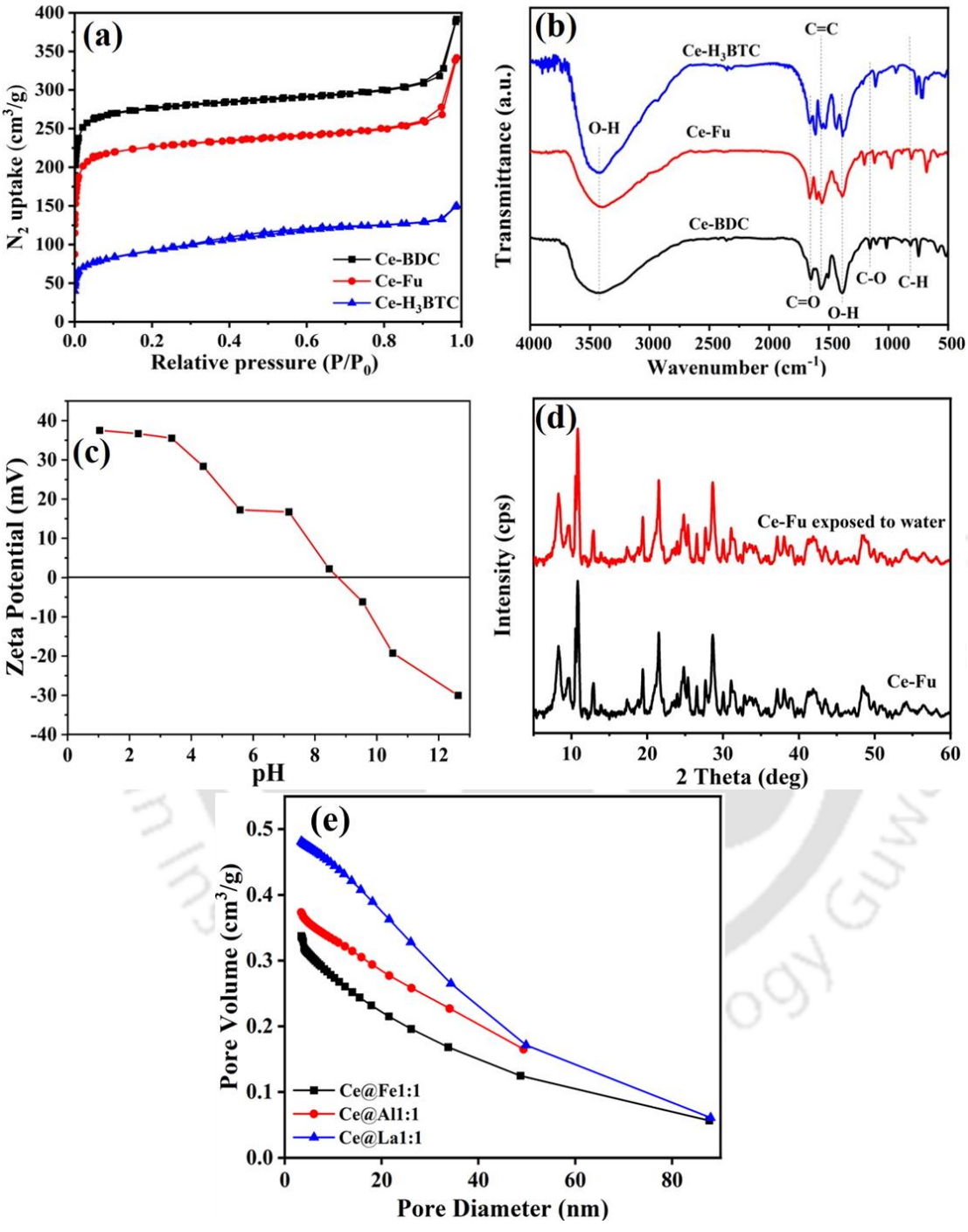

Figure 3.2. (a) N_2 adsorption-desorption isotherm of Ce–based MOFs, (b) FTIR of Ce–based MOFs, (c) Zeta potential of Ce–Fu MOFs at different pH, (d) Water stability test of Ce–Fu MOF, and (e) Pore size distribution of mixed matrix MOFs.

Figure 3.1e demonstrate the three-stage thermal degradation curves obtained from TGA thermograms of pristine Ce–BDC, Ce–Fu, and Ce–H_3BTC MOFs. The drastic weight loss in the initial stage alluded to the evaporation of unbounded water molecules observed up to 96°C. A further drop in the mass percentage was observed at a temperature ranging from 130 to 330°C, which may be because of the evaporation of bounded H_2O molecules and the trapped solvent molecules within the structure of the taken samples. Afterward, the remaining sections could maintain stability up to 520°C, as seen by the minor weight loss in that temperature range. In contrast, a further rise in temperature after 520°C resulted in a continuous weight loss occurred due to the breakage of crosslinked bonds of the linkers, which causes the destruction of the structures. Although the finding of the thermal stability behaviour is not a crucial step in the adsorption process.

The XRD pattern (**Figure 3.1f**) indicates a polycrystalline nature of Ce–based MOFs. The elements presented in Ce–BDC, Ce–Fu and Ce–H_3BTC MOFs have a different diffraction spectrum when the sample is exposed to the X-ray beam. The diffraction pattern of the beam by Ce molecules at a 2-theda indicates the existence of Ce at 28(111), 33(200), 47(220), and 56(311) [147]. The presence of cerium was also validated by the data obtained from EDX [115,148].

The adsorptive gas N_2 was used for adsorption-desorption analysis to estimate isotherms of Ce–BDC, Ce–Fu, and Ce–H_3BTC MOFs shown in **Figure 3.2**a. The study mainly estimates the size distribution of pore, total volume, and the surface area of MOFs at the analysis bath temperature of 77.3 K, shown in **Table 3.1** [118]. The analysis of the adsorbents exhibits type II isotherm, which has slit shape pores with open monolayer-multilayer adsorption [119]. The uptake trend is continuous with an increase in the pressure ratio up to 0.1 indicating a quick rise at low P/P_0 corresponds to microspores monolayer adsorption. Furthermore, a further

increase in the relative pressure shows slower adsorption of the N_2 can indicating multilayer adsorption. The average pore diameters of Ce–BDC, Ce–Fu and Ce–H_3BTC MOFs have been estimated at around 2.4, 1.2 and 2.9 nm, indicating a mesoporous structure. Fluoride ions having a radius of 0.133 nm will enter easily within the pores of the MOFs.

Table 3.1. N_2 adsorption-desorption analysis to obtain different parameters of Ce–based MOFs.

Adsorbents	**Ce–BDC**	**Ce–Fu**	**Ce–H_3BTC**
Average pore radius (nm)	2.4	1.2	2.9
Surface area ($m^2 g^{-1}$)	758	830	626
Total pore volume (cc g^{-1})	0.43	0.41	0.13

The transmittance band of the Ce–based MOFs after and before the fluoride loading are displayed in **Figure 3.2b**. The broad peak at 3426 cm^{-1} resembles the –OH due to strong stretching vibration. As a result of the coordination of the metal present in the material with the carbonyl group available in fumaric acid ligand, a strong peak appears around 1650 due to C=O stretching [147]. The distinct peak observed at 1602 cm^{-1} validates the existence of the COO group, which is attributed to the stretching of the carboxyl group. Besides, the spectrum at 1384 cm^{-1} referred to C=O of carboxylate groups present in the fumaric acid [149]. Additional small changes in the lower range owed to the Ce−O stretching and Ce−O−C vibration in the Ce–Fu [150].

The electric potential of a surface is the measure of the work required to transport a unit positive charge from infinity to the surface without inducing acceleration. The measure of electrokinetic potential and zero-point charge of the material give the excess to understand the working range of as-synthesized material to target the anionic pollutant [120]. Therefore, the electrokinetic

potential of the Ce–Fu MOF was analyzed by dispersing the material into millipore water, maintained at different pH ranges from 2 to 13, as shown in **Figure 3.2**c. The Zero point refers to the value of the pH at which the overall charge on the surface of the MOFs is zero and at pH above the zero point, the overall charge of the material surface becomes negative. The zero-point charge appeared at approximately pH 9 and gives significant removal of fluoride below the zero point. The electrokinetic potential was found +37.52 mV favourable for the removal of F^- ions by electrostatic interactions [151].

3.3.2. Water stability test of Ce–Fu MOF

Since, in this study Ce–Fu MOF is being used to remove fluoride from water, its structural deformation in water must be investigated to ensure stability throughout the adsorption process. To this objective, we examined the XRD pattern of Ce–Fu MOF after two days of exposure to water (**Figure 3.2d**). The XRD peaks of Ce–Fu MOF after and before exposure to water remain the same within the range of 5–60°. Ce–Fu MOF possesses a highly stable crystalline structure in water, suggesting a promising role for Ce–Fu MOF in aqueous applications.

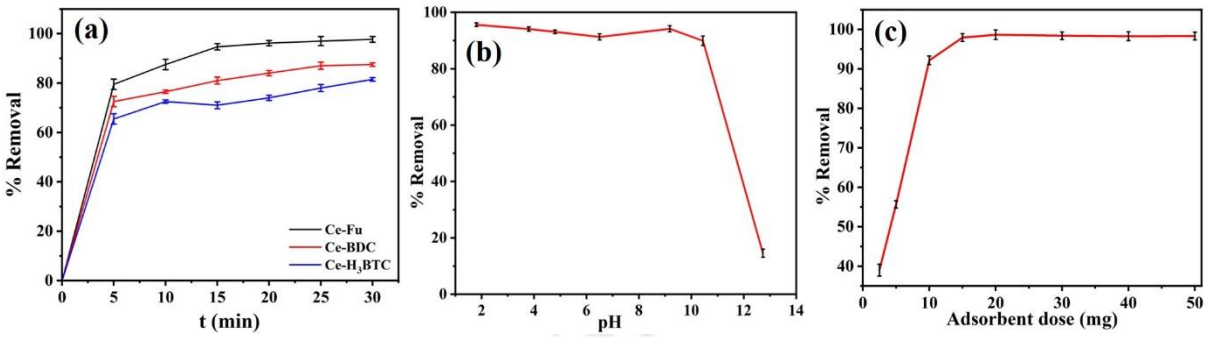

Figure 3.3. (a) Comparative assessment of Ce–based MOF, (b) effect of pH on fluoride removal, and (c) adsorbent dose-effect.

3.3.3. Comparative assessment of Ce–based MOFs

The percentage removal of fluoride using Ce–based MOFs such as, Ce–BDC, Ce–Fu and, Ce–H_3BTC MOFs was compared to find the best suitable adsorbent. The study was done using 10 mg of adsorbents in 10 mg/L of 20 ml fluoride solution. The maximum fluoride removal was obtained as 97.7% by Ce–Fu, Ce–BDC MOF exhibited 87.5%, and Ce–H_3BTC MOFs displayed 81% (**Figure 3.3**a). The Ce–Fu MOF demonstrating maximum removal of fluoride was used for further characterization and adsorption studies.

3.3.4. pH effect

The pH effect of the solution was examined to understand material behaviour for fluoride remediation ranging from pH 2 to 13 [105]. The shift in the F^- ions removal percentages can be seen in **Figure 3.3**b at optimized conditions (adsorbent dose: 10 mg, contact time: 30 min, solution volume: 20 mL, initial concentration: 10 mg/L F^- ion and temperature: 25˚). The removal percentage of F^- ions was approximately constant in the range of pH 2 to 9 since the net surface charge on the material remain positive below the zero point. The percentage removal of fluoride was observed at pH 2 i.e., 95.6% because both ionic and electrostatic force becomes responsible for desorption on the active sites as shown in Eqs. (2.3) and (2.4). Moreover, as pH increases beyond the isoelectric point, the removal percentage dropped to 4, and hydroxyl ions challenge targeting ions for the active. The increase in the ions decreases the productiveness of the as-synthesized material by neutralizing the favourable charge of the active sites for fluoride removal, therefore in adsorption process as shown in equation (2.5).

Table 3.2. Isotherms parameters obtained from different fittings.

Isotherm models		**T**		
		288 K	**298 K**	**308 K**
Langmuir	Q_0	62.189	60.790	58.513
Linear	K_L	0.00027	1.023	3.138

	R^2	0.991	0.991	0.986
Non-linear	Q_0	64.162	61.3042	59.545
	K_L	0.232	0.211	0.166
	R^2	0.909	0.955	0.955
Freundlich	K_F	1.052	1.072	1.017
Linear	n	4.456	3.355	3.146
	R^2	0.954	0.967	0.954
Non-linear	K_F	24.847	20.007	17.266
	n	4.194	3.485	3.246
	R^2	0.98	0.98	0.97
Temkin	B	7.932	10.140	10.291
Linear	K_T	31.401	5.807	3.813
	R^2	0.904	0.939	0.924
Non-linear	B	7.918	10.140	10.292
	K_T	31.598	5.807	3.813
	R^2	0.96	0.97	0.97

3.3.5. Effect of doses

The experiment was conducted using 10 mg/L of 20 ml F^- ion solution to optimize the Ce–Fu MOF at neutral pH. This is illustrated in **Figure 3.3**c, the remediation of fluoride enhanced from 51 % to 98.3 % as the adsorbent dose increased from 5 mg to 10 mg for 30 min. This is because of the rise of active spots as we increase the adsorbent dosage [77]. Further increase

in the Ce–Fu MOF from 10 to 50 mg in the fluoride solution did not demonstrate an imperative rise in the F^- ions removal. This may be because of the overlap in the active spots available on the adsorbent at higher amounts, significant to no supplementary availability of active spots on the peripheral of the adsorbent for fluoride adsorption. Thus, 0.5 g/L of Ce–Fu MOF was used for further adsorption study experiments.

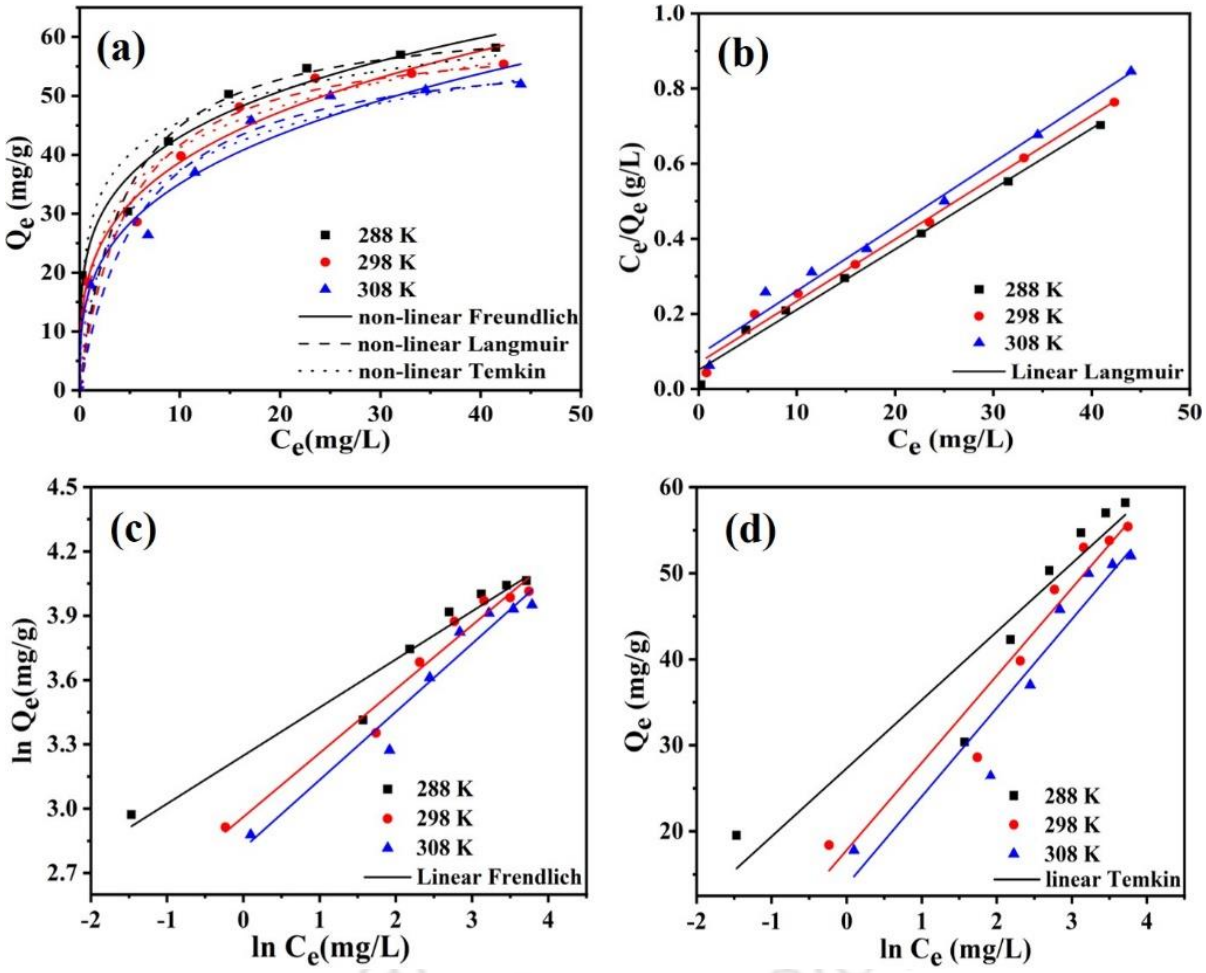

Figure 3.4. Adsorption isotherms of fluoride by Ce–Fu (a) non-linear fitting of isotherm models; (b) Langmuir linear fittings; (c) Freundlich linear fittings; and (d) Temkin linear fittings.

3.3.6. Isotherm study

The adsorption of F^- ions on Ce–Fu was further studied utilizing an adsorption isotherm at a constant temperature [124,125]. **Figure 3.4** shows the affiliation between the Q_e and C_e at various temperatures (288 K, 298 K, and 308 K) to scrutinize the best-suited model. The adsorptive data gained from the experiments were attuned to linear and non-linear isotherm models such as Freundlich, Langmuir, and Temkin (**Table 2.2)**. The isotherm parameters obtained after different linear and non-linear equations fitting are displayed in Table **3.**2. The study exhibits the rise in the temperature decreases the adsorption capacity. As a result, the adsorbent's binding capacity diminishes as the molecules kinetic energy in the MOF increases at an elevated temperature, which states the exothermic process. The values of R^2 found from the non-linear model of the Freundlich isotherm ranging from (0.97-0.98) are larger as compared to the non-linear models of Temkin and Langmuir i.e. (0. 96-0.97) and (0.91-0.95). However, R^2 value for Langmuir linear data is 0.99, becomes a best-fit isotherm model. The Q_0 value from the data fitted the Langmuir isotherm revealing 64.16 mg/g. The Ce–Fu MOF was compared with other existing adsorbents for fluoride removal listed in **Table 3.3**. The Ce–Fu MOF shows rapid kinetic and higher adsorption capacity than the most of the reported Ce-based MOF in the literatures.

Table 3.3. The literature comparison of Ce-based MOF with existing adsorbents.

Material	**Q_0 (mg/g)**	**Equilibrium time (min)**	**pH**	**ref.**
UiO-66	40.09	80	6–9	[89]
UiO-66-NH_2	41.5	30	7	[90]
UiO-66 (Hf)	33.35	80	6–9	[89]
CAU-6	24.22	80	6–9	[89]
Ce@BTC	4.930	30	7	[98]
MIL-100(Fe)	23.53	90	4–10	[152]

Sn (II)-TMA MOFs	30.86	150	3–10	[153]
MOF-801	40	40	2–10	[154]
Ce–MIL-96	38.65	240	3–10	[155]
Fe@BDC	4.90	60	7	[93]
Fe@BDC	4.90	30	7	[156]
Fe@ABDC	4.92	30	7	[156]
La@BDC	4.92	30	7	[94]
La@ABDC	4.95	30	7	[94]
La@Fu MOFs	4.92	30	7	[157]
Fe@Fu MOFs	4.85	30	7	[157]
Ce–Fu MOF	64.16	30	6.5	Present work

3.3.7. Adsorption kinetics

To describe adsorption kinetic processes, the experimental data were examined by using kinetic equations namely the PFO model, PSO model, and IPD model [28,134]. The linearized and non-linearized form of the PFO model is mentioned in Eq. (2.7) and Eq. (2.8), respectively. Additionally, the linearized and non-linearized PSO kinetic model mentioned in Eq. (2.8) and Eq. (2.9), respectively. Furthermore, the data obtained were fitted to the IPD model to find the rate-determining step to understand the diffusion process during the adsorption and represented by Eq. (2.10). The kinetic study was performed at different initial concentrations of fluoride from 10 mg/L, 20 mg/L, 30 mg/L, 40 mg/L, and 50 mg/L. 10 mg of Ce–Fu MOF was added to 20 ml of fluoride ion solution throughout the kinetic study at neutral pH for 30 min. The linear and non-linear fits of each kinetic model are shown in **Figure 3.5** and parameters obtained from fittings are cited in **Table 3.4**. The linearized PSO model provides a R^2 value of 0.99, which is greater than the R^2 obtained from the linearized PFO and IPD model ranging from

0.98 to 0.99 and 0.77–0.95, respectively. Hence, the best fitted kinetic model is PSO. Furthermore, the value of R^2 obtained from non-linear fittings of the PSO model ranges from 0.96 to 0.99 are much closed to 1 and greater than that of other non-linear kinetic models used. Chemical sorption is assumed to be the rate-limiting phase in the PSO kinetic model, which may entail valency forces via ion exchange between F^- ions and MOF. It also predicts the reaction over the entire range of adsorption. In this scenario, adsorption capacity is utilized to determine the adsorption rate, rather than the adsorbate concentration [135].

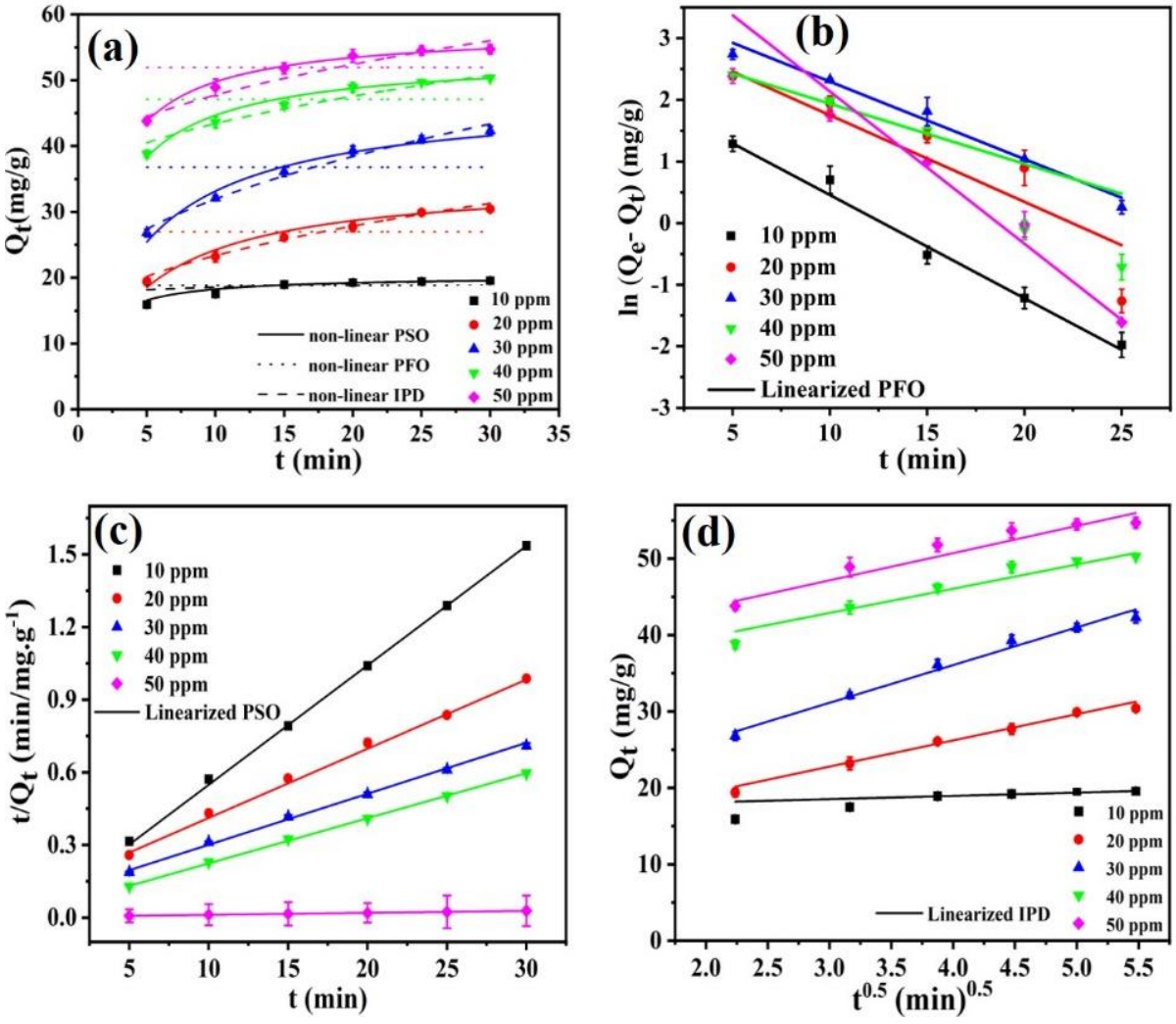

Figure 3.5. Effect of exposure time (a) non-linear fitting of kinetic models, (b) linearized PFO model, (c) linearized PSO mode, and (d) linearized IPD kinetic model fitting.

The PSO model has a substantial advantage, because the calculation of the Q_e may be done from the model itself. Whereas in the PFO model the Q_e is evaluated from the experiment [136]. Furthermore, the boundary layer and pore diffusion processes may also be used to describe how the solid diffuses from the bulk to the outside of the adsorbent and subsequently within the pores. The magnitude of the boundary layer is determined by the value of K_i, which increases with the intercept value of the Q_t vs. $t^{0.5}$ plot. As a result, boundary layer diffusion dominates the entire process. The rate of adsorption of the as-prepared MOF is considerably quicker than that described in the existing literature (**Table 3.4**), reaching equilibrium in less than 30 minutes.

Table 3.4. Kinetic parameters obtained from different fittings of kinetic model.

Kinetic models		**C_0 (mg/L)**				
		10	**20**	**30**	**40**	**50**
PFO	$Q_e\left(\frac{mg}{g}\right)$	8.4	23.5	34.9	18.4	100.4
Linear	$k_1\left(\frac{1}{min}\right)$	0.168	0.141	0.125	0.097	0.247
	R^2	0.99	0.89	0.99	0.92	0.98
Non-linear	$Q_e\left(\frac{mg}{g}\right)$	19.50	30.2	40.67	49.9	53.7
	$k_1\left(\frac{1}{min}\right)$	0. 250	0. 168	0. 177	0. 278	0. 330
	R^2	0. 82	0.90	0.89	0.88	0.94
PSO	$Q_e\left(\frac{mg}{g}\right)$	20.408	35.714	47.619	55. 55	61.276
Linear	$k_2\left(\frac{g}{mg.min}\right)$	0.043	0.006	0.004	0.008	0.0002
	R^2	0.99	0.99	0.99	0.99	0.99
Non-linear	$Q_e\left(\frac{mg}{g}\right)$	20.28	35.08	47.60	53.65	57.71

	$k_2\left(\frac{g}{mg.min}\right)$	0.044	0.0063	0.004	0.009	0.010
	R^2	0.96	0.97	0.97	0.98	0.99
IPD	$k_i \frac{mg}{g,(min)^{0.5}}$	0.426	3.428	4.93	3.169	3.557
Linear	C	17.25	12.51	16.35	33.39	36.49
	R^2	0.77	0.96	0.98	0.92	0.95
Non-linear	$k_i \frac{mg}{g,(min)^{0.5}}$	0.435	3.42	4.93	3.16	3.55
	C	17.17	12.50	16.35	33.39	36.49
	R^2	0.79	0.96	0.98	0.92	0.97

3.3.8. Thermodynamic parameter analysis

The thermodynamic assessment was conducted to investigate the practicality of the adsorption process. The thermodynamic parameters such as standard enthalpy ΔH° (kJ/mol) standard Gibb's free energy ΔG° (kJ/mol) and standard entropy ΔS° (J/mol. K) were estimated using thermodynamic relations mentioned in Eqs. (2.11) and (2.12). ΔS° and ΔH° are constants calculated from the intercept and slope of the straight line of Van't Hoff's plot of , as shown in **Figure 3.6**a. ΔG° was calculated using Eq. (2.11) at different temperatures. **Table 3.5** displays the fluoride adsorption thermodynamic parameters. The negative ΔG˚ determined at different temperatures denotes the spontaneous nature of the adsorption process. The negative ΔH˚ express that the reaction is exothermic and reductions in the randomness of the adsorption process may be validated by the small ΔS˚[137,138].

Table 3.5. Thermodynamic parameters calculated from Van't Hoff plot.

Temperature	**ΔG˚(kJ/mol)**	**ΔH˚(kJ/mol)**	**ΔS˚(kJ/mol.k)**
288 K	-17.3855	-52.1687	-0.121

298 K	-15.7035
308 K	-14.9811

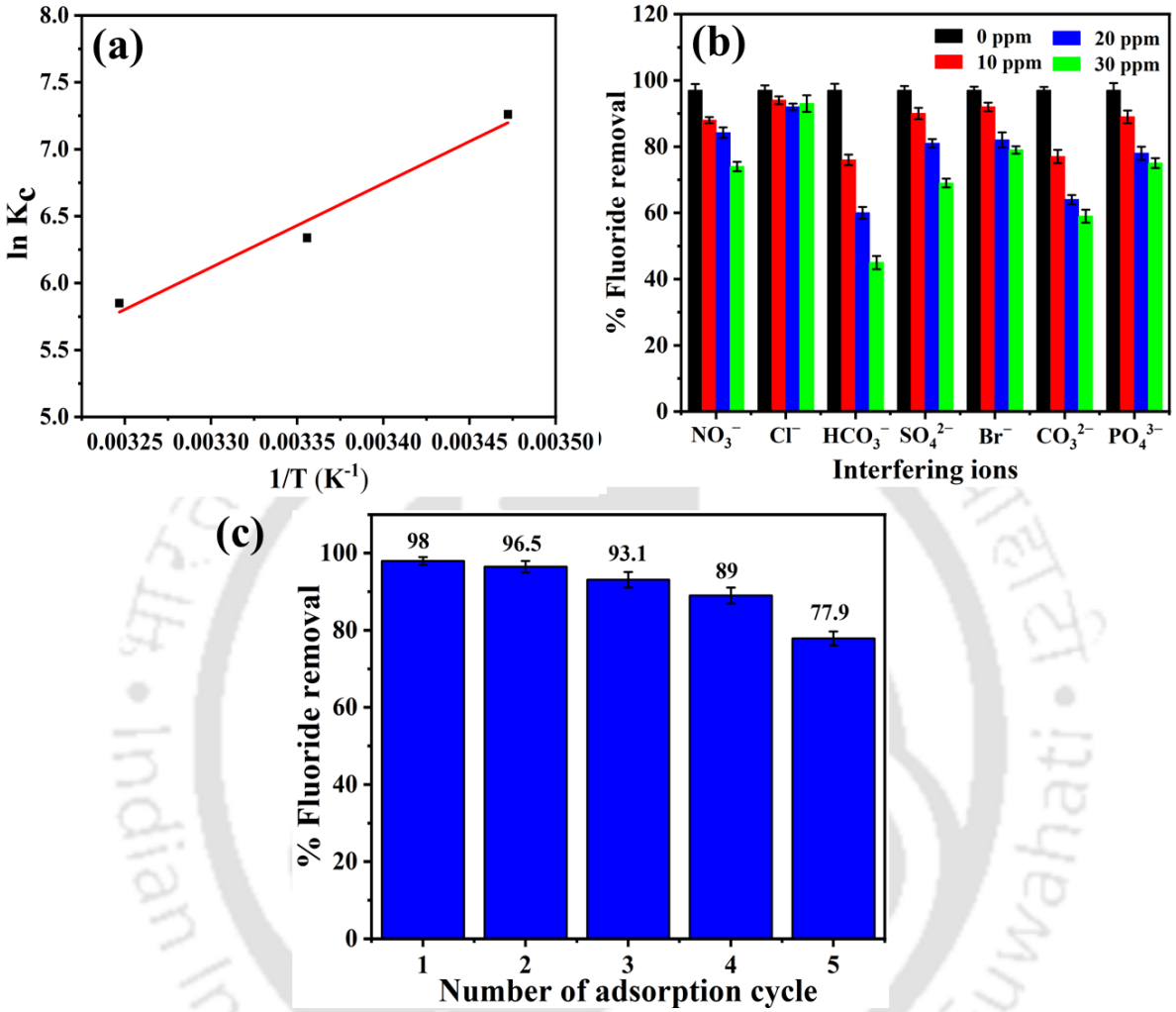

Figure 3.6. (a) Van't Hoff's plot, (b) effect of interfering ions, and (c) fluoride regeneration profile.

3.3.9. Effect of coexisting ions

It is crucial to understand the influence of various co-existing ions on the adsorption of fluoride ions, which may interfere with the fluoride removal process [139,147]. In this study, co-existing ions such as NO_3^-, Cl^-, HCO_3^-, SO_4^{2-}, Br^-, CO_3^{2-}, and PO_4^{3-} were examined in combination with fluoride ions. The Ce–Fu MOF was dosed at a concentration of 0.5 g/L, with

an initial fluoride concentration of 20 mg/L. To explore the potential of Ce–Fu MOF, concentration of co-existing ions was increased from 10 mg/L to 30 mg/L, presented in **Figure 3.6**b. With the introduction of these ions, namely NO_3^-, SO_4^{2-}, Br^-, and PO_4^{3-}, at 10 mg/L, Ce–Fu MOF demonstrated a reduction in fluoride removal percentage by 12.8, 7, 5, and 8%, respectively. Additionally, the interference of HCO_3^- and CO_3^{2-} ions resulted in a reduction in fluoride removal by 21% and 20%, respectively. The impact on fluoride adsorption became more pronounced as the ion concentrations increased. In this scenario, with NO3−, SO42−, Br−, and PO43− ions at a concentration of 30 mg/L, the interference further decreased fluoride adsorption by 23, 28, 18, and 22%, respectively. The presence of 40 mg/L of HCO3− and CO32− ions resulted in a 52% and 48% reduction in fluode elimination, respectively. Notably, even at higher concentrations, Cl− ions did not significantly interfere with fluoride removal even at higher concentrations [139]. Furthermore, the sequence of interference corresponds well to the charge to radius ratio of co-ions. The greater the charge/radius, the anion more probable be drawn to the surface of the material, preventing F− ions from adsorbing [158].

3.3.10. Adsorption regeneration test

The dumping of saturated adsorbents into the environment is a serious solid waste issue for both economic and environmental considerations. This is not only creating secondary pollutants by dispersal of toxic and hazardous material but also upsurges the operational cost involved in a huge amount of sludge handling. The multiple usages of adsorbents increase the process economy and also reduce the cost of handling solid waste. In this study, 20 mg of Ce–Fu was used for the regeneration of adsorbent to eliminate 30 mg L^{-1} of fluoride ions from 20 ml of solution. The fluoride-loaded adsorbent was collected after centrifugation and soaked in 50 ml of NaOH for 30 min under vigorous stirring. The fluoride-free adsorbent was separated via centrifugation followed by drying in the oven. After that, 20 mg of regenerated MOF was utilized to replicate the cycle and found 96.5% of fluoride removal in the 2nd cycle. This

adsorption-desorption process was repeated until the 5th cycle under similar experimental conditions and found 77.9 % removal of fluoride on the fifth cycle, as shown in **Figure 3.6**c. The desorption percentage were calculated using Eq. (2.13).

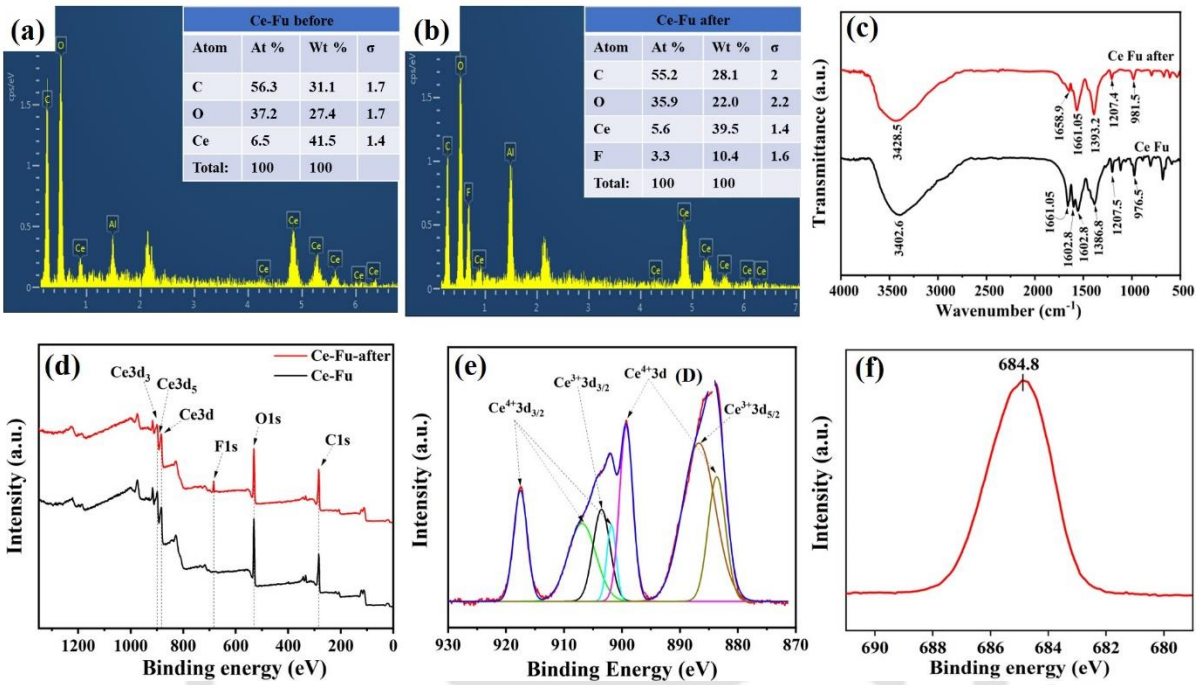

Figure 3.7. (a) EDX of Ce–Fu MOFs; (b) EDX of Ce–Fu MOFs after F^- ions loading; (c) FTIR of Ce–Fu before and after F^- ions adsorption; (d) XPS surface scan of Ce–Fu MOF after and before the fluoride loading; (e) XPS core spectra analysis of Ce3d; and (f) XPS spectra of F1s.

3.4. Fluoride Adsorption mechanism

The adsorption of fluoride can be confirmed after the elemental analysis obtained from EDX. The elemental analysis of the Ce–Fu MOF before and after the adsorption are shown in terms of weight and atomic percentage in Figure **3.7**a and b with the help of EDX analysis. The cerium weight percentage after the fluoride adsorption is decreased from 41.5 to 39.5 %. The loading of the fluoride after adsorption was confirmed by the occurrence of the fluoride peak

in **Figure 3.7**b. The additional presence of an aluminium peak was shown because the sample was drop cast on the aluminium-coated slide.

To understand the adsorption mechanism of the fluoride on Ce–Fu, characterization techniques FTIR and XPS were used. The FT-IR spectra (**Figure 3.7**c**)** of Ce–Fu after and before the fluoride loading are preliminarily examined to get important evidence regarding the adsorption mechanism. The strong peak at 1661 cm^{-1} because of the bending vibration of hydroxyls shifted to 1658.9 cm^{-1} with low intensity after the fluoride loading, demonstrating that the hydroxyls on the adsorbent may contribute to the fluoride removal [159]. After the adsorption, the peak intensity of 1602, and 1384 cm^{-1} weakens confirming the contribution of the carboxylate groups for fluoride removal [88,160]. In addition, a bond at 1114 cm^{-1} in Ce–Fu adsorbent allocated to the bending vibration of Ce–OH disappears upon fluoride adsorption, signifying OH^- bond on Ce may be exchanged by fluoride. Thus, the –OH groups present on the surface vigorously participated in the adsorption of F^- ions (**Figure 3.8**).

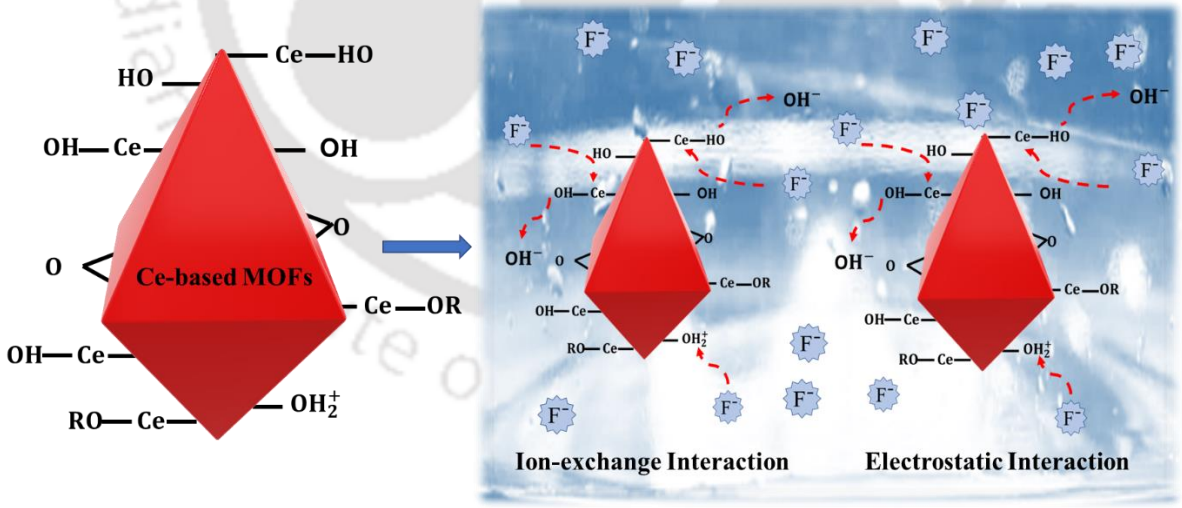

Figure 3.8. Adsorption mechanism of the fluoride on Ce–Fu MOFs.

The XPS spectra supports the presence of Ce, C, and O in the Ce–Fu, and a further peak of fluoride was identified after the adsorption, as shown in **Figure 3.7**d. Ce 3d core-level XPS

spectrum for Ce–Fu MOF reveal peaks of Ce^{3+} $3d_{3/2}$ at binding energies of 899.7 and 904.2 eV are relatively stronger than the Ce^{3+} $3d_{5/2}$ at 881.5 and 885.9 eV [161]. The increased Ce^{3+} content was attributed to reduction via surface oxygen release of Ce^{4+} to Ce^{3+}. This specifies that the Ce^{3+} ions are positioned on the Ce–Fu MOFs surface. The Ce^{3+}/Ce^{4+} ratio in crystallites is extremely dependent on synthesis circumstances and atmospheric exposure. The O1s and C1s spectra reveal a strong peak at 530 eV and 284 eV, respectively [162]. Moreover, elemental survey after fluoride loading shows F1s peak at 684 eV, whereas all other elements have the same binding energy. The intensities of the M–OH peak of adsorbent used is slightly decreased because of the interaction between metal and fluoride. It is noteworthy to mention, that the peak of the metals exhibits a considerable swing to high binding energy, which may be related to the development of complexes (M–F) between metal and F^- ions through an ion exchange process [98]. Based on this research, electrostatic attraction and ion-exchange reaction could be the mechanisms by which fluoride is adsorbed on the surface of the MOFs. The tentative adsorption mechanism of the displayed in the **Figure 3.8**.

3.5. Conclusions

This research demonstrates a robust material with remarkable adsorption capability to remove fluoride from water by using Ce (IV) open sites inside the Ce–MOF. The experiment shows Ce-based MOFs has remarkable fluoride adsorption capacity of 64.16 $mg \cdot g^{-1}$, which is better than the adsorption capacity of AC/Ce/Fe-2 (52.3 mg/g). Ce-based MOFs also displayed good water stability property and quick sorption kinetics. The adsorbent was capable of removing 85 % of the fluoride ions from the solution just in 10 min and reaches maximum adsorption capacity in 30 min. The adsorption kinetics data is well fitted with a PSO model. Thermodynamic measurements also reveal that the reaction is exothermic and spontaneous with reduced randomness at the adsorbent-solution interface. In addition, interference of co-

existing anions such as NO_3^-, SO_4^{2-}, Br^-, and PO_4^{3-} ions were noted at higher concentration, whereas even at higher concentrations, Cl^- ions did not significantly interfere with fluoride removal even at higher concentrations. The adsorbent sustained its relatively higher adsorption efficiency up to the 5th cycle. The adsorption mechanism was attributed to the ion exchange between terminal OH^- ions at the missing linker site and the fluoride ions. The conclusion of this study enables a future application of a Ce-based porous framework for contaminants remediation from water purification.

CHAPTER 4

Cerium-Based Nanoporous Metal-Organic Frameworks Incorporated with Different Metals for Remediation of Fluoride Ion from Water

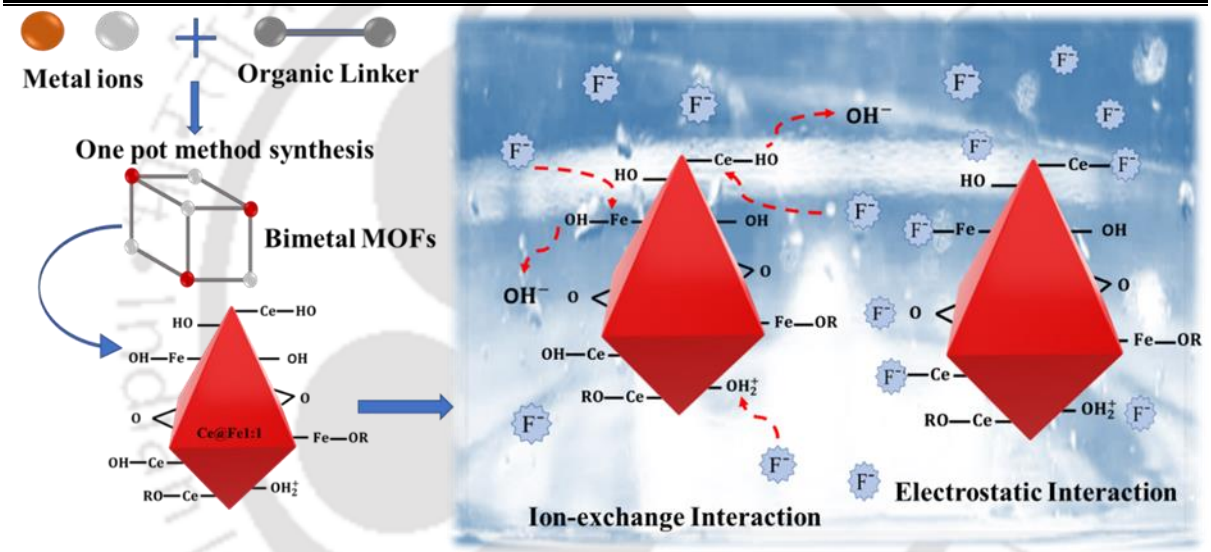

CHAPTER 4

*This section delves into significant perspectives on enhancing of MOFs for the purpose of fluoride removal. The emphasis is on the synthesis procedure, material characterization, fluoride adsorption capabilities, and the potential underlying mechanisms. Additionally, practical considerations such as regeneration and reusability are explored, offering a thorough comprehension of the developed bimetal MOFs. The outcome of the Research has been scientifically acknowledged by, '**ACS applied nano materials'**.*

4.1. Introduction

In recent times, rare earth metal elements have gained prominence in the preparation of rare earth metal-based MOFs. This preference can be attributed to their high valence, biocompatibility, and cost-effectiveness. Notably, rare earth metals possess large ionic radius and numerous extranuclear electron orbitals, conferring unique fluoride-affinity that effectively removes excess fluoride from water.[95] In this context, we produced cerium-based MOFs in the preceding chapter, employing three distinct linkers: BDC, fumaric acid, and H_3BTC. The objective was the removal of fluoride from drinking water. Among the Ce-based MOFs created with various linkers, the Ce-Fu MOFs, synthesized using fumaric acid, exhibited the highest adsorption capacity (64.16 $mg \cdot g^{-1}$). Further enhancement in the adsorption capacity of the Ce-based MOFs may be done by the use of hybrid MOFs. Even though MOF and hybrid materials derived from MOFs have been extensively described for their adaptable structures, bimetal MOFs have rarely been studied as an adsorbent in wastewater treatment.[108] Our goal in this study is to investigate the synthesis of bimetallic MOFs containing nodes composed of inorganic compounds, connected by a fumaric acid linker. Furthermore, we aim to apply the

resulting nanoporous bimetal MOFs in the fluoride removal from drinking water. Notably, to the best of our knowledge, nanoporous bimetallic MOFs such as; Ce@Fe1:1, Ce@Al1:1, and Ce@La1:1 have not been documented in existing literature. Additionally, bimetallic MOFs with the highest efficiency were further synthesized at different molar ratios to optimize the best possible compositions of the metals for F^- ions elimination from synthesized fluoride solutions in the presence of ultrasonic waves. The ultrasonication-assisted adsorption of the fluoride using a synthesized novel composite is advantageous to achieve faster kinetics while improving adsorption efficiency, which was reported in our previous work [163]. In-depth discussions have been performed by changing adsorption variables such as the initial concentration of fluoride (C_0), temperature, pH of the solution, and contact time. The water stability in the pH range of 1-14 of these bimetal MOFs was tested to meet the practical application. To support this stability test, the leaching concentration of metals in the solution after fluoride adsorption was analysed. The significant role of the surface wettability of the materials was also examined and correlated with the high adsorption capacity. Moreover, the effect of co-existing anions on the adsorption of fluorides such as NO_3^-, Cl^-, HCO_3^-, Br^-, CO_3^{2-}, PO_4^{3-}, and SO_4^{2-} have also been studied. Additionally, the regeneration study of the synthesized material was assessed for long-term fluoride-containing wastewater treatment. Consequently, fluoride remediation through adsorption is observed to be the most cost-effective wastewater treatment method. This work has explored a novel approach to creating bimetal MOFs for the elimination of fluoride from wastewater, which will be important for further studies in the field. The different adsorbents for extracting fluoride from wastewater have been explored in this work, which will be significant for future research in the area.

4.2. Experimental section

4.2.1. Materials

The chemicals such as lanthanum nitrate hexahydrate (La $(NO_3)_3 \cdot 6H_2O$), iron nitrate nonahydrate ($Fe(NO_3)_3 \cdot 9H_2O$), and aluminium chloride hexahydrate were supplied by Merck Ltd., Mumbai, India. Other chemicals used in the study has been mentioned in the chapter 3.

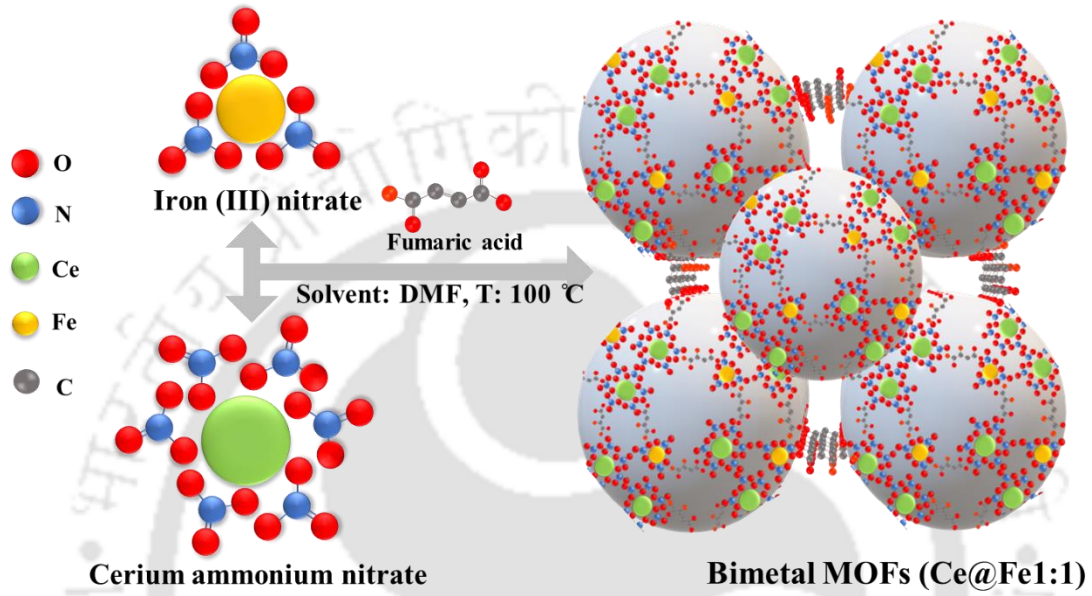

Scheme 4.1. Representation of the synthesis of bimetal MOFs.

4.2.2. Material synthesis

Three bimetal MOFs using metal salts such as ammonium cerium (IV) nitrate, iron nitrate nonahydrate, aluminium chloride hexahydrates, and lanthanum nitrate hexahydrate with fumaric acid as an organic linker were synthesized to find the best possible composite for fluoride remediation from wastewater. The one-pot method was used to synthesize these bimetal MOFs. To synthesize Ce@Fe1:1, 0.365 M of cerium and iron in 5 mL of water were dissolved separately. Simultaneously, fumaric acid (1 g) was dissolved in 40 mL of DMF using ultrasonication in a polypropylene (PP) bottle. Then, all the solution was added to a round bottom flask, whose temperature was maintained at 100 °C using an oil bath and reflux. Crystallization was seen just after 30 min of adding all the solutions. After 10 h, the solution

was withdrawn and kept for cooling at atmospheric temperature. The solid particles were separated using a centrifuge at 6000 rpm for 5 min and washed to eliminate all the unreacted reactants. Then, solid particles were kept for stirring in 150 mL DMF overnight and separated using a centrifuge. The separated solid particles were dried overnight at 90 °C in the oven. To synthesize the Ce@Al1:1, and Ce@La1:1 bimetal MOFs, 0.365 M iron used in the Ce@Fe1:1 bimetal MOFs was replaced by aluminium and lanthanum, respectively. Followed by a preceding procedure as mentioned for Ce@Fe1:1.

Ce–Fu MOFs, Fe–Fu MOFs, and their composites such as Ce@Fe2:1 (Ce/Fe; 2:1), and Ce@Fe1:2 (Ce/Fe; 1:2) were prepared to find out the best possible composition of the metals in bimetal MOFs for fluoride adsorption from wastewater. To synthesize Ce–Fu MOFs has been mentioned in chapter 3. To synthesize Fe–Fu MOFs, 0.365 M of iron was dissolved separately in 5 mL of water using ultrasonication. Another 1 g of fumaric acid was dissolved in 40 mL of DMF followed by a preceding procedure as mentioned for Ce@Fe1:1 bimetal MOFs. Ce@Fe2:1 bimetal MOFs were prepared by adding Ce/Fe salts at a 2:1 molar ratio in a separate PP bottle with 5 mL of water, respectively. Simultaneously, 2g of fumaric acid was dissolved in 80 mL of DMF in a separate bottle. After that, all these homogenous solutions were added to the round-bottom flask, which was maintained at 100 °C. Then, the aforementioned procedure was repeated to achieve the dry power of Ce@Fe2:1. Other bimetal MOFs Ce@Fe1:2 were prepared using the same procedure at Ce/Fe molar ratios of 1:2.

4.2.3. Fluoride Adsorption Tests

The solutions of F^- ion were prepared by successive dilutions of the standard solution as per the experimental need. The experiments were conducted batch-wise using an ultrasonicator as a mediator at 37 kHz frequency. The initial concentration of F^- ion varied from 10 to 100 ppm at 298 K and neutral pH to know the maximum adsorption capacity of the bimetal MOFs. The

10 ppm of F^- ion solution was maintained at different pH ranges from 3 to 11 using solutions of 0.1 M HCl and 0.1 M NaOH to investigate the pH effect. The material dose effect was considered by adding 5, 10, 15, 20, 25, and 30 mg in 10 ppm in a 20 mL fluoride ion solution. An important study to comprehend the adsorption mechanism of solute on adsorbent was done by isotherm models at 288 K, 298 K, and 308 K. The adsorption rate was investigated at different initial F^- ion concentrations by using 10 mg of material in 20 mL fluoride solution for 30 min at a neutral pH range. The final concentration of F^- ion was measured all over the study using a fluoride selective electrode. The equilibrium adsorption capacity and the fluoride removal were evaluated using the mentioned Eq.s (2.1) and (2.2), respectively.

4.2.4. Characterization

The static contact angles of the pellet were determined using a HOLMARC contact angle measuring device from OPTO-MECHATRONICS PVT. LTD., INDIA. Make and the model of the instruments used for characterization in this study has been mentioned in the chapter 2 and 3.

4.3. Results and discussion

4.3.1. Characterization of bimetal MOFs

Bimetal MOFs were synthesized via a one-pot method and applied to remove F^- ions from drinking water. The crystalline phase of the bimetal MOFs along with Ce_Fu MOFs and Fe_Fu MOFs were investigated using XRD analysis, shown in **Figure 4.1**a. The spectra indicate a polycrystalline nature of the adsorptive material. The XRD pattern of Ce–Fu MOFs found the major peaks at $2\Theta = 7.2°$, and 8.3° [146,164]. The optimized Ce@Fe1:1 MOFs exhibited peaks at 9.2°, and 10.9°. XRD pattern of Ce@Fe1:1, Ce@Al1:1, and Ce@La1:1 MOFs followed the

PDF Card No. 00-039-1873, 00-019-0266, and 00-039-0294, respectively. Moreover, the XRD pattern of samples after the fluoride loading is slightly different than the virgin adsorbents, which may be due to the existence of F^- ion. The narrow sharp peaks signify the microcrystalline nature of the materials. The occurrence of elements such as Ce, Fe, Al, La, and F could be further confirmed by XPS analysis.

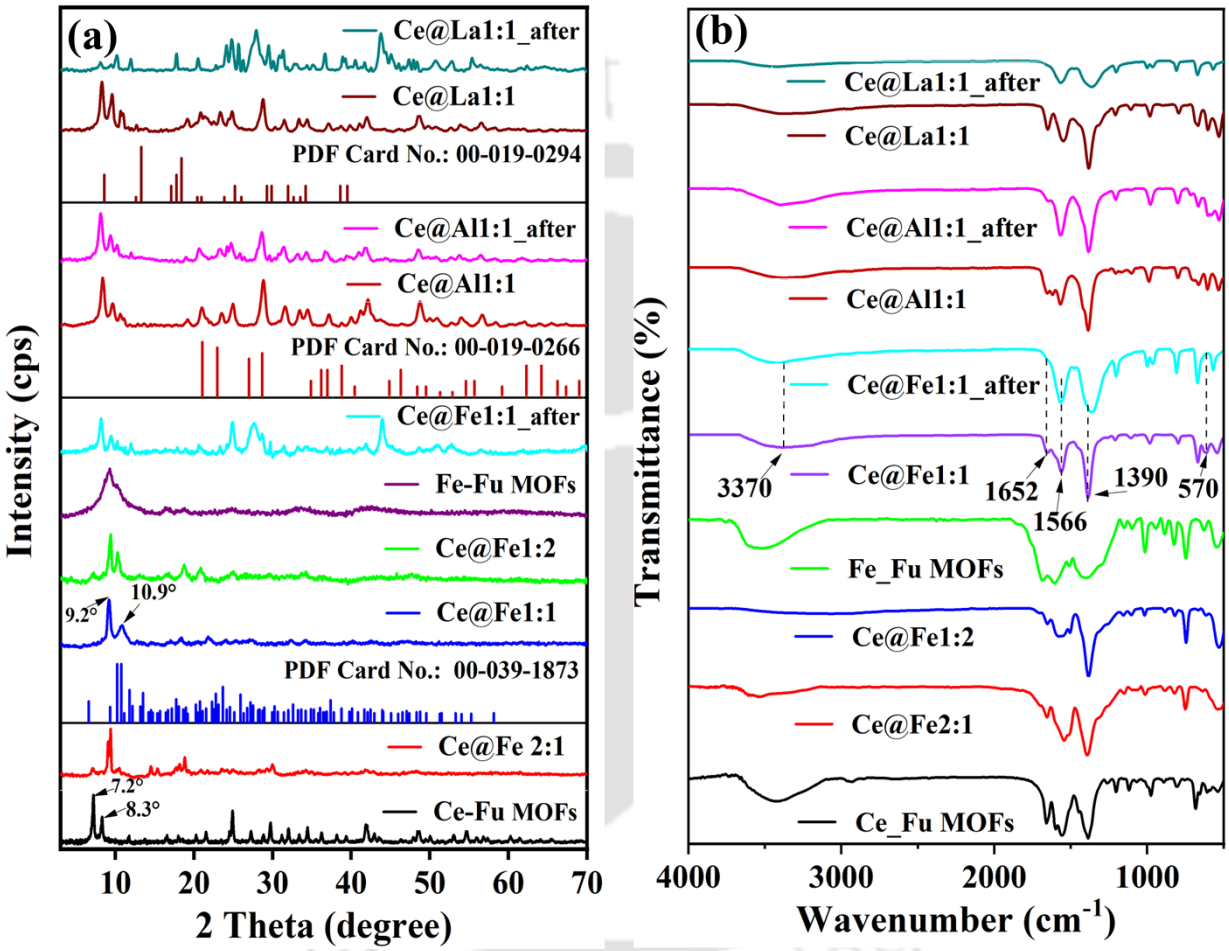

Figure 4.1. (a) XRD pattern of Ce–based MOFs composites, and (b) FTIR spectra of materials after and post the F^- ions adsorption.

The FTIR spectra of the samples after and before fluoride loading were compared to comprehend the fluoride adsorption (**Figure 4.1**b). The strong and broad adsorption bend in the range of 3350–3450 cm^{-1} was because of the O−H stretching vibration of H_2O, which was found in all the materials [163]. The shifting of the vibration peaks of −OH groups for all

adsorbents after fluoride loading was observed in comparison to the original material suggesting that the −OH groups attached to the adsorbents take part in the fluoride ion adsorption [165]. The peaks at 1652 and 1210 cm^{-1} refer to strong C=O and C−O stretching vibrations, respectively. The bend around 1566 cm^{-1} refers to either resembling the N−H bending of amine or strong N−O stretching of the nitro compound [166]. The presence of alkane in the material reflects the medium C−H bending at 1390, 983, and 796 cm^{-1}. The bend at 540 cm^{-1} was attributed to M−O (M; Ce/Fe/Al/La) vibration [95].

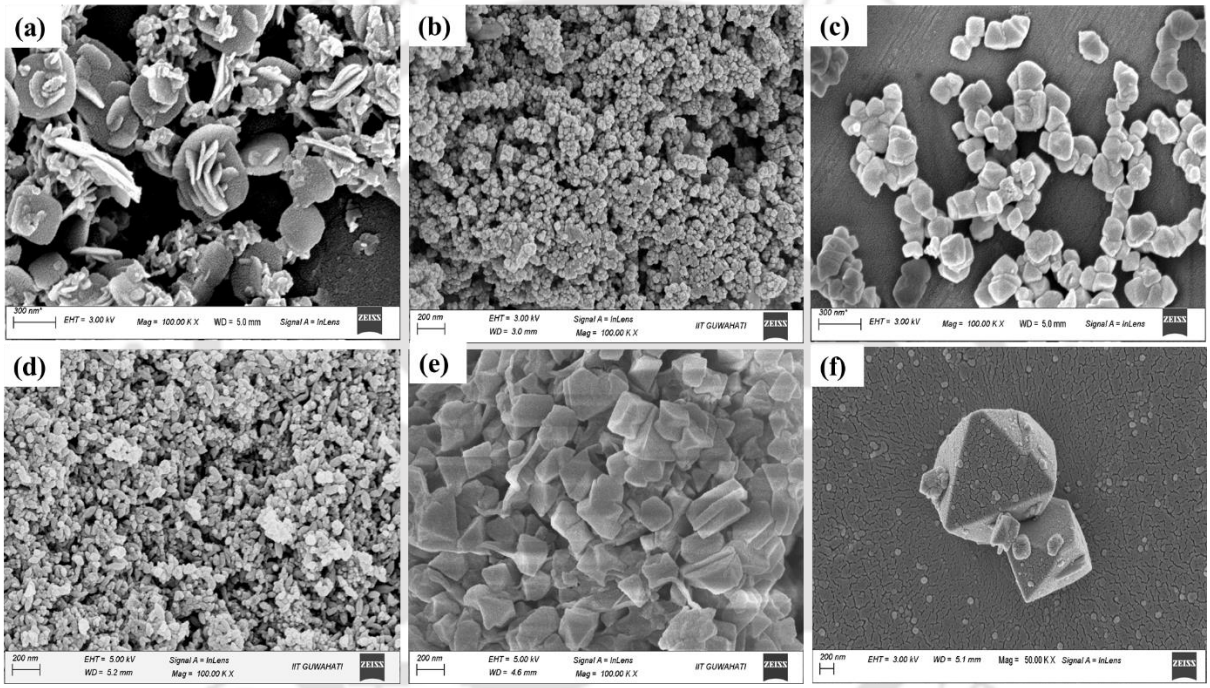

Figure 4.2. FESEM images of (a) Ce@Al1:1, (b) Ce@La1:1, (c) Ce-Fu, (d) Ce@Fe2:1, (e) Ce@Fe1:2, and (f) Fe_Fu.

FESEM analysis of the drop-cast samples was performed after sputter-coating the poorly conductive samples with gold. The gold coating prevents sample charging, reduces microscope beam damage, enhances heat transfer, and improves secondary electron emission for better image projection. FESEM images of MOFs such as Ce@Al1:1, Ce@La1:1, Ce-Fu, Ce@Fe2:1, Ce@Fe1:2, and Fe-Fu are displayed in **Figure 4.2**. The image of sample Ce@Fe1:1 was

captured to visualize the morphology, illustrated in **Figure 4.3**a. MOFs such as Ce@Fe1:1, Ce@La1:1, Ce-Fu, Ce@Fe2:1, Ce@Fe1:2, and Fe-Fu are formed primarily as agglomerates of octahedral particles. The particle size of the bimetal MOFs Ce@Fe1:1 obtained from FETEM was approximately 60±10 nm, which was further confirmed with the help of FETEM. Furthermore, the material Ce@Al1:1 MOFs composite shows nano-petal-assembled flower-like morphology. **Figure 4.3**b displays the TEM images used to further confirm the shape of the produced MOFs composites Ce@Fe1:1.[115] The TEM images of bimetal MOFs Ce@Al1:1 and Ce@La1:1 were illustrated in **Figures 4.4**a and b, respectively. The elemental analysis of Ce@Fe1:1 by EDS confirmed the presence of metals such as cerium and iron, shown in **Figure 4.3**c.

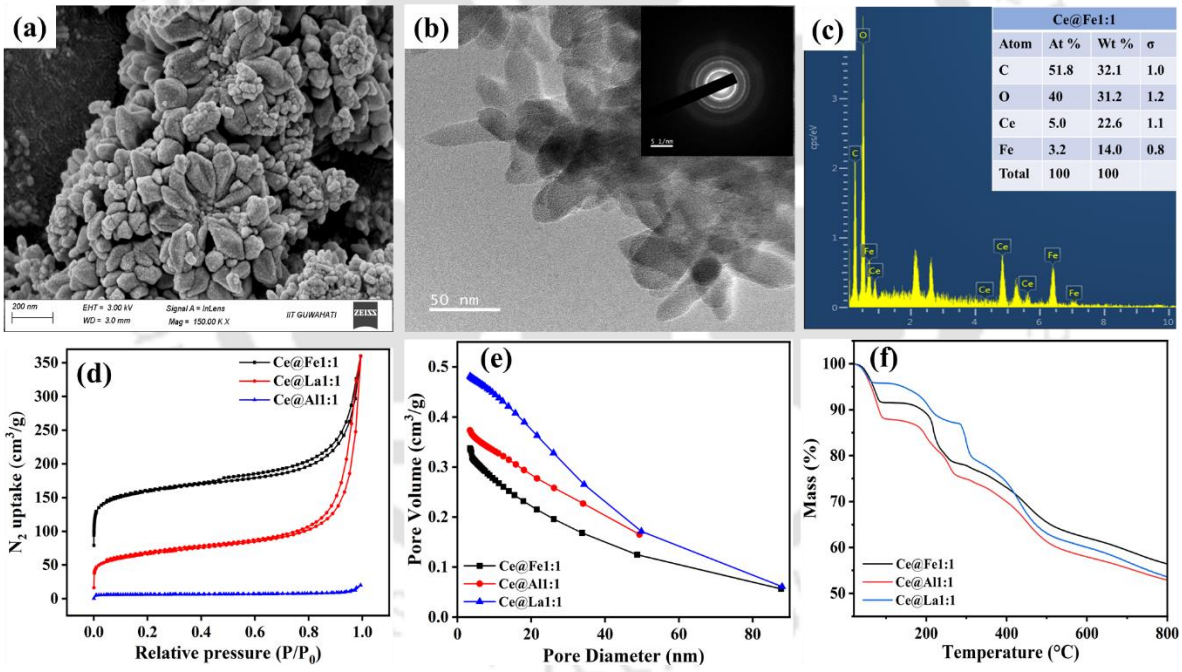

Figure 4.3. (a) FESEM image of Ce@Fe1:1, (b) FETEM image Ce@Fe1:1, (c) elemental analysis of Ce@Fe1:1, (d) N_2 adsorption–desorption isotherm of bimetal MOFs composites, (e) distribution of pore diameter, and (f) thermal degradation of the samples.

N_2 adsorption–desorption analysis was performed to discover the surface area and the average

pore diameter of all three materials (**Figure 4.3**d). The powder of the composites was degassed in a vacuum at 100 °C for 6 h before preceding the measurement. The specific surface area of Ce@Fe1:1, Ce@Al1:1, and Ce@La1:1 was computed with the help of the Brunauer-Emmett-Teller (BET) Eq.s, which were 820, 655, and 428.4 m^2/g respectively. The average pore size of Ce@Fe1:1, Ce@Al1:1, and Ce@La1:1 determined with the help of the Barrett-Joyner-Halenda (BJH) were 3.4, 15.8, and 18.2 nm, respectively (**Figure 4.3**e). The volume of the pores of the aforementioned materials were 0.57, 0.28, and 0.11 cm^3/g, respectively. The mean size of the pore is between 2 and 50 nm, which indicates that the pores of the adsorbent are mesoporous [167]. The samples displayed type II isotherms correspond to reversible monolayer–multilayer adsorption on the microporous adsorbent surface [161]. The largest surface area is noted for Ce@Fe1:1**,** corresponding to a convenience of high vigorous spots on the material.

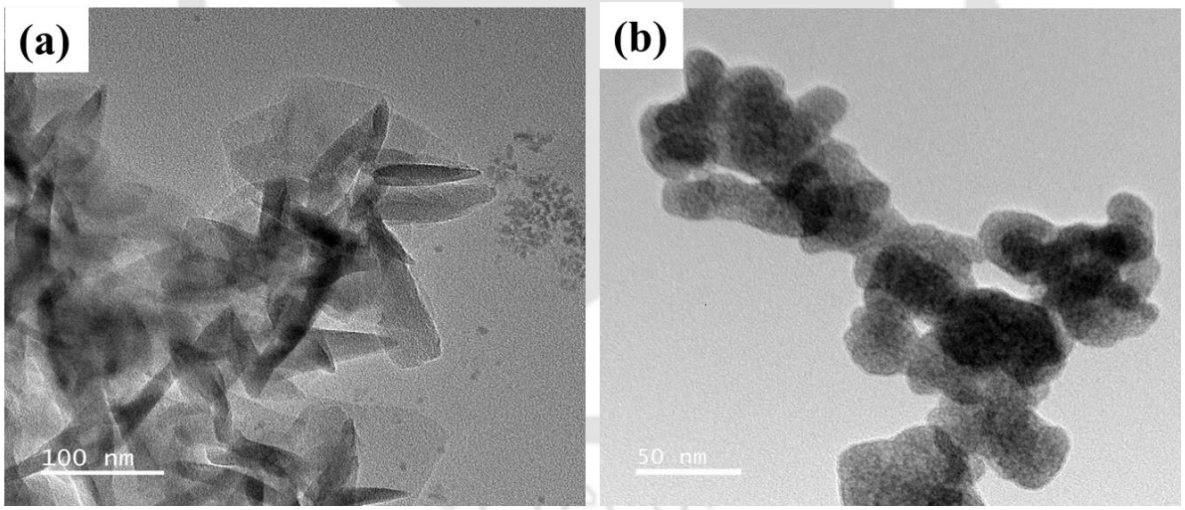

Figure 4.4. FETEM image of (a) Ce@Al1:1 and (b) Ce@La1:1

The three-stage thermal degradation curves obtained from TGA thermograms of all three bimetal MOFs are shown in **Figure 4.3**f. The drastic weight loss in the initial stage alluded to the evaporation of unbounded water molecules observed up to 96°C. A further drop in the mass

percentage was observed at a temperature ranging from 230 to 290°C, which may be because of the evaporation of bounded H_2O molecules and the trapped solvent molecules within the structure of the taken samples. Afterward, the remaining sections could maintain stability up to 420°C, as seen by the minor weight loss in that temperature range. In contrast, a further rise in temperature after 420°C resulted in a continuous weight loss due to the breakage of crosslinked bonds of the linkers, which destroys the structures.

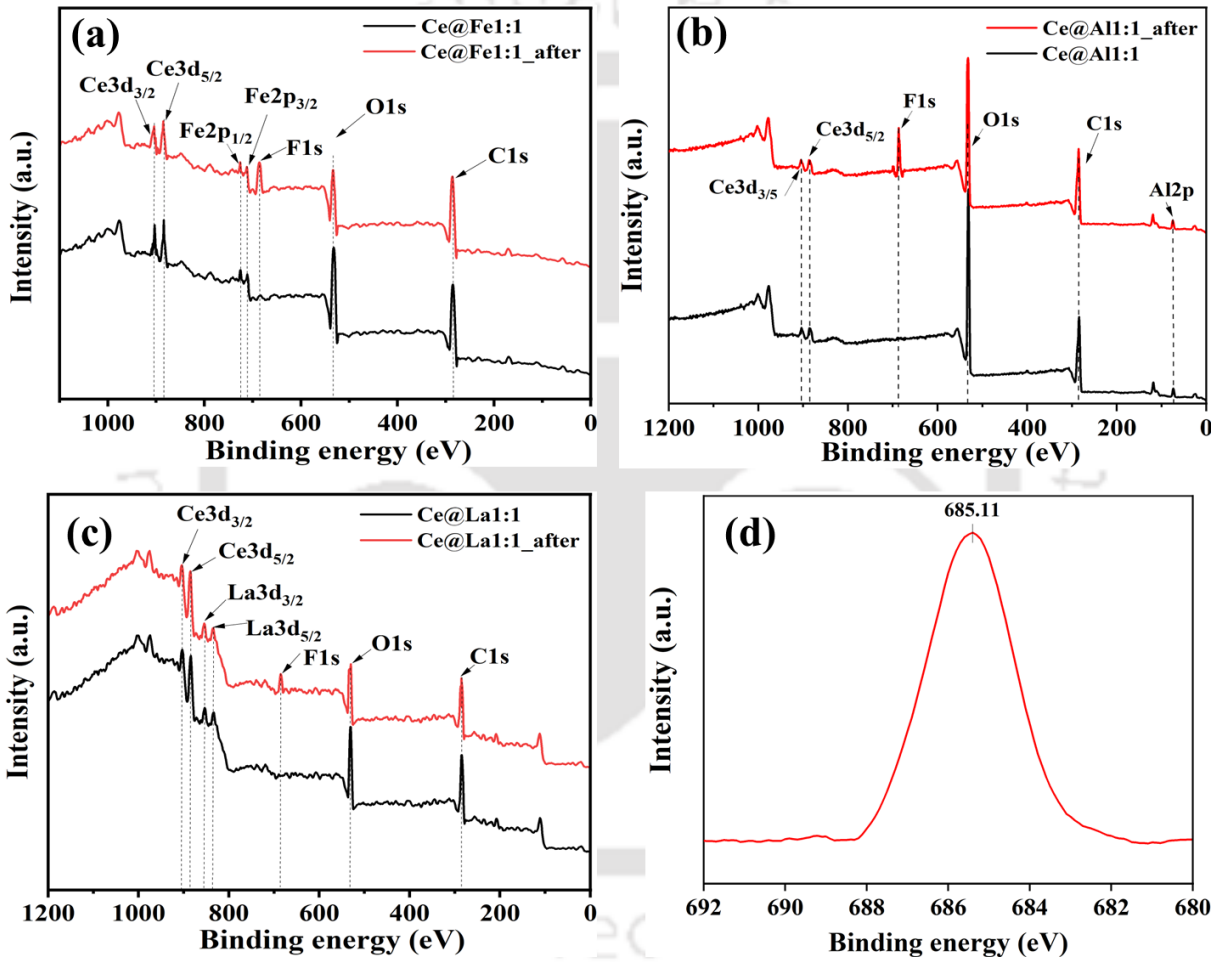

Figure 4.5. XPS surface scan of (a) Ce@Fe1:1, (b) Ce@Al1:1, (c) Ce@La1:1 MOFs after and before the fluoride loading; and (d) XPS spectra of F1s.

XPS was employed to investigate the different elements and their valence state present in the materials, illustrated in **Figure 4.5** [168]. The presence of Ce, Fe, Al, La, C, O, and F were

confirmed at their binding energies in the different materials before and after the fluoride loading. The peak at 884.3 and 903.9 eV attributed to $Ce3d_{5/2}$ and $Ce3d_{3/2}$, respectively. The peaks appeared at 725.3 and 711 eV indicating the presence of Fe in Ce@Fe1:1 in the form of $Fe2p_{1/2}$ and $Fe2p_{3/2}$, respectively [169]. The binding energy 74.37 eV holds the peak of Al2p, which is present in the Ce@Al1:1 MOFs composite. The peaks of $La3d_{3/2}$, and $La3d_{5/2}$ were at the binding energy of 854.4 and 834.4 eV in Ce@La1:1 MOFs composite, respectively [170]. XPS analysis of all materials after the fluoride loading shows a peak with a binding energy of 685.4 eV allocated to F1s, which specified that F^- ions had been adsorbed on the adsorbents.

4.3.2. Fluoride removal using different bimetal MOFs

Bimetal MOFs such as Ce@Fe1:1, Ce@Al1:1, and Ce@La1:1 were studied to know the highest removal efficiency for fluoride from drinking water (**Figure 4.6**a**)**. The adsorbent having the highest outcome was further synthesized at a different molar ratio of metals present in the respective adsorbent. For this study, 10 mg of as-synthesized bimetal MOFs were added to 10 ppm of 20 mL fluoride solution for 30 min. The study displayed adsorbent Ce@Fe1:1 has the highest fluoride removal of 88.8 %, whereas the other two bimetal MOFs Ce@Al1:1 and Ce@La1:1 were able to remove fluoride up to 84 and 74.7%, respectively.

4.3.3. Optimization of the molar ratios of Ce and Fe

Furthermore, the fluoride removal study under the same condition was carried out using Ce–Fu MOFs, Fe–Fu MOFs, and their composites at distinct Ce/Fe molar ratios such as Ce@Fe2:1, Ce@Fe1:1, and Ce@Fe1:2 (**Figure 4.6**b**)**. The outcome of the study shows Ce–Fu MOF has the highest removal efficiency and lowest with Fe–Fu MOFs, whereas bimetal MOFs Ce@Fe2:1 and Ce@Fe1:1 can remove 89.5 % and 88.8 % of 10 ppm fluoride, respectively. Despite the fact that Ce-Fu MOFs offer effective removal, the Ce used in it considerably

increases the cost, which may make large-scale use uneconomical. Contrarily, the amount of cerium used in the bimetal MOFs Ce@Fe1:1 is comparatively less and the removal efficiency is nearly the same as Ce-Fu MOFs and Ce@Fe2:1 MOFs. As a result, it is more cost-effective to employ Ce@Fe1:1 bimetal MOFs rather than Ce-Fu MOFs or Ce@Fe2:1 MOFs.

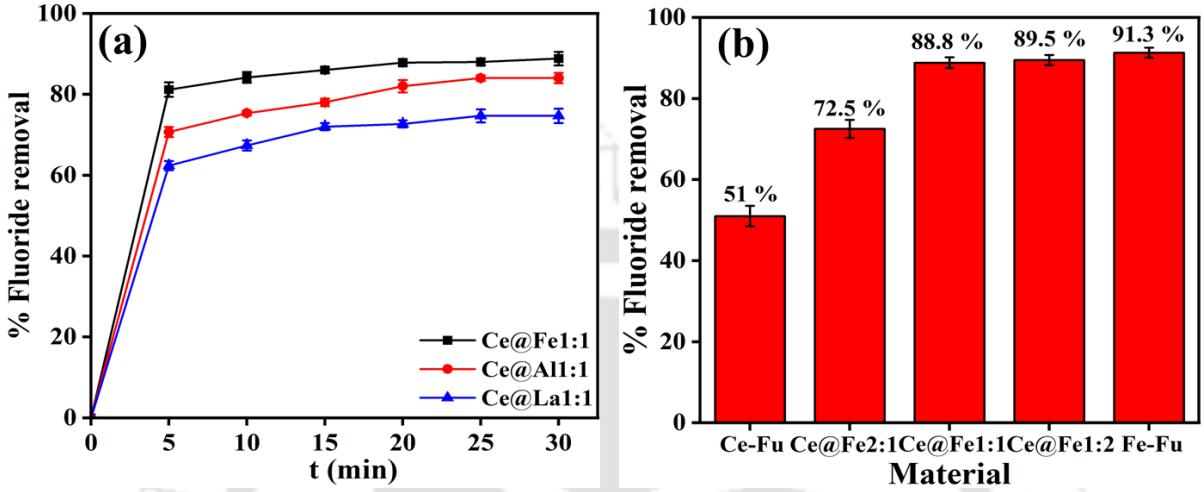

Figure 4.6. (a) fluoride removal by using different adsorbents, and (b) optimization of the molar ratios of Ce and Fe.

4.3.4. Effect of solution pH

The pH of the solution has a considerable influence on the absorption of fluoride present in water because it affects the surface charge, degree of ionization, and chemical nature of the material. The pH effect in the range of 2–13 was examined for fluoride ion (C_0: 10 ppm and V: 20 mL) removal to understand material behaviour by adding the optimum dose of the adsorbent (10 mg) for 30 min at temperature 303 K. **Figure 4.7**a shows, the adsorbents maintained higher adsorption in the pH range 2–10 since the adsorbent surface of the composites is positively charged. Therefore, the electrostatic attraction between the bimetal MOFs (Ce@Fe1:1, Ce@Al1:1, and Ce@La1:1) and the negatively charged F^- ions become prominent. Due to the strong anion exchange and abundance of surface-active binding sites, the maximum fluoride

removal was seen for all samples in the acidic range. Reversely, with the increasing pH of the fluoride solution, the % removal of F^- ion decreased drastically for all composites. This could be because there are target ions competing with the hydroxyl ions for the active sites. The decreasing trend of adsorption percentage in a basic pH (10-13) range could be as electrostatic repulsion between anionic F^- and OH^- ions [147,171,172]. In this study, the synthesized fluoride solution at 6.5± 0.2 pH was employed for the subsequent investigation of F^- ion adsorption.

4.3.5. Effect of MOFs doses

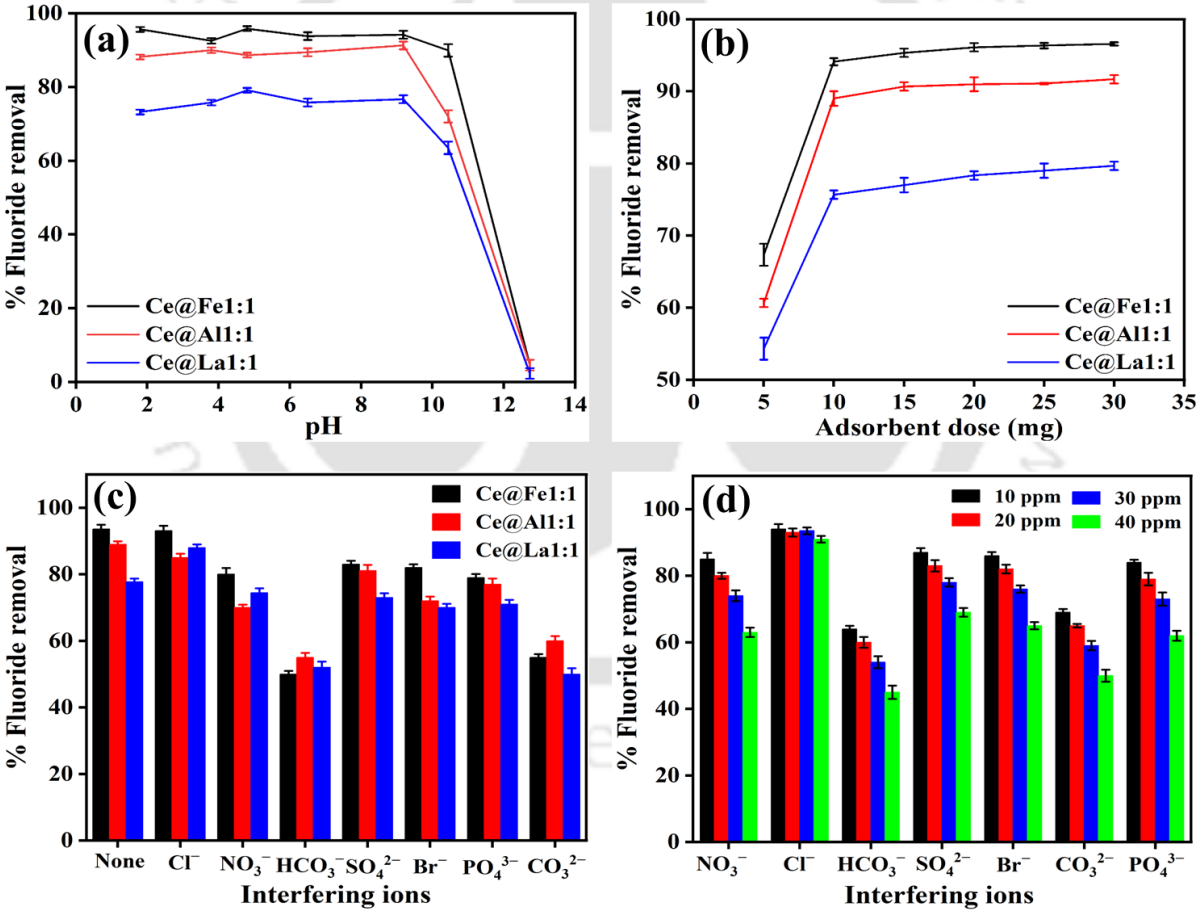

Figure 4.7. (a) effect of pH for fluoride removal, (b) adsorbent dose effect, (c) effect of coexisting ions, and (d) effect of coexisting ions at different concentrations on the Ce@Fe1:1.

The material dose effect of different bimetal MOFs for the remediation of fluoride (C_0: 10 ppm, V: 20 mL, and pH: 6.7 ± 0.2) was studied for up to 30 min at ambient temperature. The change in the percentage removal of F^- ion by changing the material (Ce@Fe1:1, Ce@Al1:1, and Ce@La1:1) dosage (0.5, 1.0, 1.5, 2.0, 2.5, and 3.0 g/L) were demonstrated using **Figure 4.7**b. The removal efficiency of the fluoride increased gradually from a material amount of 0.5 mg to a material amount of 10 mg. This signifies that an upsurge in the adsorbent dosages gives additional active sites due to increased surface area for the fluoride ions.[147,173] Consequently, further upsurge in the samples from 1 to 3 g/L in the fluoride solution did not significantly enhance the removal of F^- ions. After a given concentration of adsorbent, the adsorption stabilizes, which may be the result of active sites overlapping at increasing dosages. Thus, the optimum adsorbent dose of different composites was 1 g/L used for further study of F^- ion adsorption.

4.3.6. Effect of coexisting ions

Understanding the impact of various co-existing ions on F^- ion adsorption is extremely important to assess the actual potential of the adsorbent. For this study ions such as NO_3^-, Cl^-, HCO_3^-, SO_4^{2-}, Br^-, CO_3^{2-}, and PO_4^{3-} with fluoride ions in the contaminated water were studied to know the interference created in the fluoride removal. The dosage of the samples (Ce@Fe1:1, Ce@Al1:1, and Ce@La1:1) was kept at 0.5 gL^{-1} having 10 mg/L initial concentration of fluoride. The competing ions concentration was 20 mg/L and contact time was maintained at 30 min. The presence of Cl^- does not demonstrate a significant impact on the elimination of fluoride at the lower concentration (**Figure 4.7**c) [174]. Conversely, it has been observed that all three bimetal MOFs experience a slight reduction in their fluoride removal efficiency in the presence of ions such as NO_3^-, SO_4^{2-}, Br^-, and PO_4^{3-}.Whereas, the presence of HCO_3^- and CO_3^{2-} ions has a notably adverse impact on fluoride adsorption. Additionally, to

realize the full potential of the Ce@Fe1:1, the concentrations of co-existing ions were increased from 10 mg/L to 40 mg/L to perform the experiment presented in **Figure 4.7**d, and the initial concentration of fluoride was kept constant (10 mg/L). The Ce@Fe1:1 demonstrated a reduction in fluoride removal percentage by 10, 8, 9, and 11 %, while introducing these ions such as NO_3^-, SO_4^{2-}, Br^-, and PO_4^{3-} at 10 mg/L, respectively. Additionally, the fluoride adsorption was hindered by introducing HCO_3^- and CO_3^{2-} ions resulting in a reduction in fluoride removal by 35 and 30 %, respectively. The fluoride adsorption phenomenon is exacerbated when the ion concentrations are high. In this scenario, NO_3^-, SO_4^{2-}, Br^-, and PO_4^{3-} ions having a concentration of 40 mg/L interfere with the adsorption process using Ce@Fe1:1 resulting in a further drop in fluoride adsorption by 22, 18, 14, and 17 %, respectively. The fluoride adsorption with Ce@Fe1:1 having 40 mg/L concentration of HCO_3^- and CO_3^{2-} ions result decrease in fluoride elimination by 50 and 45 %, respectively. Whereas, even higher concentrations of Cl^- do not constitute significant interferents in the fluoride removal reduction for all the bimetal MOFs reported here [139].

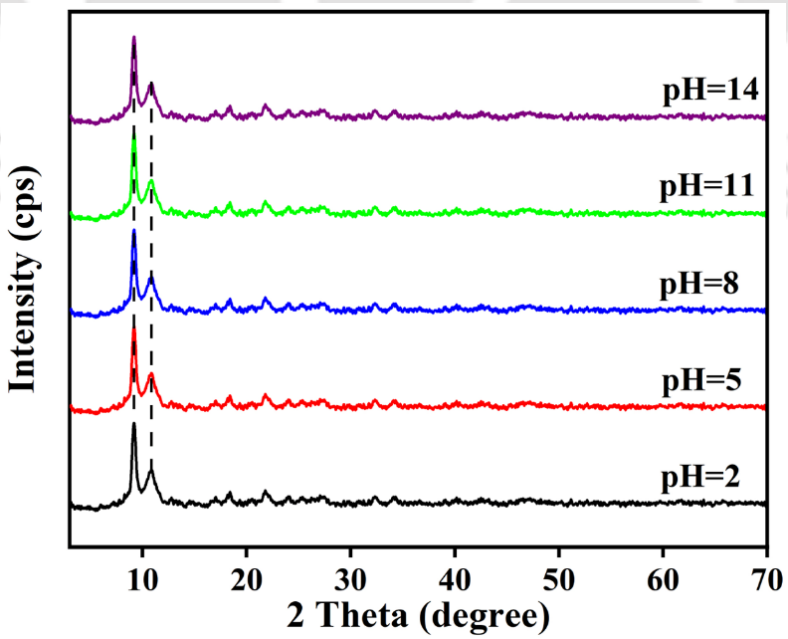

Figure 4.8. Stability analysis of bimetal MOFs Ce@Fe1:1

4.3.7. Stability analysis of bimetal MOFs

Studying the stability of bimetal MOFs in water at various pH levels is essential for understanding material stability during the fluoride removal process. The water stability of bimetal MOFs Ce@Fe1:1 was examined by adding 30 mg of a powder sample in 50 mL water maintained at different pH including 2, 5, 8, 11, and 14. Next, these solutions were kept on stirring for 2 days then the material was separated and dried in the hot air over for overnight at 90^{o}C. Therefore, the separated powder was analyzed using XRD to compare the depletion in the pick, which explains the stability of the materials, as shown in **Figure 4.8**. This observation highlights that bimetal MOFs maintain their stable crystalline structure when immersed in water at various pH levels, indicating their potential suitability for applications in aqueous environments.

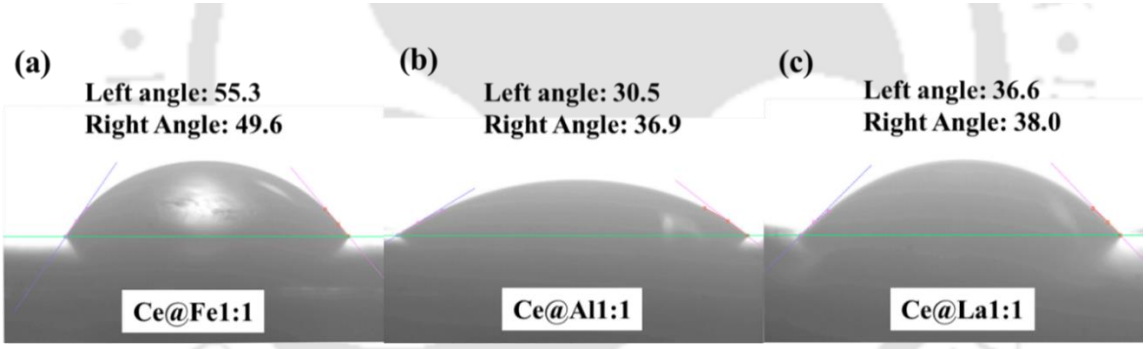

Figure 4.9. Water static contact angle of bimetal MOFs (a) Ce@Fe1:1, (b) Ce@Al1:1, and (c) Ce@La1:1.

4.3.8. Surface wettability test

Water molecules are known for their strong polarity and small size, characteristics that are advantageous for effective dispersion and adsorption onto various materials [175]. When an adsorptive material displays significant hydrophilic properties, the water molecules tend to adsorb on its surface, occupying a substantial portion of the adsorption sites. This, in turn,

limits the adsorption capacity of other molecules [176]. To investigate how the hydrophilic properties of bimetallic MOFs, specifically Ce@Fe1:1, Ce@Al1:1, and Ce@La@1:1, affect their adsorption capacities, we conducted contact angle measurements. As depicted in **Figure 4.9**, the contact angles for Ce@Fe1:1, Ce@Al1:1, and Ce@La@1:1 were found to be 49.6°, 36.9°, and 38°, respectively. These results indicate that Ce@Fe1:1 exhibited relatively weaker hydrophilic characteristics. In practical terms, when dealing with liquid-phase adsorption systems, competitive adsorption between solute and solvent is commonly observed. Consequently, the hydrophilic properties of adsorbents can significantly influence their adsorption capacity. When employed theses adsorbents for fluoride removal, Ce@Fe1:1 demonstrated a more efficient prevention of water molecule adsorption compared to other reported bimetallic MOFs, leading to a higher fluoride adsorption capacity.

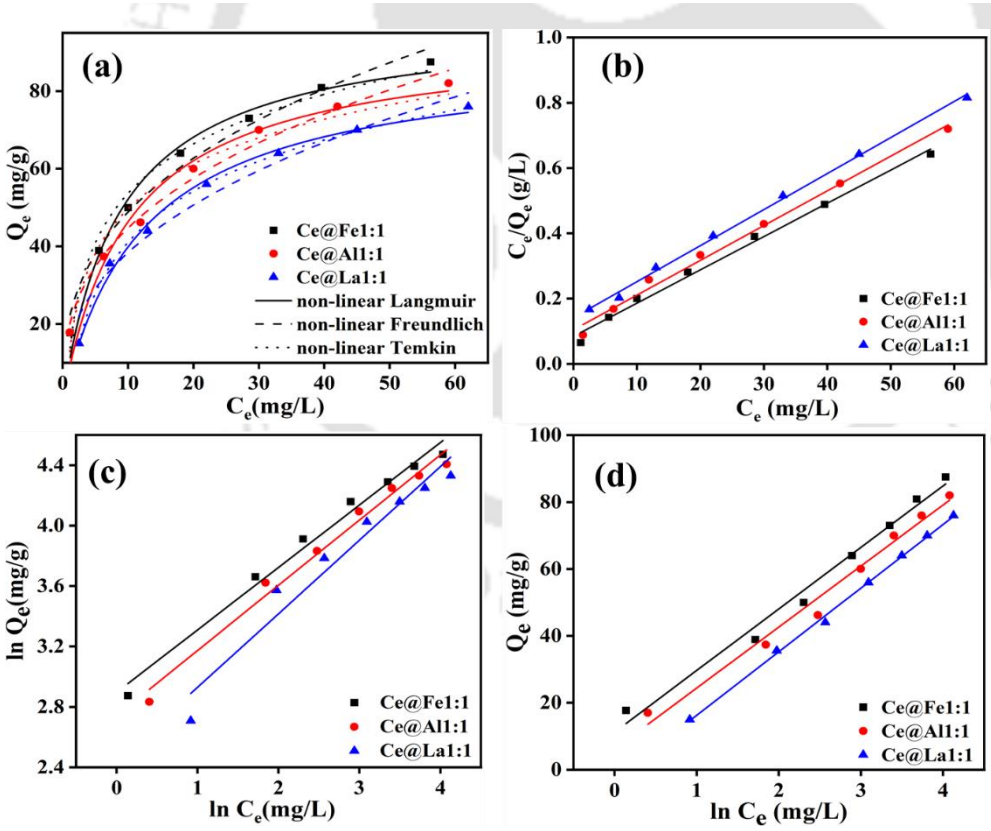

Figure 4.10. Adsorption isotherms of bimetal MOFs (a) non-linear fitting of isotherm models, (b) Langmuir linear fittings, (c) Freundlich linear fittings, and (d) Temkin linear fittings.

4.3.9. Isotherm study

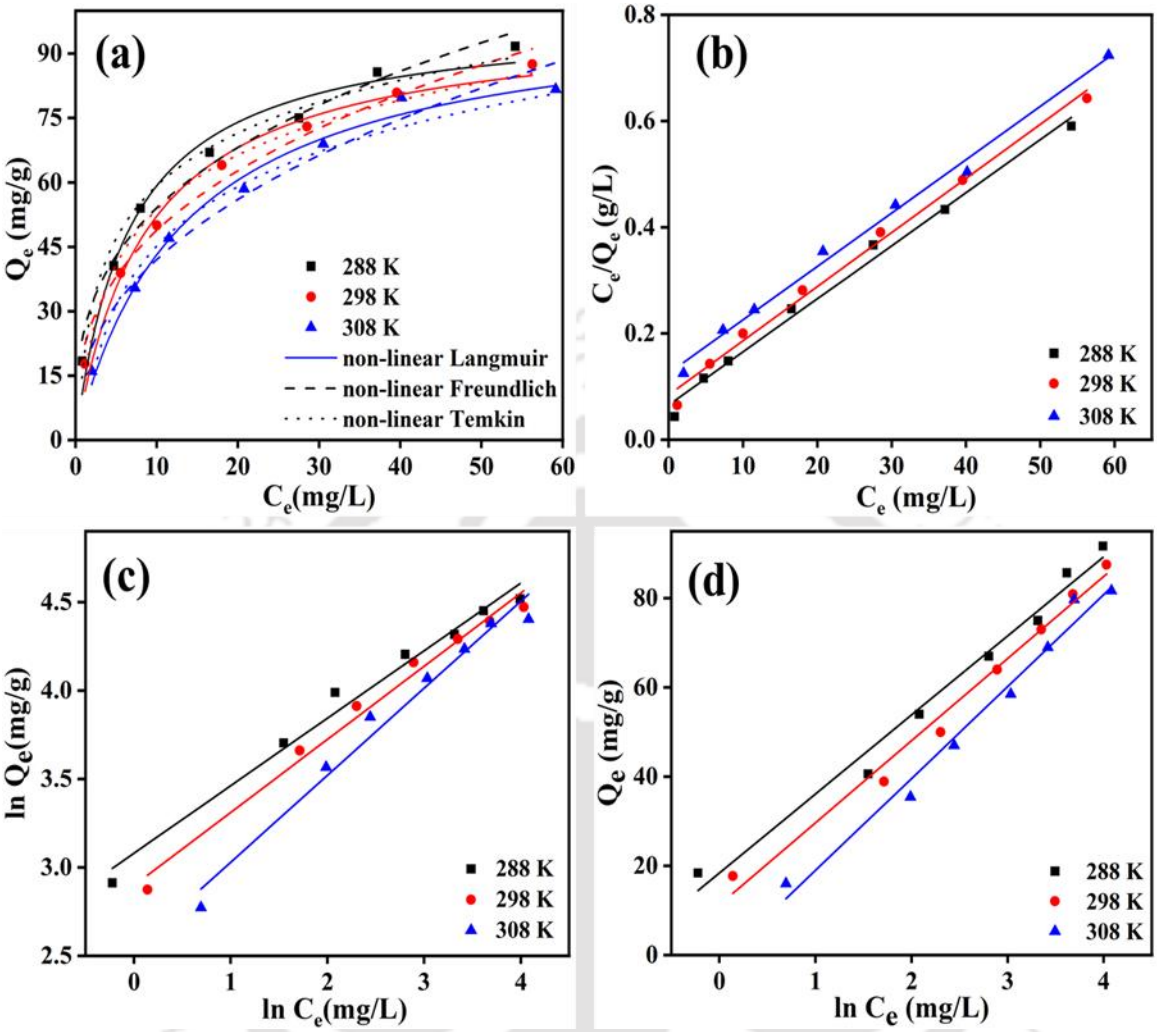

Figure 4.11. Adsorption isotherms of Ce@Fe1:1 (a) non-linear fitting of isotherm models, (b) Langmuir linear fittings, (c) Freundlich linear fittings, and (d) Temkin linear fittings.

Adsorption isotherm was studied at a constant temperature to understand the adsorption of fluoride on the bimetal MOFs surface, which shows the relationship between the equilibrium adsorption capacity and equilibrium concentration [124]. The saturated adsorption capacities of bimetal MOFs Ce@Fe1:1, Ce@Al1:1, and Ce@La1:1 are described at different initial concentrations of fluoride. The results show that as the equilibrium fluoride concentration increases, the adsorption capacity also follows the same trend and eventually reaches

saturation. To investigate the adsorption process of all bimetal MOFs the experimental data were fitted to different adsorption isotherm models such as Langmuir, Freundlich, and Temkin (**Figure 4.10**). The maximum adsorption capacities of Ce@Fe1:1, Ce@Al1:1, and Ce@La1:1 at an initial concentration of fluoride 100 ppm obtained from the fitting were 98.03, 94.33, and 90.9 mg/g, respectively (**Table 4.1**). The isotherm study of the bimetal Ce@Fe1:1 MOFs having the highest removal was carried out at various temperatures (288 K, 298 K, and 308 K) using both linear and non-linear isotherm models (**Figure 4.11**).

Table 4.1. Isotherms parameters obtained from different fittings of bimetallic Ce@Fe1:1, Ce@Al1:1, and Ce@La1:1 MOFs.

Models		**Temperature**		
		Ce@Fe1:1	**Ce@Al1:1**	**Ce@La1:1**
Langmuir	Q_0	98.03922	94.33962	90.90909
Linear	K_L	0.121284	0.101923	0.078014
	R^2	0.99134	0.99101	0.99734
Non-linear	Q_0	98.27265	96.96757	89.45875
	K_L	0.11291	0.08546	0.08027
	R^2	0.98351	0.98884	0.99446
Freundlich	K_F	17.99331	15.48699	11.47304
Linear	n	2.421308	2.320186	2.053388
	R^2	0.98259	0.9806	0.94132
Non-linear	K_F	21.23304	17.60688	15.30746

	n	2.7665	2.56718	2.50445
	R^2	0.98569	0.98081	0.96941
Temkin	B	18.4	18.24	19.02
Linear	K_T	1.843034	1.402516	0.864018
	R^2	0.983	0.98	0.99
Non-linear	B	18.4072	18.79545	19.02756
	K_T	1.84274	1.24532	0.86376
	R^2	0.98602	0.98274	0.99814

Linear and non-linear forms of the aforementioned models are listed in **Table 2.2**. Different parameters obtained from linear and non-linear fittings of isotherm models at different temperatures for Ce@Fe1:1 are displayed in **Table 4.2** [177]. The study shows that as the temperature rises the adsorption capacity of the adsorbent diminishes.[137] This results in the exothermic process, where the adsorption capacity of the adsorbent decreases as the kinetic energy of the molecules present in the composite rises at a high temperature [90]. The correlation coefficient (R^2) of Ce@Fe1:1 found from the non-linear fitting of the Langmuir model is 0.993 as compared to other fitted isotherms. The R^2 obtained from non-linear Freundlich and Temkin isotherm models at 288 K are 0.988 and 0.966, respectively. The maximum monolayer adsorption capacity of Ce@Fe1:1 is 101.3 mg/g at 288 K obtained from the best-fitted non-linear Langmuir isotherm. The equilibrium adsorption capacities derived via the Langmuir isotherm adsorption model is 90.3 mg/g at 288 K, which is close to the value observed experimentally. Additionally, the maximum monolayer adsorption capacity of Ce@Al1:1 and Ce@La1:1 is also best fitted to the Langmuir isotherm adsorption model.

Furthermore, 1/n stands for the adsorption capacity index in the Freundlich adsorption model. Adsorption is often successful when 1/n is between 0 and 1; when 1/n is more than 2, it is challenging to adsorb on the adsorbent. The 1/n values of the Ce@Fe1:1, Ce@Al1:1, and Ce@La1:1 are 0.413, 0.431, and 0.487, respectively, indicating the favourable adsorption.

Table 4.2. Isotherms parameters obtained from different fittings of for Ce@Fe1:1 at difference temperatures.

Isotherm models		**Temperature**		
		288 K	**298 K**	**308 K**
Langmuir	Q_0	99.9	98.03	99.4
Linear	K_L	0.15	0.12	0.08
	R^2	0.99	0.99	0.99
Non-linear	Q_0	101.3	98.7	98.3
	K_L	0.074	0.149	0.11
	R^2	0.99	0.97	0.98
Freundlich	K_F	21.7	18.1	12.6
Linear	n	2.6	2.4	2.03
	R^2	0.98	0.98	0.97
Non-linear	K_F	25.05	21.2	16.15
	n	2.99	2.76	2.4
	R^2	0.98	0.98	0.96
Temkin	B	17.7	18.4	20.6

Linear	K_T	2.8	1.8	0.92
	R^2	0.98	0.98	0.98
Non-linear	B	17.7	18.4	20
	K_T	2.8	1.8	0.95
	R^2	0.98	0.98	0.97

4.3.10. Comparative Assessment of Fluoride Adsorbents

The bimetal MOFs were compared with other existing adsorbents for fluoride removal, as detailed in **Table 4.3**. Ce@Fe1:1 exhibited notably rapid and higher adsorption capabilities across a broad pH range compared to most existing literature. Notably, these bimetal MOFs effectively remove fluoride across a wide pH range of 3 to 10. While the highest reported adsorption capacity for fluoride removal is 600 mg/g, the equilibrium time for the adsorbent is 1440 min, significantly longer than the 30 min required to reach equilibria in our case. However, bimetal MOFs such as Ce@Fe1:1, Ce@Al1:1 and Ce@La1:1 were able to show 101.3, 94.3, and 90.9 mg/g in the wide pH range, respectively.

Table 4.3: The literature comparison of bimetal MOFs with existing adsorbents for F^- ions adsorption.

Material	**Q_0 (mg/g)**	**Equilibrium time (min)**	**pH**	**ref.**
UiO-66	41.36	80	6.8	[89]
UiO-66-NH_2	41.5	30	7	[90]
CAU-6	24.22	80	6.8	[89]
UiO-66 (Hf)	33.35	80	6.8	[89]

Ce@BTC	4.930	30	7	[98]
MIL-100(Fe)	23.53	90	4–10	[152]
Sn (II)-TMA MOFs	30.86	150	3–10	[153]
MOF-801	40	40	2–10	[154]
Ce–MIL-96	38.65	240	3–10	[155]
Fe@BDC	4.90	60	7	[93]
Fe@ABDC	4.92	30	7	[156]
AlFu	600	1440	7	[97]
La-BDC	171.7	180	5	[95]
La@Fu MOFs	4.92	30	7	[157]
Fe@Fu MOFs	4.85	30	7	[157]
Ce@Fe1:1	101.3	30	6.5	Present work
Ce@Al1:1	94.3	30	6.5	Present work
Ce@La1:1	90.9	30	6.5	Present work

4.3.11. Adsorption kinetics

In this study, we used linear and non-linear forms of PFO and the PSO model listed in mentioned in chapter 2. The kinetic investigation was conducted at 10 ppm of initial fluoride concentration using all synthesized adsorbents and the best out of the composite was further investigated thoroughly (**Table 4.4**). The kinetic study was conducted at neutral pH using 10 mg of material in 10 mL of a fluoride solution. The finding reveals bimetal MOFs Ce@Fe1:1 found to have the highest adsorption capacity, which was targeted for kinetic investigation at various fluoride concentrations such as 10, 25, 35, 50, 65, 80, and 100 ppm. The effect of contact time at the different initial concentrations for non-linear and linear forms of the aforementioned kinetic models is shown in **Figure 4.12** and **Figure 4.13**. The studies show

that the adsorption of fluoride using these adsorbents were very quick for the first 10 min. This could be because of the combined effect of using adsorbents having a large number of active sites and ultrasound as a mediator instead of using conventional shaking methods. The comparison study of the ultrasound-assisted method with conventional shaking has been already reported in our previous work [163]. The adsorption capacity gradually becomes constant after 30 min and the active sites are gradually occupied over time. The correlation coefficients obtained from the linear and non-linear fits of each kinetic model are cited in **Table 4.3**.

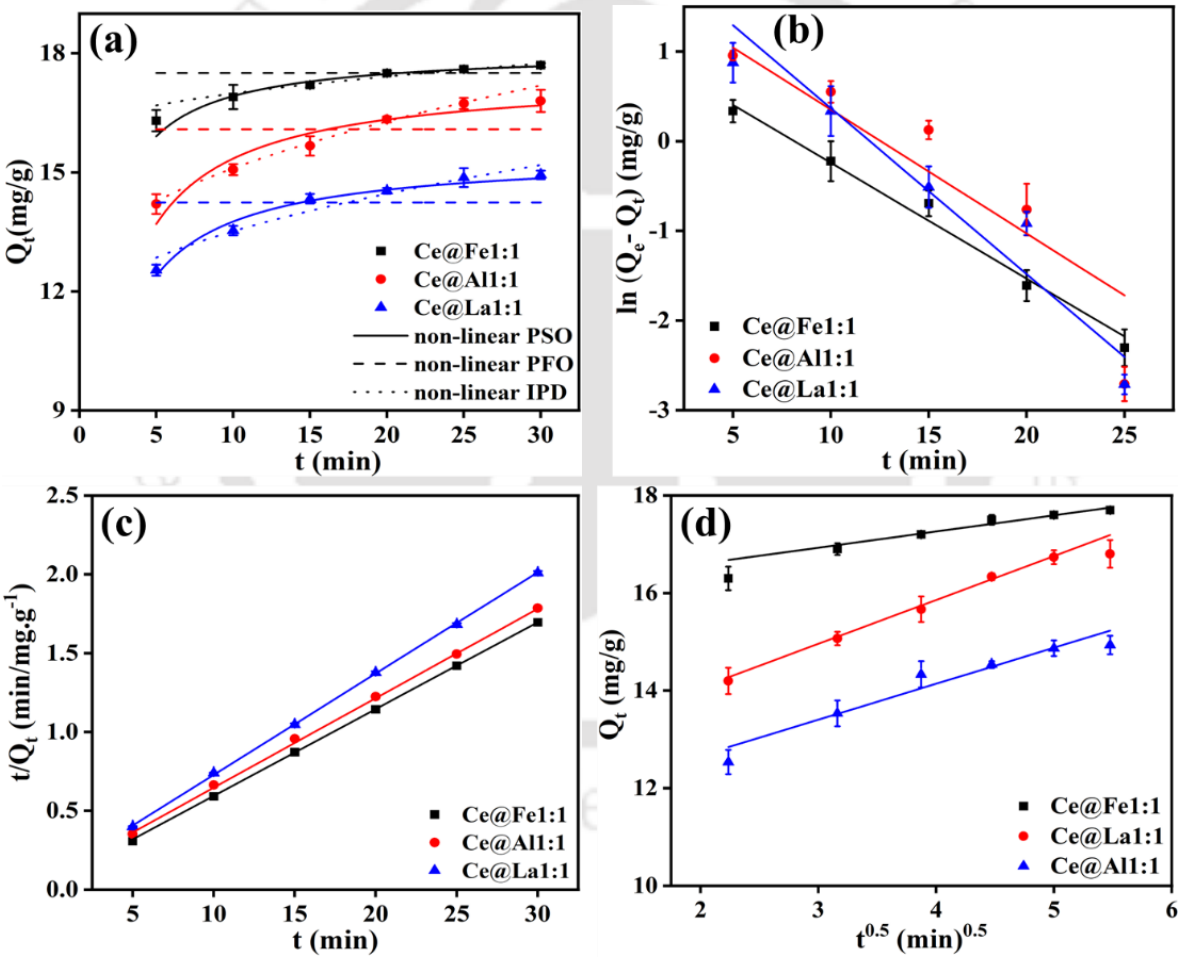

Figure 4.12. (a) non-linear fitting of kinetic models; (b) linearized form of PFO; (c) linearized form of PSO; and (d) linearized form of IPD kinetic model.

Table 4.4. Kinetic parameters obtained from different fittings of kinetic models for bimetallic MOFs (Ce@Fe1:1, Ce@Al1:1 and Ce@La1:1).

Models		**Adsorbents**		
		Ce@Fe1:1	Ce@Al1:1	Ce@La1:1
PFO	Q_e	9.0	5.6	2.86
Linear	k_1	0.12	0.14	0.18
	R^2	0.98	0.86	0.90
Non-linear	Q_e	17.5	16.3	14.5
	k_1	0.50	0.34	0.37
	R^2	0.31	0.64	0.80
PSO	Q_e	18.07	17.44	15.46
Linear	k_2	0.08	0.04	0.05
	R^2	0.93	0.92	0.97
Non-linear	Q_e	18.23	17.60	16.6
	k_2	0.06	0.04	0.04
	R^2	0.99	0.99	0.99
IPD	C	15.9	12.2	11.2
Linear	k_i	0.33	0.89	0.73
	R^2	0.94	0.98	0.93
Non-linear	C	15.9	12.2	11.2
	k_i	0.32	0.40	0.72
	R^2	0.92	0.98	0.92

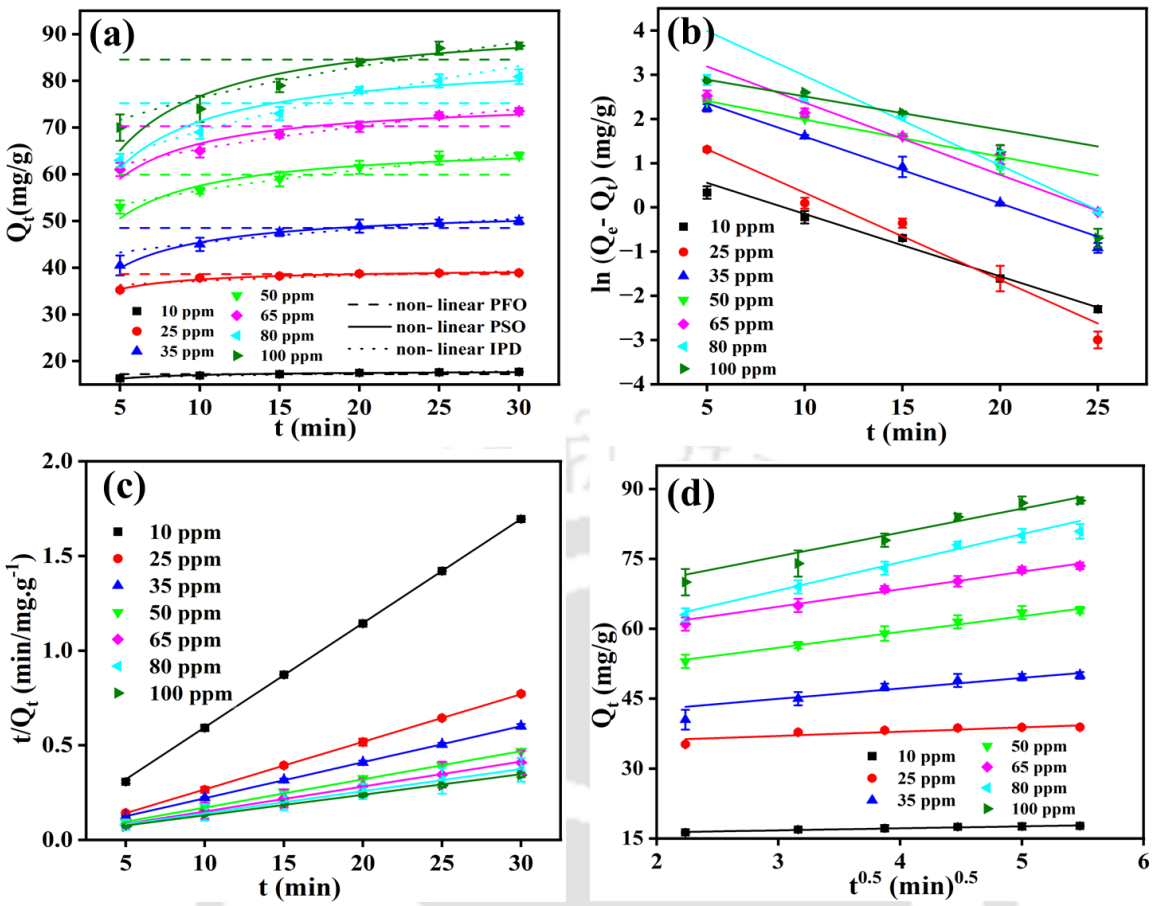

Figure 4.13. Effect of contact time for removal of fluoride by Ce@Fe1:1; (a) fitting of non-linear PFO, non-linear PSO, and non-linear IPD; (b) linearized form of PFO; (c) linearized form of PSO; and (d) linearized form of IPD kinetic model fitting.

The R^2 value obtained from the linearized PSO model is 0.99 at 10 ppm of C_0 and the calculated adsorption capacity (Q_{cal}) is adjacent to the equilibrium adsorption capacity obtained from the experiment. Therefore, the rate-controlling step for this process is chemical adsorption. Additionally, it forecasts the reaction over the entire range of adsorption, which may include valency forces *via* ion exchange between adsorbate and adsorbent material. In this case, instead of using the adsorbate concentration, adsorption capacity is used to calculate the adsorption rate [135]. The PSO model has a significant benefit since the equilibrium adsorption capacity may be calculated directly from the model. The terms for the

PSO model were θ_e and C_0/β tends to 1. β and θ_e are the equivalent concentration of the maximum amount adsorbed and the equilibrium surface coverage fraction, respectively [178]. The rate of adsorption of the Ce@Fe1:1 is considerably quicker than most of the existing literature (**Table 4.2**), reaching equilibrium in less than 30 minutes.

Table 4.5. Kinetic parameters obtained from different fittings of kinetic models for Ce@Fe1:1 at difference concentrations.

Models		**C_0 (mg/L)**						
		10	**25**	**35**	**50**	**65**	**80**	**100**
PFO	Q_e	3.52	9.965	22.39	16.97	54.87	149.01	26.31
Linear	k_1	0.140	0.19	0.15	0.084	0.16	0.20	0.07
	R^2	0.98	0.97	0.99	0.94	0.98	0.98	0.84
Non-linear	Q_e	17.2	38.6	48.8	59.9	70.3	75.2	84.7
	k_1	22.5	7.9	251.68	371.6	397.8	395.9	423.2
	R^2	-0.25	-0.25	-0.25	-0.25	-0.25	-0.25	-0.25
PSO	Q_e	18.16	39.84	52.57	67.07	75.8	85.54	92.16
Linear	k_2	0.068	0.040	0.012	0.010	0.009	0.005	0.005
	R^2	0.99	0.99	0.99	0.99	0.99	0.99	0.99
Non-linear	Q_e	17.92	39.82	52.673	66.794	76.307	85.21	93.37
	k_2	0.11	0.039	0.012	0.009	0.009	0.006	0.005
	R^2	0.96	0.98	0.99	0.921	0.920	0.94	0.892
IPD	k_i	15.43	34.264	38.22	45.84	53.53	50.17	60.15
Linear	C	0.43	0.91	2.24	3.365	3.72	6.02	5.124
	R^2	0.96	0.79	0.89	0.99	0.98	0.97	0.93

Non-linear	k_i	0.43	0.914	2.244	3.368	3.740	6.023	5.124
	C	15.45	34.26	38.22	45.84	53.52	50.176	60.15
	R^2	0.961	0.79	0.89	0.991	0.981	0.970	0.93

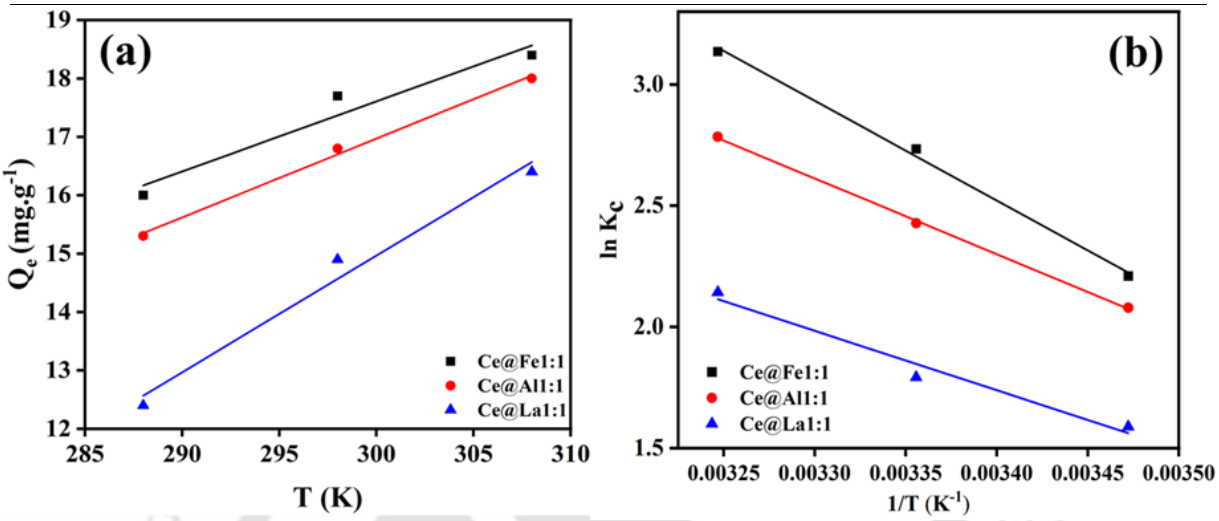

Figure 4.14: (a) Adsorption thermodynamics and (b)Van't Hoff's plot.

4.3.12. Thermodynamic evaluation

The possibility of the adsorption processes is shown in **Figure 4.14** by the thermodynamic evaluation.[90] The temperature effect on the fluoride adsorption by adsorbents Ce@Fe1:1, Ce@Al1:1, and Ce@La1:1 were studied. The adsorption capacity shows an increased trend with the increase in temperature from 288 to 308 K. The standard enthalpy (ΔH˚: kJ/mol), standard entropy (ΔS˚: kJ/mol. K), and standard Gibbs free energy (ΔG˚: kJ/mol) were calculated using the Van't Hoff plot for fluoride adsorption onto the adsorbent using Eqs. (2.11) and (2.12). The linear connection between ln K and 1/T is depicted in **Figure 4.14**, and the related thermodynamic parameters are summarised in **Table 4.6**. The positive ΔH˚ expresses that the reaction is endothermic, which means fluoride adsorption increases at higher temperatures. The negative ΔG˚ determined at different temperatures denotes the spontaneous nature of the adsorption process. The reductions in the randomness of the adsorption process

may be validated by the small value of ΔS˚ [137,138]. Furthermore, thermodynamic characteristics can also reflect the adsorption mechanism. Physical adsorption occurs when the ΔG˚ value is in the range -20 and 0 kJ/mol or the enthalpy is in the range 2.1 and 20.9 kJ/mol. At the same time, chemical adsorption occurs when either the enthalpy of the reaction is in the range of 80 to 200 kJ/mol or Gibbs free energy is in the range of 80 to 400 kJ/mol. The experimentally determined enthalpy and Gibbs free energy of the synthesized adsorbents fall within the range of physical adsorption for all temperature ranges taken in this study.

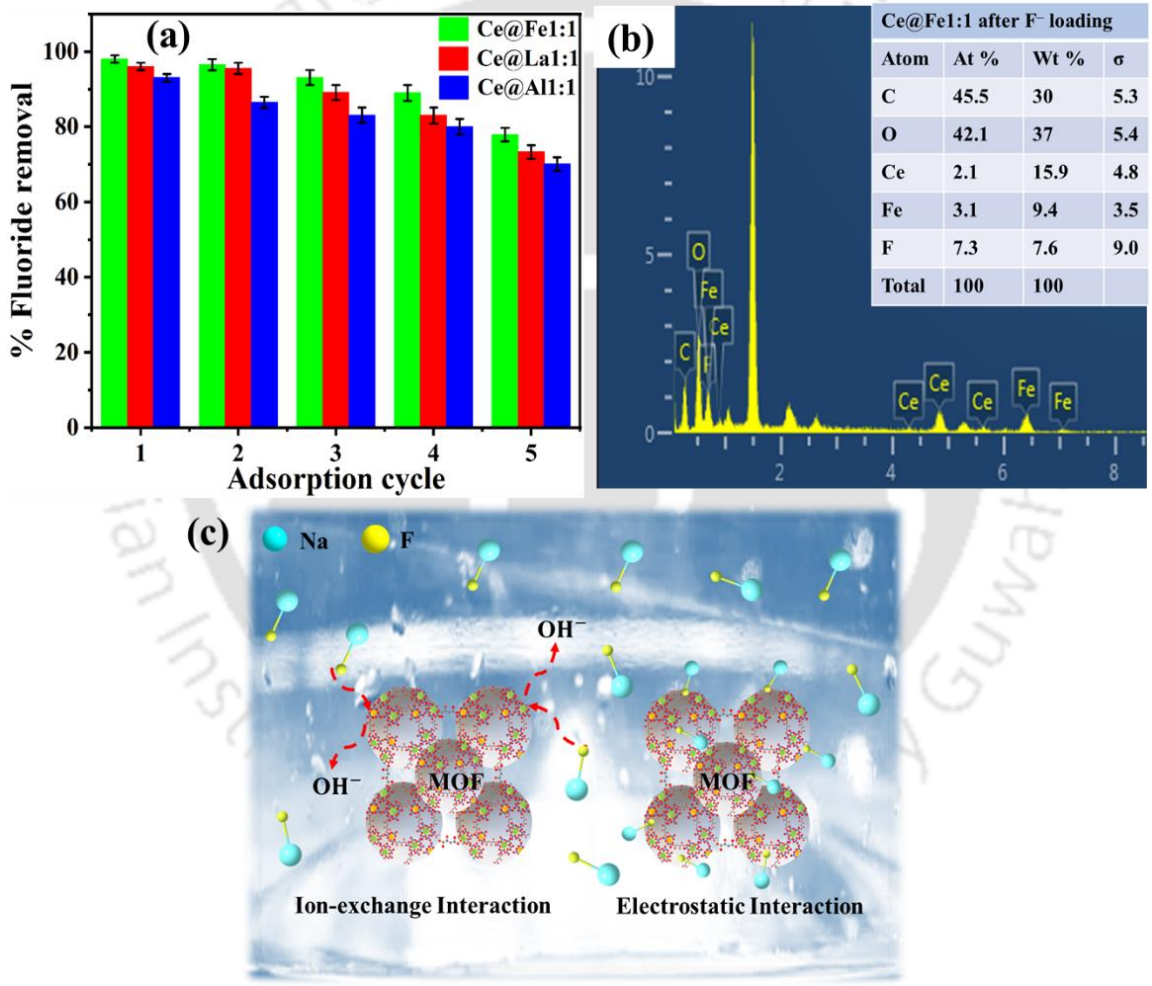

Figure 4.15. (a) adsorbents regeneration profile, (b) elemental analysis obtained from EDX, and (c) Schematic diagram of the adsorption mechanism of Ce@Fe1:1.

Table 4.6. Thermodynamic Parameters Calculated from Van't Hoff Plot.

Adsorbent	ΔG°(kJ/mol)			ΔH°(kJ/mol)	ΔS°(kJ/mol. K)
	288 K	298 K	308 K		
Ce@Fe1:1	-5.290739275	-6.77351	-8.029483	-34.185	0.137191
Ce@Al1:1	-4.97932	-5.855	-7.1290	-25.911	0.107043
Ce@La1:1	-3.80381	-4.43943	-5.48827	-20.384	0.083761

4.3.13. Adsorption regeneration test

Saturated adsorbents being dumped into the environment is a significant solid waste problem from both an economic and environmental perspective. Disposal of saturated poisonous and hazardous adsorbent increases the operational cost associated with processing a large volume of sludge. For the regeneration study, adsorbents were saturated in 10 mg/L of 20 mL fluoride solution. Then, the fluoride-loaded adsorbents were separated using centrifugation. Afterward, it was thoroughly washed in a sufficient amount of water followed by overnight stirring in 0.1 M of NaOH solution to eliminate fluoride ions.[179] Centrifugation was used to isolate the fluoride-free adsorbents, which were then dried in an oven. The cycle was repeated using regenerated mixed-metal MOFs up to 5^{th} consecutive cycles at pH 6.5. The percentage desorption was calculated using Eq. (2.13). Ce@Fe1:1 was to remove 98% of the fluoride in the second adsorption-desorption cycle and eventually in the 5th cycle it removed 77.9 % of fluoride as shown in **Figure 4.15**a. Other two materials such as Ce@Al1:1 and Ce@La1:1 were able to remove 73. 3 and 70.1 % of fluoride in the 5th regeneration cycle, respectively.

4.3.14. Adsorption mechanism

In this study, the probable interaction mechanism of Ce@Fe1:1 becomes complex due to the incorporation of two metals (Ce and Fe) in the MOFs, as depicted in **Figure 4.15**c. To enhance

understanding, we can break down the entire mechanism into a few distinct phases. Water molecules dissociate, giving rise to hydrogen and hydroxyl radicals, which function as Lewis sites. Metal salts like $Ce(NO_3)_3$ and $Fe(NO_3)_3$ break down into metal ions and serve as Lewis acids [147]. When these metal ions are introduced into an aqueous solution, they form metal aqua ions, which subsequently undergo hydrolysis. The hydrolysis reactions of the metals are provided below:

$$(NH_4)_2[Ce(NO_3)_6] \rightarrow Ce^{3+} + 6NO_3^- + 2NH_4^+ \quad (4.1)$$

$$Ce^{3+} + 3H_2O \rightarrow Ce(HO)_3 + 3H^+ \quad (4.2)$$

Similarly,

$$Fe(NO_3)_3.9H_20 \rightarrow Fe^{3+} + 3NO_3^- + 9H_2O \quad (4.3)$$

$$Fe^{3+} + 3H_2O \rightarrow Fe(HO)_3 + 3H^+ \quad (4.4)$$

Polycondensation takes place after the creation of $Fe(OH)_3$ and $Ce(OH)_3$ through olation and oxolation processes, leading to the formation of hydroxyl and oxo-bridges between tetramer units.

$$Ce - OH + H_2O - Ce \rightarrow Ce - OH - Ce + H_2O \quad (4.5)$$

$$Ce - OH + OH - Ce \rightarrow Ce - O - Ce + H_2O \quad (4.6)$$

Similarly,

$$Fe - OH + H_2O - Fe \rightarrow Fe - OH - Fe + H_2O \quad (4.7)$$

$$Fe - OH + OH - Fe \rightarrow Fe - O - Fe + H_2O \quad (4.8)$$

The hydrolysis of metals yields $Fe(OH)_3$ and $Ce(OH)_3$ attract fluoride ions through protonation or deprotonation processes in the aqueous medium, which is influenced by the solution pH. This results in the attachment of F^- ions to $Ce(OH)_3$ and $Fe(OH)_3$ as follows:

$$Ce\,(HO)_3 + xF^- \leftrightarrow Ce\,(HO)_{3-x}\,F_x + OH^- \quad (4.9)$$

Similarly,

$$Fe\,(HO)_3 + xF^- \leftrightarrow Fe\,(HO)_{3-x}\,F_x + OH^- \quad (4.10)$$

In support of this, characterization techniques such as EDX, zeta potential measurement, and XPS of all the synthesized adsorbents were collected. These instrumental analyses were conducted both before and after fluoride adsorption to determine the corresponding surface alterations that took place after fluoride adsorption.

EDX analysis was executed to confirm that the fluoride was adsorbed on bimetal MOFs (**Figure 4.15**b). The atomic (At) % of Ce and Fe were decreased upon fluoride loading from 5 and 3.2 to 2.1 and 3.1, respectively. The elemental analysis of the fluoride-loaded sample showed an additional peak of fluoride having 7.3 At %, which confirms the fluoride adsorption on the Ce@Fe1:1.

The zeta potential of bimetal MOFs Ce@Fe1:1, Ce@Al1:1, and Ce@La1:1 before and after fluoride adsorption were done to predict interactions of fluoride ions on the adsorbent surfaces. The positive charge surfaces of the materials such as Ce@Fe1:1, Ce@Al1:1, and Ce@La1:1 were confirmed by determining the zeta potential values 15.2±0.4, 9.3±0.5, and 6.1±0.4 mV, respectively. After the high uptake of fluoride ions on the material, the surface charge shifts to the negative region. The zeta potential values of the materials after the fluoride loading are –8.5±0.3, –3.1±0.4, –1.7±0.6 mV, respectively. Adsorption of fluoride on bimetal MOFs can happen via two different interactions, one is hydrogen bonding and the other is through the ion exchange. Based on the zeta potential measurement, the point of zero charge (pH_{pzc}) of Ce@Fe1:1MOFs was obtained at 9.8 pH. When the pH of the solution is less than the pH_{pzc}, the overall surface charge of the material becomes positive as fluoride is electronegative, it shows higher adsorption capacity at lower pH via hydrogen bonding [180]. Reversely, If the

solution pH is greater than pH_{pzc}, the fluoride removal is very low, this could be because of the electrostatic repulsion between the F^- ions and the negatively charged surface of the material [151].

XPS examination was conducted to know the existence states of Ce, Fe, Al, La, C, O, and F based on their binding energies in the bimetal MOFs both before and after the fluoride loading, illustrated in **Figure 4.5** [168]. A peak at binding energy 685.4 eV in the bimetal MOFs after fluoride adsorption was visible, which specified that F^- ions had been adsorbed on the adsorbents. The intensities of the O1s peak in all the adsorbents used after adsorption are decreased, this could be because of involvement in the hydrogen bonding with fluoride. The intensities of the M–OH peak in all the adsorbents used are slightly decreased because of the interaction between metal and fluoride. It is noteworthy to mention, that the peak of the metals exhibits a considerable swing to high binding energy, which may be related to the development of complexes (M–F) between metals and F^- ions through an ion exchange process [98]. Based on this research, electrostatic attraction and ion-exchange reaction could be the mechanisms by which fluoride is removed by bimetal MOF composites.

3.6. Conclusions

In this study, the synthesis of novel nanoporous bimetal MOFs such as Ce@Fe1:1, Ce@Al1:1, and Ce@La1:1 with outstanding performance in removing fluoride from water has been investigated. Ce@Fe1:1, Ce@Al1:1, and Ce@La1:1 adsorbents exhibited rapid sorption kinetics, showcasing impressive maximum fluoride uptake capacities of 101.3, 94.33, and 90.9 mg/g, respectively. These values significantly surpass the adsorption capacity of Ce-Fu MOFs, synthesized with fumaric acid, which reached a maximum of 64.16 $mg \cdot g^{-1}$. The bimetallic MOFs reaches its maximum adsorption capacity in 30 minutes and removes 85% of the fluoride

from the solution in 10 minutes, which follows a PSO kinetic model. The emergence of a fluoride peak by the EDX and XPS analysis confirmed the successful adsorption of fluoride ions on the synthesized bimetal MOFs. The findings from Zeta potential analysis, and XPS spectra demonstrated that all the synthesized materials support the electrostatic attraction and ligand exchange reaction for the removal of fluoride by adsorption. The existence of Cl^- ions does not exhibit a substantial influence on the reduction of fluoride removal at lower concentrations. On the contrary, it has been noted that when ions such as NO_3^-, SO_4^{2-}, Br^-, and PO_4^{3-} are present, all three nanoporous bimetal MOFs experience a slight decrease in their efficiency in removing fluoride. However, it is important to note that the presence of HCO_3^- and CO_3^{2-} ions significantly hampers the adsorption of fluoride. Examining the stability of bimetal MOFs underscores their ability to retain a stable crystalline structure even when exposed to water at different pH levels, suggesting their potential suitability for use in aqueous environments. Additionally, the contact angles for Ce@Fe1:1, Ce@Al1:1, and Ce@La@1:1 were found to be 49.6°, 36.9°, and 38°, respectively. These results indicate that Ce@Fe1:1 exhibited relatively weaker hydrophilic characteristics. The adsorbent maintained its adsorption efficiency up to the fifth cycle. The process is exothermic, and spontaneous at the adsorbent−solution interface, according to thermodynamic measurements. This work has explored several adsorbents for removing fluoride from wastewater, which will be important for further studies in the field.

CHAPTER 5

Investigating the Efficacy of Bimetallic Metal-Organic Frameworks (MOFs) as Fluoride Adsorbent in Fixed-Bed Adsorption Columns: Experimental and Modeling Insights

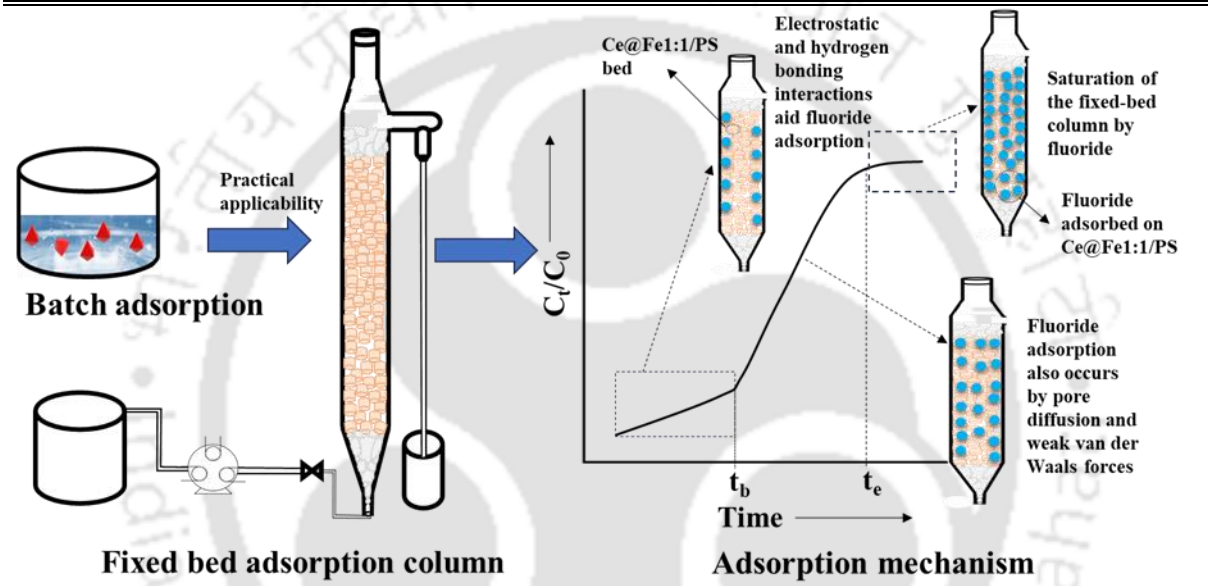

CHAPTER 5

This research chapter explores fluoride removal from wastewater using a fixed bed adsorption column. Various characterization techniques were used to analyze Ce@Fe1:1/PS morphology to confirm fluoride capture on it. The experimental design assesses the impact of various parameters on FBAC performance. Mathematical models are utilized to analyze breakthrough curves and kinetics, offering detailed insights into Ce@Fe1:1/PS effectiveness. The study emphasizes the significance of operational parameters in optimizing the FBAC system.

5.1. Introduction

While MOF (Metal-Organic Framework) and hybrid materials derived from MOFs have been extensively studied for their multipurpose applications, bimetallic MOFs have received limited attention as adsorbents in wastewater treatment [108,181,182]. To bridge this research gap, we explored the synthesis of bimetallic MOFs in the previous chapter, in which the nodes consist of inorganic compounds (Ce, Fe, Al, and La) connected by a fumaric acid linker. The synthesis of nanoporous bimetallic MOFs such as Ce@Fe1:1, Ce@Al1:1, and Ce@La1:1 with outstanding performance in removing fluoride from water has been investigated. Ce@Fe1:1, Ce@Al1:1, and Ce@La1:1 adsorbent exhibited rapid sorption kinetics, showcasing impressive maximum fluoride uptake capacities of 101.3, 94.33, and 90.9 mg/g, respectively. The best outcome obtained using bimetallic Ce@Fe1:1 MOFs was further implicated in practical scenario. Various adsorption techniques is being employed to create a connection between the adsorbent and adsorbate including batch, pulsed-bed adsorption methods, continuous fluidized bed, continuous moving bed, and continuous fixed-bed [183]. While batch adsorption studies are efficacious for optimizing numerous parameters, continuous adsorption studies are

instrumental in demonstrating the real-world suitability of adsorbents for wastewater treatment [184]. Numerous studies are available using batch operation for the elimination of fluoride, whereas the literature lacks sufficient reports on fixed-bed column studies. This scarcity is mainly due to the time-consuming nature of the column studies, requiring an extended period for optimization [185]. However, the application of mathematical models to the column studies can significantly reduce the optimization time for process parameters, making it more effective [186]. Additionally, it is challenging to obtain precise scale-up data for fixed bed adsorption columns (FBAC) solely from batch results, making it necessary to assess the column operations to meet the practical applicability [109].

To overcome these challenges, we aim to utilize bimetallic MOFs Ce@Fe1:1 having best adsorption capacity matrixed with polysulfone (Ce@Fe1:1/PS) to eliminate fluoride from drinking water. This bimetallic MOF has not been documented in the existing literature. Batch adsorption experiments were studied to get the fundamental information regarding the fluoride adsorption performance of adsorbents. This Ce@Fe1:1/PS was characterized through various techniques to understand the physio-chemical properties of the material concerning the elimination of fluoride from wastewater. The effects of fluoride solution flow rate, the height of the bed, and influent initial concentration were evaluated to measure the adsorptive behaviour of Ce@Fe1:1/PS. The performance of the column was tested using effluent from the Brahmaputra River. Furthermore, several mathematical models were applied to understand the data gathered from FBAC experiments to describe breakthrough curves and parameters [187]. Regeneration cycles in the column were performed to examine the reusability of Ce@Fe1:1/PS to understand the stability and effectiveness of the adsorbent beads. The goal is to enhance comprehension of column behaviour, identify performance-enhancing conditions, gain deeper visions for material selection, and design fixed-bed adsorption operations.

5.2. Experimental

5.2.1. Materials

The chemicals used in the synthesis of adsorbent are polysulfone was supplied by Merck Ltd., Mumbai, India. The suppers of all the other chemicals used in this work have already been mentioned in Chapter 4.

5.2.2. Methodology to prepare Ce@Fe1:1/PS beads

The synthesis method Ce@Fe1:1 of bimetal MOFs has been described in chapter 4. Ce@Fe1:1/PS beads were fabricated by following the subsequent procedure. To begin, 0.5 g of polysulfone was gradually dissolved in 5 ml of DMF by stirring overnight on a magnetic stirrer at 100 °C. Subsequently, Ce@Fe1:1 was introduced 0.1 g to the obtained homogeneous polymer solution by stirring for another 6 h. Subsequently, the solution was utilized for the fabrication of beads using a 1000 µL Microliter variable volume micropipette. The Ce@Fe1:1/PS was precipitated in the deionized water at room temperature under continuous agitation to prevent bead aggregation. Following this step, the adsorbent was kept immersed in the deionized water for 4 h and was subsequently separated and washed with deionized water. Subsequently, the beads were separated followed by washing multiple times using deionized water. Finally, the resulting beads were dried in an oven at 50 °C for 24 hours, resulting in the formation of small beads of bimetal MOF with polysulfone.

5.2.3. Characterization instruments

Make and models of all the instruments used in this study have been listed in the previous chapters.

5.2.4. Mathematical analysis of breakthrough curve

Breakthrough curves represent a graphical representation of the ratio of fluoride concentration at the inlet to the outlet (C_t/C_0) over time [31] The shape of the breakthrough curve and the time takes to reach breakthrough (t_b) are vital for understanding the dynamic behaviour of the column. The steepness of this curve also offers insights into the degree to which the adsorbent bed can be effectively utilized [32]. The t_b is determined when C_t is less than or equal to 1.5 ± 0.2 mg/L. The calculation of throughput volume (V_{eff}) was performed using Eq. (5.1),

$$V_{eff} = Qt_e \tag{5.1}$$

where, Q is the flow rate and t_e is the column exhaustion time and F is the flow rate (L min^{-1}). Exhaustion is typically regarded when the effluent concentration remains consistent for an extended duration, closely resembling the influent concentration. In this research, exhaustion was defined as the point when the C_t/C_0= 0.99. The quantity of F^- ions in the fixed bed system (m_{in}, mg) at a given time (t; min) is expressed by Eq. (5.2),

$$m_{in} = QC_0t \tag{5.2}$$

where, fluoride initial concentration of solution is (C_0, mg L^{-1}). The quantity of fluoride at the outlet (m_{out}, mg) at a specific time is determined by the area under the dimensionless curve times the C_0 and Q, as described by the following equation.

$$m_{out} = Q\ C_0 \int_{t=0}^{t=total} \left(\frac{C_t}{C_0}\right) dt \tag{5.3}$$

The quantity of fluoride adsorbed (m_{ads}, mg) in FBAC can be calculated by using the given equation.

$$m_{ads} = m_{in} - m_{out} \tag{5.4}$$

The adsorption capacity at equilibrium (Q_e, mg g^{-1}) at saturation time(t_e) is given by Eq. (5.5),

$$Q_e = \frac{m_{ads}}{M} = \frac{Q\, C_0 \int_0^{te}\left(1-\frac{C_t}{C_0}\right)dt}{M} \quad (5.5)$$

where M is the amount of adsorbent used in the fixed bed system in grams. The adsorption capacity at breakthrough is given by the Eq. (5.6).

$$Q_b = \frac{Q\, C_0 \int_0^{t_b}\left(1-\frac{C_t}{C_0}\right)dt}{M} \quad (5.6)$$

The overall column efficiency for fluoride elimination from the influent solution is R.

$$\%R = \frac{m_{ads}}{m_{in}} \times 100 \quad (5.7)$$

The difference between the breakthrough time (t_b) and t_e given mass transfer zone is Δt.

$$\Delta t = t_e - t_b \quad (5.8)$$

The mass transfer zone (MTZ) is intricately linked to the height of the bed (Z), exhaustion time, and breakthrough time.

$$MTZ = Z\left[1 - \frac{t_b}{t_e}\right] \quad (5.9)$$

Higher values of breakthrough time, saturation time, and removal efficiency specify that the Ce@Fe1:1/PS contained within the column possesses a substantial adsorption capacity.

5.2.5. Column adsorption models

5.2.5.1. Bed depth service time (BDST) model

The BDST model is utilized to assess the AC of the column by assuming that the effects of external mass transfer resistance and intra-particle diffusion can be disregarded [190]. The

derivation of this model is centered around the idea that the uptake rate is predominantly governed by the surface chemical reaction between the adsorbate and the untapped site. This approach also works well for evaluating the effectiveness of columns running under different process factors [191]. For fixed-bed columns, the primary application lies in predicting the duration the adsorbent material can effectively remove a specific amount of adsorbate from the influent solution before requiring regeneration. The time duration during which the bed can effectively operate is referred to as the service time of the bed. Among the various models used for studying the adsorption of fluoride on column systems, the BDST model is one of the most relevant and widely employed [192]. BDST offers a straightforward and comprehensive approach to forecasting the correlation between bed height (Z) and service time (t). Its primary objective is to estimate characteristics like the maximum AC and adsorption rate constant (K_{BDST}; L mg^{-1} min^{-1}). However, it is important to note that this model is specifically suitable for describing the initial part of the breakthrough curve, covering the region up to the breakpoint. Hutchins (1973) made modifications to the Bohart-Adams equation and introduced a linear correlation between Z and t. This modified equation necessitates just three experiments using fixed beds to obtain the required data and can be expressed as given below.

$$t = \frac{N_0 Z}{C_0 u} - \frac{1}{K_{BDST} C_0} \ln\left(\frac{C_0}{C_b} - 1\right) \quad (5.10)$$

Service time at the breakthrough point and saturation concentration are represented as t and N_0 (mg/L). C_0 (mg/L), C_b (mg/L), and u (cm/min) are the initial concentration, breakthrough concentration, and linear flow rate, respectively. Furthermore, the equation can be reformulated into the straight-line equation.

$$t = mZ - C \quad (5.11)$$

$$C = \frac{1}{K_{BDST} C_0} ln\left(\frac{C_0}{C_b} - 1\right) \quad (5.12)$$

The intercept (C) and the slope ($m = N_0/C_0 v$) of the plot of (t) versus Z can be utilized for the determination of N_0 and K_{BDST}.

5.2.5.2. Thomas Model

Thomas model is considered extremely versatile and commonly applied model in fixed bed performance theory [193]. This model is founded on the assumption of Langmuir kinetics of adsorption-desorption without any axial dispersion as it follows second-order reversible reaction kinetics [194]. A constant separation factor is another assumption made. To analyze the breakthrough curves, the Thomas model is employed using the following Equation.

$$\frac{C_t}{C_0} = \frac{1}{1 + exp\left(\frac{K_{th}}{Q}(Q_e m - k_{TH} C_0 t)\right)} \quad (5.13)$$

The linear form of this can be expressed as follows,

$$ln\left(\frac{C_0}{C_t} - 1\right) = \frac{K_{th} Q_e M}{Q} - K_{th} C_0 t \quad 5.14)$$

where, K_{th} (L mg^{-1} min^{-1}) is the rate constant and Q_0 is the maximum AC in mg g^{-1}. C_t and C_0 are the fluoride concentrations at the outlet and inlet in mg/L, respectively. M and Q are the total amount of the adsorbent packed in the column (g) and flow rate (L/min), respectively. The volume of fluoride solution flow through the column is expressed as V_{eff} (L).

5.2.5.3. Yoon-Nelson Model

The Yoon and Nelson (1984) model presents a relatively simple approach to modeling adsorption. One of the significant advantages of the Yoon and Nelson model is its simplicity [195]. It is postulated that the reduction in the possibility of uptake for each fluoride is directly

proportional to both the uptake of the fluoride and the likelihood of breakthrough on the adsorbent [196]. Moreover, it does not necessitate comprehensive data regarding the characteristics of the adsorption bed. Yoon and Nelson's equation can be expressed as,

$$\frac{C_t}{C_0} = \frac{exp(K_{yn}t - \tau K_{yn})}{1 + exp(K_{yn}t - \tau K_{yn})} \quad (5.15)$$

which can be rearranged in the linear to get the question given below.

$$ln\left(\frac{C_t}{C_o - C}\right) = K_{yn}t - \tau K_{yn} \quad (5.16)$$

where, K_{yn} (min^{-1}), and τ are the rate constant and the time required for 50% adsorbate breakthrough (min).

5.2.5.4. Clark Model

The Clark model holds particular importance out of the numerous models documented in the literature for FBAC. It is investigated due to its capacity to incorporate both equilibrium adsorption principles and mass transfer for predicting the characteristics of breakthrough data. The key assumptions underlying the Clark model are: (i) mass transfer within the column accompanies the Freundlich model and (i) the inflow into the column is of a piston-type nature [197]. The Clark model is expressed as,

$$ln\left(\left(\frac{C_0}{C_t}\right)^{n-1} - 1\right) = -rt + \ln A \quad (5.17)$$

in these equations, C_0 and C_t represent the influent and effluent concentrations in mg/L, respectively. n represents the Freundlich constant, whereas, r (min^{-1}) and A are Clark model constants.

5.2.5.5. Yan Model

Yet another commonly employed model for investigating breakthrough curves in FBAC is the Yan model, expressed mathematically as follows:

$$\frac{C_t}{C_0} = 1 - \frac{1}{1+\left(\frac{Q_t}{b}\right)^a} \tag{5.18}$$

In the Yan model, the constants a and b are defined as follows:

$$a = \frac{K_y C_0}{Q}; b = \frac{Q_e m}{C_0}$$

The final expression after linearizing is derived as follows,

$$ln\frac{C_t}{C_0 - C_t} = \frac{K_y C_0}{Q} \ln t + \frac{K_y C_0}{Q} ln\frac{C_0 Q}{Q_0 m} \tag{5.19}$$

where, Q (L/min), t (min), Q_e (mg/g), K_y (L mg^{-1} min^{-1}), and m (g) are entitling the flow rate at the inlet, duration of flow, adsorption capacity, rate constant and mass of adsorbent in the column, respectively.

5.2.6. Column experiments

For the study, borosilicate glass columns were constructed with inner diameters of 0.9 cm. The dynamic studies were carried out at room temperature. Glass wool was stuffed right above the inlet point and near the exit point of the column with a thickness of 0.5 cm to achieve a uniform inlet flow, and prevent the adsorbent from floating up throughout the process. **Figure 5.1**a illustrates the schematic diagram of the reactor. The peristaltic pump (NEXQUA, WaterQuality Association) was utilized to pump the fluoride solution upward through the column. To prevent the flow rate fluctuations, the flow rate was periodically monitored and validated at the outflow of the FBAC at specific periods. To eliminate trapped air, the Ce@Fe1:1/PS FBAC was

thoroughly soaked with deionized water for 5 hours before commencing the experiments. The breakthrough concentration was established at 1.5 mg/L of fluoride solution. The water was collected from the Brahmaputra River, Guwahati, India and fluoride was added to make the desired concentration. Approximately 60 ± 2 mg of Ce@Fe1:1/PS (Ce@Fe1:1/PS) were loaded into the glass column to achieve a bed height of approximately 40 cm. The experiments were carried out using three different bed heights such as 30 ± 0.2 cm, 35± 0.2 cm, and 40± 0.2 cm while keeping fixed fluoride concentration and flow rate. Additionally, three different flow rates (0.3 mL/min, 0.5 mL/min, and 0.7 mL/min) were employed with a constant bed depth and fluoride concentration to understand the flow rate effect. Furthermore, variations in the initial fluoride concentrations (40 mg/ L, 50 mg/ L, and 60 mg/L) were studied, keeping the flow rate of fluoride and the height of the bed unchanged. The solution at the outlet was gathered from the upper section of the column, which was periodically collected and measured. The experiments were concluded upon reaching bed saturation. Throughout the experiment, the following precautions were meticulously observed: (a) the column was positioned vertically, (b) there was no occurrence of bed leakage or flow disruption, and (c) the influent supply to the column was consistently maintained until the experiment completion. A concise overview of the study specifications is presented in **Table 5.1.**

5.3. Results and discussion

5.3.1. Characterization of Ce@Fe1:1/PS

SEM analysis provides insight into the top surface morphology of Ce@Fe1:1/PS displays wide pores within its structure. SEM micrographs depicted in **Figure 5.1**b reveal an uneven and rugged structure characterized by asymmetrical channels and furrows distributed across the exterior of the material. The wrinkles or crevices present on the surface of the Ce@Fe1:1/PS

could be attributed to a physical adsorption process by allowing contaminant molecules to adhere to these recesses. As a result, these findings illustrate that the adsorbent may be able to adsorb fluoride from wastewater.

The XRD analysis was conducted on PS, Ce@Fe1:1/PS, and Ce@Fe1:1 (**Figure 5.1**c**)**. The XRD pattern of Ce@Fe1:1 displayed a semi-crystalline nature and a prominent peak was visible at 9.2°, 10.8°, 18.7°, 24.06°, and 34.1° [198]. On the other hand, the XRD spectrum exhibits a broad characteristic peak of the PS at 18.4°, indicating the amorphous nature [199]. After the incorporation of bimetal Ce@Fe1:1 MOFs into the polysulfone, the mixed matrix bead (Ce@Fe1:1/PS) showed a combined characteristic of the raw materials. A broad peak at 18.4° was visible, which may be because of the presence of polymer in Ce@Fe1:1/PS. The appearance of peaks such as at 18.7 °, 24.06 °, and 34.1 ° was also seen, which may be because of the incorporation of bimetallic MOFs into the polymer.

Concerning the characterization of the surface, N_2 adsorption-desorption study of the Ce@Fe1:1 MOFs and Ce@Fe1:1/PS were performed and displayed BET surface areas 594 and 20 m^2/g, respectively (**Figure 5.1**d). The total pore volume of Ce@Fe1:1 bimetal MOFs and Ce@Fe1:1/PS displayed 0.53 and 6.8e-02 cm^3/g, respectively. The sample displays a Type II isotherm typically indicates a multi-layer adsorption process, which means that after the initial monolayer of adsorption, additional layers are formed on the surface. Moreover, as indicated by the BJH (Barrett-Joyner-Halenda) analysis, the bimetal MOFs Ce@Fe1:1 and Ce@Fe1:1/PS exhibited pore diameters between 4.3 and 13.7 nm, signifying a mesoporous structure (with diameters ranging from 2 to 50 nm) according to the IUPAC classification. This adsorbent can facilitate the rapid diffusion of fluoride ions within the adsorbent pores due to its relatively smaller size.

Table 5.1. The fluoride adsorption properties using FBAC under different operating circumstances.

Z (cm)	**Q (L/min)**	**C_0 (mg/L)**	**m (g)**	**t_b (min)**	**t_e (min)**	**V_{eff} (L)**	**EBCT (min)**	**MTZ (cm)**	**M_{in} (mg)**	**M_{out} (mg)**	**M_{ads} (mg)**	**%R**	**Q_e (mg/g)**
30	0.0003	40	4.5	900	1740	0.522	73.33	14.5	20.9	3.5	17.3	83.1	3.8
35	0.0003	40	5.3	1200	2160	0.648	83.33	15.5	25.9	4.9	20.9	80.9	3.9
40	**0.0003**	**40**	**6**	**1560**	**2580**	**0.774**	**100**	**15.8**	**30.9**	**5.6**	**25.3**	**81.8**	**4.2**
40	**0.0005**	40	6	1020	2100	1.05	100	20.57	42	18.7	23.3	55.4	3.9
40	**0.0007**	40	6	660	1680	1.176	100	24.28	47.0	24.8	22.2	47.2	3.7
40	0.0003	**50**	6	1020	2220	0.666	100	21.6	33.3	7.7	25.6	76.9	4.3
40	0.0003	**60**	6	780	1920	0.576	100	23.7	34.6	8.4	26.2	75.7	4.4

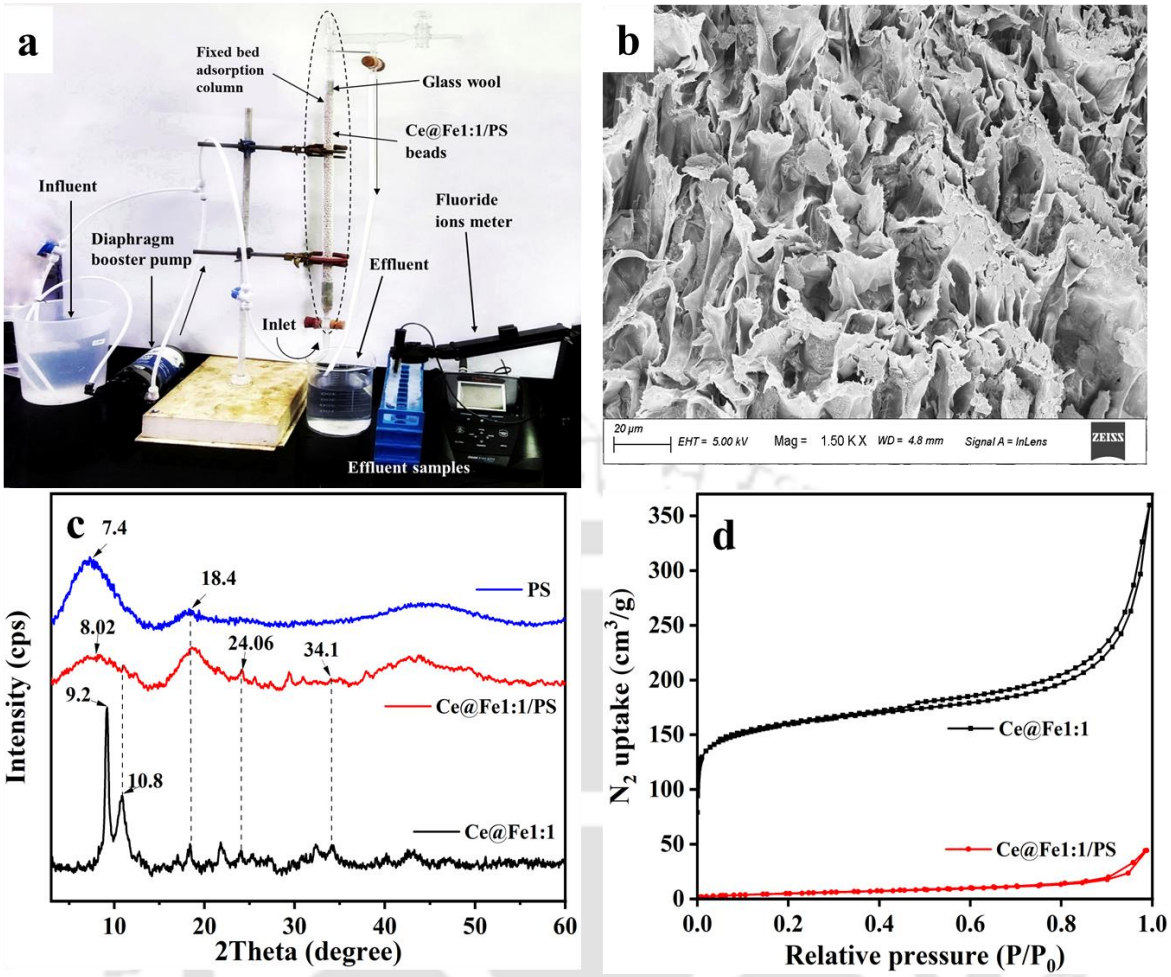

Figure 5.1. (a) The setup for the fixed-bed adsorption column experiment with diaphragm booster pump, column, and fluoride ion meter, (b) SEM image of Ce@Fe1:1/PS, (c) XRD analysis of polysulfone, Ce@Fe1:1/PS and Ce@Fe1:1, and (d) N_2 adsorption-desorption cycles.

5.3.2. Isotherm study

Adsorption isotherm was studied at a constant temperature to understand the adsorption of fluoride on the Ce@Fe1:1/PS MOFs surface, which shows the relationship between the equilibrium AC and equilibrium concentration [124,125]. An isotherm study in batch mode at 298 K was performed to investigate the maximum uptake of F^- ions on Ce@Fe1:1/PS MOFs. The study was performed in the sonicator (frequency: 50 – 60 Hz and voltage: 110–240 V) using a beads dose of 1 g/L at 6.5 pH. The fluoride ion concentration at the inlet was varied up

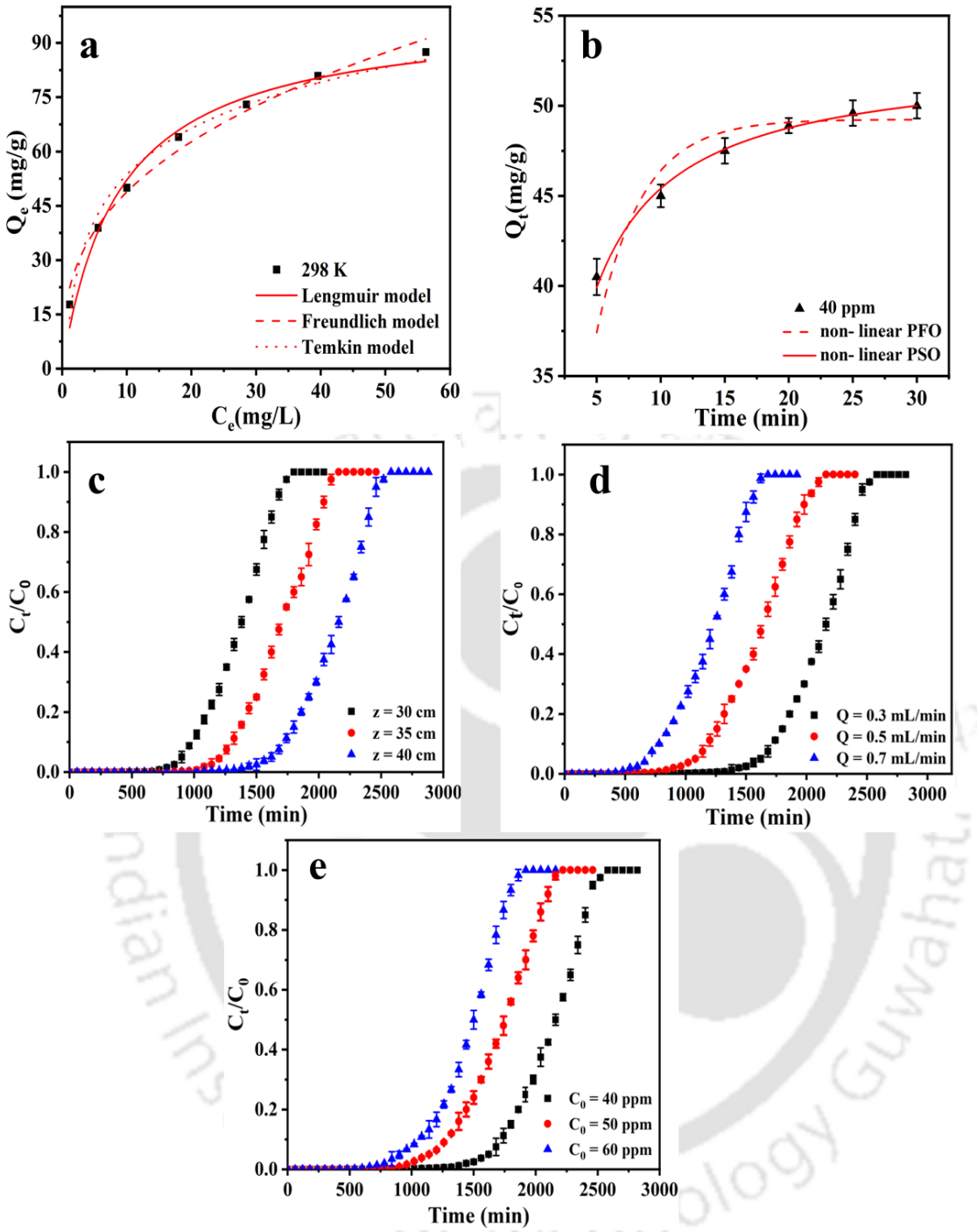

Figure 5.2. Non-linear fitting of (a) isotherm models, and (b) kinetic models; Effect of variation in (c) bed height, (d) flow rate, and (e) the initial fluoride concentration.

to 100 mg/L for this study. To investigate the adsorption process of Ce@Fe1:1/PS, the experimental data were fitted to non-linear isotherm models such as Langmuir, Freundlich, and Temkin (**Table 2.2)**. The correlation coefficient (R^2) of Ce@Fe1:1/PS found from the non-

linear fitting of the Langmuir model is 0.993, which is the highest as compared to other fitted isotherms models in this study, making it the best model (**Figure 5.2**a). The maximum monolayer AC of Ce@Fe1:1/PS is 101.3 mg/g at 288 K obtained from the best-fitted non-linear Langmuir isotherm. The Langmuir model predicts that fluoride ions will uniformly distribute all over the active sites of the adsorbent. It also predicts that once the F^- ions have taken up the whole adsorbent surface, there is no longer any lateral adsorption [124]. Furthermore, the n value obtained from the Freundlich adsorption model is 2.6 indicating favourable adsorption.

Adsorption should also be studied from a kinetic perspective to learn more about its operational and working aspects [68,133,200]. Here we used linear and non-linear forms of pseudo-first-order (PFO) and the PSO model, to characterize the adsorption kinetic processes mentioned in chapter 2 [28,134]. The kinetic investigation was conducted at 40 ppm of initial fluoride concentration (**Figure 5.2**b). The kinetic study was conducted at neutral pH using 10 mg of material in 10 mL of a fluoride solution. The correlation coefficient (R^2) obtained from the non-linear fit for the PSO model is 0.99 and the calculated AC (Q_{cal}) by this model is adjacent to the equilibrium AC obtained experimentally. The found rate constants for PFO and PSO kinetic models are k_1=0.113 min^{-1} and k_2=21.23 g $mg^{-1}min^{-1}$, respectively.

5.3.3. Effect of Bed Height

An adsorbate solution with a fluoride content of 40 mg/L, pH 6.5, and a flow rate of 0.3 ml/min was circulated through the adsorption column while the bed height was changed to examine the variation in bed depth on the breakthrough curve. **Figure 5.2**c illustrates the breakthrough curve performance at bed heights of 30 cm, 35 cm, and 40 cm. As the height of the bed increased, the saturation time of the bed and throughput volume also increased, likely because of an extended contact time with the adsorbent. A comparatively lesser contact time resulted

in a faster exhaustion of the adsorbent. The treated volume ranged from 0.522 to 0.774 L, once the height of the bed increased from 30 to 40 cm, respectively. Likewise, fluoride uptakes and total fluoride adsorbed quantity have increased with the column height. This may be attributed to the enhanced adsorbent surface area, providing additional active spots for adsorption. Furthermore, the breakthrough time also improved with the rise in packing height. The characteristic 'S' shape profile of the breakthrough curve was accompanied by adsorbates of smaller diameter and simpler structure. Increasing the bed height (30 cm, 35 cm, and 40 cm) led to an increase in both breakthrough time (t_b; 900, 1200, and 1560 min) and saturation time (t_e; 1740, 2160, and 2580 min). The results indicate that the higher values of t_b and t_e are favourable for column performance. The data also suggest that beds with greater depth take longer to saturate compared to shallower beds, causing the breakthrough curves to shift further from the origin. Additionally, with increasing bed height, the breakthrough curve exhibits a more pronounced bending nature, contributing to the broadening of the mass transfer zone. **Table 5.1** illustrates that the AC of Ce@Fe1:1/PS varies from 3.8 to 4.2 mg/g as the bed height increases from 30 cm to 45 cm. The greater bed height results in a higher quantity of adsorbent, providing more binding spots, which explains the observed variation in adsorption capacity. This also leads to an increase in the removal percentages of adsorbate (**Table 5.1**), indicating that the height of the bed significantly affects the adsorption of adsorbate in the FBAC. Furthermore, the increased bed height allows for extended contact time for fluoride ion capture, resulting in the observed increases in t_b and t_e. Similar findings have been reported by other researchers [201,202].

5.3.4. Effect of flow rate

To assess the influence of flow rate on the breakthrough curve, we employed varying flow rates of 0.3, 0.5, and 0.7 mL/min for FBAC experiments. The initial concentrations of the adsorbate,

the pH of the solution, and the height of the bed were kept constant at 40 mg/L, 6.5, and 40 cm, respectively. **Figure 5.2**d illustrates the flow rate effect on the breakthrough curve under the specified operational parameters. The optimal uptake capacity for flow rates of 0.3, 0.5, and 0.7 mL/min was 4.2, 3.8, and 3.6 mg/g, respectively. The graph demonstrates that lower flow rates lead to higher adsorption efficiency. This can be described by the slower diffusion process at higher flow rates, which necessitates a longer contact time for the effective binding of the fluoride to the adsorbent. Put simply, the solute spends insufficient time within the column at higher flow rates to achieve adsorption equilibrium, causing the fluoride solution to exit the column before equilibrium is established. The findings demonstrated that the saturation of the adsorbent was rapid at higher flow rates, which in turn decreased the fluoride uptake. It can be observed from the figure that the saturation occurred after 2580, 2100, and 1680 min for flow rates of 0.3, 0.5, and 0.7 mL/min, respectively.

5.3.5. Effect of fluoride concentration

Column studies were done to examine the influence of fluoride concentration at the inlet from 40 to 60 mg/L on the performance of the breakthrough curve. Parameters such as bed height, flow rate, and pH were maintained constant at 40 cm, 0.3 ml/min, and 6.5 during these experiments, respectively. As the inlet fluoride concentration increase (40, 50, and 60 mg/L), the breakthrough time decrease (1560, 1040, and 780 min). This was because the active spots turned out to be saturated more rapidly due to the higher concentration of fluoride ions competing for adsorbent sites. However, the fluoride removal percentage decreased with the rise in fluoride concentration. This suggests that at higher fluoride concentrations, the AC of the adsorbent might be reaching its limit, resulting in a lower percentage of fluoride removal compared to lower concentrations. As the fluoride concentration at the inlet rose from 40 to 60 mg/L, the fluoride AC showed an increase from 4.2 mg/g to 4.4 mg/g, respectively. The AC of

the adsorbent increased, which could be attributed to the higher driving force provided by the elevated inlet fluoride concentration, enabling a faster mass transfer rate. **Figure 5.2**e illustrates that at low fluoride concentrations at the inlet, the breakthrough happened later, and the adsorbent surface was saturated with fluoride after a longer period. Reversely, at higher fluoride concentrations, the breakthrough occurred more quickly, resulting in a decreased saturation time of the adsorbent. The breakthrough curves were flatter at lower fluoride concentrations at the inlet, representing a film-controlled process and a relatively wide MTZ. Whereas, the breakthrough curves were sharper at higher inlet fluoride concentrations, suggesting an intra-particle diffusion-controlled process and a relatively smaller MTZ. Similar trends were also observed by other researchers concerning metal ion adsorption [202]**.**

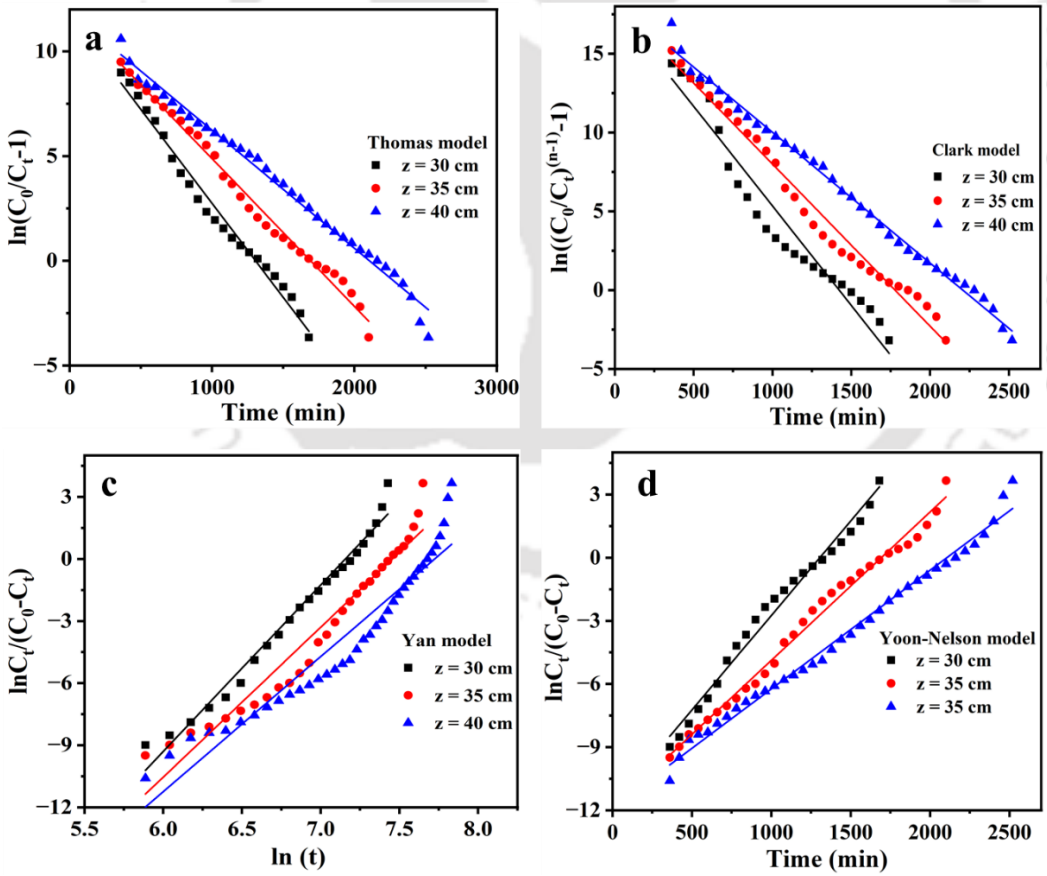

Figure 5.3. Effect of bed depth (a) Thomas model, (b) Clark model, (c) Yan model, and (d) Yoon-Nelson model fitting.

Table 5.2. Specifications of the packed-bed study.

Z (cm)	**Q (mL/min)**	**C_0 (mg/L)**	**Thomas model**			**Clark model**			**Yan model**				**Yoon-Nelson model**		
			K_{th}	**Q_e**	**R^2**	**r**	**A**	**R^2**	**a**	**b**	**Q_e**	**R^2**	**K_{yn}**	**τ**	**R^2**
30	0.3	40	0.00022	3.4	0.99	0.00106	63687572	0.99	8.0	0.38	3.4	0.98	0.0089	1305.7	0.98
35	0.3	40	0.00018	3.8	0.98	0.00127	86012225.4	0.96	7.2	0.51	3.9	0.95	0.0071	1690.8	0.97
40	**0.3**	**40**	**0.00014**	**4.2**	**0.96**	**0.00829**	**88410385.2**	**0.94**	**6.5**	**0.67**	**4.5**	**0.92**	**0.0056**	**2105.3**	**0.94**
40	**0.5**	40	0.00015	4	0.99	0.0030	2185904	0.96	5.5	0.80	4.3	0.94	0.0060	1595.1	0.99
40	**0.7**	40	0.00017	3.7	0.97	0.0008	286963.4	0.94	5.0	0.79	4.1	0.94	0.0070	1175.4	0.97
40	0.3	**50**	0.00013	4.23	0.98	0.00975	91640743	0.96	6.5	0.52	4.6	0.96	0.0068	1683.60	0.97
40	0.5	**60**	0.00012	4.3	0.96	0.01022	97538392	0.94	7.2	0.41	4.7	0.94	0.0076	1369.68	0.94

5.3.6. Column performance indicator

The breakthrough curves are an important factor in the designing of a FBAC. To achieve a successful design of a FBAC, two key aspects need to be predicted: (1) the concentration-time profile of the outlet flow and (2) the maximum AC of the material used for adsorption. There are several mathematical models available to describe and model fixed-bed adsorption processes. In this context, breakthrough curves obtained at different bed heights (Z), flow rates (Q), and concentrations were analyzed using these mathematical models: Thomas, Yoon-Nelson, Clark, and Yan Model models. Each of these models provides valuable insights into the behavior and efficiency of the adsorption process in the packed-bed column. Furthermore, the BDST model has been used to predict the correlation with the data obtained from FBAC experiments.

Thomas model was utilized in the data obtained from the FBAC studies to examine the breakthrough behaviour of fluoride on Ce@Fe1:1/PS. To determine the kinetic coefficients, the Thomas model was used to interpret the data by transforming the concentration values (C_t) to ln $[C_0/C_t - 1]$ versus time. Linear regression was then accomplished on each set of transformed data to obtain the slope and intercept. The assessed values of K_{th} and q_0 under various process parameters are provided in **Table 5.2**. The R^2 value obtained in the range of 0.96 to 0.99 from linear fitting of the Thomas model, gives the best correlation to the experimental data (**Figures 5.3**a**, 5.4**a**, and 5.5**a). Therefore, it can be concluded that the Thomas model effectively represents the uptake of fluoride on Ce@Fe1:1/PS in FBAC. The AC (q_0) of the column increases as the bed height (Z) rises, likely because of the greater mass driving force resulting from the higher bed height. Conversely, the K_{th} decreases with an increase in Z, possibly due to increased flow resistance, which hampers mass transfer [187]. The value of q_0 decreases with an increase in flow rate (Q), possibly because of the fixed

number of active sites and inadequate contact time between the adsorbate (F^-) and the Ce@Fe1:1/PS. Whereas, Q_0 increases with a rise in the fluoride concentration (C_0) at the inlet, that is because of the enhancement in the concentration gradient [189] The maximum fluoride uptake capacity (Q_0) of Ce@Fe1:1/PS, determined through the Thomas model fitting to the data obtained from column studies, which has been compared with reports available in the literature (**Table 5.6**). The results demonstrate that the Q_0 of Ce@Fe1:1/PS is competitive and efficient compared to other adsorbents.

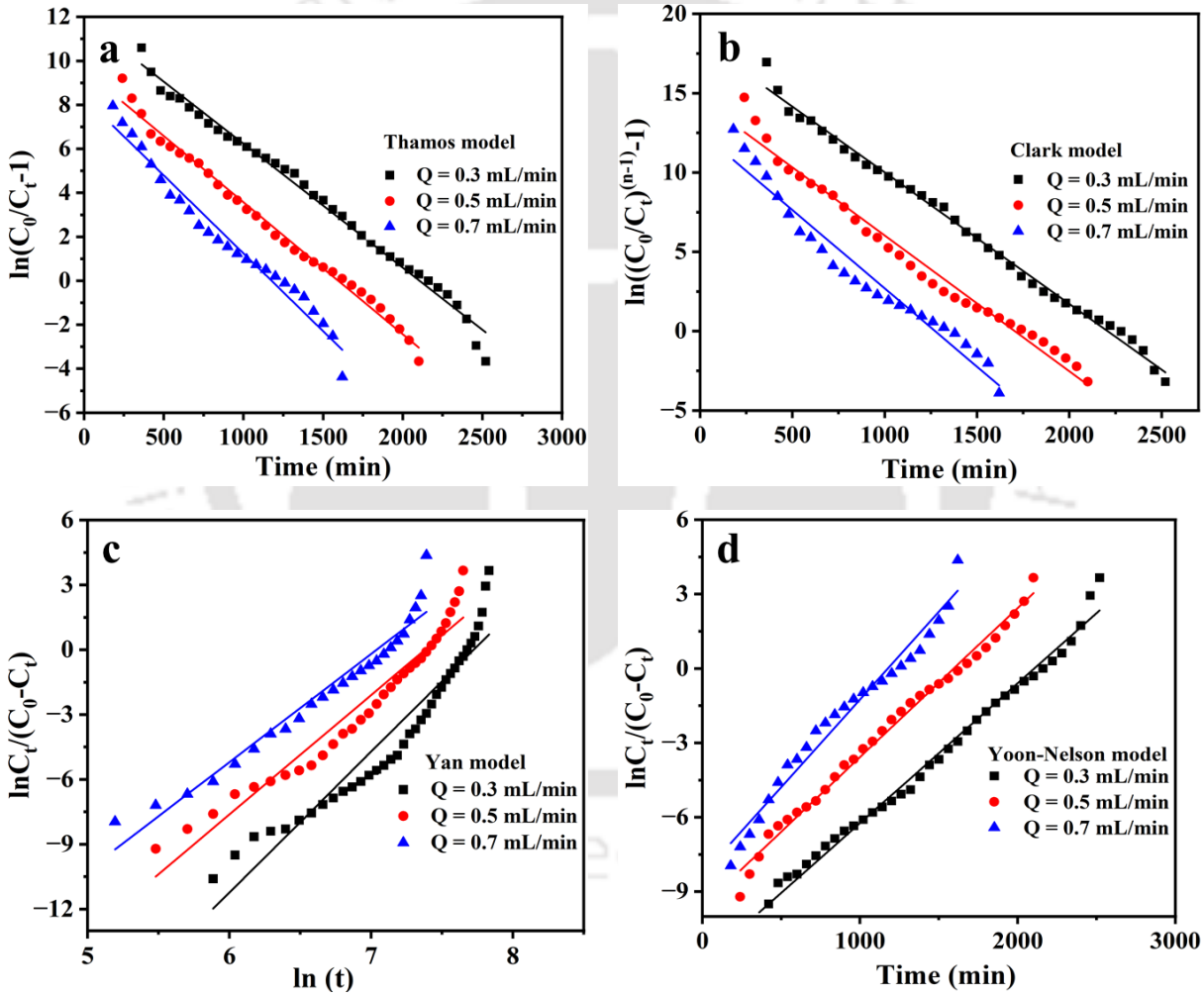

Figure 5.4. Effect of flow rate (a) Thomas model, (b) Clark model, (c) Yan model, and (d) Yoon-Nelson model fitting.

The outcomes of the Clark linear model of the breakthrough curves are depicted in **Figures 5.3**b**, 5.4**b**, and 5.5**b. The Clark parameters A and r determined under various conditions, including changes in inlet flow rate, bed height, and initial concentration of fluoride, are listed in **Table 5.2**. These values are assessed from the data obtained from the intercept and slope of the linearized Clark model. The model has been investigated with the value of the Freundlich constant (n=2.6) obtained from the batch study. The high correlation coefficients ($R^2 > 0.94$) for the breakthrough curves fitting to the Clark models show a decent fit, suggesting that the data obtained from the column study also adhere to the Clark model. An increase in adsorbent fluoride concentration (C_0) in the influent and bed height (Z) leads to higher r and A values. Conversely, a rise in feed flow rate results in lower values of r and A. This parallel variation in r and A is also consistent with findings from other researchers [185].

The experimental breakthrough curve for various factors affecting performance is illustrated in **Figure 5.3**c**, 5.4**c**,** and **5.5**c using the linear Yan model. The degree of correlation between the data obtained from FBAC experiments and the Yan model is indicated by the correlation coefficient values ($R^2 > 0.92$). **Table 5.2** demonstrates corresponding fitting parameters and also shows that the values of AC obtained from the Yan model and Thomas model are almost similar.

The Yoon-Nelson model was used to examine the breakthrough characteristic of fluoride onto Ce@Fe1:1/PS in a FBAC (**Figures 5.3**d**, 5.4**d**, and 5.5**d). The linear plots of ln $[C_t/(C_0 - C_t)]$ over time (t) were used to establish the model parameters K_{yn} (rate constant) and τ at different variables such as flow rate, initial fluoride concentration, and bed height. The model parameter τ represents the treatment time taken by the adsorbent to reach effluent fluoride concentration half of its initial concentration ($0.5C_0$). It is evident from the R^2 (0.94-0.98) that there is a strong association between the Yoon-Nelson model and the experimental data (**Table 5.2)**. The fitting

parameters of the Yoon-Nelson model suggest that a rise in influent concentration leads to an upsurge in the K_{yn} value and a decrease in the τ value. This is possible because of the rapid exhaustion of the Ce@Fe1:1/PS beads in the FBAC. Conversely, an increase in the height of the bed consequences in a reduction of the K_{yn} value and an increase in the τ value owing to the greater amount of Ce@Fe1:1/PS beads. Additionally, as the bed height (Z) rises, K_{yn} decreases, and τ increases. Similar results have been observed by other researchers [197].

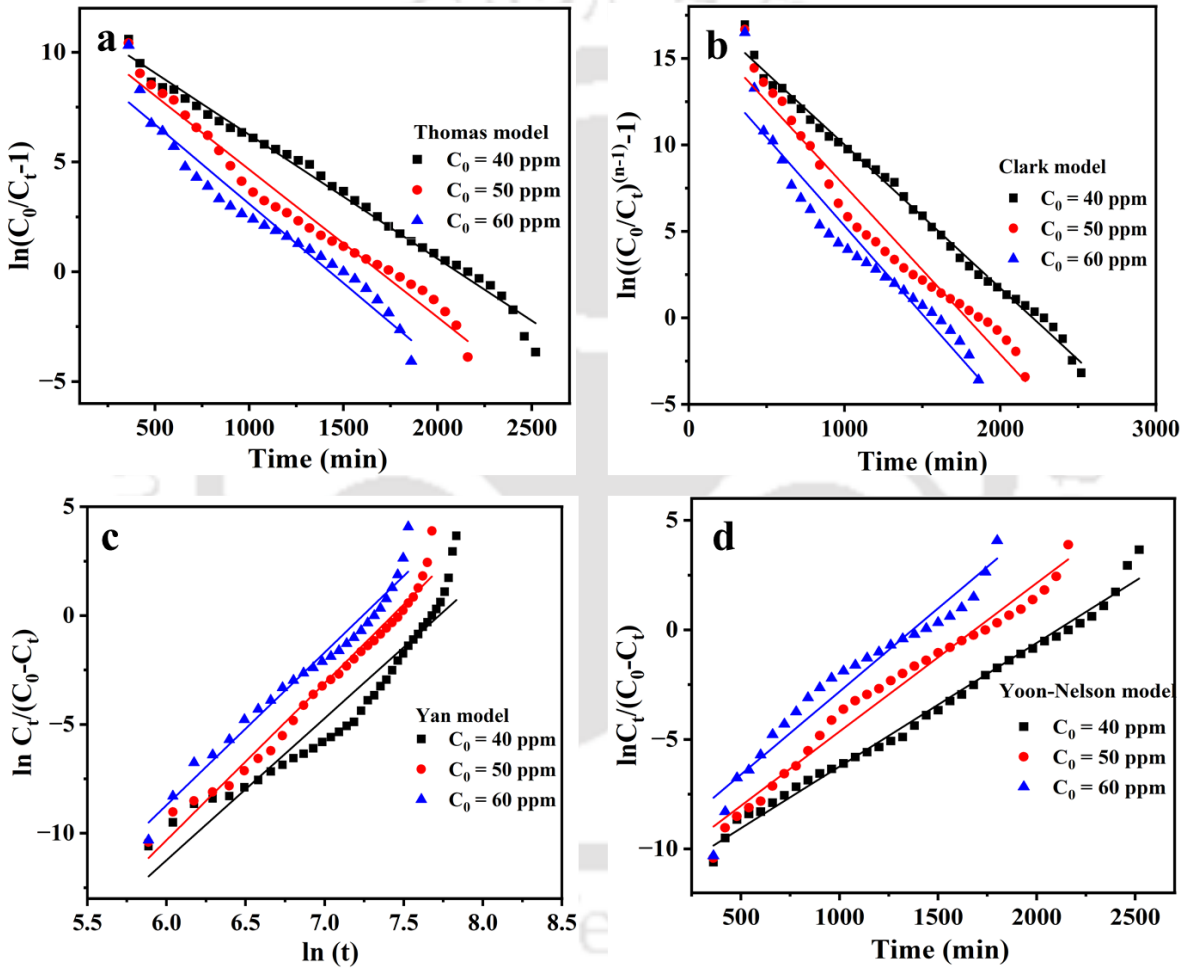

Figure 5.5. Effect of fluoride inlet concentration on adsorption of fluoride on Ce@Fe1:1/PS a) Thomas model, (b) Clark model, (c) Yan model, and (d) Yoon-Nelson model fitting.

The BDST model was employed to analyse the data obtained from FBAC studies for a better understanding of the behaviour of the breakthrough curve. The goal was to evaluate the BDST

characteristic parameters K_{BDST} and N_0 from the model. Linear relationships between the variation of service time and column bed heights of 30, 35, and 40 cm were observed for 5%, 10%, 30%, and 80% saturation. The flow rate of feed was 0.3 mL/min with the initial concentration of fluoride 40 mg/L (**Figure 5.6**a). The calculated values of K_{BDST} and N_0 are presented in **Table 5.3**. The value of R^2=0.99 or higher is generally considered very high and often indicates an excellent fit of the experimental data to the BDST. The BDST model provides a comprehensive and straightforward method for assessing adsorption column tests [197]. Additionally, the BDST model suggests the certainty of the service time of FBAC. The K_{BDST} values indicate the rate of mass transfer from the fluid to the solid phase. Furthermore, as depicted in **Figure 5.6**a, the increase in bed height corresponds to an extended service time for the FBAC. This is attributed to the higher amount of Ce@Fe1:1/PS in the FBAC, consequential in an improvement of the service time.

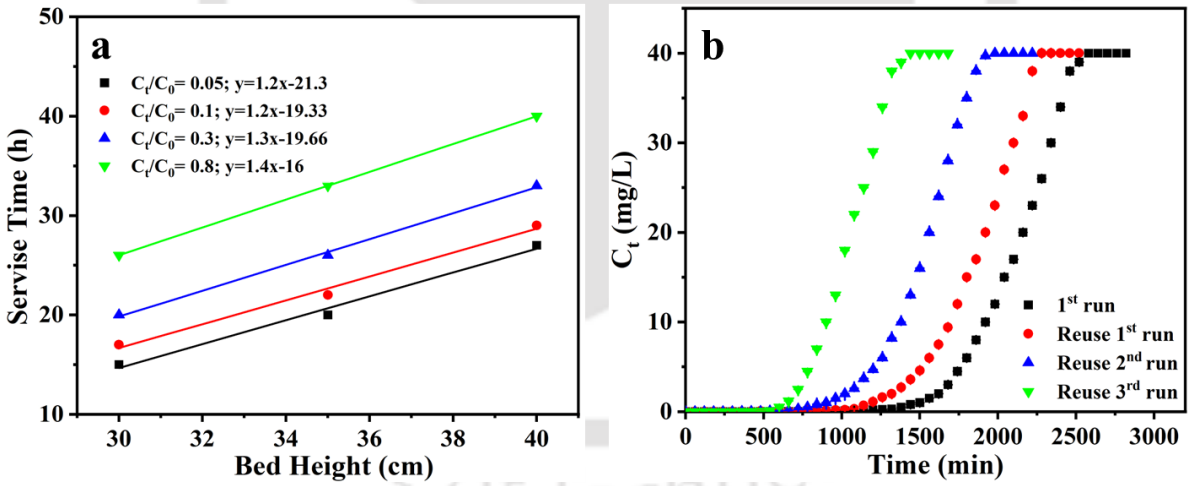

Figure 5.6. (a) BDST model fitting at various bed heights and (b) Reusability study of Ce@Fe1:1/PS adsorbent.

Table 5.3. Parameters of BDST model for adsorption of fluoride on Ce@Fe1:1/PS at the diverse range of bed height and saturation percent.

BDST parameters	5%	10%	30%	80%
N_0	45.6	45.6	49.4	53.2
K_{BDST}	0.10	0.11	0.11	0.13
R^2	0.99	0.99	0.99	1

5.3.7. Adsorbent regeneration and reusability of Ce@Fe1:1/PS in FBAC

The economic feasibility of the Ce@Fe1:1/PS is evaluated based on its reusability. Sodium hydroxide serves as a source of free OH^- when dissolved in its aqueous solution. Numerous studies have reported the use of NaOH solution as a desorption component for adsorbents loaded with F^- ions [203]. This is attributed to the similar isoelectric nature and size of OH^- and fluoride ions, which facilitates the replacement of fluoride ions with hydroxyl ions [204]. Therefore, the fluoride-loaded Ce@Fe1:1/PS adsorbent in the column was attempted to be regenerated using a 0.1M NaOH solution in this study. The study was examined with an exhausted bed having a bed height of 40 cm. This was done under fixed operating conditions, including a fluoride concentration of 40 mg/L, a pH of 6.5, and a flow rate of 0.3 mL/min. After regeneration, deionized water flowed through the FBAC to eliminate any traces of NaOH. This procedure persisted until a noticeable decrease in the alkalinity of the effluent was observed. An additional decrease in the alkalinity of the Ce@Fe1:1/PS adsorbent was achieved by introducing a dilute 0.1 M sulfuric acid solution at a flow rate of 0.3 mL/min to maintain a pH of around 7.5 ± 0.2. Deionized water was once more circulated over the column to confirm the effective elimination of chemicals from the Ce@Fe1:1/PS, persisting until the effluent attained a pH near 7. After completing these steps, the same methodology of regenerating and reusing the Ce@Fe1:1/PS MOF was replicated until a noteworthy drop in the breakthrough time (t_b) and exhaustion time (t_e) was observed. The reusability study of the Ce@Fe1:1/PS beads is presented in **Figure 5.6**b. The adsorbent Ce@Fe1:1/PS was able to remove 81.8% of

fluoride at the beginning of the reusability tests. As the reusability cycles increased consecutively 1st, 2nd, and 3rd, the fluoride removal percentages dropped by 2.6, 9.5, and 13.8 %. The reduction in exhaustion times (t_e) of column operation for the 0th, 1st, 2nd, and 3rd cycles are 2580 min, 2280 min, 1920 min, and 1440 min, respectively. This shift in breakthrough curves to the left (**Figure 5.6**b) is attributed to the gradual decrease of active spots of Ce@Fe1:1/PS with the progression of reusability operations. Additionally, the fluoride removal rates for the 0th to 3rd cycles of reuse have decreased from 81.8% to 55.9% (**Table 5.4**).

Table 5.4. Regeneration of Ce@Fe1:1/PS post fluoride adsorption.

Cycle	%R	Q_e (mg/g)	V_{eff} (L)
0th	81.8	4.2	0.774
1st	79.2	3.6	0.684
2nd	69.7	2.6	0.576
3rd	55.9	1.6	0.432

5.4. Fluoride adsorption mechanism

Achieving adsorption equilibrium between the solute in a liquid medium and the solid adsorbent within a FBAC is commonly affected by several factors. These factors encompass axial dispersion, resistance resulting from intra-particle diffusion (which includes both surface and pore diffusion), as well as film resistance. The process can be understood by the subsequent adsorption stages [205]:

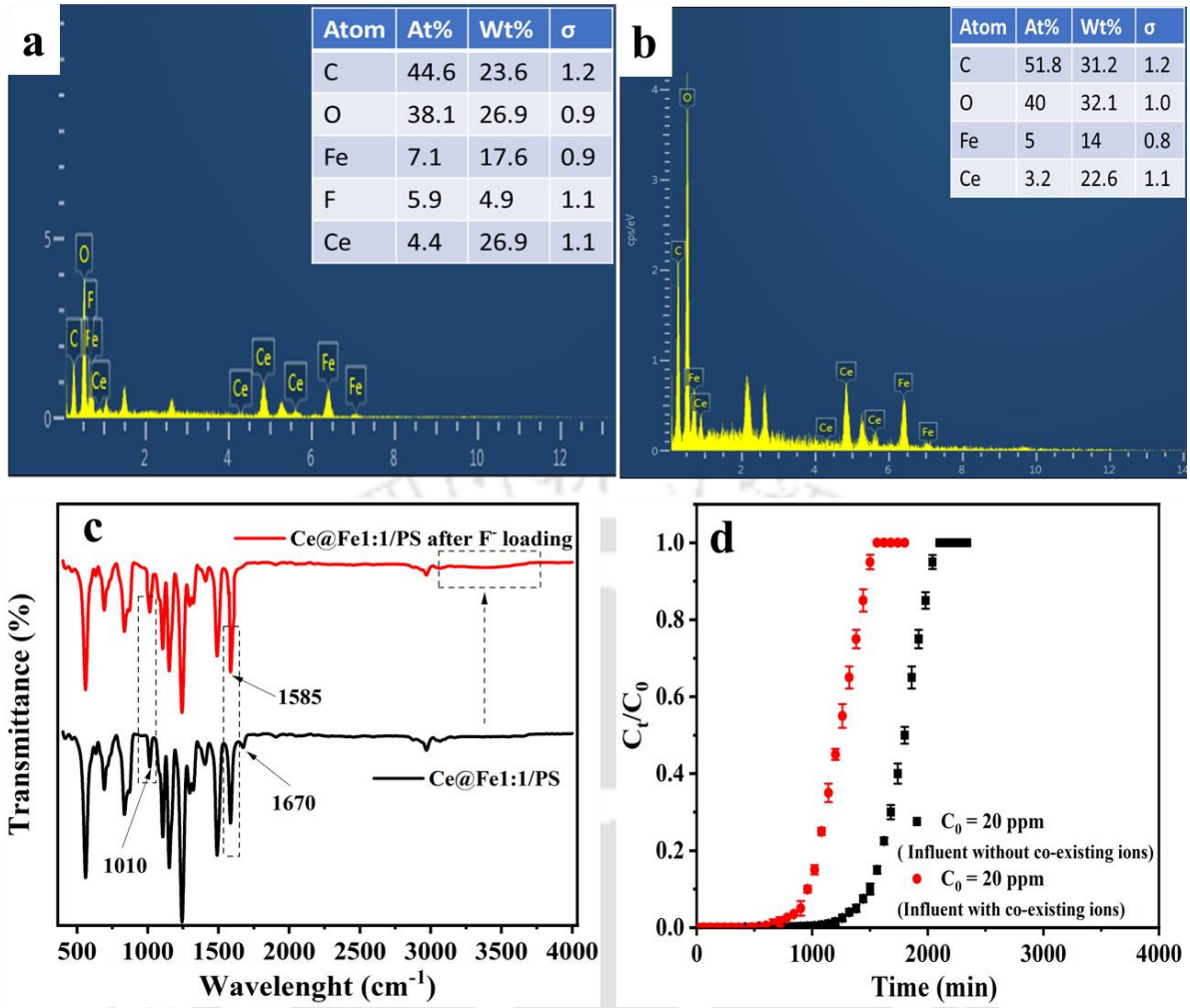

Figure 5.7. (a) EDX analysis of Ce@Fe1:1/PS before fluoride adsorption, (b) EDX analysis after column run with fluoride solution, (c) FTIR analysis of Ce@Fe1:1/PS with and without fluoride loading, and (d) Effect of co-existing ions.

(i) Transport to immobile layer: Initially, fluoride ions are conveyed from the bulk phase into a stagnant layer of ions adjacent to the Ce@Fe1:1/PS. This transport can occur through either advective transport or axial dispersion towards the Ce@Fe1:1/PS.

(ii) Penetration to Ce@Fe1:1/PS surface: Subsequently, fluoride ions can penetrate through the previously mentioned immobile layer, reaching the surface sites of the adsorbent.

(iii) Adsorption binding: The adsorption process involves the binding of fluoride ions to specific sites on the Ce@Fe1:1/PS surface.

(iv) Intraparticle diffusion: F^- ions can also diffuse into the pores of the Ce@Fe1:1/PS through intraparticle diffusion, contributing to the overall equilibrium attainment.

These stages collectively contribute to the overall adsorption process and equilibrium between the adsorbate and the adsorbent within the FBAC. The rate at which Ce@Fe1:1/PS removes fluoride is influenced by one or more of the phenomena commonly reported. In batch adsorption studies, stages 1 and 2 can often be overlooked due to the vigorous stirring of the adsorbent. However, in FBAC studies, both stages 1 and 2 become relevant, particularly for columns with greater bed heights. The binding of F^- ions to metal can occur through electrostatic interactions, pore diffusion, and hydrogen bonding.

In the EDX spectrum of the adsorbent, there are notable peaks corresponding to carbon (C), iron (Fe), cerium (Ce), and oxygen (O) (**Figure 5.7**a). The appearance of a peak of fluoride (F) after scanning the Ce@Fe1:1/PS after water treatment, confirms the fluoride ions adsorption by the Ce@Fe1:1/PS adsorbent (**Figure 5.7**b).

The FT-IR spectrum of Ce@Fe1:1/PS reveals distinct peaks including C-O, O-H, C=O, and C-H, groups [205]. The O-H stretching peak is observed in the range 3400-3380 cm^{-1}, attributable to both free -OH and M-OH groups existing at the surface of Ce@Fe1:1/PS. Another peak at 1670 cm^{-1} corresponds to C=C stretching [198]. Furthermore, peaks in the 550-750 cm^{-1} region correspond to M-O bonds, where M represents the metal ions [184]. The FTIR analysis also provides insights into the adsorption mechanism of fluoride onto Ce@Fe1:1/PS, revealing the involvement of functional groups present on the adsorbent's surface (**Figure 5.7**c). The process of fluoride adsorption is governed by a combination of electron donor-acceptor attraction, hydrogen bonding, and π-π interactions between the fluoride ion and the adsorbent. Moreover,

a comparison of FTIR spectra before and post-fluoride uptake reveals the development of hydrogen bridges among the fluoride and Ce@Fe1:1/PS. This interaction is responsible for the increased intensity of -OH groups (3400-3380 cm^{-1}) observed in the FTIR spectrum. These findings collectively shed light on the intricate molecular interactions that underlie the fluoride adsorption process onto Ce@Fe1:1/PS. A peak at 1670 cm^{-1} in the Ce@Fe1:1/PS, diminished post-adsorption of fluoride, shows the involvement of the C=C group. The results suggest that the electron donor-acceptor mechanism plays a significant role, wherein functional groups having oxygen on the surface of the adsorbent behave as electron donors to fluoride [206]. This interaction is highlighted by the heightened intensity of the C-O band (1010±2 cm^{-1}) observed in the FTIR spectrum post-fluoride loading, a phenomenon also supported by previous studies. Furthermore, the intensified C-C vibrations stretching (1585± 2 cm^{-1}) indicate the occurrence of π-π interactions. Furthermore, the peak intensities of M-O at 561 and 690 cm^{-1} are reduced post-fluoride loading [207]. The observed changes in the FT-IR spectra are indicative of adsorbate interacting with the metal ions, as the M-F binding that typically occurs in the far IR regions is not detectable by the FT-IR spectrophotometer [208].

The breakthrough curve exhibits a steep initial rise, indicating rapid fluoride adsorption before the breakthrough, which is attributed to the accessibility of active spots (**Figure 5.8**). As F^- ions are attached to the adsorbent available in the bottom layer of the column, the adsorption kinetics gradually reduces owing to a reduction in the accessibility of active spots (**Figure 5.8**). Subsequently the breakthrough point, adsorption of fluoride may involve both pore diffusion and physisorption. The adsorption process at this point is mainly governed by mass transfer including the diffusion of fluoride ions into the pores. This is reflected in the lower rate constant values found from breakthrough curves fitting in the column models (**Table 5.2**).

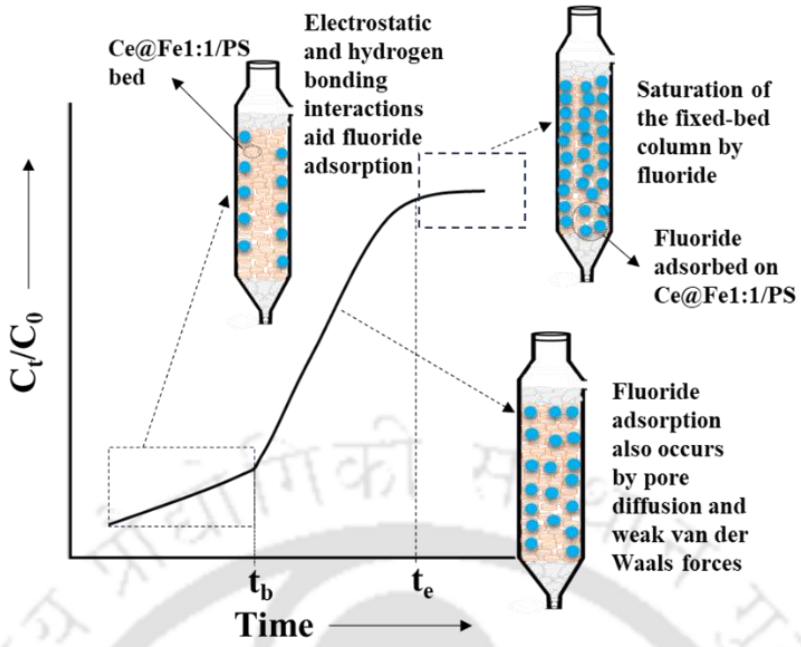

Figure 5.8. Mechanism of fluoride adsorption by FBAD of Ce@Fe1:1/PS Beads.

5.5. Practical Applicability of Ce@Fe1:1/PS for Water Treatment

The Ce@Fe1:1/PS exhibits notable selectivity towards fluoride. The practical applicability of the fixed-bed column containing Ce@Fe1:1/PS is tested by introducing a continuous feed collected from the Brahmaputra River of Assam, India. The feed was synthesized to make 20 mg L^{-1} fluoride in the first run and the second run 100 mg L^{-1} of co-existing ions including, bicarbonates, phosphates, chlorides, nitrates, and sulphates. The feed is introduced into a 40 cm bed height column at a flow rate of 0.30 mL min^{-1}. The results indicate that the feed containing no interfering ions has a longer duration of exhaustion (**Figure 5.7**d). However, a minor reduction in the treated effluent volume, saturation time (t_e), and column breakthrough time (t_b) are detected in the presence of co-existing ions. The results indicate that the presence of different co-existing ions influences the column performance, t_b is reduced to 960 min from 1440, when compared to the influent without co-existing ions. Similarly, the corresponding t_e is reduced to 1560 from 2100 min (**Table 5.5**). Additionally, the fluoride removal efficiency

of the Ce@Fe1:1/PS slightly diminishes by approximately 6% by using a simulated solution containing interfering ions compared to a fed without co-existing ions. Typically, these competing ions opt for adsorbent sites, leading to a decrease in fluoride removal efficiency.

Table 5.5. Parameters of FBAC studies for fluoride adsorption using Ce@Fe1:1/PS beads in the presence of interfering ions.

Influent	t_b	t_e	V_{eff}	M_{in}	M_{out}	M_{ads}	**%R**	Q_{eq}
without co-existing ions	1440	2100	0.63	12.6	2.02	10.6	83.9	1.763
with co-existing ions	960	1560	0.468	9.36	2.04	7.3	78.1	1.219

5.6. Comparative evaluation of adsorbents in FBAC research

Recently, the use of Metal-Organic Frameworks (MOFs) for adsorption has gained prominence as a powerful method for removing harmful chemicals and undesirable ions from water. MOFs are characterized by their diverse structures, expansive surface areas, numerous active metal sites, and substantial pore volumes. In this context, we synthesized novel bimetallic MOFs, specifically Ce@Fe1:1. These bimetallic MOFs were then utilized to create beads through the incorporation of polysulfone. These beads were designed to efficiently remove fluoride from water. The efficiency of these beads was then compared with other adsorbents employed in column studies, as outlined in existing literature (**Table 5.6**).

Table 5.6. Adsorbents Reported in Literature for FBAC Studies.

Material	**pH**	**t_e (h)**	**C_0 (mg/mL)**	**Q (mL/min)**	**Z (cm)**	**Q_e (mg/g)**	**Ref.**
SAA	6.5	14.5	40	1.5	2.5	6	[197]
PCZH	6.5	79	10	1	4	25.6	[205]

PZH	6.5	135	10	1	4	38.1	[205]
PFZH	6.5	56	10	1	4	13.7	[205]
okra stems biochar	2	NA	5	4	8	6	[109]
magnesia-pullulan	4	NA	10	16	20	16.6	[209]
rGO/ZrO2	7	84	25	1.6	7.5	45.7	[196]
kanuma mud	5-7	80	20	5	10	1.5	[186]
Ce@Fe1:1/PS	**6.5**	**43**	**40**	**0.3**	**40**	**4.2**	**This work**

5.7. Conclusions

The research article focuses on the removal of fluoride ions from wastewater using a FBAC with Ce@Fe1:1/PS as the adsorbent. The study employs various characterization techniques such as Scanning Electron Microscopy (SEM), Energy Dispersive X-ray Spectroscopy (EDX), Brunauer–Emmett–Teller (BET) analysis, Fourier Transform Infrared Spectroscopy (FTIR), and X-ray Diffraction (XRD) to analyze the morphology of Ce@Fe1:1/PS and to confirm the capture of fluoride by Ce@Fe1:1/PS. The experimental design investigates the impact of different parameters on the FBAC process, including fluoride concentration in the influent, flow rate of feed, and bed height of adsorbent. The percentage of fluoride removal, exhaustion time (t_e), and breakthrough time (t_b) are key indicators of the system's performance. The findings suggest that increasing the height of the bed in the column significantly improves fluoride removal percentages, exhaustion time, and breakthrough time. Conversely, an increase in flow rate and fluoride concentration in the influent leads to a reduction in breakthrough time, exhaustion time, and fluoride removal percentage. The optimal performance of the FBAC system is reported at specific conditions: a fluoride concentration of 40 mg/L, a flow rate of 0.3 mL/min, and an adsorbent bed height of 40 cm. Under these conditions, the breakthrough time is 1560 minutes, exhaustion time is 2580 minutes, and fluoride removal is 81.8%. To

further understand the experimental results, the study employs mathematical models such as the Thomas model, Yoon-Nelson model, Clark model, and Yan model to analyze breakthrough curves and kinetics. In summary, the research provides insights into the effectiveness of Ce@Fe1:1/PS in removing fluoride from wastewater using a Fixed Bed Adsorption Column, emphasizing the importance of various operational parameters in optimizing the system's performance.

CHAPTER 6

Conclusions and Recommendations for Future Work

CHAPTER 6

A glance of previous chapters are reviewed in this chapter. The salient features and major findings that arise from this thesis work with the key outcome of all the experiments have been highlighted. Significant characteristics of all the synthesized materials, their application towards the removal of fluoride from water have been summarized in this chapter. The future line of research is also included in this chapter.

6.1. Major conclusions

The major conclusions of the thesis are summarized below:

- In conclusion, the utilization of ultrasound in both the synthesis of adsorbents and the adsorption study proved to be advantageous, enhancing molecular interactions and shortening diffusion paths. The sonochemical method, compared to the conventional method, demonstrated increased kinetics, reaching equilibrium within 20 minutes and showing 80% fluoride removal in just 5 minutes using AC/Ce/Fe-1. The adsorption kinetics aligned well with the PSO model, and the as-synthesized adsorbent exhibited a maximum capacity of 52.3 mg/g within 20 minutes at 25 °C. AC/Ce/Fe–1 maintained high adsorption efficiency over multiple cycles, and thermodynamic data indicated a spontaneous exothermic reaction with reduced randomness at the adsorbent-solution interface. The study suggests that sonochemical methods increase the active sites on the interior of the adsorbent, offering a rapid and efficient fluoride removal process with potential for practical applications at a relatively low cost.

- The subsequent research focused on Ce-based MOFs for fluoride removal, showcasing remarkable efficiency. The Ce–Fu MOF exhibited a maximum adsorption capacity of 64.16 mg·g−1 with good water stability and quick sorption kinetics. The adsorbent removed 85%

of fluoride ions within 10 minutes and achieved maximum adsorption capacity in 30 minutes across a wide pH range. The adsorption kinetics conformed to the PSO model, and thermodynamic measurements indicated an exothermic and spontaneous reaction with reduced randomness at the adsorbent-solution interface. Co-existing anions interfered to varying degrees, but the adsorbent sustained high efficiency over multiple cycles. The study suggested a future application of Ce-based porous frameworks for water purification, emphasizing their stability and efficiency in removing fluoride.

- A further study looked into innovative nanoporous bimetal MOFs, such as Ce@Fe1:1, Ce@Al1:1, and Ce@La1:1, which showed quick sorption kinetics and high fluoride absorption capabilities. Following the PSO kinetic model, these materials removed fluoride efficiently in 30 minutes across a wide pH range. The synthesized MOFs were stable in a wide pH range and exhibited varied hydrophilic properties. Over numerous cycles, the adsorbents maintained high efficiency, and the process was discovered to be exothermic and spontaneous at the adsorbent-solution interface. The study emphasized the potential application of these bimetal MOFs for fluoride removal, offering useful insights for further research in this field.

- In the final investigation, FBAC with bimetallic MOFs Ce@Fe1:1 having highest adsorption capacity all over the study (Table 6.1) has been matrixed with polysulfone to make beads Ce@Fe1:1/PS in order to eliminate fluoride from water.

Table 6.1 A comparative account on the fluoride removal performance by the as-synthesised adsorbents conducted under this research study.

Adsorbents	**Equilibrium time (min)**	**pH**	**Adsorption capacity(mg/g)**
AC/Ce/Fe-1	30	6.5	52.3

Ce-Fu MOF	30	6.5	64.2
Ce@La1:1	30	6.5	90.9
Ce@Al1:1	30	6.5	94.3
Ce@Fe1:1	30	6.5	101.3

To improve system performance, several factors such as fluoride concentration, flow rate, and bed height were studied. Increasing the bed height enhanced fluoride removal percentages, breakthrough time, and exhaustion time greatly, but increasing flow rates and fluoride concentrations had the reverse effect. The ideal parameters for the FBAC system were discovered, resulting in a breakthrough time of 1560 minutes, an exhaustion time of 2580 minutes, and a fluoride removal rate of 81.8%. Breakthrough curves and kinetics were analyzed using mathematical models, revealing the effectiveness of Ce@Fe1:1/PS in fluoride removal. The study emphasizes the relevance of operational factors in optimizing FBAC system performance and provides useful information for practical use.

6.2. Recommendation for future work

Based on the current investigation's findings, the following recommendations for further research are made:

- Continuous packed-bed studies using real industrial wastewater to assess and optimise for commercial application.
- Estimation of kinetic, isotherm, and thermodynamic parameters in multi-pollutant system.
- To carry out a pilot scale column study to remove multi-contaminants effectively.
- Experiment with the synthesised adsorbents to remove additional unknown industrially relevant heavy metal ions, dyes, and other phenolic chemicals in batch and column mode.

- The desorption characteristics of synthesised adsorbents at different temperatures, as well as their reuse capacities with the intended pollutant.
- To make well-informed choices about the future deployment of these material, it is strongly advised to carry out a thorough economic evaluation. This evaluation will be crucial in assessing the appropriateness and practical uses of the developed MOFs.

REFERENCES

[1] C. FN, M. MF, Factors Affecting Water Pollution: A Review, J Ecosyst Ecography. 07 (2017). https://doi.org/10.4172/2157-7625.1000225.

[2] M.K. Jha, A. Shekhar, M.A. Jenifer, Assessing groundwater quality for drinking water supply using hybrid fuzzy-GIS-based water quality index, Water Res. 179 (2020) 115867. https://doi.org/10.1016/j.watres.2020.115867.

[3] N.M. Mourad, T. Sharshar, T. Elnimr, M.A. Mousa, Radioactivity and fluoride contamination derived from a phosphate fertilizer plant in Egypt, Applied Radiation and Isotopes. 67 (2009) 1259–1268. https://doi.org/10.1016/j.apradiso.2009.02.025.

[4] C.G. Daughton, Non-regulated water contaminants: emerging research, Environ Impact Assess Rev. 24 (2004) 711–732. https://doi.org/10.1016/J.EIAR.2004.06.003.

[5] R.P. Schwarzenbach, T. Egli, T.B. Hofstetter, U. Von Gunten, B. Wehrli, Global water pollution and human health, Annu Rev Environ Resour. 35 (2010) 109–136. https://doi.org/10.1146/annurev-environ-100809-125342.

[6] A. Gupta, M.R. Singh, WATER POLLUTION-SOURCES,EFFECTS AND CONTROL, n.d. https://www.researchgate.net/publication/321289637.

[7] A. Pawełczyk, Assessment of health risk associated with persistent organic pollutants in water, Environ Monit Assess. 185 (2013) 497–508. https://doi.org/10.1007/s10661-012-2570-8.

[8] M.F. Hanafi, N. Sapawe, A review on the current techniques and technologies of organic pollutants removal from water/wastewater, Mater Today Proc. 31 (2020) A158–A165. https://doi.org/10.1016/J.MATPR.2021.01.265.

[9] O.M.L. Alharbi, A.A. Basheer, R.A. Khattab, I. Ali, Health and environmental effects of persistent organic pollutants, J Mol Liq. 263 (2018) 442–453. https://doi.org/10.1016/J.MOLLIQ.2018.05.029.

[10] C. A. Martínez-Huitle, M. A. Rodrigo, I. Sirés, O. Scialdone, Single and Coupled Electrochemical Processes and Reactors for the Abatement of Organic Water Pollutants: A Critical Review, Chem Rev. 115 (2015) 13362–13407. https://doi.org/10.1021/acs.chemrev.5b00361.

[11] Y. Zhang, M. Yang, X. Huang, Arsenic(V) removal with a Ce(IV)-doped iron oxide adsorbent, Chemosphere. 51 (2003) 945–952. https://doi.org/10.1016/S0045-6535(02)00850-0.

[12] P.K. Jha, P. Tripathi, Arsenic and fluoride contamination in groundwater: A review of global scenarios with special reference to India, Groundw Sustain Dev. 13 (2021) 100576. https://doi.org/10.1016/J.GSD.2021.100576.

[13] Y. Yu, L. Yu, K.Y. Koh, C. Wang, J.P. Chen, Rare-earth metal based adsorbents for effective removal of arsenic from water: A critical review, Crit Rev Environ Sci Technol. 48 (2018) 1127–1164. https://doi.org/10.1080/10643389.2018.1514930.

[14] A. Farooqi, H. Masuda, N. Firdous, Toxic fluoride and arsenic contaminated groundwater in the Lahore and Kasur districts, Punjab, Pakistan and possible contaminant sources, Environmental Pollution. 145 (2007) 839–849. https://doi.org/10.1016/j.envpol.2006.05.007.

[15] E.E. Merodio-Morales, H.E. Reynel-Ávila, D.I. Mendoza-Castillo, C.J. Duran-Valle, A. Bonilla-Petriciolet, Lanthanum- and cerium-based functionalization of chars and activated carbons for the adsorption of fluoride and arsenic ions, International Journal of Environmental Science and Technology. 17 (2020) 115–128. https://doi.org/10.1007/s13762-019-02437-w.

[16] X. Dou, Y. Zhang, M. Yang, Y. Pei, X. Huang, T. Takayama, S. Kato, Occurrence of arsenic in groundwater in the suburbs of Beijing and its removal using an iron-cerium bimetal oxide adsorbent, Water Quality Research Journal of Canada. 41 (2006) 140–146. https://doi.org/10.2166/wqrj.2006.016.

[17] J. Goel, K. Kadirvelu, C. Rajagopal, V.K. Garg, Removal of lead(II) by adsorption using treated granular activated carbon: Batch and column studies, J Hazard Mater. 125 (2005) 211–220. https://doi.org/10.1016/J.JHAZMAT.2005.05.032.

[18] G.C. Chen, X.Q. Shan, Y.S. Wang, Z.G. Pei, X.E. Shen, B. Wen, G. Owens, Effects of copper, lead, and cadmium on the sorption and desorption of atrazine onto and from carbon nanotubes, Environ Sci Technol. 42 (2008) 8297–8302. https://doi.org/10.1021/es801376w.

[19] D.Q. Ng, S.W. Liu, Y.P. Lin, Lead as a legendary pollutant with emerging concern: Survey of lead in tap water in an old campus building using four sampling methods, Science of The Total Environment. 636 (2018) 1510–1516. https://doi.org/10.1016/J.SCITOTENV.2018.04.402.

[20] Q. Wang, Z. Yang, Industrial water pollution, water environment treatment, and health risks in China, Environmental Pollution. 218 (2016) 358–365. https://doi.org/10.1016/J.ENVPOL.2016.07.011.

[21] M. Haseena, Water pollution and human health., (n.d.). http://www.alliedacademies.org/environmental-risk-assessment-and-remediation/.

[22] G.S. Achary, Studies on Ground Water Pollution due to Iron Content in Bhubaneswar, Odisha, India, 2014. http://inpressco.com/category/ijcet.

[23] Md.K. Hasan, A. Shahriar, K.U. Jim, Water pollution in Bangladesh and its impact on public health, Heliyon. 5 (2019) e02145. https://doi.org/10.1016/j.heliyon.2019.e02145.

[24] C.H. Tseng, C. Lei, Y.C. Chen, Evaluating the health costs of oral hexavalent chromium exposure from water pollution: A case study in Taiwan, J Clean Prod. 172 (2018) 819–826. https://doi.org/10.1016/J.JCLEPRO.2017.10.177.

[25] X. He, P. Li, Surface Water Pollution in the Middle Chinese Loess Plateau with Special Focus on Hexavalent Chromium (Cr6+): Occurrence, Sources and Health Risks, Expo Health. 12 (2020) 385–401. https://doi.org/10.1007/s12403-020-00344-x.

[26] M.N. Georgaki, M. Charalambous, N. Kazakis, M.A. Talias, C. Georgakis, T. Papamitsou, C. Mytiglaki, Chromium in Water and Carcinogenic Human Health Risk, Environments - MDPI. 10 (2023). https://doi.org/10.3390/environments10020033.

[27] M. Tumolo, V. Ancona, D. De Paola, D. Losacco, C. Campanale, C. Massarelli, V.F. Uricchio, Chromium pollution in European water, sources, health risk, and remediation

strategies: An overview, Int J Environ Res Public Health. 17 (2020) 1–25. https://doi.org/10.3390/ijerph17155438.

[28] M. Sarkar, A. Banerjee, P.P. Pramanick, Kinetics and mechanism of fluoride removal using latrite, Ind Eng Chem Res. 45 (2006) 5920–5927. https://doi.org/10.1021/ie060016j.

[29] A.R. Abida, F. Tangfu, X. Waqar, A. Sifat, N. Oyebamiji, A. Salar, A.W. Nasim, A. Rasool, Á.T. Xiao, Á.W. Ali, Á.O. Abiola, A. Farooqi, Á.S. Noor, T. Xiao, O. Abiola, S. Ali, W. Nasim, A review of global outlook on fluoride contamination in groundwater with prominence on the Pakistan current situation, Environ Geochem Health. 40 (2018) 1265–1281. https://doi.org/10.1007/s10653-017-0054-z.

[30] Q. Zhang, P. Xu, H. Qian, F. Yang, Hydrogeochemistry and fluoride contamination in Jiaokou Irrigation District, Central China: Assessment based on multivariate statistical approach and human health risk, Science of the Total Environment. 741 (2020) 140460. https://doi.org/10.1016/j.scitotenv.2020.140460.

[31] S. Ali, Y. Fakhri, M. Golbini, S.K. Thakur, A. Alinejad, I. Parseh, S. Shekhar, P. Bhattacharya, Concentration of fluoride in groundwater of India: A systematic review, meta-analysis and risk assessment, Groundw Sustain Dev. 9 (2019) 100224. https://doi.org/10.1016/J.GSD.2019.100224.

[32] J.E. Podgorski, P. Labhasetwar, D. Saha, M. Berg, † Eawag, Prediction Modeling and Mapping of Groundwater Fluoride Contamination throughout India, (2018). https://doi.org/10.1021/acs.est.8b01679.

[33] J. Hussain, I. Husain, M. Arif, Fluoride contamination in groundwater of central Rajasthan, India and its toxicity in rural habitants, Toxicol Environ Chem. 95 (2013) 1048–1055. https://doi.org/10.1080/02772248.2013.832545.

[34] B. Vijay K, G. Arup, K. Krishna, Fluoride Sources, Toxicity and Its Amelioration: A Review, Annals of Environmental Science and Toxicology. 2 (2018) 021–032. https://doi.org/10.17352/aest.000009.

[35] A.K. Samal, P.K. Mishra, A. Biswas, Assessment of origin and distribution of fluoride contamination in groundwater using an isotopic signature from a part of the Indo-

Gangetic Plain (IGP), India, HydroResearch. 3 (2020) 75–84. https://doi.org/10.1016/J.HYDRES.2020.05.001.

[36] V.K. Saxena, S. Ahmed, Dissolution of fluoride in groundwater: A water-rock interaction study, Environmental Geology. 40 (2001) 1084–1087. https://doi.org/10.1007/s002540100290.

[37] P. Aravinthasamy, D. Karunanidhi, T. Subramani, K. Srinivasamoorthy, B. Anand, Geochemical evaluation of fluoride contamination in groundwater from Shanmuganadhi River basin, South India: implication on human health, Environ Geochem Health. 42 (2020) 1937–1963. https://doi.org/10.1007/s10653-019-00452-x.

[38] M.F. Chang, J.C. Liu, Precipitation Removal of Fluoride from Semiconductor Wastewater, Journal of Environmental Engineering. 133 (2007) 419–425. https://doi.org/10.1061/(asce)0733-9372(2007)133:4(419).

[39] Y. Qiu, L.F. Ren, L. Xia, J. Shao, Y. Zhao, B. Van der Bruggen, Investigation of fluoride and silica removal from semiconductor wastewaters with a clean coagulation-ultrafiltration process, Chemical Engineering Journal. 438 (2022) 135562. https://doi.org/10.1016/J.CEJ.2022.135562.

[40] C.C. Liu, J.C. Liu, Coupled precipitation-ultrafiltration for treatment of high fluoride-content wastewater, J Taiwan Inst Chem Eng. 58 (2016) 259–263. https://doi.org/10.1016/J.JTICE.2015.05.038.

[41] R. A. Rocha, D. Rojas, M. Jesús Clemente, A. Ruiz, V. Devesa, D. Vélez, Quantification of Fluoride in Food by Microwave Acid Digestion and Fluoride Ion-Selective Electrode, J Agric Food Chem. 61 (2013) 10708–10713. https://doi.org/10.1021/jf403728r.

[42] C.P.G. Emenike, I.T. Tenebe, P. Jarvis, Fluoride contamination in groundwater sources in Southwestern Nigeria: Assessment using multivariate statistical approach and human health risk, Ecotoxicol Environ Saf. 156 (2018) 391–402. https://doi.org/10.1016/j.ecoenv.2018.03.022.

[43] G. Viswanathan, A. Jaswanth, S. Gopalakrishnan, S. Siva ilango, G. Aditya, Determining the optimal fluoride concentration in drinking water for fluoride endemic regions in South India, Science of The Total Environment. 407 (2009) 5298–5307. https://doi.org/10.1016/J.SCITOTENV.2009.06.028.

[44] R. Ranjan, A. Ranjan, Sources of Fluoride Toxicity, (2015) 11–20. https://doi.org/10.1007/978-3-319-17512-6_2.

[45] S. Ayoob, A.K. Gupta, Fluoride in drinking water: A review on the status and stress effects, Crit Rev Environ Sci Technol. 36 (2006) 433–487. https://doi.org/10.1080/10643380600678112.

[46] A. Narsimha, V. Sudarshan, Contamination of fluoride in groundwater and its effect on human health: a case study in hard rock aquifers of Siddipet, Telangana State, India, Appl Water Sci. 7 (2017) 2501–2512. https://doi.org/10.1007/s13201-016-0441-0.

[47] K.K. Yadav, S. Kumar, Q.B. Pham, N. Gupta, S. Rezania, H. Kamyab, S. Yadav, J. Vymazal, V. Kumar, D.Q. Tri, A. Talaiekhozani, S. Prasad, L.M. Reece, N. Singh, P.K. Maurya, J. Cho, Fluoride contamination, health problems and remediation methods in Asian groundwater: A comprehensive review, Ecotoxicol Environ Saf. 182 (2019) 109362. https://doi.org/10.1016/j.ecoenv.2019.06.045.

[48] J. Han, L. Kiss, H. Mei, A.M. Remete, M. Ponikvar-Svet, D.M. Sedgwick, R. Roman, S. Fustero, H. Moriwaki, V.A. Soloshonok, Chemical Aspects of Human and Environmental Overload with Fluorine, Chem Rev. 121 (2021) 4678–4742. https://doi.org/10.1021/acs.chemrev.0c01263.

[49] N.J. Chinoy, M. V. Narayana, In vitro fluoride toxicity in human spermatozoa, Reproductive Toxicology. 8 (1994) 155–159. https://doi.org/10.1016/0890-6238(94)90022-1.

[50] D.L. Ozsvath, Fluoride and environmental health: A review, Rev Environ Sci Biotechnol. 8 (2009) 59–79. https://doi.org/10.1007/s11157-008-9136-9.

[51] O. Barbier, L. Arreola-Mendoza, L.M. Del Razo, Molecular mechanisms of fluoride toxicity, Chem Biol Interact. 188 (2010) 319–333. https://doi.org/10.1016/J.CBI.2010.07.011.

[52] D. Karunanidhi, P. Aravinthasamy, T. Subramani, P.D. Roy, K. Srinivasamoorthy, Risk of Fluoride-Rich Groundwater on Human Health: Remediation Through Managed Aquifer Recharge in a Hard Rock Terrain, South India, Natural Resources Research. 29 (2020). https://doi.org/10.1007/s11053-019-09592-4.

[53] N. Vivek Narayanan, M. Ganesan, Use of adsorption using granular activated carbon (GAC) for the enhancement of removal of chromium from synthetic wastewater by electrocoagulation, J Hazard Mater. 161 (2009) 575–580. https://doi.org/10.1016/j.jhazmat.2008.03.113.

[54] D. Clímaco Patrocínio, C.C. Neves Kunrath, M.A. Siqueira Rodrigues, T. Benvenuti, F. Dani Rico Amado, Concentration effect and operational parameters on electrodialysis reversal efficiency applied for fluoride removal in groundwater, J Environ Chem Eng. 7 (2019) 103491. https://doi.org/10.1016/j.jece.2019.103491.

[55] J. Pan, Y. Zheng, J. Ding, C. Gao, B. Van Der Bruggen, J. Shen, Fluoride Removal from Water by Membrane Capacitive Deionization with a Monovalent Anion Selective Membrane, Ind Eng Chem Res. 57 (2018) 7048–7053. https://doi.org/10.1021/acs.iecr.8b00929.

[56] S.S. Waghmare, T. Arfin, Fluoride removal from water by various techniques, Int J Innov Sci Eng Technol. 2 (2015) 560–571.

[57] P. Mondal, S. George, A review on adsorbents used for defluoridation of drinking water, Rev Environ Sci Biotechnol. 14 (2015) 195–210. https://doi.org/10.1007/s11157-014-9356-0.

[58] P.C. Bhomick, A. Supong, R. Karmaker, M. Baruah, C. Pongener, D. Sinha, Activated carbon synthesized from biomass material using single-step KOH activation for adsorption of fluoride: Experimental and theoretical investigation, Korean Journal of Chemical Engineering. 36 (2019) 551–562. https://doi.org/10.1007/s11814-019-0234-x.

[59] A.W. Kalsido, B. Tekola, B. Mogessie, E. Alemayehu, Excess fluoride issues and mitigation using low-cost techniques from groundwater: A review, in: Cost Effective Technologies for Solid Waste and Wastewater Treatment, Elsevier, 2022: pp. 241–263. https://doi.org/10.1016/B978-0-12-822933-0.00004-8.

[60] B.D. Turner, P. Binning, S.L.S. Stipp, Fluoride removal by calcite: Evidence for fluorite precipitation and surface adsorption, Environ Sci Technol. 39 (2005) 9561–9568. https://doi.org/10.1021/es0505090.

[61] H. Lounici, L. Addour, D. Belhocine, H. Grib, S. Nicolas, B. Bariou, N. Mameri, Study of a new technique for fluoride removal from water, Desalination. 114 (1997) 241–251. https://doi.org/10.1016/S0011-9164(98)00016-2.

[62] A. Heikens, S. Sumarti, M. Van Bergen, B. Widianarko, L. Fokkert, K. Van Leeuwen, W. Seinen, The impact of the hyperacid Ijen Crater Lake: Risks of excess fluoride to human health, Science of the Total Environment. 346 (2005) 56–69. https://doi.org/10.1016/j.scitotenv.2004.12.007.

[63] K. Majewska-Nowak, M. Grzegorzek, M. Kabsch-Korbutowicz, Removal of fluoride ions by batch electrodialysis, Environment Protection Engineering. 41 (2015) 67–81. https://doi.org/10.5277/epe150106.

[64] P.P. Sharma, V. Yadav, P.D. Maru, B.S. Makwana, S. Sharma, V. Kulshrestha, Mitigation of Fluoride from Brackish Water via Electrodialysis: An Environmentally Friendly Process, ChemistrySelect. 3 (2018) 779–784. https://doi.org/10.1002/slct.201701170.

[65] Z. Amor, S. Malki, M. Taky, B. Bariou, N. Mameri, A. Elmidaoui, Optimization of fluoride removal from brackish water by electrodialysis, Desalination. 120 (1998) 263–271. https://doi.org/10.1016/S0011-9164(98)00223-9.

[66] M. Zeni, R. Riveros, K. Melo, R. Primieri, S. Lorenzini, Study on fluoride reduction in artesian well - Water from electrodialysis process, Desalination. 185 (2005) 241–244. https://doi.org/10.1016/j.desal.2005.03.080.

[67] S. Meenakshi, N. Viswanathan, Identification of selective ion-exchange resin for fluoride sorption, J Colloid Interface Sci. 308 (2007) 438–450. https://doi.org/10.1016/j.jcis.2006.12.032.

[68] M.T. Samadi, M. Zarrabi, M.N. Sepehr, S.M. Ramhormozi, S. Azizian, A. Amrane, Removal of fluoride ions by ion exchange resin: Kinetic and equilibrium studies, Environ Eng Manag J. 13 (2014) 205–214. https://doi.org/10.30638/eemj.2014.025.

[69] J. Rodríguez-Iglesias, L. Alcalá, L. Megido, L. Castrillón, Removal of fluoride from coke wastewater by aluminum doped chelating ion-exchange resins: a tertiary treatment, (n.d.). https://doi.org/10.1007/s11356-021-16299-8/Published.

[70] P. Kumar, A. Pournara, K. Kim, V. Bansal, S. Rapti, M.J. Manos, Progress in Materials Science Metal-organic frameworks : Challenges and opportunities for ion-exchange / sorption applications, 86 (2017) 25–74.

[71] H. Luo, Y. Zeng, D. He, X. Pan, Application of iron-based materials in heterogeneous advanced oxidation processes for wastewater treatment: A review, Chemical Engineering Journal. 407 (2021) 127191. https://doi.org/10.1016/J.CEJ.2020.127191.

[72] S. Bakhta, Z. Sadaoui, U. Lassi, H. Romar, R. Kupila, J. Vieillard, Performances of metals modified activated carbons for fluoride removal from aqueous solutions, Chem Phys Lett. 754 (2020) 137705. https://doi.org/10.1016/j.cplett.2020.137705.

[73] A. Bhatnagar, E. Kumar, M. Sillanpää, Fluoride removal from water by adsorption-A review, Chemical Engineering Journal. 171 (2011) 811–840. https://doi.org/10.1016/j.cej.2011.05.028.

[74] P. Mondal, S. George, A review on adsorbents used for defluoridation of drinking water, Rev Environ Sci Biotechnol. 14 (2015) 195–210. https://doi.org/10.1007/s11157-014-9356-0.

[75] M. Kim, C.E. Choong, S. Hyun, C.M. Park, G. Lee, Mechanism of simultaneous removal of aluminum and fluoride from aqueous solution by La/Mg/Si-activated carbon, Chemosphere. 253 (2020). https://doi.org/10.1016/j.chemosphere.2020.126580.

[76] S. Kalidindi, M. Vecha, A. Kar, T. Raychoudhury, Aluminum-cerium double-metal impregnated activated carbon: A novel composite for fluoride removal from aqueous solution, Water Sci Technol Water Supply. 17 (2017) 115–124. https://doi.org/10.2166/ws.2016.114.

[77] G. Wendimu, F. Zewge, E. Mulugeta, Aluminium-iron-amended activated bamboo charcoal (AIAABC) for fluoride removal from aqueous solutions, Journal of Water Process Engineering. 16 (2017) 123–131. https://doi.org/10.1016/j.jwpe.2016.12.012.

[78] E. Tchomgui-Kamga, V. Alonzo, C.P. Nanseu-Njiki, N. Audebrand, E. Ngameni, A. Darchen, Preparation and characterization of charcoals that contain dispersed aluminum oxide as adsorbents for removal of fluoride from drinking water, Carbon N Y. 48 (2010) 333–343. https://doi.org/10.1016/j.carbon.2009.09.034.

[79] C. Liu, J. Wang, J. Wan, C. Yu, MOF-on-MOF hybrids: Synthesis and applications, Coord Chem Rev. 432 (2021) 213743. https://doi.org/10.1016/j.ccr.2020.213743.

[80] M. Ding, X. Cai, H.L. Jiang, Improving MOF stability: Approaches and applications, Chem Sci. 10 (2019) 10209–10230. https://doi.org/10.1039/c9sc03916c.

[81] V. V Butova, M.A. Soldatov, A.A. Guda, K.A. Lomachenko, C. Lamberti, Metal-organic frameworks: structure, properties, methods of synthesis and characterization, Russian Chemical Reviews. 85 (2016) 280–307. https://doi.org/10.1070/rcr4554.

[82] D. Haldar, P. Duarah, M.K. Purkait, MOFs for the treatment of arsenic, fluoride and iron contaminated drinking water: A review, Chemosphere. 251 (2020) 126388. https://doi.org/10.1016/J.CHEMOSPHERE.2020.126388.

[83] P. Kumar, A. Pournara, K.H. Kim, V. Bansal, S. Rapti, M.J. Manos, Metal-organic frameworks: Challenges and opportunities for ion-exchange/sorption applications, Prog Mater Sci. 86 (2017) 25–74. https://doi.org/10.1016/J.PMATSCI.2017.01.002.

[84] A. Huang, L. Wan, J. Caro, Microwave-assisted synthesis of well-shaped UiO-66-NH2 with high CO2 adsorption capacity, Mater Res Bull. 98 (2018) 308–313. https://doi.org/10.1016/j.materresbull.2017.10.038.

[85] M.O.F. Topologies, N. Stock, S. Biswas, Synthesis of Metal-Organic Frameworks (MOFs): Routes to Various, (2012) 933–969.

[86] Q. Wang, D. Astruc, State of the Art and Prospects in Metal-Organic Framework (MOF)-Based and MOF-Derived Nanocatalysis, Chem Rev. 120 (2020) 1438–1511. https://doi.org/10.1021/acs.chemrev.9b00223.

[87] M. Safaei, M.M. Foroughi, N. Ebrahimpoor, S. Jahani, A. Omidi, M. Khatami, A review on metal-organic frameworks: Synthesis and applications, TrAC - Trends in Analytical Chemistry. 118 (2019) 401–425. https://doi.org/10.1016/j.trac.2019.06.007.

[88] Y. Cao, Y. Zhao, Z. Lv, F. Song, Q. Zhong, Preparation and enhanced CO2 adsorption capacity of UiO-66/graphene oxide composites, Journal of Industrial and Engineering Chemistry. 27 (2015) 102–107. https://doi.org/10.1016/j.jiec.2014.12.021.

[89] X. Zhao, D. Liu, H. Huang, W. Zhang, Q. Yang, C. Zhong, The stability and defluoridation performance of MOFs in fluoride solutions, Microporous and

Mesoporous Materials. 185 (2014) 72–78. https://doi.org/10.1016/J.MICROMESO.2013.11.002.

[90] K.Y.A. Lin, Y.T. Liu, S.Y. Chen, Adsorption of fluoride to UiO-66-NH2 in water: Stability, kinetic, isotherm and thermodynamic studies, J Colloid Interface Sci. 461 (2016) 79–87. https://doi.org/10.1016/j.jcis.2015.08.061.

[91] M. Massoudinejad, M. Ghaderpoori, A. Shahsavani, M.M. Amini, Adsorption of fluoride over a metal organic framework Uio-66 functionalized with amine groups and optimization with response surface methodology, J Mol Liq. 221 (2016) 279–286. https://doi.org/10.1016/j.molliq.2016.05.087.

[92] F. Ke, G. Luo, P. Chen, J. Jiang, Q. Yuan, H. Cai, C. Peng, X. Wan, Porous metal–organic frameworks adsorbents as a potential platform for defluoridation of water, Journal of Porous Materials. 23 (2016) 1065–1073. https://doi.org/10.1007/s10934-016-0164-5.

[93] A. Jeyaseelan, M. Naushad, T. Ahamad, N. Viswanathan, Design and development of amine functionalized iron based metal organic frameworks for selective fluoride removal from water environment, J Environ Chem Eng. 9 (2021) 104563. https://doi.org/10.1016/j.jece.2020.104563.

[94] A. Jeyaseelan, N. Viswanathan, Design of Amino-Functionalized Benzene-1,4-Dicarboxylic Acid-Fabricated Lanthanum-Based Metal–Organic Frameworks for Defluoridation of Water, Journal of Chemical & Engineering Data. 65 (2020) 5328–5340. https://doi.org/10.1021/acs.jced.0c00492.

[95] C. Yin, Q. Huang, G. Zhu, L. Liu, S. Li, X. Yang, S. Wang, High-performance lanthanum-based metal–organic framework with ligand tuning of the microstructures for removal of fluoride from water, J Colloid Interface Sci. 607 (2022) 1762–1775. https://doi.org/10.1016/j.jcis.2021.09.108.

[96] X. Wang, H. Zhu, T. Sun, Y. Liu, T. Han, J. Lu, H. Dai, L. Zhai, F. Ke, Synthesis and study of an efficient metal-organic framework adsorbent (MIL-96(Al)) for fluoride removal from water, J Nanomater. 2019 (2019). https://doi.org/10.1155/2019/3128179.

[97] S. karmakar, J. Dechnik, C. Janiak, S. De, Aluminium fumarate metal-organic framework: A super adsorbent for fluoride from water, J Hazard Mater. 303 (2016) 10–20. https://doi.org/10.1016/j.jhazmat.2015.10.030.

[98] A. Jeyaseelan, N. Viswanathan, Facile synthesis of tunable rare earth based metal organic frameworks for enhanced fluoride retention, J Mol Liq. 326 (2021) 115163. https://doi.org/10.1016/j.molliq.2020.115163.

[99] Q. Huang, L. Zhao Data analysis, G. Zhu, D. Chen, X. Ma, X. Yang, S. Wang, Outstanding performance of thiophene-based metal-organic frameworks for fluoride capture from wastewater, Sep Purif Technol. 298 (2022) 121567. https://doi.org/10.1016/J.SEPPUR.2022.121567.

[100] J. Joseph, S. Iftekhar, V. Srivastava, Z. Fallah, E.N. Zare, M. Sillanpää, Iron-based metal-organic framework: Synthesis, structure and current technologies for water reclamation with deep insight into framework integrity, Chemosphere. 284 (2021) 131171. https://doi.org/10.1016/J.CHEMOSPHERE.2021.131171.

[101] M. Hossien Saghi, B. Chabot, S. Rezania, M. Sillanpää, A. Akbar Mohammadi, M. Shams, A. Alahabadi, Water-stable zirconium and iron-based metal-organic frameworks (MOFs) as fluoride scavengers in aqueous medium, Sep Purif Technol. 270 (2021) 118645. https://doi.org/10.1016/J.SEPPUR.2021.118645.

[102] M. Chigondo, H.K. Paumo, M. Bhaumik, K. Pillay, A. Maity, Rapid high adsorption performance of hydrous cerium-magnesium oxides for removal of fluoride from water, J Mol Liq. 265 (2018) 496–509. https://doi.org/10.1016/j.molliq.2018.06.015.

[103] K. Mukhopadhyay, A. Ghosh, S.K. Das, B. Show, P. Sasikumar, U. Chand Ghosh, Synthesis and characterisation of cerium(IV)-incorporated hydrous iron(III) oxide as an adsorbent for fluoride removal from water, RSC Adv. 7 (2017) 26037–26051. https://doi.org/10.1039/c7ra00265c.

[104] V. Sivasankar, S. Murugesh, S. Rajkumar, A. Darchen, Cerium dispersed in carbon (CeDC) and its adsorption behavior: A first example of tailored adsorbent for fluoride removal from drinking water, Chemical Engineering Journal. 214 (2013) 45–54. https://doi.org/10.1016/j.cej.2012.10.023.

[105] P.K. Mishra, P. Gahlyan, R. Kumar, P.K. Rai, Aero-Gel Based Cerium Doped Iron Oxide Solid Solution for Ultrafast Removal of Arsenic, ACS Sustain Chem Eng. 6 (2018) 10668–10678. https://doi.org/10.1021/acssuschemeng.8b02006.

[106] A. Mullick, S. Neogi, Ultrasound assisted synthesis of Mg-Mn-Zr impregnated activated carbon for effective fluoride adsorption from water, Ultrason Sonochem. 50 (2019) 126–137. https://doi.org/10.1016/j.ultsonch.2018.09.010.

[107] L. Huang, Z. Yang, X. Li, L. Hou, S.I. Alhassan, H. Wang, Synthesis of hierarchical hollow MIL-53(Al)-NH2 as an adsorbent for removing fluoride: experimental and theoretical perspective, Environmental Science and Pollution Research. 28 (2021) 6886–6897. https://doi.org/10.1007/s11356-020-10975-x.

[108] H. ya Chen, Y. qiu Huo, K. zhe Cai, Y. Teng, Controllable preparation and capacitance performance of bimetal Co/Ni-MOF, Synth Met. 276 (2021) 116761. https://doi.org/10.1016/J.SYNTHMET.2021.116761.

[109] H. Kumar, M. Patel, D. Mohan, Simplified Batch and Fixed-Bed Design System for Efficient and Sustainable Fluoride Removal from Water Using Slow Pyrolyzed Okra Stem and Black Gram Straw Biochars, ACS Omega. 4 (2019) 19513–19525. https://doi.org/10.1021/acsomega.9b00877.

[110] M. Barathi, A. Santhana Krishna Kumar, N. Rajesh, A novel ultrasonication method in the preparation of zirconium impregnated cellulose for effective fluoride adsorption, Ultrason Sonochem. 21 (2014) 1090–1099. https://doi.org/10.1016/j.ultsonch.2013.11.023.

[111] S. Cheng, L. Zhang, A. Ma, H. Xia, J. Peng, C. Li, J. Shu, Comparison of activated carbon and iron/cerium modified activated carbon to remove methylene blue from wastewater, J Environ Sci (China). 65 (2018) 92–102. https://doi.org/10.1016/j.jes.2016.12.027.

[112] K. Mukhopadhyay, A. Ghosh, S.K. Das, B. Show, P. Sasikumar, U. Chand Ghosh, Synthesis and characterisation of cerium(IV)-incorporated hydrous iron(III) oxide as an adsorbent for fluoride removal from water, RSC Adv. 7 (2017) 26037–26051. https://doi.org/10.1039/c7ra00265c.

[113] M. Kim, C.E. Choong, S. Hyun, C.M. Park, G. Lee, Mechanism of simultaneous removal of aluminum and fluoride from aqueous solution by La/Mg/Si-activated carbon, Chemosphere. 253 (2020). https://doi.org/10.1016/j.chemosphere.2020.126580.

[114] A.A.M. Daifullah, S.M. Yakout, S.A. Elreefy, Adsorption of fluoride in aqueous solutions using KMnO4-modified activated carbon derived from steam pyrolysis of rice straw, J Hazard Mater. 147 (2007) 633–643. https://doi.org/10.1016/j.jhazmat.2007.01.062.

[115] K. Mukhopadhyay, U.C. Ghosh, P. Sasikumar, Enhanced capacity of fluoride scavenging from contaminated water by nano-architectural reorientation of cerium-incorporated hydrous iron oxide with graphene oxide, Environmental Science and Pollution Research. 26 (2019) 26112–26133. https://doi.org/10.1007/s11356-019-05756-0.

[116] A. Lassoued, B. Dkhil, A. Gadri, S. Ammar, Control of the shape and size of iron oxide (α-Fe2O3) nanoparticles synthesized through the chemical precipitation method, Results Phys. 7 (2017) 3007–3015. https://doi.org/10.1016/J.RINP.2017.07.066.

[117] G.I. Danmaliki, T.A. Saleh, Effects of bimetallic Ce/Fe nanoparticles on the desulfurization of thiophenes using activated carbon, Chemical Engineering Journal. 307 (2017) 914–927. https://doi.org/10.1016/j.cej.2016.08.143.

[118] E. Kacan, Optimum BET surface areas for activated carbon produced from textile sewage sludges and its application as dye removal, J Environ Manage. 166 (2016) 116–123. https://doi.org/10.1016/j.jenvman.2015.09.044.

[119] C. Saka, BET, TG-DTG, FT-IR, SEM, iodine number analysis and preparation of activated carbon from acorn shell by chemical activation with ZnCl2, J Anal Appl Pyrolysis. 95 (2012) 21–24. https://doi.org/10.1016/j.jaap.2011.12.020.

[120] S. Bhattacharjee, DLS and zeta potential - What they are and what they are not?, Journal of Controlled Release. 235 (2016) 337–351. https://doi.org/10.1016/j.jconrel.2016.06.017.

[121] S.E. McNeil, Challenges for nanoparticle characterization., 2011. https://doi.org/10.1007/978-1-60327-198-1_2.

[122] E. Nägele, The zeta-potential of cement, Cem Concr Res. 15 (1985) 453–462. https://doi.org/10.1016/0008-8846(85)90118-8.

[123] B.B. Johnson, Effect of pH, Temperature, and Concentration on the Adsorption of Cadmium on Goethite, Environ Sci Technol. 24 (1990) 112–118. https://doi.org/10.1021/es00071a014.

[124] M.A. Al-Ghouti, D.A. Da'ana, Guidelines for the use and interpretation of adsorption isotherm models: A review, J Hazard Mater. 393 (2020) 122383. https://doi.org/10.1016/j.jhazmat.2020.122383.

[125] K.Y. Foo, B.H. Hameed, Insights into the modeling of adsorption isotherm systems, Chemical Engineering Journal. 156 (2010) 2–10. https://doi.org/10.1016/j.cej.2009.09.013.

[126] M.G. Sujana, H.K. Pradhan, S. Anand, Studies on sorption of some geomaterials for fluoride removal from aqueous solutions, J Hazard Mater. 161 (2009) 120–125. https://doi.org/10.1016/j.jhazmat.2008.03.062.

[127] A. Proctor, J.F. Toro-Vazquez, The Freundlich Isotherm in Studying Adsorption in Oil Processing, in: Bleaching and Purifying Fats and Oils: Theory and Practice, Elsevier Inc., 2009: pp. 209–219. https://doi.org/10.1016/B978-1-893997-91-2.50016-X.

[128] T. Pang, T.S. Aye Chan, Y.A.C. Jande, J. Shen, Removal of fluoride from water using activated carbon fibres modified with zirconium by a drop-coating method, Chemosphere. 255 (2020) 126950. https://doi.org/10.1016/j.chemosphere.2020.126950.

[129] A.K. Yadav, R. Abbassi, A. Gupta, M. Dadashzadeh, Removal of fluoride from aqueous solution and groundwater by wheat straw, Sawdust and activated bagasse carbon of sugarcane, Ecol Eng. 52 (2013) 211–218. https://doi.org/10.1016/j.ecoleng.2012.12.069.

[130] E. Vences-Alvarez, L.H. Velazquez-Jimenez, L.F. Chazaro-Ruiz, P.E. Diaz-Flores, J.R. Rangel-Mendez, Fluoride removal in water by a hybrid adsorbent lanthanum-carbon, J Colloid Interface Sci. 455 (2015) 194–202. https://doi.org/10.1016/j.jcis.2015.05.048.

[131] M.H. Dehghani, M. Farhang, M. Alimohammadi, M. Afsharnia, G. Mckay, Adsorptive removal of fluoride from water by activated carbon derived from CaCl2-modified

Crocus sativus leaves: Equilibrium adsorption isotherms, optimization, and influence of anions, Chem Eng Commun. 205 (2018) 955–965. https://doi.org/10.1080/00986445.2018.1423969.

[132] H. Moussout, H. Ahlafi, M. Aazza, H. Maghat, Critical of linear and nonlinear equations of pseudo-first order and pseudo-second order kinetic models, Karbala International Journal of Modern Science. 4 (2018) 244–254. https://doi.org/10.1016/j.kijoms.2018.04.001.

[133] L. Largitte, R. Pasquier, A review of the kinetics adsorption models and their application to the adsorption of lead by an activated carbon, Chemical Engineering Research and Design. 109 (2016) 495–504. https://doi.org/10.1016/j.cherd.2016.02.006.

[134] M. Sarkar, D. Santra, Modeling fluoride adsorption on cerium-loaded cellulose bead - Response surface methodology, equilibrium, and kinetic studies, Water Air Soil Pollut. 226 (2015). https://doi.org/10.1007/s11270-015-2307-8.

[135] J. Wang, X. Guo, Adsorption kinetic models: Physical meanings, applications, and solving methods, J Hazard Mater. 390 (2020) 122156. https://doi.org/10.1016/j.jhazmat.2020.122156.

[136] S. Azizian, Kinetic models of sorption: a theoretical analysis, J Colloid Interface Sci. 276 (2004) 47–52. https://doi.org/10.1016/J.JCIS.2004.03.048.

[137] C. Sun, J. Qiu, Z. Zhang, T.F. Marhaba, Y. Zhang, Removal of Arsenite from Water by Ce-Al-Fe Trimetal Oxide Adsorbent: Kinetics, Isotherms, and Thermodynamics, J Chem. 2016 (2016). https://doi.org/10.1155/2016/8617219.

[138] C. Silveira, Q.L. Shimabuku, M. Fernandes Silva, R. Bergamasco, Iron-oxide nanoparticles by the green synthesis method using Moringa oleifera leaf extract for fluoride removal, Environmental Technology (United Kingdom). 39 (2018) 2926–2936. https://doi.org/10.1080/09593330.2017.1369582.

[139] M.H. Hassan, R. Stanton, J. Secora, D.J. Trivedi, S. Andreescu, Ultrafast Removal of Phosphate from Eutrophic Waters Using a Cerium-Based Metal-Organic Framework, ACS Appl Mater Interfaces. 12 (2020) 52788–52796. https://doi.org/10.1021/acsami.0c16477.

[140] X. Zhao, J. Wang, F. Wu, T. Wang, Y. Cai, Y. Shi, G. Jiang, Removal of fluoride from aqueous media by Fe3O4@Al(OH)3 magnetic nanoparticles, J Hazard Mater. 173 (2010) 102–109. https://doi.org/10.1016/J.JHAZMAT.2009.08.054.

[141] A. Mullick, S. Neogi, Acoustic cavitation induced synthesis of zirconium impregnated activated carbon for effective fluoride scavenging from water by adsorption, Ultrason Sonochem. 45 (2018) 65–77. https://doi.org/10.1016/j.ultsonch.2018.03.002.

[142] Z. Bonyadi, P.S. Kumar, R. Foroutan, R. Kafaei, H. Arfaeinia, S. Farjadfard, B. Ramavandi, Ultrasonic-assisted synthesis of Populus alba activated carbon for water defluorination: Application for real wastewater, Korean Journal of Chemical Engineering. 36 (2019) 1595–1603. https://doi.org/10.1007/s11814-019-0373-0.

[143] K. Biswas, K. Gupta, A. Goswami, U.C. Ghosh, Fluoride removal efficiency from aqueous solution by synthetic iron(III)-aluminum(III)-chromium(III) ternary mixed oxide, Desalination. 255 (2010) 44–51. https://doi.org/10.1016/j.desal.2010.01.019.

[144] M. Kurian, Cerium oxide based materials for water treatment – A review, J Environ Chem Eng. 8 (2020) 104439. https://doi.org/10.1016/J.JECE.2020.104439.

[145] R. Dalapati, B. Sakthivel, M.K. Ghosalya, A. Dhakshinamoorthy, S. Biswas, A cerium-based metal-organic framework having inherent oxidase-like activity applicable for colorimetric sensing of biothiols and aerobic oxidation of thiols, CrystEngComm. 19 (2017) 5915–5925. https://doi.org/10.1039/c7ce01053b.

[146] J. Zhou, H. Liu, Y. Lin, C. Zhou, A. Huang, Synthesis of well-shaped and high-crystalline Ce-based metal organic framework for CO2/CH4 separation, Microporous and Mesoporous Materials. 302 (2020) 110224. https://doi.org/10.1016/J.MICROMESO.2020.110224.

[147] M. Chigondo, H.K. Paumo, M. Bhaumik, K. Pillay, A. Maity, Rapid high adsorption performance of hydrous cerium-magnesium oxides for removal of fluoride from water, J Mol Liq. 265 (2018) 496–509. https://doi.org/10.1016/j.molliq.2018.06.015.

[148] S. Cheng, L. Zhang, A. Ma, H. Xia, J. Peng, C. Li, J. Shu, Comparison of activated carbon and iron/cerium modified activated carbon to remove methylene blue from wastewater, J Environ Sci (China). 65 (2018) 92–102. https://doi.org/10.1016/j.jes.2016.12.027.

[149] L. Zhang, P. Chen, G. Gu, Q. Wu, W. Yao, Novel synthesis and photocatalytic performance of Ce 1 - X Zr x O 2 /silica fiber, Appl Surf Sci. 382 (2016) 155–161. https://doi.org/10.1016/j.apsusc.2016.04.122.

[150] B. Ksapabutr, E. Gulari, S. Wongkasemjit, One-pot synthesis and characterization of novel sodium tris(glycozirconate) and cerium glycolate precursors and their pyrolysis, Mater Chem Phys. 83 (2004) 34–42. https://doi.org/10.1016/J.MATCHEMPHYS.2003.08.016.

[151] X. Wu, Y. Zhang, X. Dou, M. Yang, Fluoride removal performance of a novel Fe-Al-Ce trimetal oxide adsorbent, Chemosphere. 69 (2007) 1758–1764. https://doi.org/10.1016/j.chemosphere.2007.05.075.

[152] W. Li, T. Zhang, L. Lv, Y. Chen, W. Tang, S. Tang, Room-temperature synthesis of MIL-100(Fe) and its adsorption performance for fluoride removal from water, Colloids Surf A Physicochem Eng Asp. 624 (2021) 126791. https://doi.org/10.1016/j.colsurfa.2021.126791.

[153] A. Ghosh, G. Das, Green synthesis of a novel water-stable Sn(ii)-TMA metal-organic framework (MOF): An efficient adsorbent for fluoride in aqueous medium in a wide pH range, New Journal of Chemistry. 44 (2020) 1354–1361. https://doi.org/10.1039/c9nj05861c.

[154] X.H. Zhu, C.X. Yang, X.P. Yan, Metal-organic framework-801 for efficient removal of fluoride from water, Microporous and Mesoporous Materials. 259 (2018) 163–170. https://doi.org/10.1016/j.micromeso.2017.10.001.

[155] X. Yang, S. Deng, F. Peng, T. Luo, A new adsorbent of a Ce ion-implanted metal-organic framework (MIL-96) with high-efficiency Ce utilization for removing fluoride from water, Dalton Transactions. 46 (2017) 1996–2006. https://doi.org/10.1039/c6dt03934k.

[156] S. Karmakar, S. Bhattacharjee, S. De, Experimental and modeling of fluoride removal using aluminum fumarate (AlFu) metal organic framework incorporated cellulose acetate phthalate mixed matrix membrane, J Environ Chem Eng. 5 (2017) 6087–6097. https://doi.org/10.1016/j.jece.2017.11.035.

[157] A. Jeyaseelan, M. Naushad, N. Viswanathan, Development of Multivalent Metal-Ion-Fabricated Fumaric Acid-Based Metal-Organic Frameworks for Defluoridation of Water, J Chem Eng Data. 65 (2020) 2990–3001. https://doi.org/10.1021/acs.jced.0c00005.

[158] X. Zhao, J. Wang, F. Wu, T. Wang, Y. Cai, Y. Shi, G. Jiang, Removal of fluoride from aqueous media by Fe3O4@Al(OH)3 magnetic nanoparticles, J Hazard Mater. 173 (2010) 102–109. https://doi.org/10.1016/J.JHAZMAT.2009.08.054.

[159] H.R. Abid, Z.H. Rada, Y. Li, H.A. Mohammed, Y. Wang, S. Wang, H. Arandiyan, X. Tan, S. Liu, Boosting CO2 adsorption and selectivity in metal-organic frameworks of MIL-96(Al): Via second metal Ca coordination, RSC Adv. 10 (2020) 8130–8139. https://doi.org/10.1039/d0ra00305k.

[160] D. Xie, Y. Gu, H. Wang, Y. Wang, W. Qin, G. Wang, H. Zhang, Y. Zhang, Enhanced fluoride removal by hierarchically porous carbon foam monolith with high loading of UiO-66, J Colloid Interface Sci. 542 (2019) 269–280. https://doi.org/10.1016/j.jcis.2019.02.027.

[161] P. Zhao, F. Qin, Z. Huang, C. Sun, W. Shen, H. Xu, MOF-derived hollow porous Ni/CeO2 octahedron with high efficiency for N2O decomposition, Chemical Engineering Journal. 349 (2018) 72–81. https://doi.org/10.1016/j.cej.2018.05.044.

[162] G. Grzybek, P. Stelmachowski, S. Gudyka, P. Indyka, Z. Sojka, N. Guillén-Hurtado, V. Rico-Pérez, A. Bueno-López, A. Kotarba, Strong dispersion effect of cobalt spinel active phase spread over ceria for catalytic N2O decomposition: The role of the interface periphery, Appl Catal B. 180 (2016) 622–629. https://doi.org/10.1016/J.APCATB.2015.07.027.

[163] S. Sikha, B. Mandal, Ultrasound-Assisted facile synthesis of Ce/Fe nanoparticles impregnated activated carbon for fluoride remediation, Sep Purif Technol. 289 (2022) 120785. https://doi.org/10.1016/J.SEPPUR.2022.120785.

[164] D. Yu, M. Wu, Q. Hu, L. Wang, C. Lv, L. Zhang, Iron-based metal-organic frameworks as novel platforms for catalytic ozonation of organic pollutant: Efficiency and mechanism, J Hazard Mater. 367 (2019) 456–464. https://doi.org/10.1016/J.JHAZMAT.2018.12.108.

[165] P. Mondal, M.K. Purkait, Preparation and characterization of novel green synthesized iron–aluminum nanocomposite and studying its efficiency in fluoride removal, Chemosphere. 235 (2019) 391–402. https://doi.org/10.1016/j.chemosphere.2019.06.189.

[166] G. Özçelik, F.C. Çavuşoğlu, Ş. Özkara-Aydınoğlu, Ş.S. Bayazit, Enhanced & effective phosphate recovery from water by indium fumarate & zirconium fumarate metal-organic frameworks: Synthesis, characterization, adsorption, kinetic and isotherm studies, Surfaces and Interfaces. 29 (2022) 101719. https://doi.org/10.1016/J.SURFIN.2021.101719.

[167] S.K. Swain, T. Patnaik, V.K. Singh, U. Jha, R.K. Patel, R.K. Dey, Kinetics, equilibrium and thermodynamic aspects of removal of fluoride from drinking water using meso-structured zirconium phosphate, Chemical Engineering Journal. 171 (2011) 1218–1226. https://doi.org/10.1016/J.CEJ.2011.05.030.

[168] L. Chen, B.Y. He, S. He, T.J. Wang, C.L. Su, Y. Jin, Fe-Ti oxide nano-adsorbent synthesized by co-precipitation for fluoride removal from drinking water and its adsorption mechanism, Powder Technol. 227 (2012) 3–8. https://doi.org/10.1016/j.powtec.2011.11.030.

[169] C. Di Dong, C.P. Huang, T.B. Nguyen, C.F. Hsiung, C.H. Wu, Y.L. Lin, C.W. Chen, C.M. Hung, The degradation of phthalate esters in marine sediments by persulfate over iron–cerium oxide catalyst, Science of the Total Environment. 696 (2019). https://doi.org/10.1016/j.scitotenv.2019.133973.

[170] S.I. Alhassan, H. Wang, Y. He, L. Yan, Y. Jiang, B. Wu, T. Wang, H. Gang, L. Huang, L. Jin, Y. Chen, Fluoride remediation from on-site wastewater using optimized bauxite nanocomposite (Bx-Ce-La@500): Synthesis maximization, and mechanism of F─ removal, J Hazard Mater. 430 (2022) 128401. https://doi.org/10.1016/J.JHAZMAT.2022.128401.

[171] S. Kundu, M. Kanti Naskar, Carbon-layered double hydroxide nanocomposite for efficient removal of inorganic and organic based water contaminants-unravelling the adsorption mechanism †, Cite This: Mater. Adv. 2 (2021) 3600. https://doi.org/10.1039/d1ma00064k.

[172] S. Kundu, M. Kanti Naskar, Al−Mg−Ca-Layered Double Oxides for Efficient Removal of As(V) from Water: The Role of Amides, J. Chem. Eng. Data. 64 (2019) 24. https://doi.org/10.1021/acs.jced.8b01154.

[173] D. Kang, X. Yu, S. Tong, M. Ge, J. Zuo, C. Cao, W. Song, Performance and mechanism of Mg/Fe layered double hydroxides for fluoride and arsenate removal from aqueous solution, Chemical Engineering Journal. 228 (2013) 731–740. https://doi.org/10.1016/J.CEJ.2013.05.041.

[174] J. Zhu, X. Lin, P. Wu, Q. Zhou, X. Luo, Fluoride removal from aqueous solution by Al(III)–Zr(IV) binary oxide adsorbent, Appl Surf Sci. 357 (2015) 91–100. https://doi.org/10.1016/J.APSUSC.2015.09.012.

[175] F. Xu, G. Cheng, S. Song, Y. Wei, R. Chen, Insights into Promoted Adsorption Capability of Layered BiOCl Nanostructures Decorated with TiO2 Nanoparticles, ACS Sustainable Chemistry & Engineering. 4 (2016) 7013–7022. https://doi.org/10.1021/acssuschemeng.6b01920.

[176] K. Yang, B. Xing, Adsorption of organic compounds by carbon nanomaterials in aqueous phase: Polanyi theory and its application, Chem Rev. 110 (2010) 5989–6008. https://doi.org/10.1021/cr100059s.

[177] X. Guo, J. Wang, Comparison of linearization methods for modeling the Langmuir adsorption isotherm, J Mol Liq. 296 (2019) 111850. https://doi.org/10.1016/J.MOLLIQ.2019.111850.

[178] A.W. Marczewski, Analysis of Kinetic Langmuir Model. Part I: Integrated Kinetic Langmuir Equation (IKL): A New Complete Analytical Solution of the Langmuir Rate Equation, Langmuir. 26 (2010) 15229–15238. https://doi.org/10.1021/la1010049.

[179] G.I. Danmaliki, T.A. Saleh, Effects of bimetallic Ce/Fe nanoparticles on the desulfurization of thiophenes using activated carbon, Chemical Engineering Journal. 307 (2017) 914–927. https://doi.org/10.1016/j.cej.2016.08.143.

[180] L. Chai, Y. Wang, N. Zhao, W. Yang, X. You, Sulfate-doped Fe3O4/Al2O3 nanoparticles as a novel adsorbent for fluoride removal from drinking water, Water Res. 47 (2013) 4040–4049. https://doi.org/10.1016/j.watres.2013.02.057.

[181] H.-M. Ma, J.-W. Yi, S. Li, C. Jiang, J.-H. Wei, Y.-P. Wu, J. Zhao, D.-S. Li, Stable Bimetal-MOF Ultrathin Nanosheets for Pseudocapacitors with Enhanced Performance, Inorg Chem. 58 (2019) 9543–9547. https://doi.org/10.1021/acs.inorgchem.9b00937.

[182] W. Li, W. Fang, C. Wu, K.N. Dinh, H. Ren, L. Zhao, C. Liu, Q. Yan, Bimetal-MOF nanosheets as efficient bifunctional electrocatalysts for oxygen evolution and nitrogen reduction reaction, J Mater Chem A Mater. 8 (2020) 3658–3666. https://doi.org/10.1039/c9ta13473e.

[183] M.F. Oliveira, V. M. de Souza, M. G. C. da Silva, M. G. A. Vieira, Fixed-Bed Adsorption of Caffeine onto Thermally Modified Verde-lodo Bentonite, Industrial & Engineering Chemistry Research. 57 (2018) 17480–17487. https://doi.org/10.1021/acs.iecr.8b03734.

[184] S. Sikha, B. Mandal, Ultrasound-Assisted facile synthesis of Ce/Fe nanoparticles impregnated activated carbon for fluoride remediation, Sep Purif Technol. 289 (2022) 120785. https://doi.org/10.1016/J.SEPPUR.2022.120785.

[185] M.A. Acheampong, K. Pakshirajan, A.P. Annachhatre, P.N.L. Lens, Removal of Cu(II) by biosorption onto coconut shell in fixed-bed column systems, Journal of Industrial and Engineering Chemistry. 19 (2013) 841–848. https://doi.org/10.1016/J.JIEC.2012.10.029.

[186] N. Chen, Z. Zhang, C. Feng, M. Li, R. Chen, N. Sugiura, Investigations on the batch and fixed-bed column performance of fluoride adsorption by Kanuma mud, Desalination. 268 (2011) 76–82. https://doi.org/10.1016/J.DESAL.2010.09.053.

[187] Z. Du, T. Zheng, P. Wang, Experimental and modelling studies on fixed bed adsorption for Cu(II) removal from aqueous solution by carboxyl modified jute fiber, Powder Technol. 338 (2018) 952–959. https://doi.org/10.1016/J.POWTEC.2018.06.015.

[188] A.A. Ahmad, B.H. Hameed, Fixed-bed adsorption of reactive azo dye onto granular activated carbon prepared from waste, J Hazard Mater. 175 (2010) 298–303. https://doi.org/10.1016/J.JHAZMAT.2009.10.003.

[189] S. Chen, Q. Yue, B. Gao, Q. Li, X. Xu, K. Fu, Adsorption of hexavalent chromium from aqueous solution by modified corn stalk: A fixed-bed column study, Bioresour Technol. 113 (2012) 114–120. https://doi.org/10.1016/J.BIORTECH.2011.11.110.

[190] G. de V. Brião, M.G.C. da Silva, M.G.A. Vieira, Reusable and efficient clay material for the fixed-bed neodymium recovery, Sustain Chem Pharm. 25 (2022) 100623. https://doi.org/10.1016/J.SCP.2022.100623.

[191] M.J. Ahmed, B.H. Hameed, Removal of emerging pharmaceutical contaminants by adsorption in a fixed-bed column: A review, Ecotoxicol Environ Saf. 149 (2018) 257–266. https://doi.org/10.1016/J.ECOENV.2017.12.012.

[192] J. Tejedor, R. Álvarez-Briceño, V.H. Guerrero, C.A. Villamar-Ayala, Removal of caffeine using agro-industrial residues in fixed-bed columns: Improving the adsorption capacity and efficiency by selecting adequate physical and operational parameters, Journal of Water Process Engineering. 53 (2023) 103778. https://doi.org/10.1016/J.JWPE.2023.103778.

[193] R. Han, Y. Wang, X. Zhao, Y. Wang, F. Xie, J. Cheng, M. Tang, Adsorption of methylene blue by phoenix tree leaf powder in a fixed-bed column: experiments and prediction of breakthrough curves, Desalination. 245 (2009) 284–297. https://doi.org/10.1016/J.DESAL.2008.07.013.

[194] Y. Ye, J. Yang, W. Jiang, J. Kang, Y. Hu, H.H. Ngo, W. Guo, Y. Liu, Fluoride removal from water using a magnesia-pullulan composite in a continuous fixed-bed column, J Environ Manage. 206 (2018) 929–937. https://doi.org/10.1016/J.JENVMAN.2017.11.081.

[195] H. Kumar, M. Patel, D. Mohan, Simplified Batch and Fixed-Bed Design System for Efficient and Sustainable Fluoride Removal from Water Using Slow Pyrolyzed Okra Stem and Black Gram Straw Biochars, ACS Omega. 4 (2019) 19513–19525. https://doi.org/10.1021/acsomega.9b00877.

[196] S. Mohan, D.K. Singh, V. Kumar, S.H. Hasan, Effective removal of Fluoride ions by rGO/ZrO2 nanocomposite from aqueous solution: Fixed bed column adsorption modelling and its adsorption mechanism, J Fluor Chem. 194 (2017) 40–50. https://doi.org/10.1016/J.JFLUCHEM.2016.12.014.

[197] U. Kumari, A. Mishra, H. Siddiqi, B.C. Meikap, Effective defluoridation of industrial wastewater by using acid modified alumina in fixed-bed adsorption column:

Experimental and breakthrough curves analysis, J Clean Prod. 279 (2021) 123645. https://doi.org/10.1016/J.JCLEPRO.2020.123645.

[198] X. Tang, W. Xia, X. Qu, C. Wang, W. Wang, Y. Liang, Y. Zeng, W. Xiong, M. Cheng, B. Song, C. Zhou, X. Zhao, Structure–performance correlation guided cerium-based metal–organic frameworks: Superior adsorbents for fluoride removal in water, Chemosphere. 312 (2023) 137335. https://doi.org/10.1016/J.CHEMOSPHERE.2022.137335.

[199] S. Singh, A. Mathai Varghese, K. Suresh Kumar Reddy, G. E. Romanos, G. N. Karanikolos, Polysulfone Mixed-Matrix Membranes Comprising Poly(ethylene glycol)-Grafted Carbon Nanotubes: Mechanical Properties and CO2 Separation Performance, Industrial & Engineering Chemistry Research. 60 (2021) 11289–11308. https://doi.org/10.1021/acs.iecr.1c02040.

[200] H. Moussout, H. Ahlafi, M. Aazza, H. Maghat, Critical of linear and nonlinear equations of pseudo-first order and pseudo-second order kinetic models, Karbala International Journal of Modern Science. 4 (2018) 244–254. https://doi.org/10.1016/j.kijoms.2018.04.001.

[201] S. Chatterjee, S. Mondal, S. De, Design and scaling up of fixed bed adsorption columns for lead removal by treated laterite, J Clean Prod. 177 (2018) 760–774. https://doi.org/10.1016/J.JCLEPRO.2017.12.249.

[202] A. Gupta, A. Garg, Adsorption and oxidation of ciprofloxacin in a fixed bed column using activated sludge derived activated carbon, J Environ Manage. 250 (2019) 109474. https://doi.org/10.1016/J.JENVMAN.2019.109474.

[203] Y. Zhang, L. Xiong, Y. Xiu, K. Huang, Defluoridation in fixed bed column filled with Zr(IV)-loaded garlic peel, Microchemical Journal. 145 (2019) 476–485. https://doi.org/10.1016/J.MICROC.2018.11.007.

[204] U. Kumari, S. Biswas, B.C. Meikap, Defluoridation characteristics of a novel adsorbent developed from ferroalloy electric arc furnace slag: Batch, column study and treatment of industrial wastewater, Environ Technol Innov. 18 (2020) 100782. https://doi.org/10.1016/J.ETI.2020.100782.

[205] S. Kiran Mani, R. Bhandari, Efficient Fluoride Removal by a Fixed-Bed Column of Self-Assembled Zr(IV)-, Fe(III)-, Cu(II)-Complexed Polyvinyl Alcohol Hydrogel Beads, ACS Omega. 7 (2022) 15048–15063. https://doi.org/10.1021/acsomega.2c00834.

[206] X. Tang, W. Xia, X. Qu, C. Wang, W. Wang, Y. Liang, Y. Zeng, W. Xiong, M. Cheng, B. Song, C. Zhou, X. Zhao, Structure–performance correlation guided cerium-based metal–organic frameworks: Superior adsorbents for fluoride removal in water, Chemosphere. 312 (2023) 137335. https://doi.org/10.1016/J.CHEMOSPHERE.2022.137335.

[207] H. Zhang, K. Wan, J. Yan, Q. Li, Y. Guo, L. Huang, S.R.B. Arulmani, J. Luo, The function of doping nitrogen on removing fluoride with decomposing La-MOF-NH2: Density functional theory calculation and experiments, Journal of Environmental Sciences. 135 (2024) 118–129. https://doi.org/10.1016/J.JES.2023.01.015.

[208] Y. Ren, F. Wu, G. Qu, N. Ren, P. Ning, X. Chen, M. He, Y. Yang, Z. Wang, Y. Hu, Extraction and preparation of metal organic frameworks from secondary aluminum ash for removal mechanism study of fluoride in wastewater, Journal of Materials Research and Technology. 23 (2023) 3023–3034. https://doi.org/10.1016/J.JMRT.2023.01.198.

[209] Y. Ye, J. Yang, W. Jiang, J. Kang, Y. Hu, H.H. Ngo, W. Guo, Y. Liu, Fluoride removal from water using a magnesia-pullulan composite in a continuous fixed-bed column, J Environ Manage. 206 (2018) 929–937. https://doi.org/10.1016/J.JENVMAN.2017.11.081.

RESEARCH OUTPUT

Published/Accepted Articles in International Refereed Journals

1. **Sikha**, S.; Mandal, B. Ultrasound-Assisted Facile Synthesis of Ce/Fe Nanoparticles Impregnated Activated Carbon for Fluoride Remediation. ***Separation and Purification Technology,*** **2022**, *289*, 120785. **(Elsevier,** Impact Factor 9.136**)**
2. **Sikha**, S.; Mandal, B. Cerium-Based Nanoporous Metal-Organic Frameworks Incorporated with Different Metals for Remediation of Fluoride Ion from Water. ***ACS Applied Nano Materials,*** **2023**. **(ACS,** Impact Factor 6.14**)**.

Communicated/Under Review in Refereed International Journals

1. **Sikha**, S.; Mandal, B. Investigating the Efficacy of Bimetallic Metal-Organic Frameworks (MOFs) as Fluoride Adsorbent in Fixed-Bed Adsorption Columns***. (Under review)***
2. **Sikha**, S.; Mandal, B. Cerium-Based Nanoporous Metal-Organic Frameworks Incorporated with Different Metals for Remediation of Fluoride Ion from Water. ***(Under review)***

Conference Presentations (National and International)

1. **Sikha, S** and Mandal, B. (2022). Graphene Oxide Impregnated MOF for the Effective Remediation of Fluoride from Ground Water. **"*International Conference on Advances in Chemical &Material Science"* (ACMS-2022)**, April 14-16, HIT Kolkata, INDIA.
2. **Sikha, S** and Mandal, B. (2022). Graphene Oxide Impregnated UiO-66 for the Effective Remediation of Fluoride from Ground Water **"*Research and Industrial Conclave"* (RIC-2022)**, January 20-23, IIT Guwahati, INDIA.
3. **Sikha, S** and Mandal, B. (2022). Hierarchical Graphite Oxide Decorated MOFs for Adsorption of Fluoride with Synergistic Effect of Ultrasonication **"*Sustainable Science and Technology"* (NERC-2022)**, April 20-22, IIT Guwahati, India.

4. **Sikha, S** and Mandal, B. (2022). Cerium-Based Metal-Organic Frameworks Incorporated with Metal for the Tuning of Adsorbent Properties to Remediate Fluoride Ion from Water **"*Research and Industrial Conclave"* (RIC-2023)**, April 07-08, IIT Guwahati, INDIA.
5. **Sikha, S** and Mandal, B. (2023). Cerium-based Metal-Organic-Frameworks with Ligand Tuning of the Microstructures for Fluoride Adsorption: Linear and Nonlinear Kinetic and Isotherm Adsorption Models **"*IIChe-CHEMCON"* (2023)**, Dec 27-30, Kolkata, INDIA.

Awards and Achievements

1. Best poster awards, INDIAN INSTITUTE OF CHEMICAL ENGINEERS '***IIChe-CHEMCON'*** **(2023)**, Dec 27-30, Kolkata, INDIA.

Front Page of the Papers Published in Various Reputed International Journals

Separation and Purification Technology 289 (2022) 120785

Contents lists available at ScienceDirect

Separation and Purification Technology

journal homepage: www.elsevier.com/locate/seppur

Ultrasound-Assisted facile synthesis of Ce/Fe nanoparticles impregnated activated carbon for fluoride remediation

Sikha Sikha, Bishnupada Mandal *

Department of Chemical Engineering, Separation Science Laboratory, Indian Institute of Technology Guwahati, Guwahati 781039, Assam, India

ARTICLE INFO

Keywords:
Water treatment
AC/Ce/Fe composite
Fluoride
Ultrasound
Adsorption mechanism

ABSTRACT

Fluoride contamination is a severe problem affecting the safety of drinking water around the world. The study focused on the facile synthesis of activated carbon (AC) impregnated with cerium and iron via ultrasonication and performance evaluation of these novel adsorbents using sono-sorption for defluoridation of drinking water. The use of ultrasound demonstrated maximum removal efficiency of 95.4% just after 20 min compared to shaker, where only 87% fluoride was removed after 60 min using AC having Ce/Fe molar ratios of 2:1 (AC/Ce/Fe–1). The key finding which makes our study outstanding is the rapid increase in adsorption rate upon application of ultrasonication while improving the adsorption capacity. The kinetics data obtained was best fitted with the pseudo-second-order model. The maximum adsorption capacity of AC/Ce/Fe–1 was obtained as 52.3 mg/g at room temperature and the synthesized material maintained its relatively high fluoride uptake up to the fourth cycle. The material shows the highest adsorption capacity as compared to the metal-modified AC available in the literature, making it ideal for fluoride removal from drinking water.

1. Introduction

There are plenty of sources leading to water contamination, usually resulting from the human deed and natural sources posing a severe threat for sustainable water supply worldwide [1]. In industrialization and urbanization, activities like mining and the disposal of untreated domestic and industrial waste containing different toxic chemicals lead to the deterioration of water quality [2]. Fluoride is one such pollutant, which is a threat to human life [3]. Moreover, the right amount of fluoride intake protects a tooth or bone from crumbling, but excess can lead to a chronic disease called fluorosis. Non-treatable fluorosis includes skeleton and dental disease caused by excess accumulation of fluoride [4-6]. Skeletal fluorosis is common in a particular area where the fluoride level in groundwater is high [7]. Furthermore, naturally occurring minerals such as fluorapatite, fluorite, and sodium *hexa*-fluoro-aluminate release fluoride by long exposure to the atmosphere [8]. A variety of remediation techniques, such as membrane filtration [9], electrodialysis [10], ion exchange [11], adsorption [12], coagulation, and chemical precipitation [13] have been explored to tackle the contaminated fluoride water over the years [14,15]. Adsorption has emerged as the most popular and cost-effective technology because of facilitated operation cost, accessible equipment, high adsorption capacity, and cheap adsorbents [16]. Feasible studies on the adsorbent such as mixed metal oxides [17], bio-char impregnated with metal [18], bauxite [19], zeolites [20], activated charcoal [21], metal–organic framework [22], and nanocomposites have been explored for the remediation of fluoride ion from the drinking water. Despite the fact, extensive reports are available for remediation of fluoride from water, it is important to think of some economical and eco-friendly adsorbents with an abundant porous structure to reduce fluoride to a permissible extent from the groundwater. Although activated carbon (AC) can absorb a wide range of contaminants, its adsorption capacity and efficiency might be improved. However, in recent times composite adsorbents infused with one or more metal oxides have gained noteworthy consideration as they have a high affinity towards fluoride [23-26]. Zirconium-modified activated carbon for fluoride remediation was reported in the literature with a maximum adsorption capacity of 28.5 mg/g at 25C temperature within the pH range 3–6 [27]. Lanthanum-modified activated carbon reported in the literature shows 5 times higher adsorption of fluoride ion in contrast to unmodified AC [28]. Impregnation of three metals (magnesium, manganese, and zirconium) on powdered AC using the sonochemical method was reported for effective fluoride ion uptake with the maximum adsorption capacity of 26.3 mg/g in 3 h for the wide pH range 2–10 [29]. Surface-altered

* Corresponding author.
E-mail addresses: sikha@iitg.ac.in (S. Sikha), bpmandal@iitg.ac.in (B. Mandal).

https://doi.org/10.1016/j.seppur.2022.120785
Received 9 January 2022; Received in revised form 1 March 2022; Accepted 3 March 2022
Available online 5 March 2022

ACS APPLIED NANO MATERIALS

www.acsanm.org Article

Cerium-Based Nanoporous Metal−Organic Frameworks Incorporated with Different Metals for the Remediation of Fluoride Ions from Water

Sikha Sikha and Bishnupada Mandal*

Cite This: https://doi.org/10.1021/acsanm.3c04921 Read Online

ACCESS | Metrics & More | Article Recommendations | Supporting Information

ABSTRACT: The adsorption capacity (AC) of the material can be significantly enhanced by the composite synergy between various metals, which in turn modifies the morphology, structure, and functional groups of the material. In this view, the nanoporous bimetal metal−organic frameworks (MOFs) using metals (Ce, Fe, Al, and La), namely, Ce@Fe1:1, Ce@Al1:1, and Ce@La1:1, were synthesized via a one-pot method. The nanoporous bimetal MOFs applied to remove F^- ions from drinking water followed the order of Ce@Fe1:1 > Ce@Al1:1 > Ce@La1:1. Based on the above findings, Ce@Fe1:1 was further synthesized using cerium and iron at different molar ratios to optimize the best possible compositions, namely, Ce-Fu, Ce@Fe2:1, Ce@Fe1:1, Ce@Fe1:2, and Fe-Fu. These nanoporous bimetal MOF composites were applied to remediate the F^- ion from wastewater and Ce@Fe1:1 exhibited the maximum AC of 84.4 mg g^{-1} at 288 K. It is worth mentioning that the utilization of ultrasonication as a mediator for the adsorption study over the conventional method gives excellent relaxation in time as it enhances the reaction kinetics. As a result, the study demonstrated rapid adsorption kinetics, which follows the pseudo-second-order (PSO) model. Moreover, coexisting ions such as NO_3^-, Cl^-, HCO_3^-, and SO_4^{2-} had less effect on the adsorption of fluoride. The adsorption mechanism of Ce@Fe1:1 bimetal MOFs supports the electrostatic attraction and ligand exchange processes, which were confirmed using characterization instruments, such as X-ray photoelectron spectroscopy (XPS) and zeta potential.

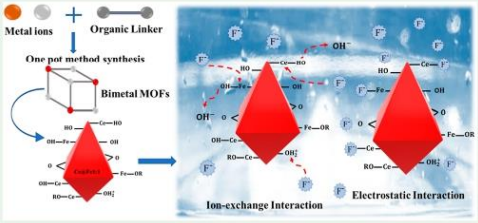

KEYWORDS: *fluoride removal, bimetal MOFs, adsorption, metal−organic framework, wastewater treatment*

1. INTRODUCTION

The main sources of fluoride contamination in groundwater are rocks that contain fluoride-bearing minerals, including fluorapatite [$Ca_5(PO_4)_3F$], fluorite (CaF_2), cryolite (Na_3AlF_6), etc.[1] The dissociation of fluoride from fluoride-rich rocks is demonstrated by eqs 1 and 2.

$$CaF_2 + 2NaHCO_3 \rightarrow 2F^- + CaCO_3 + 2Na^+ + H_2O + CO_2 \quad (1)$$

$$Ca_5(PO_4)_3F + 3H^+ \rightarrow 5Ca^{2+} + 3HPO_4^{3-} + F^- \quad (2)$$

Fluoride leaches out of the rocks as groundwater percolates through them, and as a result, concentrations increase far above the safe level. Additionally, fluoride can leak into groundwater from anthropogenic sources such as coal burning, septic tank seepage, and agricultural applications of pesticides and fertilizers.[2] Fluoride pollution in groundwater is a major concern in countries such as Argentina, Pakistan, Ethiopia, Kenya, India, and China.[2,3] The groundwater consumers in the states of India, i.e., Delhi, Gujrat, Madhya Pradesh, Rajasthan, Chhattisgarh, Punjab, Andhra Pradesh, and Karnataka, are at considerable threat and children are at higher risk than adults.[3,4] The acceptable range of F^- ions in consumable water is 0.8 to 1.5 mg/L, which is set by the World Health Organization.[5] The absorption of excess fluoride in the body causes two types of fluorosis (skeleton fluorosis and dental fluorosis). It is injurious to the common functioning of the kidneys and liver in young children.[6] As a result, removing fluoride from groundwater has been a popular research topic for a while. Techniques including adsorption, filtration, membrane separation, ion exchange, precipitation, and reverse osmosis are frequently used to eliminate fluoride ions from wastewater.[7] The adsorption technique has received increased consideration because of its low cost, operational simplicity, effectiveness, and quick response.[8] Adsorbents like carbon

Received: October 16, 2023
Revised: December 6, 2023
Accepted: December 11, 2023

https://doi.org/10.1021/acsanm.3c04921
ACS Appl. Nano Mater. XXXX, XXX, XXX−XXX